UNIVERSITÀ DEGLI STUDI DI PAVIA

DOTTORATO IN SCIENZE CHIMICHE E FARMACEUTICHE

XXX CICLO

Coordinatore: Chiar.mo Prof. Mauro Freccero

SYNTHESIS AND CHARACTERIZATION OF NANOSTRUCTURED OXIDES FOR THERMOELECTRIC APPLICATIONS

Tutor

Chiar.mo Prof. Umberto Anselmi Tamburini

Tesi di Dottorato di

Alessandro Soffientini

aa. aa. 2014- 2017

UNIVERSITÀ DEGLI STUDI DI PAVIA

DOTTORATO IN SCIENZE CHIMICHE E FARMACEUTICHE

XXX CICLO

Coordinatore: Chiar.mo Prof. Mauro Freccero

SYNTHESIS AND CHARACTERIZATION OF NANOSTRUCTURED OXIDES FOR THERMOELECTRIC APPLICATIONS

Tutor

Chiar.mo Prof. Umberto Anselmi Tamburini

Tesi di Dottorato di

Alessandro Soffientini

aa. aa. 2014- 2017

Abstract

Thermoelectricity is a phenomenon observed in conductive materials allowing the direct conversion of a temperature difference into a potential difference. The efficiency of the thermoelectric conversion is related to the thermoelectric figure of merit (*ZT*), an adimensional parameter which depends on the mean temperature (*T*) between the hot and the cold side of the conductor and on some intrinsic properties of the material: the electrical conductivity (σ), the thermal conductivity (κ) and the Seebeck coefficient (*S or* α), according to the equation $ZT=S^2\sigma T/\kappa$. Higher ZT values allow a more efficient conversion. The properties appearing in the ZT definition, however, are related each other and cannot be optimized independently. The best thermoelectric materials ($1\leq ZT\leq 1.5$) are represented by intermetallic compounds based on toxic and/or expensive elements such as Bi, Te, Se and Sb, that deteriorate in air at temperatures higher than 673 K. Complex oxides has been recently proposed as a potential alternative to these phases, as oxides are generally cheaper, environmentally friendly and more resistant to high temperatures. Their thermoelectric efficiency, however, is considerably lower ($ZT<<1$) than in traditional TE materials. Several approaches have been proposed recently in order to improve the thermoelectric properties of these materials. They include nanostructuring, complex doping and formation of composites.

In this thesis, the attention has been mainly focused on the layered calcium cobaltite ($Ca_3Co_4O_9$, CCO), one of the most promising *p*-type thermoelectric oxides. Pure CCO was synthesized using a simplified sol-gel synthesis starting from stoichiometric amount of metal nitrates, citric acid as complexing agent and water as solvent. The decrease of the thermal conductivity was investigated following the nanostructuring approach. Amorphized powders characterized by a grain size of about 5 nm were obtained by means of a mild ball milling procedure and then sintered using an HP-FAST apparatus. The sintering conditions were optimized in order to maintain the nanostructure (grain size below 10 nm) even in bulk dense samples. The thermal conductivity was significantly reduced, but the residual porosity of the samples (due to geometrical restrictions of the apparatus) affected κ more than the nanostructure did. The electrical conductivity was about halved in dense amorphized samples (ρ>90%), while the Seebeck coefficient was unaffected. An improvement in σ was obtained in silver-doped CCO samples deriving from both micrometric and ball milled sol-gel powders. The sintering caused the silver cations to be reduced into the respective metal, therefore, a general increase of σ and a decrease of *S* was observed. Both these effects resulted less accentuated in amorphized sample. Finally, the improvement of the Seebeck coefficient was investigated in composite samples sintered from mixtures of micrometric and amorphized powders. With non-

homogenized 10% wt amount of amorphized phase a large improvement of *S* of about 40% was achieved, but a reduction of σ of about one order of magnitude was also observed.

The research about nanostructured TE oxides focused also on the thermoelectric properties of homogeneous and patterned films of zinc oxide nanorods as potential standalone thermoelectric generators. A simple and mild hydrothermal approach allowed to obtain well defined nanostructured films, while efficient N-based *p*-type doping was achieved through a thermal treatment using NH_3 gas decomposed at 1173 K as nitrogen source. A doping temperature of 753 K was sufficient to improve the TE properties of homogeneous samples of several orders of magnitude, while a further improvement by about a factor of 5 was observed in patterned samples. These large improvements, together with a theoretical strong reduction in the thermal conductivity induced by the complex nanostructured architecture, could result into a significant improvement of the figure of merit of ZnO in these devices. Finally, the thermoelectric properties of reduced and heavily doped samples of the *n*-type oxide strontium barium niobate ($Sr_xBa_{1-x}Nb_2O_6$, SBN) were investigated. The doping strategy was effective in improving the thermoelectric properties. The, cation substitution, however, was not successful in avoiding the reoxidation process that normally occurs in undoped SBN starting from 573 K, even in presence of low oxygen concentration.

Riassunto

L'effetto termoelettrico è un fenomeno che è possibile osservare in materiali conduttivi sottoposti ad un gradiente termico e che permette di convertire la differenza di temperatura in una differenza di potenziale. L'efficienza della conversione è correlata alla figura di merito termoelettrica (*ZT*), un parametro adimensionale che dipende dalla temperatura media (*T*) tra l'estremità calda e quella fredda e da alcune proprietà intrinseche del materiale: la conducibilità elettrica (σ), la conducibilità termica (κ) ed il coefficiente di Seebeck (*S*), secondo l'equazione $ZT=S^2\sigma T/\kappa$. Alti valori di ZT permettono una conversione del calore più efficiente, tuttavia le proprietà che appaiono nell'equazione della figura di merito sono strettamente correlate l'una con l'altra e non possono essere ottimizzate indipendentemente. Attualmente i materiali termoelettrici più efficienti ($1\leq ZT\leq 1.5$) sono costituiti da composti intermetallici che si basano su elementi tossici e costosi, come Bi, Te, Se and Sb, che si deteriorano in aria a temperature superiori a 673 K. Recentemente, gli ossidi complessi sono stati proposti come una potenziale alternativa poiché, rispetto a questi composti, sono più economici, meno tossici e molto resistenti alle alte temperature sebbene la loro efficienza sia considerevolmente minore ($ZT<<1$). A tal proposito, diverse strategie sono state proposte allo scopo di incrementare le proprietà termoelettriche di questi materiali ed includono l'utilizzo di nanostrutture, il drogaggio e la formazione di compositi.

Questo lavoro di tesi si è focalizzato principalmente sulla cobaltite di calcio ($Ca_3Co_4O_9$, CCO), uno degli ossidi a strati di tipo "*p*" più promettenti. Polveri pure di CCO si possono ottenere utilizzando una sintesi sol-gel semplificata a partire da quantità stechiometriche dei nitrati metallici, acido citrico come complessante ed acqua distillata come solvente. L'effetto della nanostruttura sulla conducibilità termica è stato studiato sinterizzando polveri amorfizzate, caratterizzate da una dimensione dei grani di circa 5 nm, ottenute tramite una blanda macinazione (*ball mill*) ed infine densificate utilizzando la tecnica HP-FAST. A tal proposito, sono state ottimizzate le condizioni di sinterizzazione per ottenere sinterizzati densi caratterizzati da una dimensione dei grani inferiore ai 10 nm. I risultati di questa strategia hanno dimostrato che è possibile ridurre notevolmente la conducibilità termica, tuttavia la porosità residua dei campioni (inevitabile, a causa di restrizioni geometriche dell'apparato di misura), ha avuto un effetto maggiore nel ridurre κ rispetto alla nanostruttura. È stata studiata anche la possibilità di incrementare la conducibilità elettrica di campioni drogati con Ag, ottenuti sinterizzando sia polveri micrometriche che amorfizzate. Tuttavia, durante uno degli step della sintesi sol-gel (la calcinazione) è stata indotta involontariamente la riduzione di Ag nella rispettiva fase metallica, il che ha portato ad un forte incremento di σ ed una rispettiva forte diminuzione di *S*. Infine è stata studiata la possibilità di

aumentare il coefficiente di Seebeck in campioni compositi sinterizzati da miscele di polvere micrometrica ed amorfizzata. Con polveri non omogeneizzate ed un contenuto di polvere amorfizzata pari al 10% in peso, è stato osservato un incremento di S di circa il 40%, ma, allo stesso tempo, una riduzione di σ di circa un ordine di grandezza. La ricerca sui materiali termoelettrici si è focalizzata anche sulle nanostrutture di ossido di zinco. Film omogenei e patternati di nanorods di ZnO sono stati ottenuti con una semplice sintesi idrotermale e drogati con azoto, utilizzato un trattamento termico a base di ammoniaca, ad una temperatura di drogaggio di 753 K. Questa strategia ha permesso di ottenere un efficace drogaggio dell'ossido di zinco di tipo "*p*", che attualmente è ancora poco utilizzato in ambito termoelettrico. È stato raggiunto un sostanziale incremento delle proprietà termoelettriche nei campioni omogenei di diversi ordini di grandezza, mentre l'utilizzo di campioni patternati ha prodotto un ulteriore incremento di circa un fattore 5. Tali significativi miglioramenti, insieme alla forte riduzione della conducibilità termica indotta dalla nanostruttura complessa di queste architetture può risultare in un notevole innalzamento della figura di merito. Infine, sono state studiate anche le proprietà termoelettriche di un ossido termoelettrico di tipo "*n*", il niobato di stronzio e bario ($Sr_xBa_{1-x}Nb_2O_6$, SBN). Campioni ridotti e drogati ad alte concentrazioni sono stati caratterizzati, tuttavia, nonostante un generale miglioramento sotto l'aspetto termoelettrico osservato a seguito del drogaggio, non è stato possibile evitare il processo di riossidazione che si osserva normalmente nell' SBN non drogato a partire da 573 K anche in presenza di una bassa concentrazione di ossigeno.

Summary

1. Introduction

In last 40 years, the worldwide total energy supply has increased from 6101 to 13699 Mtoe (toe = tonne of oil equivalent, 1 toe = 11.63 MWh) in order to face the continuously increasing energy consumption (from 4661 to 9425 Mtoe). The main energy sources are oil (31.3%), coal (28.6%) and natural gas (21.2%). Biofuels, nuclear energy, hydroelectricity and other energy sources (including renewable energy) are still limited to 18.9%,[1], although they experienced a considerable expansion.

Various energy harvesting processes, capable to produce energy from low-intensity sources, have been receiving considerable attention in the last two decades, particularly for applications involving low-power electronic devices, which otherwise must rely on batteries or external electricity suppliers. Piezoelectricity, which transform mechanical energy into electrical energy, is the most widely investigated energy harvesting method, for its ease of application and efficiency. Thermoelectricity (TE), on the other hand, can be employed to increase the overall efficiency of several processes producing large quantities of heat, such as in power plants, incinerators, melting furnaces, gas heaters and many others, by converting part of the waste heat into electric energy. In this regard, thermoelectric devices are competitive compared to other types of generator, as they are relatively simple to fabricate and require very low maintenance, since they have no moving parts or fluids, and present a long lifetime. Moreover, thermoelectric energy is particularly attractive for its possibility to recover energy from the human body heat, in order to sustain small-power wearable electronics or even medical devices or implants.

Thermoelectricity includes three different phenomena: the Seebeck, the Peltier and the Thomson effect. The Seebeck effect and the Peltier effect are conceptually opposite effects, as they describe, respectively, the direct conversion of temperature differences to electric voltage and the opposite process, while the Thompson effect describes the heating or cooling of a current-carrying conductor presenting a temperature gradient. The Seebeck effect owes its name to its discoverer, Thomas Johann Seebeck, which in 1821 found that a thermal gradient formed between two dissimilar conductors can produce electricity. In fact, when two ends of a conductor (a metal or a semiconductor) are held at different temperatures, the charge carriers (electrons or holes) on the hot side present higher thermal velocities and diffuse towards the cold site, where an excess of charge carriers is produced, preventing further diffusion. As a result, a voltage is developed across the conductor (fig. 1-1).

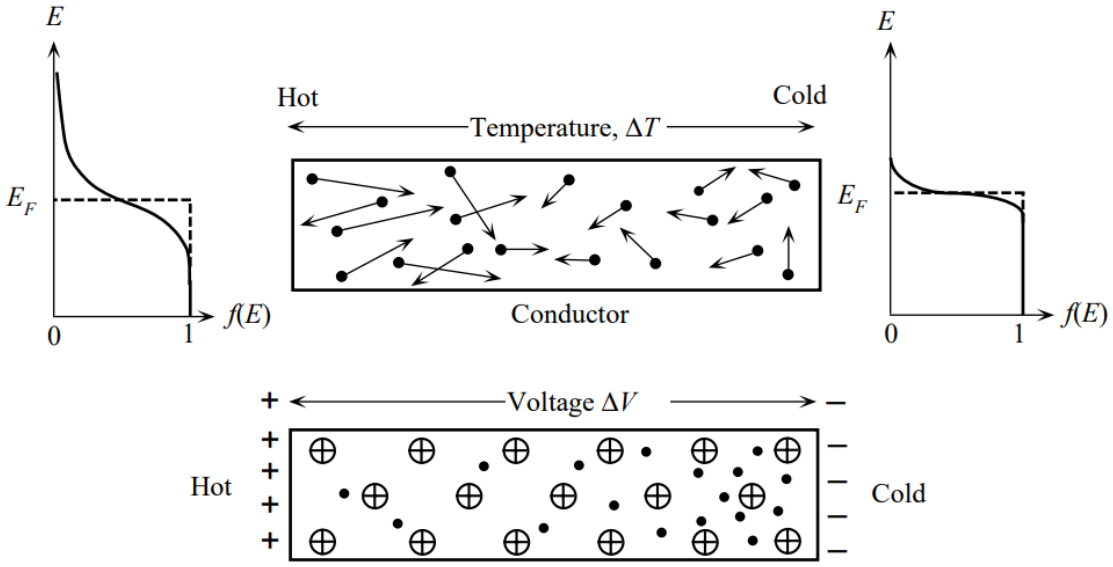

Figure 1-1 Schematic description of the Seebeck effect. The charge carriers at the hot side have higher average velocities and diffuse at the hot side creating an electric potential.

The ratio between the electric potential (ΔV) and the temperature difference (ΔT) is called Seebeck coefficient (S) and is generally expressed as:

$$S = -\frac{\Delta V}{\Delta T}$$

The Seebeck coefficient is defined as positive for holes and negative for electrons. In fact, the sign of the Seebeck coefficient conventionally represents the potential of the cold side with respect to the hot side of the conductor [2]:

$$S = -\frac{V_{hot} - V_{cold}}{T_{hot} - T_{cold}}$$

So, as effect of the thermal gradient, the Seebeck coefficient of *n*-type materials is negative, because the cold side is negatively charged, while *p*-type materials show positive S values, because positive holes are accumulated on the cold side. However, the simple magnitude of the generated thermoelectric potential is not enough to characterize the effectiveness of different thermoelectric materials. The efficiency of the overall heat-to-voltage conversion, in fact, is influenced also by the materials electrical conductivity (σ) and thermal conductivity (κ). The absolute temperature (T), or, to be precise, the mean temperature between the hot and the cold side of the conductor plays also a role.

All these parameters are grouped into a unique adimensional parameter, the thermoelectric figure of merit (*ZT*), proposed by Ioffe in 1949 [3], which represent the intrinsic efficiency of a thermoelectric material and is defined as:

$$ZT = \frac{PF}{\kappa}T$$

where the term *PF* is the so-called power factor and is the product between the square of the Seebeck coefficient and the electrical conductivity:

$$PF = S^2\sigma$$

Thermoelectric materials are generally integrated into a thermoelectric device in form of a series of thermoelements called "legs" to obtain a thermoelectric module, otherwise known as thermoelectric generator (TEG). These legs are connected electrically in series and thermally in parallel and are generally made of the same type of material (*n*-type or *p*-type) or using both *p*- and *n*-type elements, in set-ups that are named respectively "unileg" (fig. 1.2b) or "dual-leg" geometry (fig. 1.2a).

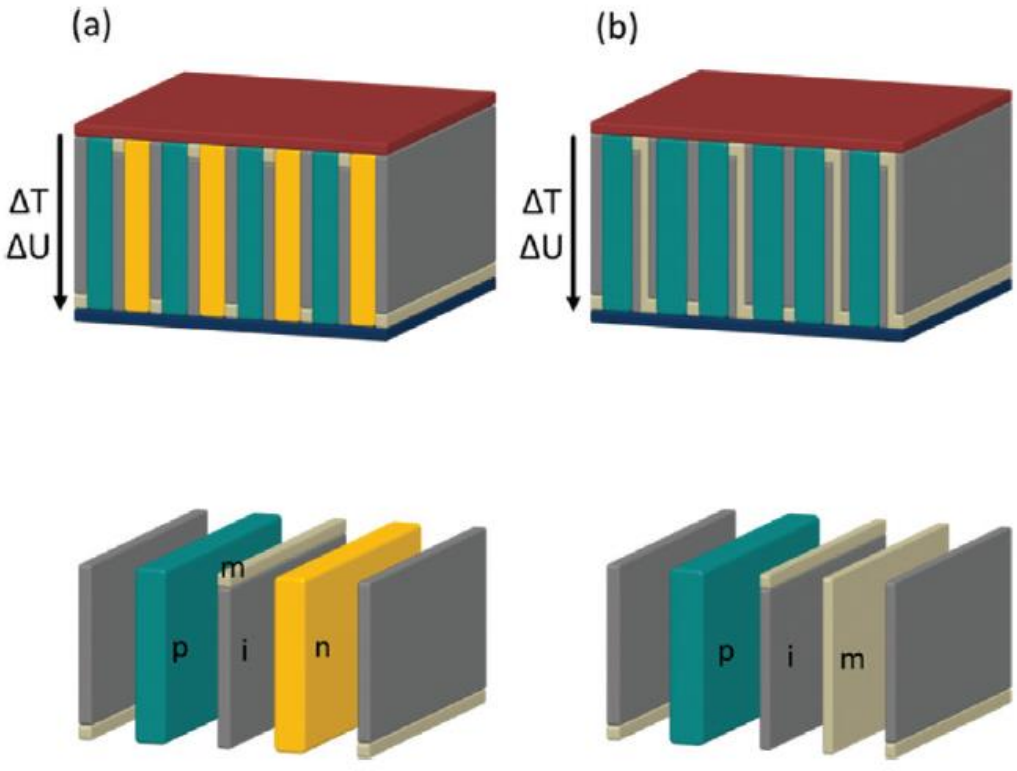

Figure 1-2 Schematic illustration of the dual-leg (a) and unileg (b) thermoelectric generator. Dual leg generators are made of alternating n-type and p-type materials. Unileg generators are made of only one type of thermoelectric material. Modified from [4].

The efficiency of the conversion (η) of a thermoelectric device is directly related to the average figure of merit (ZT_{ave}) between the materials of the thermoelements, according to the equation:

$$\eta_{max} = \frac{T_H - T_C}{T_H} \frac{\sqrt{1 + ZT_{ave}} - 1}{\sqrt{1 + ZT_{ave}} + (T_C/T_H)}$$

Therefore, the higher is the figure of merit, the more efficient is the thermoelectric device (fig. 1.3).

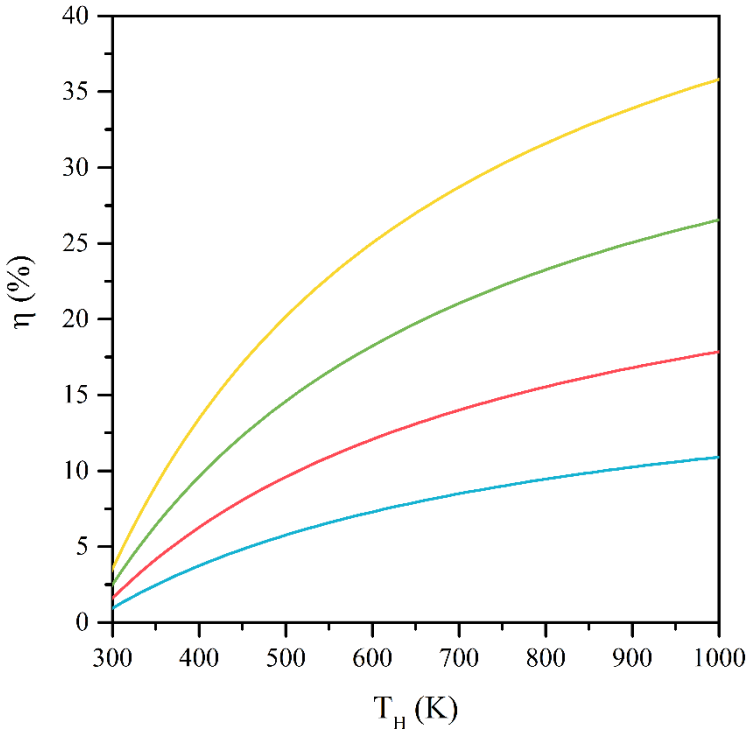

Figure 1-3 Thermoelectric efficiency for ZT_{ave}=0.5 (blue line), ZT_{ave}=1 (red line), ZT_{ave}=2 (green line), ZT_{ave}=4 (yellow line) against the temperature of the hot side. The temperature of the cold side is 298 K.

Achieving high *ZT* values requires maximizing the power factor while keeping the thermal conductivity as low as possible, in order to maintain the thermal gradient across the device. These are conflicting requirements since σ, S and κ are generally related each other. In particular, Seebeck coefficient and electrical conductivity present opposite dependence form the carrier concentration (n) [5]:

$$S = \frac{8\pi^2 {k_B}^2}{3eh^2} m^* T \left(\frac{\pi}{3n}\right)^{3/2}$$

$$\sigma = ne\mu$$

As a result, at a fixed temperature, an increase in σ leads generally to a decrease in S. For example, high conductive metals like silver or copper present generally low Seebeck coefficient (~ 6.5 μV/K at RT), while low-conductive material, such as undoped silicon, exhibits a Seebeck coefficient of 440 μV/K at RT. On the other hand, the thermal conductivity can be expressed as the sum of an electronic (κ_{el}) and a lattice, or phononic, (κ_{ph}) contribution:

$$\kappa = \kappa_{el} + \kappa_{ph}$$

According to the Wiedemann-Franz law, the electronic part of the thermal conductivity is proportional to the electrical conductivity:

$$\frac{\kappa_{el}}{\sigma} = \left(\frac{\pi^2 {k_B}^2}{3e^2}\right) T$$

where k_B is the Boltzmann constant and e is the charge of an electron, and the constant between the brackets, generally indicated by L, is the Lorenz number and is equal to 2.44 x 10^{-8} $W\Omega K^{-2}$. Hence, an increase in σ leads necessarily to an increase in κ. On the other hand, the phononic heat transport is characterized by the following relationship:

$$\kappa_{ph} \propto cvl$$

Where l is the phonon mean free path, v the sound velocity, and c the specific heat of the material. In many materials the total thermal conductivity is dominated by the phononic contribution. Since κ_L is a lattice-based property, the phononic contribution to the thermal conductivity can be related to other lattice-based parameters such as the compressibility (χ), the thermal expansion coefficient, the melting point (T_m), the density (ρ), and the atomic weight (A) of the constituent atoms. All of these parameters can be related each other in the Keyes' equation[6]:

$$T \cdot \kappa_{ph} = \frac{R^{3/2}}{3\gamma^2 \varepsilon^3 {N_A}^{1/3}} \frac{{T_M}^{3/2} \rho^{2/3}}{A^{7/6}}$$

where R is the universal gas constant, γ is the Grüneisen parameter, ε the ratio between vibrations and atomic distances, N_A the Avogadro number, T_m the melting point, ρ the density of the material and A the mean atomic weight [7].

The optimal concentration of charge carriers has been calculated for heavily doped semiconductors to be between 10^{19} and 10^{21} carriers/cm^3 [8] (fig. 1.4).

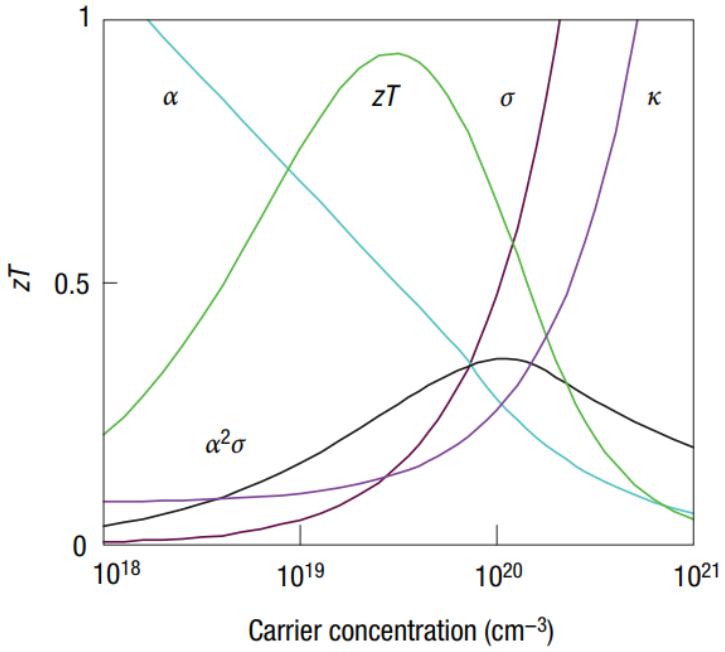

Figure 1-4 Dependency of the thermoelectric parameter on the concentration of the charge carriers in doped Si. The highest figure of merit can be obtained between 10^{19} and 10^{20} cm^{-3}. Taken from ref. [8].

In the last twenty years the research activity on thermoelectric materials has been driven by the concept of phonon-glass electron-crystal (PGEC) introduced in 1995 by Slack [9]. According to this model, semiconductor materials should be designed with suitable crystal structures to allow the best diffusion of the charge carriers, thus achieving high *PF*s, but with thermal conductivity as close as possible to the values presented by disordered solids (κ_{min})[10]. Thermoelectric compound matching these characteristics are represented by cage-like compounds with heavy atoms trapped and rattling inside their cages, due to their efficiency in scattering the heat-carrying phonons. Example of these materials are represented by Co_4Sb_{12}-based filled skutterudites[11]–[13] or intermetallic clathrates[14], [15]. Together with the most competitive trigonal Bi_2Te_3[16]–[18] and the tellurium-, antimony- and germanium-based compounds they can achieve figure of merit higher than unity, while the highest figure of merit achieved up to now of 2.62 at 923 K has been reported by Zhao for SnSe bulk crystals[19]. However, these materials are generally toxic and include rare and expensive elements. Moreover, they present low melting points and must be used in an oxygen-free environment; characteristics limiting their use in high-temperature applications.

A valid alternative to traditional thermoelectric materials is represented by thermoelectric oxides. This class of materials presents several potentially attractive features, as they are environmentally friendly, resistant to high temperatures (oxides can sustain T > 1250 K), while the abundance of their constituents makes them relatively cheap. However, their figures of merit are significantly lower than in traditional thermoelectric material. In recent years, both *p*-type and *n*-type simple or complex oxides have been investigated for their thermoelectric properties. The first observation of an interesting figure of merit in oxides was reported in 1997 by Yakabe *et al* [20] for the *p*-type layered cobaltite $NaCoO_2$ (ZT = 0.54 at 673 K). This was later improved up to 0.78 at 1053 K by Othaki *et al*[21]. However, the use of $NaCoO_2$ in high temperature applications is hampered by the compositional and structural changes deriving from the hygroscopic nature of sodium and by its sublimation at high temperatures (>1073 K) [22], [23]. Other layered cobaltites such as $Ca_3Co_4O_9$, $Bi_2Sr_2Co_2O_9$ and $TlSr_2Co_2O_y$ have attracted attention as promising candidates for thermoelectric applications. This class of materials is characterized by the presence of conducting layers of CdI_2-type CoO_2 alternating with different insulating blocks and exhibit simultaneously large value of electrical conductivity and Seebeck coefficient. The origin of such large *S* can be ascribed to the degeneracy and ratio of the Co^{3+} and Co^{4+} low-spin electronic states together with strong electron correlation, while the low-spin state of Co^{3+} is responsible to bring about the large thermopower. Among *n*-type thermoelectric oxides the most promising are the perovskite-type $SrTiO_3$ and $CaMnO_3$. Strontium titanate has been has been calculated to potentially reach a figure of merit of 0.7 at 1400 K[24], but it can only be used in a strict oxygen-free environment while theoretical studies predicted a figure of merit above unity for calcium manganate[25].

2. Techniques and apparatuses

2.1. HP-FAST

Traditionally, ceramic powders are sintered by means of long thermal treatments carried out at high temperatures. This kind of approach is not suitable to densify nanometric powders as the diffusion mechanisms lead to significant grain growth. The key strategy in maintaining the nanostructure even in high density materials has been the use of a technique called High Pressure-Field Assisted Sintering (*HP-FAST*), also referred as Spark Plasma Sintering (*SPS*)[26]. The HP-FAST apparatus is schematically described in fig. 2-1.

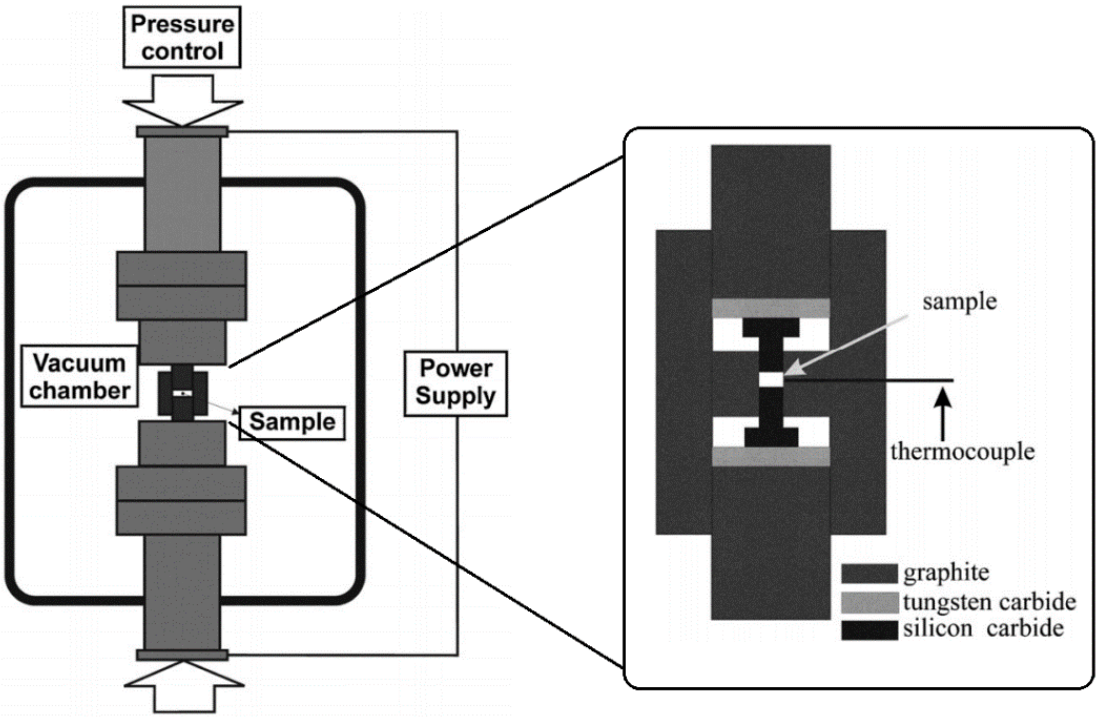

Figure 2-1 Schematic illustration of the HP-FAST apparatus. Modified from ref. [26].

This technique takes advantage from the applications of high uniaxial pressures to allow the densification of powders into dense bulk samples at temperatures lower than in conventional pressureless sintering. Moreover, thanks to the fast heating rates obtained from low-voltage high-intensity current flowing directly though the graphite die, rather than using furnaces or heating elements, high heating rates (even up to 1000 K/min) can be obtained, resulting in shorted densification cycles and allowing to obtained dense samples in few minutes. As a result, the grain growth is strongly reduced.

Briefly, the sintering procedure consists in inserting the ceramic powder into a hollow die typically made of high-density graphite. The cavity can have different diameters: 5, 10, 12,7 and 15 mm. The lower is the diameter, the higher is the maximum sintering pressure that can be transmitted by the plungers to the powder. These die plungers must sustain the pressure, so they are made of silicon carbide for lower dimensions (5 and 10 mm) or high-density graphite for larger diameters (12.7 and 15 mm). The die was then placed between two water-cooled copper electrodes in a vacuum chamber. The electrodes applied also a uniaxial pressure to the die. A minimum pressure was applied to guarantee a good electrical contact between the elements. The heating of the die was achieved through the passage of a low-voltage, high-intensity current. A heating rate of 200 K/min was used for all samples characterized throughout this work. Once the sintering temperature (T_S) is reached, the uniaxial pressure is raised to the required value (P_S) and kept for 5 minutes before cooling at room temperature.

2.2. X-Ray Diffraction

Diffraction patterns of both powders and samples were recorded using the Bruker D8 Advance diffractometer in Bragg-Brentano configuration equipped with a Cu cathode as X-ray source (Cu K_α, λ=1.54 Å). In the case of powders, a zero-background sample holder was used. In the case of sintered samples, the XRD have been taken on the surface parallel to the plane of compression, after polishing the surface using a grinding paper. The sample crystallite size has been determined using the Scherrer equation:

$$< d >= \frac{k\lambda}{\beta cos\theta}$$

Where $<d>$ is the grain size (Å), k is a constant and is equal to 0.9, λ is the wavelength of the x-ray radiation, β is the *FWHM* (full width at half maximum) and θ is the reflection angle. Phase identification was carried out using the PANalytical HighScore Plus software.

2.3. Density measurements

The relative or absolute densities of the samples was calculated using the Archimedes' method, using a specific pycnometer. The measure is performed by weighing a sintered sample both in air and immersed into a solvent of known density. Then, the bulk density of the samples could be calculated according to the following equations:

$$\rho_A = \frac{m_d \cdot \rho_S}{(m_d - m_W)}$$

$$\rho_R = \frac{\rho_A}{\rho_M} \cdot 100$$

where ρ_A and ρ_R are the absolute and the relative density of the sample, m_D and m_W are the weight of the sample in presence and in absence of the solvent, ρ_M the theoretical density of the compound and ρ_S the density of the solvent. The difference between the dry and the wet masses is equal to the mass of the solvent displaced from which the volume of the sample can be obtained using the density of the solvent. Finally, the absolute density can be calculated by dividing the dry mass for the volume, while the relative density can be obtained from the ratio between the absolute density and the theoretical density of the material, Ethanol (ρ=0.789 g/cm^3) was used as solvent to prevent the formation of bubbles on the surface of the sample.

2.4. Planetary mill (ball mill)

The ball milling is a technique that allows the grinding of a material, typically in form of a powder, through impact and attrition forces between the material and the components of the mill: the container (then grinding jar), where a suitable amount of powder is inserted, and the spheres (the grinding balls). Both the jar and the balls must be made of the same materials (tungsten carbide, agate, stainless steel…). A schematic illustration of how the apparatus works is reported in fig. 2-2.

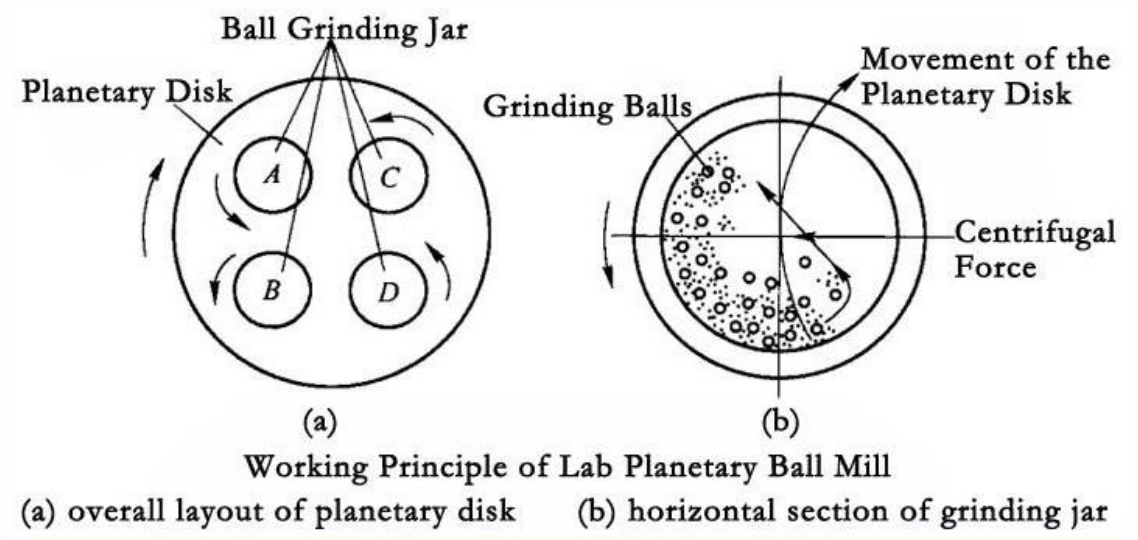

Figure 2-2 Schematic illustration of the working principle of the planetary ball mill. The disk and the grinding jars rotate in opposite direction. The impact forces are enough energetic to reduce the grain size to the nanometric range.

During the milling, the central body of the mill (the planetary disk) rotates around the center of the instrument while the direction of movement of the grinding jar is opposite to that of the disk. The difference in speeds between the balls and grinding jars produces an interaction between frictional and impact forces, which releases high dynamic energies. The interplay between these forces produces the high and very effective degree of size reduction of the planetary ball mill. Solvents such as ethanol or acetone can be added together with the powder to facilitate the reduction of the grain size.

Ball milling procedures were performed using the Fritsch Premium line P7 apparatus, equipped with tungsten carbide grinding jars and grinding balls.

2.5. Thermoelectric measurements

2.5.1. Electrical conductivity and Seebeck coefficient

The electrical conductivities and the Seebeck coefficients of the sintered samples were measured using different apparatuses. One set of devices was available in our laboratory: a four-probe electrochemical cell, a two-probe electrochemical cell and a home-made apparatus for the determination of the Seebeck coefficient. These apparatuses will be referred throughout the thesis as 4P1, 2P1 and S1, respectively. A second device, available at CNR-ICMATE of Padova (Consiglio Nazionale delle Ricerche, Istituto di Chimica della Materia Condensata e di Tecnologie per l'Energia), allowed the simultaneous measurement of the Seebeck coefficient and electrical conductivity, using a four-point setup. This apparatus will be referred as 4PS2 throughout the text.
The 2P1 and 4P1 measurement apparatuses are schematically illustrated in fig. 2-3.

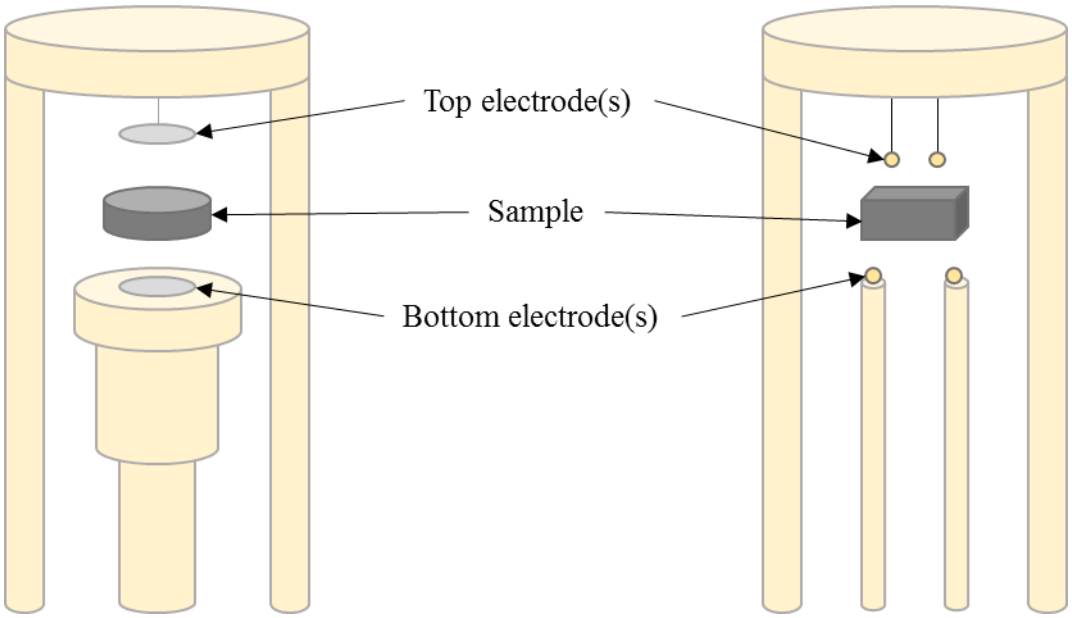

Figure 2-3 Schematic illustration of the two-probe (2P1, left) and four-probe (4P1, right) electrochemical cell. The first is used for low-conducting materials, the second for high-conducting materials.

Briefly, in the 2P1 device (left), the bottom and the top Pt electrodes are mounted onto an alumina support, while the sample is placed between them. This apparatus is made for low conducting samples, so they should be covered by sputtering with a thin layer of a conducting metal (Pt or Au) to improve the electrical contact between the electrodes and the sample. No requirements about the shape of the sample are needed. The 4P1 device (right) is used for high conducting materials. No sputtering of the surfaces is required but the samples must be shaped into suitable rectangular bars (a grinding paper was used for this purpose).

The sample is placed between two couples of Au electrodes. The bottom ones, called the “source” or “signal” electrodes and are used to provide the alternate current to the sample. They are mounted on two alumina rods that can be moved freely and are kept in in tight contact with the sample by means of two springs. The top electrodes are called the “sense” electrodes and are used to measure the voltage drop across the sample. They are fixed to a distance of 1.8 mm. Both 2P1 and 4P1 apparatuses can be sealed using a quartz tube allowing the measure to be performed in controlled atmosphere (Air, N2, O2 or Ar/H2) and can be inserted into a furnace to investigate temperatures from RT up to 923 K.

The electrical conductivities (σ) of the sintered samples were determined by means of impedance spectroscopy connecting the electrochemical cell to a Frequency Response Analyzer (MaterialMates mod. 7260). The impedance spectroscopy technique allows to investigate different conduction processes and measures the response of an electrochemical system afterward the application of a low-intensity alternate signal (a current or a potential) in a range of frequencies. The measured quantity is the impedance (Z), which is the alternate current equivalent of the electrical resistance and, analogously to the Ohm’s law for direct current circuits, it is defined by the ratio between the time-dependent voltage, $V(t)$, and current, $I(t)$:

$$Z=V(t)/I(t)$$

The impedance is also a complex quantity:

$$Z=Z'+Z''=R+iX$$

Where Z' and Z'' are the real and complex contributions to the total impedance, and corresponds to the resistance and to i times the admittance (X), respectively. Generally, by plotting the total impedance in a Z’ vs Z’’ chart, the typical impedance spectra reported in fig. 2-4 can be obtained.

Each point corresponds to a different frequency.

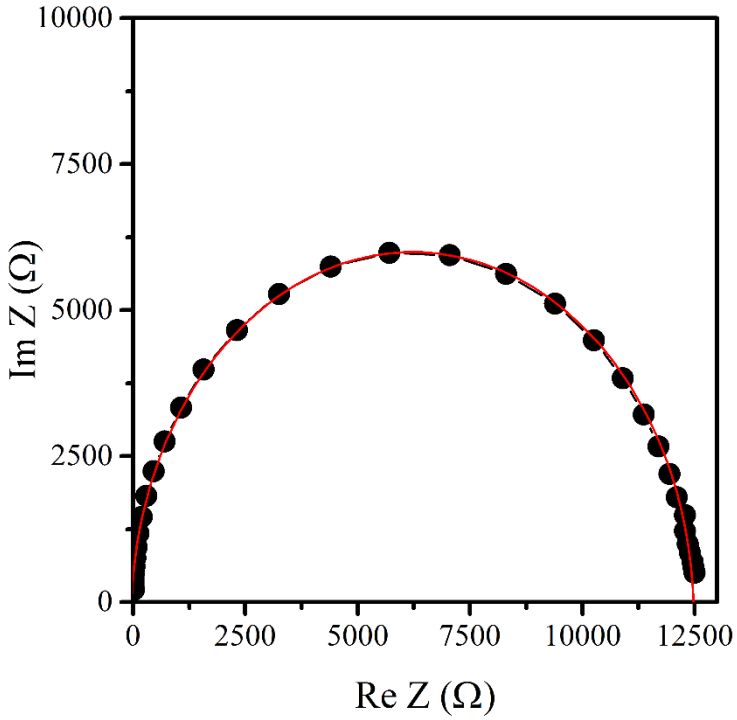

Figure 2-4 Typical impedance spectra of low-conducting materials. The resistance of the sample can be obtained from the intercept of the fit (red line) on the abscissa.

Once the points are fitted, the high intercept of the fit with the abscissa corresponds to the total resistance (R) of the sample. The electrical conductivity can be calculated according to the following equation:

$$\sigma = 1 / \rho$$

$$\rho = R / K$$

$$K = l / A$$

Where ρ is the electrical resistivity calculated by dividing R by the cell constant (K), that is the ratio of the distance between the probe's electrodes (l) to the effective surface area of the samples (A). By measuring the electrical conductivity at different temperatures (T), the activation energy of the process (E_a) can be obtained by plotting the natural logarithm of the electrical conductivity ($ln\sigma$) against $1/T$. The slope of the fit corresponds to minus the activation energy of the process divided by the universal gas constant (8.31 J K^{-1} mol^{-1}). It should be noted that for high conductive materials (4P1 apparatus), the typical impedance spectra are not generated. In their places, points are scattered at low frequencies around the actual resistance of the sample. R is calculated from the average values of the points recorded between 100 and 1 Hz.

The S1 setup for the determination of the thermopower is schematically described in fig. 2-5.

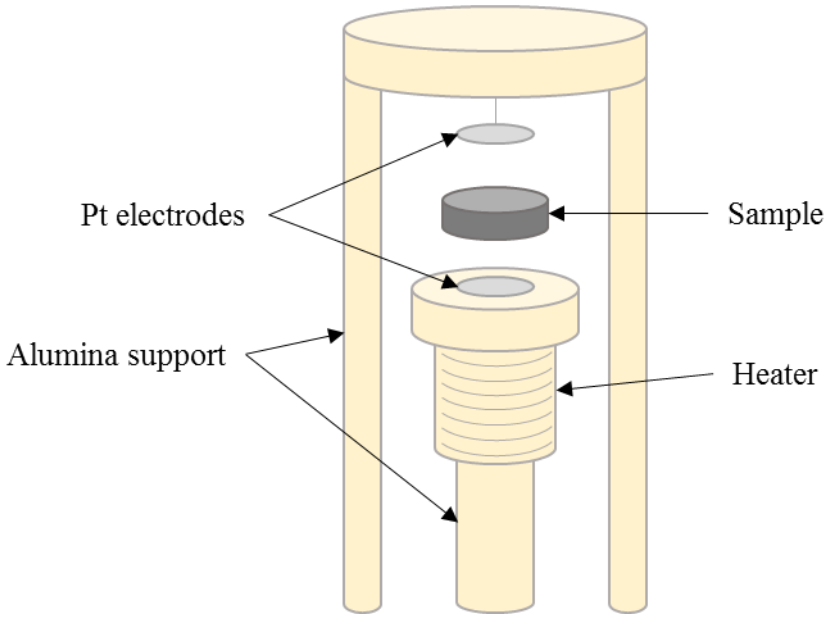

Figure 2-5 Schematic illustration of the electrochemical cell for the determination of the Seebeck coefficient.

The sample is placed between two Pt electrodes and a temperature gradient is produced between them through the Joule heating of an electric heater located in proximity of the lower electrode and powered by a EA-PS 2042-06 B power supply. The temperature of the hot and the cold side can be measured by means of two separated thermocouples. Like already said for the 2P1 and 4P1 apparatuses, the cell can be closed with a quartz tube whenever a specific atmosphere is required and can be inserted into a furnace to determine the Seebeck coefficient at different temperatures.

The thermopower is calculated according to the differential method[27]. For each temperature chosen, three different temperature gradients (ΔT) are produced by flowing an electric current of 0, 0.5 and 1 A (a ΔT is present even with I=0 because of the instrumental geometry) and the generated potential differences (ΔV) are recorded using a multimeter (Hewlett-Packard 34401A). The Seebeck coefficients can be calculated from the slope of the curve fitting the points in ΔV vs ΔT plots.

It should be noted that the S1, 2P1 and 4P1 apparatuses require the manual setting of each temperature and current (for S1) and the thermal stabilization of the system. For these reasons, the determination of the samples' power factors requires from three to five days to be completed.

The 4PS2 apparatus allows the simultaneous determination of the electrical conducitivity and of the Seebeck coefficient. It is schematically illustrated in fig. 2-6.

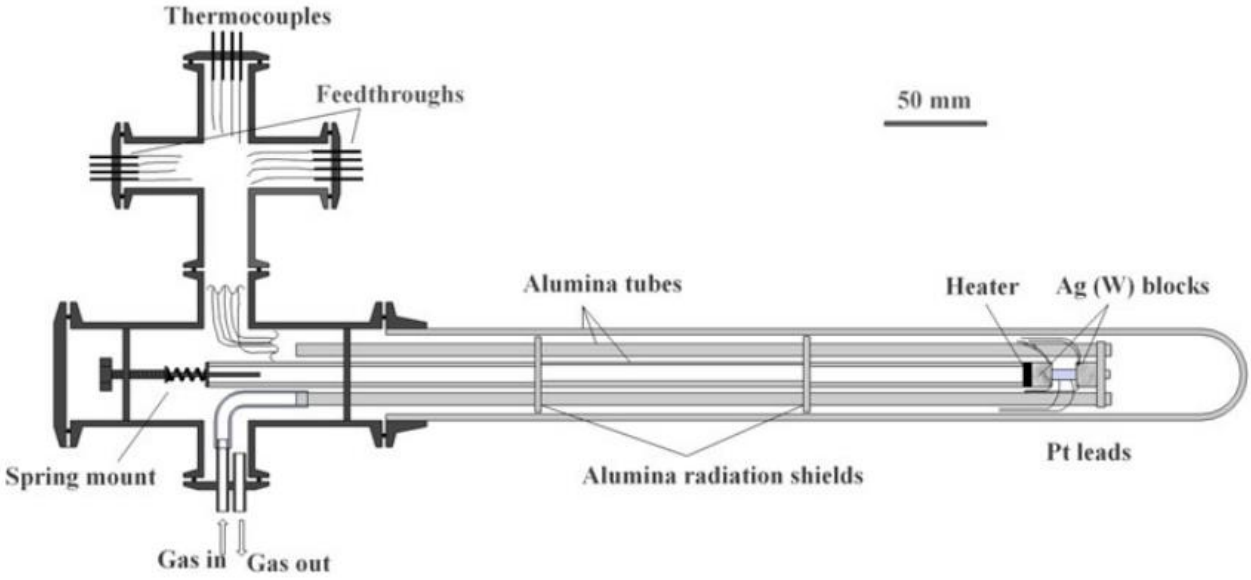

Figure 2-6 Schematic illustration of the 4PS2 apparatus for the simultaneous determination of Seebeck coefficient and electrical conductivity. Taken from [28].

Briefly, the sample is placed between two cylindrical silver blocks (the Ag blocks) mounted on an alumina support. One of them, the hot-side, is in thermal contact with a heater to allow the local increase of the temperature (2 K to 5 K in 10s to 20s), while the sample is kept pressed between the blocks by means of a spring mount that can apply a force up to about 10^2 N. The thermocouples and the Pt loads are inserted into the silver blocks in order to be as close as possible to the sample ends, while the probes for the electrical conductivity are made of two stainless steel needles (at a known distance) pressed onto the sample by means of a specifically designed tool. The apparatus is connected to a Keithley 2182A nanovoltmeter for the measure of the thermopower. To measure the voltage drop for the determination of the electrical conductivity, the apparatus is connected to a Keithley 2636 Source Measure Unit that provides the alternate current signal and to a National Instruments 9211 module for thermocouple readings. A specific LabView software controls these instruments and the power unit of the heater. Prior to the measure, the apparatus is sealed using an alumina tube connected to a gas line. The electrical conductivity is measured using the equation:

$$\sigma = R\frac{l}{A}$$

where l and A are, respectively, the distance between the probes and the area of the sample in contact with the Ag blocks.

R is the resistance of the sample measured from the slope of the ΔV versus I graph, obtained by measuring the voltage drop following a current signal sequence formed of positive and negative alternating steps increasing in modulus imposed onto the silver blocks. The Seebeck coefficient is determined by increasing the temperature of the hot side block and measuring the thermoelectric voltage with respect to the other silver block as a function of the temperature difference. The slope of the line obtained (S_M), taking into account the thermopower of the leads (S_{Pt}), is the Seebeck coefficient of the thermoelectric material (S_{TE}) [28].

$$S_{TE} = S_{Pt} - S_M$$

The thermoelectric properties of thin film samples were measured using the home-made apparatus illustrated in fig. 2-7.

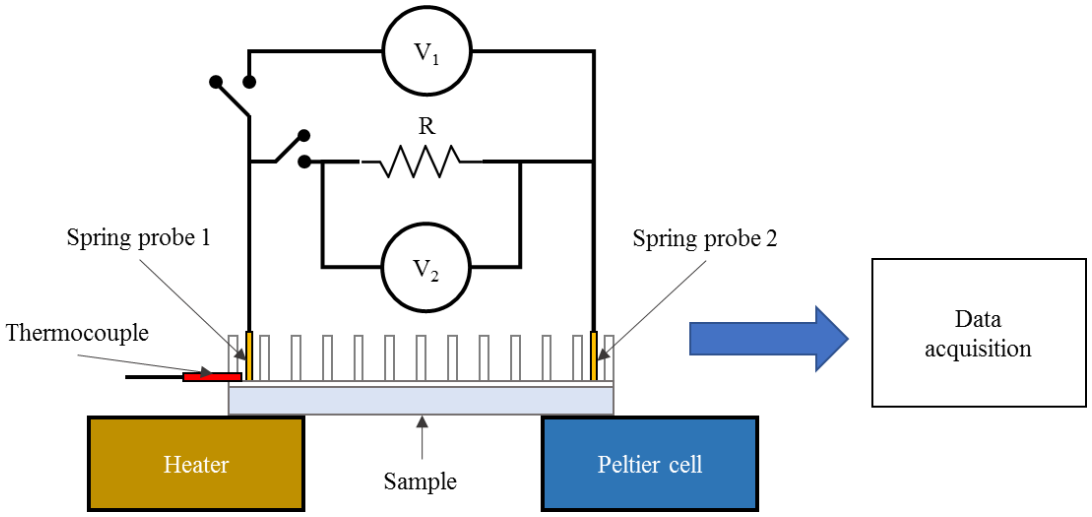

Figure 2-7 Schematic illustration of the apparatus for the thermoelectric characterization of thin film samples.

The sample is placed across a heater (the hot side) and a Peltier cell (the cold side). The temperatures of the two sides are controlled by a system of thermocouples and an Arduino board. The temperature of the Peltier cell was fixed at 298 K, while the hot site was gradually heated from RT to 523 K with a heating ramp of 3 K/min. Two spring probes (the electrodes) made of phosphor bronze for its negligible effect on the thermoelectric properties[29] are electrically connected to two metallic contacts placed at the two end of the substrate and obtained using a silver conductive paste cured at 423 K for 30 minutes. A third thermocouple in contact with the surface of the sample in proximity of the hot side was used to measure the actual temperature while a data acquisition device (Measurement Computing USB-2408) managed by the software TracerDaq was used to measure the output voltage (V_1) generated by the sample. The flowing current (I) was determined measuting the

voltage drop acress and external reference resistance. The generated electric power was calculated by multiplying the voltage and the current generated by the sample.

The Seebeck coefficient (S) was calculated using the integral method[30] determining the thermoelectric potential as a function of the temperature (T_H) of the hot side and then differentiating the curve. The resistance of the samples (R_S) was measured using the HP 34401A multimeter maintaining the entire sample at the same temperature (fig.). It was determined at different temperatures, from RT to 473 K.

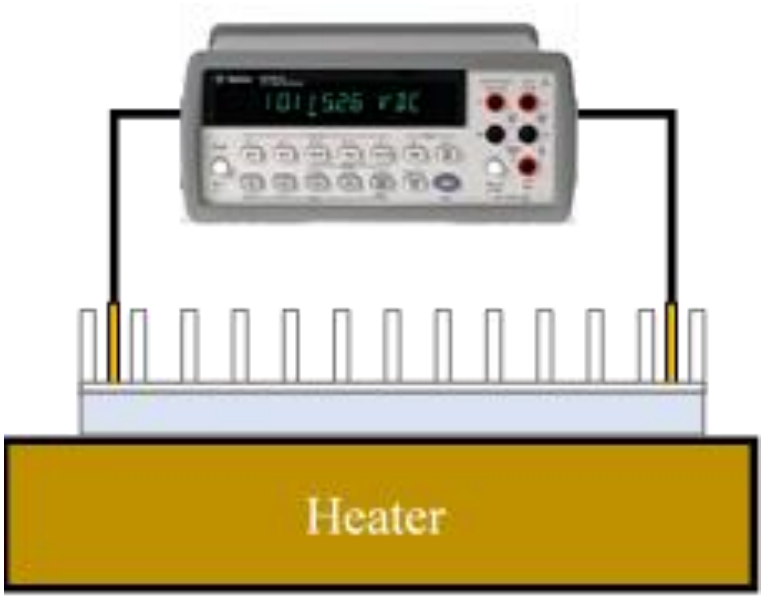

Figure 2-8 Schematic illustration of the setup used for the determination of the resistance of thin films samples.

The electrical conductivity (σ) was calculated from the equations:

$$\sigma = 1/\rho = \frac{l}{R_S \times A}$$

Where ρ is the electrical resistivity, l is the distance between the electrodes and A is the cross-section of the samples perpendicular to the direction of the current.

2.5.2. Thermal conductivity

Thermal conductivities of the samples were measured using two different apparatuses: the Laser Flash Apparatus (Netzsch LFA 457 MicroFlash) and the Physical Properties Measurement System (PPMS, Quantum Design).

The laser flash apparatus is schematically illustrated in fig. 2-6.

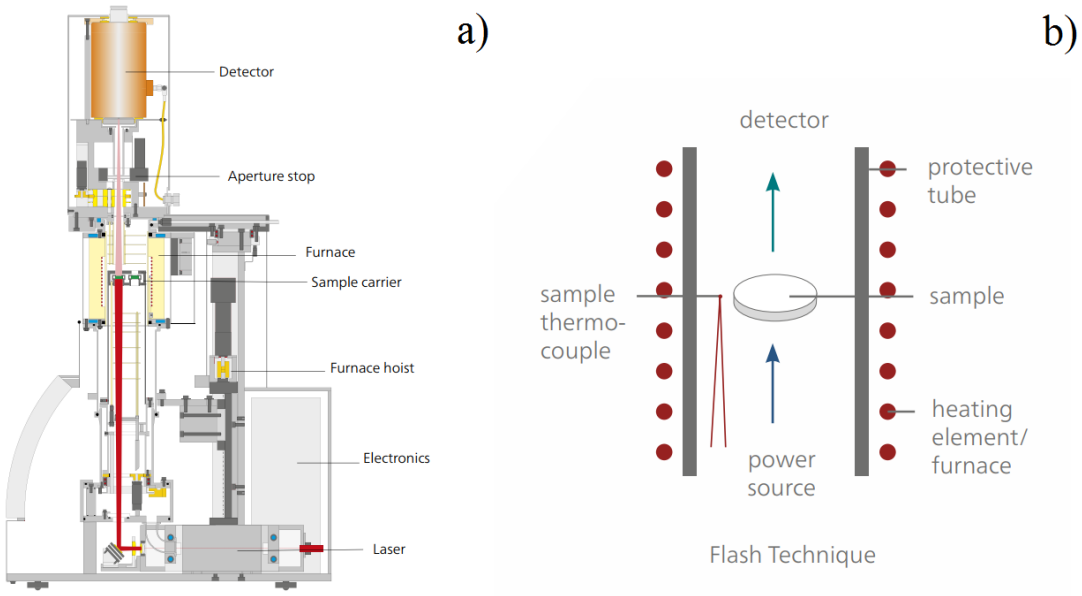

Figure 2-9 Schematic illustration of the Laser Flash Apparatus (LFA). The details about the instrument are reported in (a), while the working principle is briefly described in (b).

Briefly, in a sealed Ar atmosphere (flux of 100 ml/min) a light energy laser pulse is used to heat a graphite cover placed on top of the sample. The temperature increase observed over time on the opposite face of the sample is then detected by an infrared sensor. Temperatures up to 1073 K can be investigated and for each temperature the measure should be performed. However, the LFA apparatus doesn't allow the direct measurement of the thermal conductivity, κ is calculated accord according to the formula:

$$\kappa = \alpha \cdot d \cdot C_p$$

where α is the thermal diffusivity (mm^2/s), d is the geometrical density (g/cm^3) and C_P is the specific heat (J/gK) of the material; α and C_p are the parameter directly acquired from the LFA.

The thermal diffusivity is calculated by the Netzsch Proteus analysis software according to the equation:

$$\alpha = 0.1388 \cdot \frac{h^2}{t_{1/2}}$$

where h is the sample thickness (mm) and $t_{1/2}$ is the time required to reach half (s) of the maximum signal. The specific heat is calculated by comparison with samples of a standard ceramic material with known C_p (Netzsch Pyroceram 9606) close to the specific heat of the material under analysis. The declared relative uncertainty is 3% for diffusivity, 5% for specific heat and 7% for thermal conductivity. The geometrical density was calculated from the mass of cylindrical samples with a diameter of 12.7 mm and a thickness of 2/3 mm (the sample holder dimension).

On the contrary, the PPMS apparatus allows to directly measure the thermal conductivity despite only up to a temperature of 393 K. The system is equipped with a TTO cell (Thermal Transport Option) and Au electrodes are mounted to the samples with the aid of a high thermally conductive thermal paste. The measures are performed by creating a thermal gradient equal to 3%, with respect to the chosen temperature, between the two ends of the sample where two thermocouples are installed. Thanks to the TTO system, the thermal conductivity can be calculated directly considering the power applied, the real temperature difference and the geometry of the samples. The declared uncertainty is 5%.

3. Calcium cobaltite ($Ca_3Co_4O_9$)

3.1. Introduction

The beginning of the study on the *p*-type semiconductor calcium cobaltite (or calcium cobalt oxide, CCO or C-349) as a thermoelectric material could be dated back at 2003, when Shikano and Funahashi extrapolated for this material a figure of merit of ~0.87 at 923 K[31] in a single crystal. This high value of ZT derives from the good combination of thermoelectric properties presented by this material: an electrical conductivity higher than 10^4 S m^{-1}, a relatively low thermal conductivity and a Seebeck coefficient close to 200 μV K^{-1}[32]–[35]. These features, along with its good thermal stability, particularly when compared to the more commonly studied $NaCoO_2$, made calcium cobalt oxide very attractive for high-temperatures thermoelectric applications. Nowadays calcium cobaltite can be considered as one of the most interesting *p*-type thermoelectric oxides. Its properties are strongly related to its unusual crystal structure. In fact, $Ca_3Co_4O_9$ presents a misfit layered structure (fig. 3-1) that should be most properly written as $[Ca_2CoO_3]_{0.62}CoO_2$.

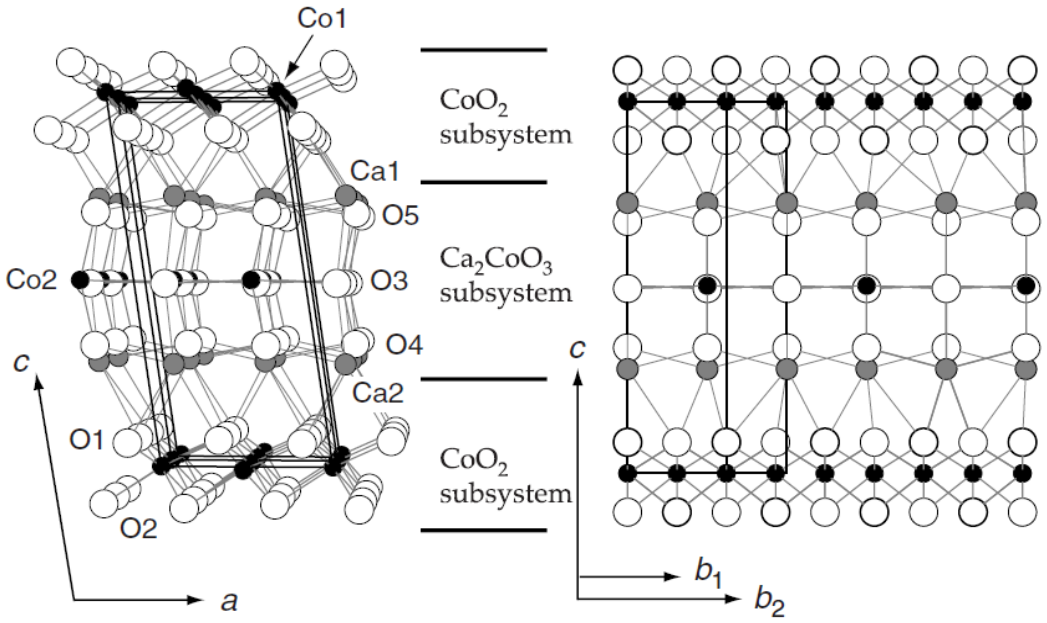

Figure 3-1 Crystal structure of the calcium cobaltite. Black points represent the cobalt ions, white point the oxygen ions and grey point the calcium ions. The monoclinic structure can be observed by looking at the atomic position in the ac-plane (left) and the misfit between the "b" parameters of the CoO_2 and Ca_2CoO_3 layers in the cb-plane (right). Taken from ref. [36].

It can be considered as a monoclinic superstructure which consists in two interpenetrating lattices: one presenting conductive CdI_2-type hexagonal CoO_2 layers with an estimated cobalt valence of 3.5+ and one presenting Ca_2CoO_3 triple-rock-salt-type layers, where the average valence state is calculated to be +2.8 [37]. These two subsystems share the same *a*, *c* and β lattice parameters with *a*=4.8339 Å, *c*=10.8436 Å and β=98.14 ° but differ on the *b*-axis which is equal to 2.8238 Å and to 4.5582 Å for the CoO_2 and the Ca_2CoO_3 layers respectively ($b_{CoO2}/b_{Ca2CoO3}$=0.62)[36]. The electronic conduction is associated to the presence of the CoO_2 layers, which provide a preferential pathway for the charge carriers. On the other hand, the low thermal conductivity derives from the presence of the insulating Ca_2CoO_3 layers, which provide also charge carriers to the CoO_2 layers. Some authors described the electrical conductivity of calcium cobaltite at high temperatures on the basis of the polaron theory. In this model the charge-transport process is driven by the hopping of a hole from Co^{4+} to Co^{3+} and can be represented using the following equation:

$$\sigma = \frac{\sigma_0}{T} exp\left(-\frac{E_a}{k_B T}\right)$$

where E_a is the activation energy of the process, k_B is the Boltzmann constant, T is the temperature and σ_0 is a parameter which contains the charge carrier concentration, the number of neighboring atoms, the hopping frequency, etc. Other authors describe this material as a metallic conductor presenting mobile holes within the CoO_2 layers, with the Ca_2CoO_3 acting as a charge carrier reservoir [38]. Also the Seebeck coefficient of calcium cobaltite has been described on the basis of two different models. In the first, the Mott formula, which is only valid for metallic conduction,

$$S = \frac{\pi^2 {k_B}^2 T}{3e}\left(\frac{\partial ln\sigma}{\partial E}\right)\Big|_{E=E_F}$$

is modified by considering $\sigma = ne\mu$[39]

$$S = \frac{C_e}{n}\frac{\pi^2 {k_B}^2 T}{3e}\left(\frac{\partial ln\mu}{\partial E}\right)\Big|_{E=E_F}$$

where C_e is the electronic specific heat and μ is the energy-dependent mobility.
In an alternative approach, the behavior of the Seebeck coefficient at high temperatures in calcium cobaltite is represented by the Heikes formula:

$$S = \frac{k_B}{e} ln(\frac{g_{3+}}{g_{4+}}\frac{1-x}{x})$$

where g_{3+} and g_{4+} are the orbital degeneracy of Co^{3+} and Co^{4+} in the CoO_2-layer and x is the concentration of Co^{4+}. The Seebeck coefficient can be estimated considering the different spin-state of Co^{4+} and Co^{3+} and all the possible combinations of Co^{3+} low spin state (LS, t_2g^6 eg^0), Co^{3+} intermediate-spin state (IS, t_2g^5 eg^1), Co^{3+} high-spin state (HS, t_2g^4 eg^2), Co^{4+} low-spin state (LS, t_2g^5 eg^0) and Co^{4+} intermediate-spin state (IS, t_2g^4 eg^1) [40].

The layered structure of CCO is reflected in the lamellar microstructure, often presented by its crystals, and in a strong anisotropy in the thermoelectric properties. In fact, the electrical and the thermal conductivity are larger in the *ab* plane than along the *c* direction[41]–[43]. However, single crystals are not suitable for any practical use. When dealing with a polycrystalline material one must face a dramatic reduction in the thermoelectric efficiency, that generally results in lower values of the figure of merit, mainly because of grain size, electrical properties of grain boundary, porosity and grain orientation.

In the last few years, the effort towards the improvement in the thermoelectric properties of calcium cobaltite followed several different strategies that can be classified in three categories: doping, texturing and formation of composites. Doping is the most commonly employed strategy and it aims to increase the valence of cobalt from Co^{3+} to Co^{4+}[44]. Substitution can be obtained on both calcium and cobalt crystallographic sites. Several elements have been investigated as substituent atoms. Up to now, the highest figure of merit (0.74) has been achieved using terbium as dopant in substitution of calcium ($Ca_{2.5}Tb_{0.5}Co_4O_9$)[45] while other rare earth resulted less effective. For example, at temperature lower than 300 K ytterbium on Ca site decreases all the thermoelectric properties [46]. A power factor of 0.553 mW/m K^2 has been obtained for the composition $Ca_{2.9}Yb_{0.1}Co_4O_9$. The substitution of Ho or Lu for Ca resulted also in an increase of both thermopower and electrical resistivity and in a reduction of the thermal conductivity[47], [48]. Among transition metals, a figure of merit of ~0.5 at 1000 K was achieved using a combination of Ag-doped and Ag-added $Ca_3Co_4O_9$[49]. Other metals such as Ir ($Ca_3Co_{4-x}Ir_xO_9$) has also been found to increase the electrical resistivity and the Seebeck coefficient, while reducing the thermal conductivity[50]. W ($Ca_3Co_{4-x}W_xO_9$) reduces both electrical and thermal conductivity, but with $x>0.2$, secondary phases are formed [51], while Ti ($Ca_3Co_{4-x}Ti_xO_9$) can be used to reduce the electrical resistivity without appreciably modifying the Seebeck coefficient values [52]. Cr was used both on calcium or on cobalt site [53], [54].

Cu ($Ca_3Co_{4-x}Cu_xO_9$) decreases the Seebeck coefficient by suppressing the spin entropy[55], while Cd ($Ca_{3-x}Cd_xCo_4O_9$) can increase the electrical conductivity, the thermopower and reduce the thermal conductivity because of the formation of CdO nanoinclusions [56].

Constantinescu and coworkers investigated the effect on the thermoelectric properties deriving from the substitution of alkali and alkali-earth metals, such as Ba, Na, Mg or Sr on the Ca site [57]–[60]. Other strategies involved co-doping. The dual doping with NaF ($Ca_{3-x}Na_xCo_4O_{9-y}F_y$) resulted to increase both electrical conductivity and thermal conductivity, but produced no significant enhancement in the figure of merit [61]. Lu- and Ni- co-doping ($Ca_{3-x}Lu_xCo_{4-y}Ni_yO_9$) decreased electrical and thermal conductivity and increased thermopower [62]. Eu- and Fe- co-doping ($Ca_{3-x}Eu_xCo_{4-y}Fe_yO_9$), on the other hand, allowed to reduce the thermal conductivity[63]. A power factor of 0.51 mW/m K^2 has been be achieved using yttrium instead of europium ($Ca_{3-x}Y_xCo_{4-y}Fe_yO_9$)[64]. Finally, a large figure of merit (~ 0.4 at 973 K) could be achieved using Bi- and Fe- as dopants ($Ca_{2.7}Bi_{0.3}Co_{3.9}Fe_{0.1}O_9$) [65], while the co-doping on the same site ($Ca_{2.8}Ba_xPr_yCo_4O_9$), with *x* and y equal to 0.1, resulted in a ZT of 0.31 at 973 K [66].

Texturing is another strategy that has commonly been used to improve the thermoelectric properties of calcium cobaltite. It consists in inducing the preferential alignment of the CCO *lamellae* along the direction parallel to the CoO_2 conduction layer (the *ab* plane). Texturing takes advantage of the anisotropic properties of calcium cobaltite. Generally, it is achieved using pressure-assisted sintering techniques such as SPS, hot press or sinter forging. The transport properties (both electrical and thermal) result enhanced along the direction of the texturing while the Seebeck coefficient remains unaltered [67]–[70]. The increase in the electrical conductivity is generally larger than the increase in thermal conductivity, resulting in an overall increase in the power factor. In 2010 Yin and coworkers reported the results of the texturing strategy applied on CCO fibers prepared by electrospinning and sintered with SPS. A simultaneous increase in the electrical conductivity and Seebeck coefficient, together with a reduction in the thermal conductivity, was observed, resulting in a figure of merit of 0.4 at 975 K [71].

A last strategy towards an improvement of CCO thermoelectric properties is represented by the formation of composite materials where CCO can be employed as both primary or secondary phases. Up to now, the highest efficiency obtained through this approach derived from the addition of 25% of $La_{0.8}Sr_{0.2}CoO_3$ to CCO, leading to a figure of merit of 0.41 at 1000 K [72]. CCO composite with SiO_2 ($Ca_3CO_4O_9$/0.5 wt.% SiO_2) have been reported to present a power factor of 0.349 mW/m K^2 at 1073 K[73], while in 1-x$Na_{0.77}CoO_2$/x$Ca_3Co_4O_9$ composites, both Seebeck coefficient and electrical conductivity appear to be enhanced (x=0.7), but the high thermal conductivity prevents ZT to be substantially increased[74].

Composites containing Co_3O_4 present reduced thermoelectric properties for all compositions (10, 20 and 50%)[75].

Composite with carbon nanotubes (CNTs) was used by Tang to reduce the thermal conductivity at values lower than the Cahill's limit, however a large increase in the electrical resistivity was also observed and, as a result, the addition of CNTs into the CCO matrix failed in improving the figure of merit[76].

CCO has also been used as secondary phase in composites presenting a matrix based on organic TE materials, such as PEDOT-PSS (poly[3,4-ethylenedioxythiophene]-poly[styrenesulfonate]). In this case an enhanced Seebeck coefficient has been reported, although it was observed that the increase in the thermopower with the CCO content is associated to a strong reduction in the electrical conductivity leading to a reduced power factor [77]. Addition of 15 wt% of CCO to sulfosalicylic acid-doped polyaniline (SSA-PANI) produced an increase of 50 times of the figure of merit of pure SSA-PANI[78].

It has been observed that the thermoelectric properties of calcium cobaltites can be affected by oxygen non-stoichiometry. Oxygen vacancies can be formed in the rock-salt Ca_2CoO_3 layer[79] so that the chemical formula can be written as $[Ca_2CoO_{3-\delta}]_q[CoO_2]$. Up to 5% of oxygen can be removed from this layer (δ=0.14) while maintaining the same crystal structure $[Ca_2CoO_{2.86}]_{0.617}[CoO_2]$ [80]. It has been observed that a reduction in the oxygen stoichiometry leaves the *a*-axis unaltered, while b_{CoO2} and $b_{Ca2CoO3}$ increases and decreases, respectively, and the *c*-axis increases[81]. Karppinen *et al* [81] reported the low temperature (up to 300 K) thermoelectric properties of CCO for different values of δ, and showed that a decrease in the oxygen content induce a small increase in both the Seebeck coefficient and of the electrical conductivity. Moser *et al* [82] investigated the effect of different annealing atmospheres (air and Ar) on the thermoelectric properties of Bi-doped CCO and found that the electrical conductivity is generally higher for air-annealed samples while in the same conditions the Seebeck coefficient is lower, as effect of the counterbalancing effect of the oxygen toward the bismuth doping. A defect chemical model for the oxygen stoichiometry as a function of oxygen partial pressure and temperature has been proposed by Schrade[83]. These authors suggested that the electrical conductivity and the Seebeck coefficient could be explained considering a weakly temperature-dependent itinerant holes model, excluding the small polaron-hopping.

Calcium cobaltite has been already used for the realization of actual thermoelectric modules, in a dual-leg all-oxide configuration together with various *n*-type materials. Since calcium manganate ($CaMnO_3$, CMO) is considered one of the best *n*-type thermoelectric oxides, several CCO/CMO-based prototype TEGs have been reported such as $Ca_{2.7}Bi_{0.3}Co_4O_9$ / $CaMn_{0.98}Mo_{0.02}O_3$[84], $Ca_{2.75}Gd_{0.25}Co_4O_9$ / $Ca_{0.92}La_{0.08}MnO_3$[85], $Ca_{2.76}Cu_{0.24}Co_4O_9$ / $Ca_{0.8}Dy_{0.2}MnO_3$[86], CCO / $Ca_{0.95}Sm_{0.05}MnO_3$[87] or CCO / $Ca_{0.9}Nd_{0.1}MnO_3$[88]. Indium oxide is another *n*-type material that

has been used in association with CCO in the form of both undoped In_2O_3[89] or of layered compound with zinc oxide $(ZnO)_mIn_2O_3$[90].

In this thesis, different strategies have been explored in order to modify the thermoelectric properties of calcium cobaltite:

1. Nanostructuring has been thoroughly investigated as a mean to reduce the thermal conductivity of the material. CCO nanopowders were synthesized using a simplified sol-gel method and then "amorphized" through a mild ball milling procedure. Bulk sintered samples with a grain size of 5 nm (T_S=723 K) have been sintered and characterized for their thermoelectric properties.
2. The electrical conductivity has been increased by Ag substitution on the calcium site to compensate the reduction of the transport properties caused by the nanostructuring. $Ca_{3-x}Ag_xCo_4O_9$ with x=0.1, 0.3 and 0.5 has been synthesized. The highest electrical conductivity was achieved with the highest silver content, but a reduction in the Seebeck coefficient has been observed, despite the highest *PF* was obtained with x=0.3. The x=0.5 powder, the one giving the most conductive sample, underwent a ball milling treatment like undoped powders. As expected, an increase of the electrical conductivity compared to the undoped calcium cobaltite has been observed, but also an increase of the Seebeck coefficient compared to the micrometric analogous.
3. The formation of bimodal composite samples sintered from milled and unmilled powder has been investigated to take advantage of both the anisotropic features and the reduction of the thermal conductivity induced by the nanostructure. No dramatic improvements have been observed, but an increase of more than 40% of the Seebeck coefficient in a specific set of samples (10% wt of milled powder). This result suggested the occurrence of an energy filtering effect.

3.2. Results and discussion

3.2.1. Undoped $Ca_3Co_4O_9$

3.2.1.1. Synthesis of the nanopowders

Calcium cobaltite has been prepared using a modified Pechini sol-gel synthesis, a technique that takes advantage of a chelating agent to bind metallic ions into a polymeric matrix that is then thermally decomposed into oxides. This approach resulted to be very effective, allowing to produce pure $Ca_3Co_4O_9$ using mild conditions and inexpensive reactants. Large-grained $Ca_3Co_4O_9$ powders are often synthesized by a solid-state route using the components metal oxides or related compounds (such as carbonates) as starting materials. The reactants undergo generally a milling procedure in presence or in absence of a solvent like acetone or isopropanol and an annealing generally performed at high temperatures for several hours, even days[83]. On the other hand, solution chemistry approaches are based on the use of metal nitrates or acetates in presence of a surfactant (usually PEG) and allows a precise control over the stoichiometry and a good chemical homogeneity of the final product. Moreover, this approach involves only short annealing treatment, making it suitable for the synthesis of nanometric materials.

The sol-gel synthesis in in a citrate-nitrate system can be considered an auto-combustion process involving a thermal oxidation-reduction reaction and can be described by the Pederson' reaction model[91] as follows:

$$9M(NO_3)_x + (5/2)xC_6H_8O_7 \rightarrow 15xCO_2 + (9/2)xN_2 + 10xH_2O + 9MO_{x/2}$$

where the nitrates act as oxidizing agents and the citric acid as the fuel. *M* indicates the metal ions Ca^{2+} and Co^{2+} ions and x=2 for $Ca_3Co_4O_9$[92].

To obtain the pure CCO phase, stoichiometric quantities of $Co(NO_3)_2$ and $Ca(NO_3)_2$ were weighted and dissolved into a suitable volume of a citric acid solution 0.39 M (distilled water was used a solvent), so that the final concentration of all the metal nitrates was 0.3 M and the molar ratio between the citric acid and all the metal cations was 1.3[93]. This red solution was heated overnight at 373 K under continuous stirring to evaporate most of the solvent until a purple glassy gel is formed. The gel was then dried at 393 K for 2 hours to ensure the complete removal of the solvent. This process caused a significant swelling of the gel that produces a pink solid organic precursor that was grounded and calcined following two different procedures.

The calcination was optimized to realize the best compromise between crystallinity, phase purity and grain size.

Pure calcium cobaltite can be obtained treating the organic precursor at temperatures above 1023 K. At lower temperatures the presence of residual $CaCO_3$ and Co_3O_4 is generally observed. At higher temperatures (1073 K < T_A < 1173 K) highly crystalline pure $Ca_3Co_4O_9$ can be obtained, but at temperatures above 1223 K calcium cobaltite starts to decompose into $Ca_3Co_2O_6$ and Co_3O_4 [94].

In fig. 3-2 are reported the XRD patterns relative to precursor powders calcined in a tube furnace at different temperatures for 2 hours.

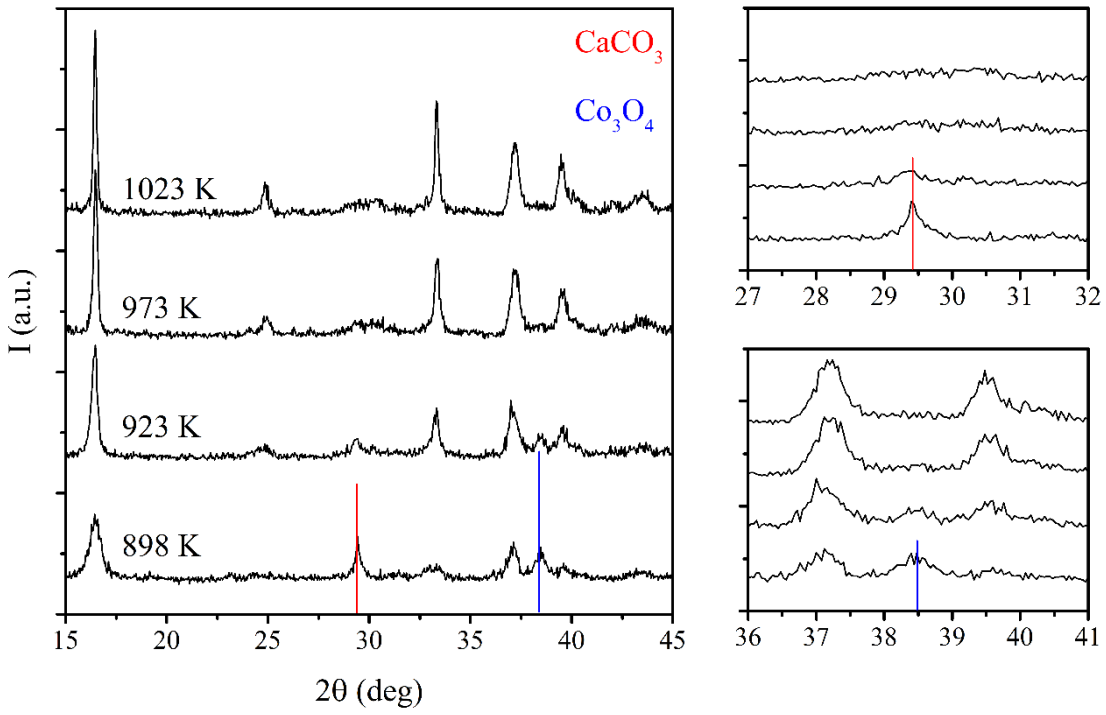

Figure 3-2 XRD patterns of the CCO powder calcined at different temperatures (left). The minimum annealing temperature required to achieve the purity of the phase is 973 K, as observed by the disappearance of the peaks of the impurities ($CaCO_3$ and Co_3O_4).

The phase identification shows that an annealing at 898 K is generally enough to produce the calcium cobaltite phase (42%) which can be indexed using its CoO_2 component (*ICSD* 98-009-5440), although a considerable amount of calcite ($CaCO_3$) and Co spinel (Co_3O_4) can also be identified. These phases amount at 43% and 15%, of the final material, respectively. Increasing the temperature to 923 K the CCO phase content increase to 66%, while the calcite is reduced to 25% and the spinel to 9%. Above 973 K both $CaCO_3$ and Co_3O_4 phases disappear and only the pure calcium cobaltite phase can be observed, while at 1023 K only a slight increase in the intensity of the reflections can be observed, indicating an increase in the crystallinity of the phase. The purity of the phase obtained at 973 K could be related to the quantity of heat-treated organic precursor.

It has in fact been noticed that when a considerable volume of precursor is treated, the annealing of the material at the bottom of the crucible tend not to be complete leading to the formation of calcium carbonate, thus affecting the purity of final product (fig 3-3).

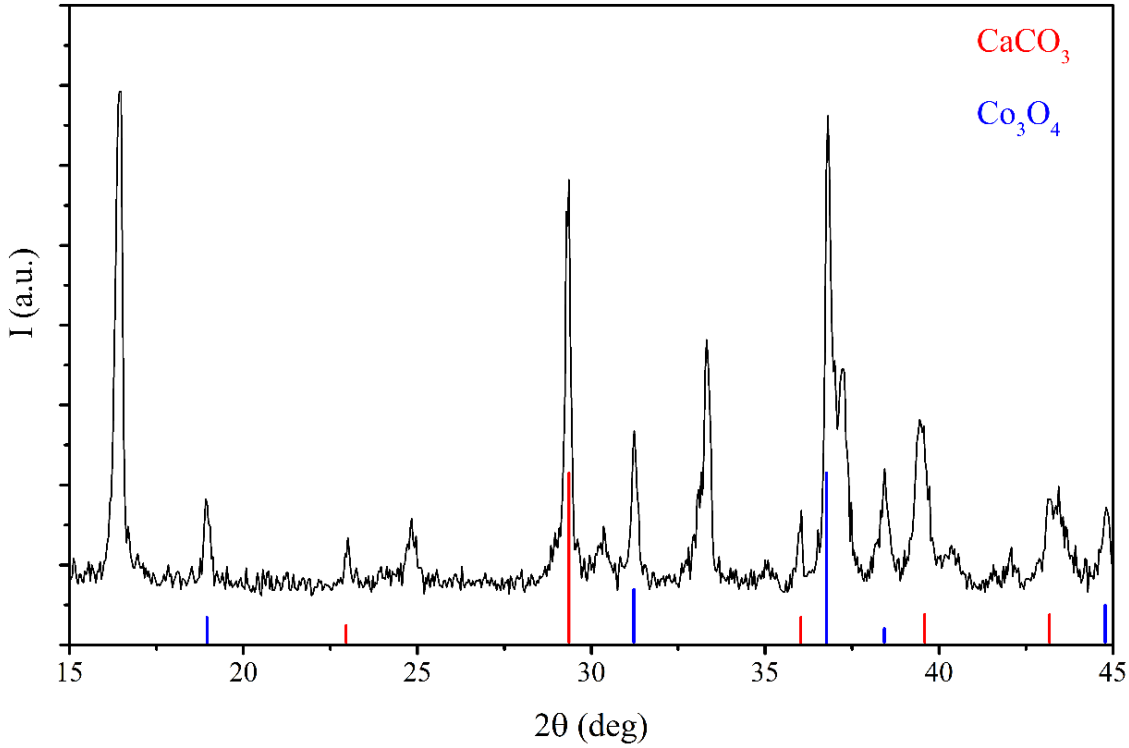

Figure 3-3 XRD pattern of the CCO material at the bottom of the crucible when a considerable volume of organic precursor is heat-treated. The peaks of the $CaCO_3$ (red) and Co_3O_4 (blues) are clearly visible.

This problem can be reduced by increasing the annealing temperature. The larger is the amount of the material, the higher is the temperature necessary to produce pure $Ca_3Co_4O_9$.

On the basis of these observations, two annealing strategies have been optimized in order to obtained pure calcium cobaltite characterized by different grain size. The first strategy, named "method A", consists in the direct calcination of the entire precursor in a muffle furnace at an annealing temperature (T_A) of 1073 K for 2 hours. Calcium cobaltite prepared with this strategy and sintered at both 1023 K and 1073 K was characterized by a grain size of more than 200 nm, so it will be referenced in the following as "sub-micrometric", or CCO-A. The second strategy, called "method B", involves a pre-treatment of the precursor at 673 K to remove the organic matrix, followed by a calcination in a tube furnace at 973 K for 2 hours. The pre-treatment helped to achieve a better purity of the phase. Calcium cobaltite prepared using this method was characterized by a lower grain size and it will be referred in the following as "nanometric", or CCO-B.

This method, however, resulted unsuitable for the synthesis of large quantity of material. Fig. 3-4 shows the diffraction patterns of CCO powders prepared following the method A and B. The peaks were indexed using four Miller indices according to the method used by Miyazaki *et al*[36]:

$$\boldsymbol{q} = h\boldsymbol{a}^* + k\boldsymbol{b_1}^* + l\boldsymbol{c}^* + m\boldsymbol{b_2}^*$$

with b_1 and b_2 referring to the CoO_2 part and to the Ca_2CoO_3 part of the structure, respectively.

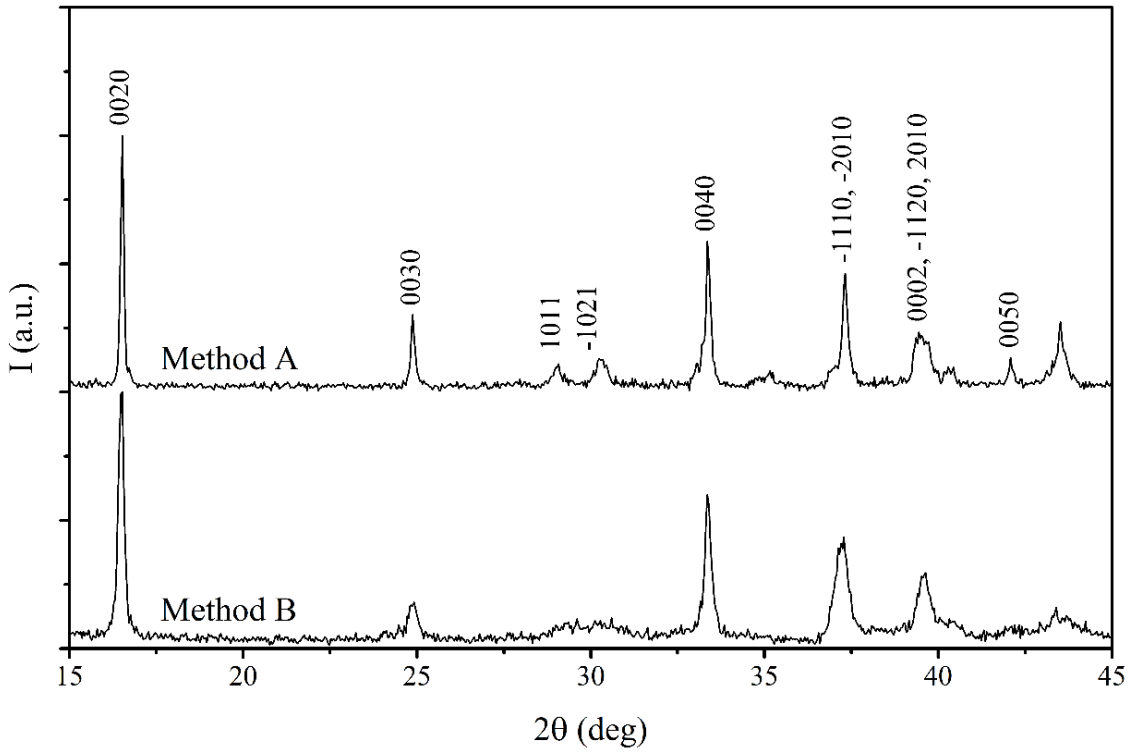

Figure 3-4 XRD pattern of the CCO powder annealed using method A (top) and method B (bottom). Method B ensures the purity of the phase starting from 923 K (no extraneous peaks are present) and the lower annealing temperature allows to achieve a lower grain size of the CCO particles, as it can be clearly seen from the broadening of the diffraction peaks. The peaks are indexed according to ref. [36].

The analysis of the average crystallite size resulted to be difficult in this phase, presenting a strongly anisotropic *habitus*. For this reason, we decided to report the grain size calculated using the most intense diffraction peak (*0020*). This represents the maximum grain size, as it refers to a crystallographic plane parallel to the basal planes of the *lamellae*. The grain size measured considering other crystallographic planes are considerably smaller. In the sub-micrometric samples (CCO-A) it was not possible to evaluate the grain size using the XRD data, because the diffraction peaks were too narrow.

The grain size was calculated for the nanometric powders (CCO-B) only, and are reported in tab. 3-1:

Table 3-1 Grain size of CCO powders calculated using different diffraction peaks from method "B" XRD pattern.

Peak (hkl)	***Calculated grain size (nm)***
0020	62
0030	25
1011	10
−1021	5
0040	44

As mentioned before, the grains anisotropy causes the grain size to be strongly dependent on the family of planes responsible of the XRD reflection. In fact, all the peaks relative to the *00l0* family were sharper. A grain size of about 60 nm was evaluated for the *0020* reflection. Other peaks appeared to be very broad, in some cases leading to a diffuse band.

From the SEM micrographs of the powders, taken using a Tescan Mira3 HR-SEM with an accelerating voltage of 20 kV, reported in fig. 3-5 it was possible to observe the difference in the grain size (<*d*>) of the particles annealed with method A and B. In fact, CCO-A powders can reach a grain size of about 500 nm, while CCO-B particles are clearly smaller.

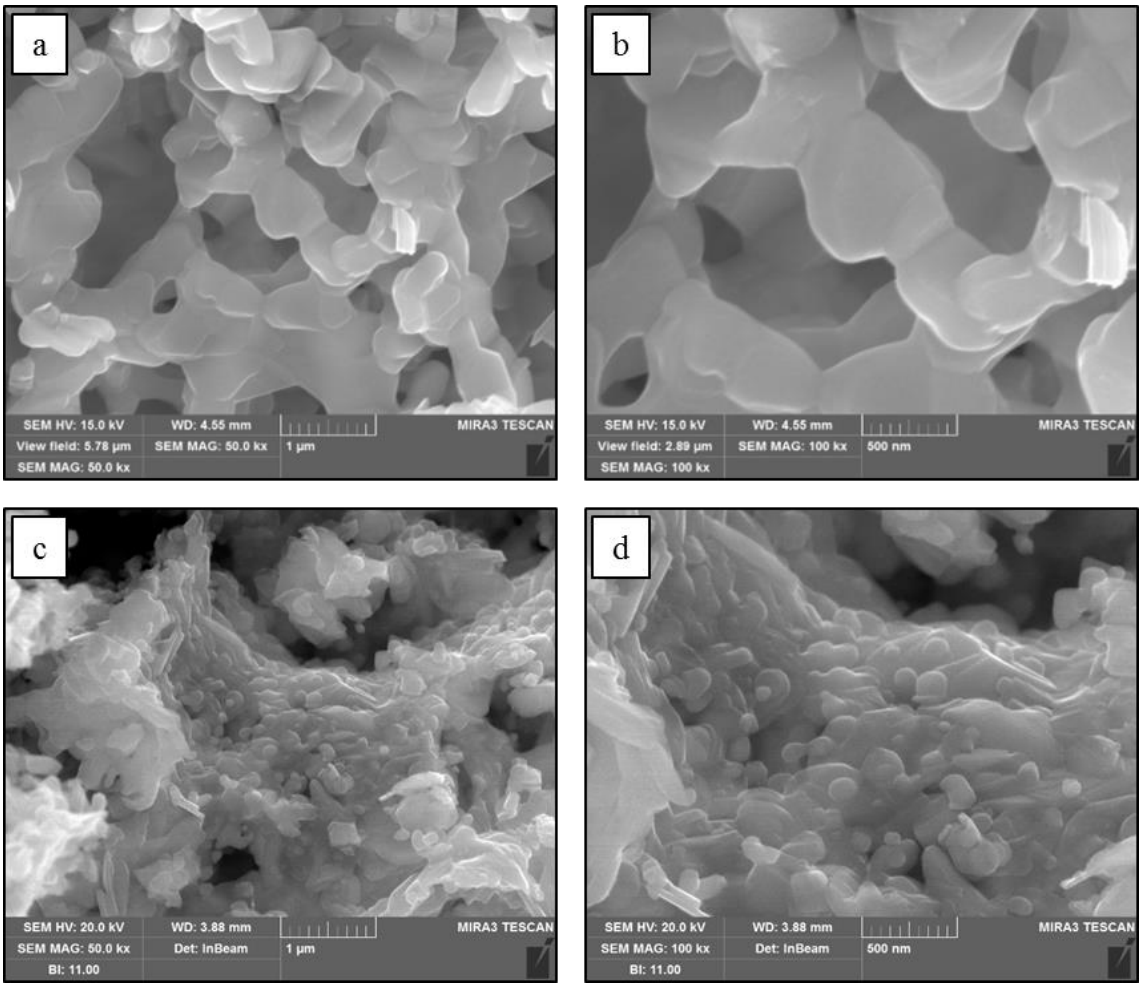

Figure 3-5 SEM micrographs of CCO powder annealed with method "A" (a, b) and with method "B" (c, d).

The grain size in these samples was also evaluated using also an image processing software (ImageJ). The $<d>$ values for the submicrometric powder resulted to be about 1 μm, while for CCO-B powders the dimension was about 100 nm, one order of magnitude lower compared to CCO-A powders, but considerably higher if compared to the results obtained using the Scherrer equation on the XRD data.

Other research groups were able to produce CCO nanoparticles characterized by a grain size of about 20 nm by simply adding PEG as dispersant, a dimension that was retained even at higher annealing temperatures (1023 K)[95]. However, those powders were then sintered using conventional annealing treatment at 1123 K with no indication of the grain size in the sintered samples.

3.2.1.2. Sintering of the undoped powders

To overcome the problems related to the conventional sintering, both the A- and B-CCO powders were densified using a home-made High Pressure-Field Assisted Sintering (*HP-FAST*) apparatus.

The sintering of the calcium cobaltite powders produced a microstructural change, which involved an increase in the anisotropy of the CCO sample. In fact, the diffraction pattern of sintered samples (fig. 3-6) evidences as all the peaks belonging to the *00l0* family are intensified (in particular the *0020*, *0030* and *0040* reflections), while the peaks relative to the other families result depressed.

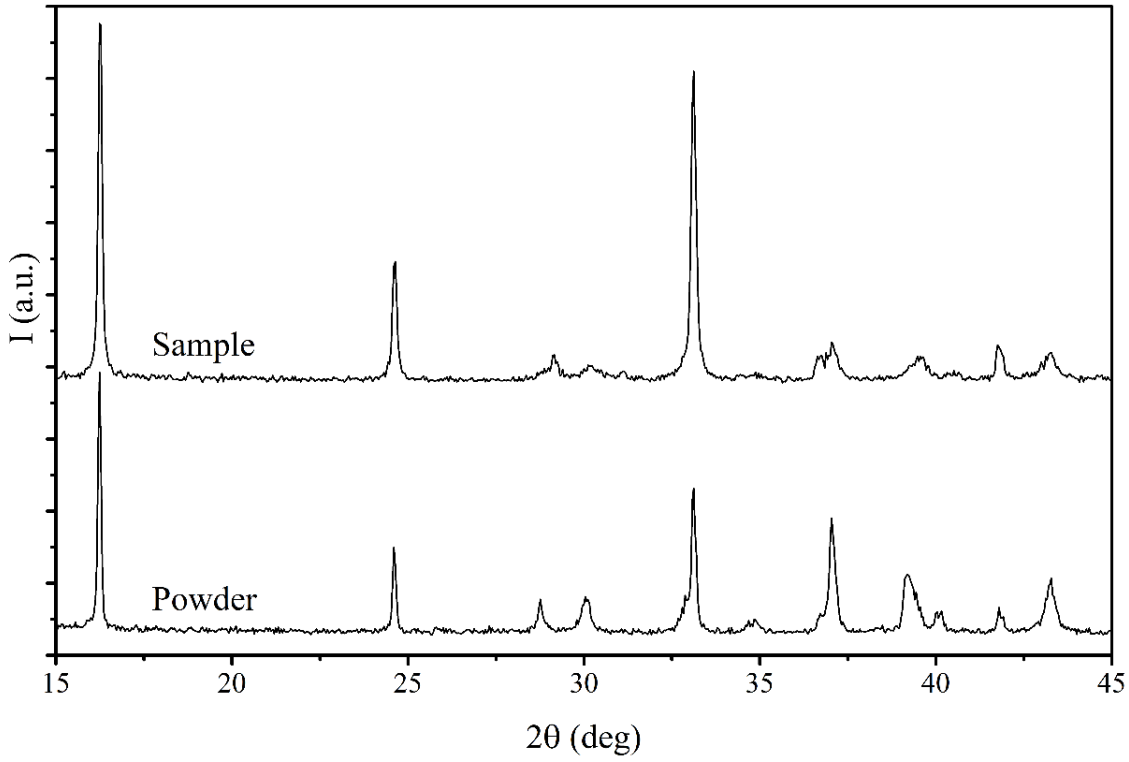

Figure 3-6 XRD patterns of CCO sample and CCO powder. The CCO sample exhibits intensified peaks belonging to the 00l0 family because of the preferred orientation of the lamellae on the c-plane following the HP-FAST sintering.

This result suggests an enhancement in the preferred orientation of the lamellae parallel to basal *c*-plane, deriving in part from the growth of the crystals and part from the pressure applied during the sintering process.

The SEM micrographs confirm this observation (fig. 3-7) showing how the sintering process increases drastically the lamellar habitus of the material.

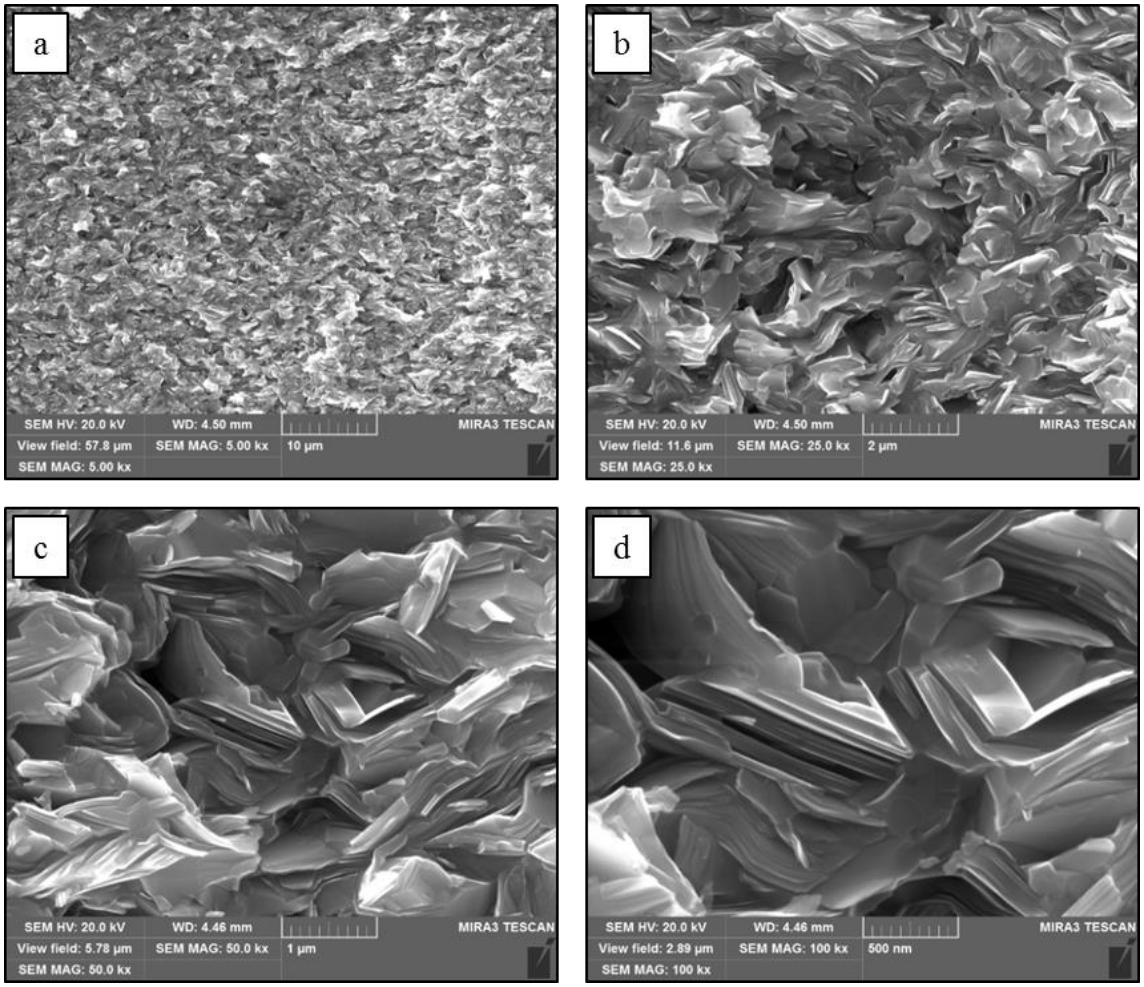

Figure 3-7. SEM micrographs of sintered CCO sample. The lamellar habitus of the powders is clearly visible, in particular with higher magnification (d).

To obtain high-density bulk sintered samples there are some aspects which must be considered. First, the sintering temperature can be deduced by looking at the displacement profile, a parameter related to the thermal behavior of the powder (expansion or contraction), shown in (fig3-8).

Evidences of densification of CCO powders were observed between 673 and 773 K, when the displacement and the sintering pressure underwent an evident collapse.

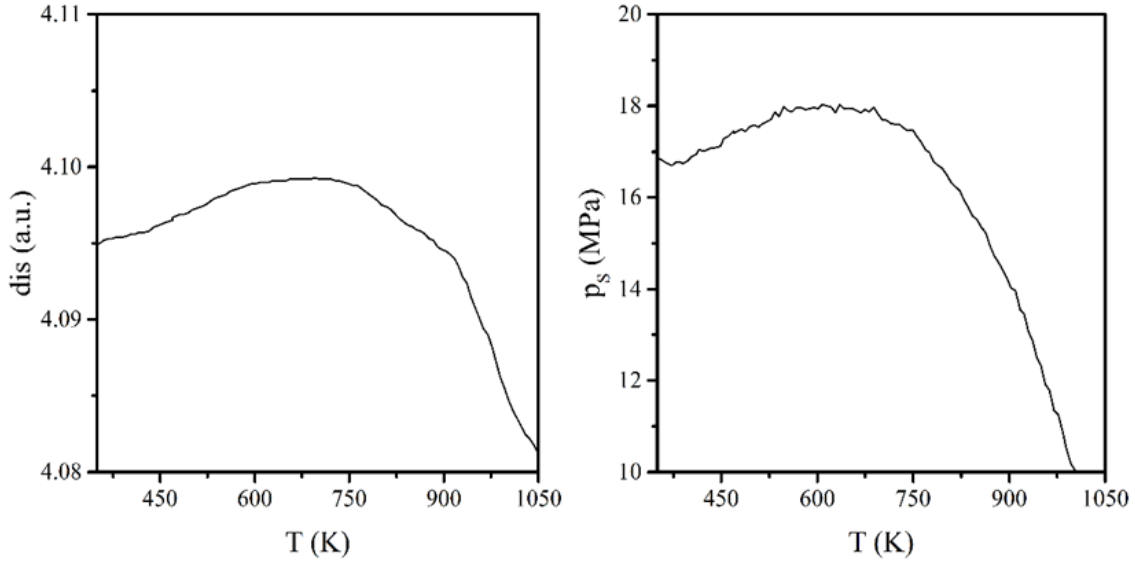

Figure 3-8 Typical displacement (left) and pressure profile (right) during the HP-FAST sintering of CCO powders. Evidences of densification of CCO powders were observed between 673 and 773 K when the signal starts to collapse.

Then, it must be noted as this oxide presents a peculiar behavior during the FAST sintering process. The oxide, in fact, evidences a dramatic plastic deformation when the uniaxial pressure is applied at high temperature. The deformation is so severe to make difficult the containment of the sample when high pressures are applied. Most of the sample, in fact, flows through the interstice existing between the plungers and the body of the die and is lost. This is a behavior extremely unusual in oxide phases and is worth further investigations. From our perspective, however, it complicated the densification process, making impossible to apply very high pressures in order to obtain high level of densification at relatively low temperatures. On the other hand, the use of low sintering temperatures is essential not only for maintaining the nanometric nature of the material, but also for avoiding the decomposition in a reducing environment of the material into CoO and CaO, a process that is observed on the surface of the sample at temperatures above 923 K (fig. 3-9) [80].

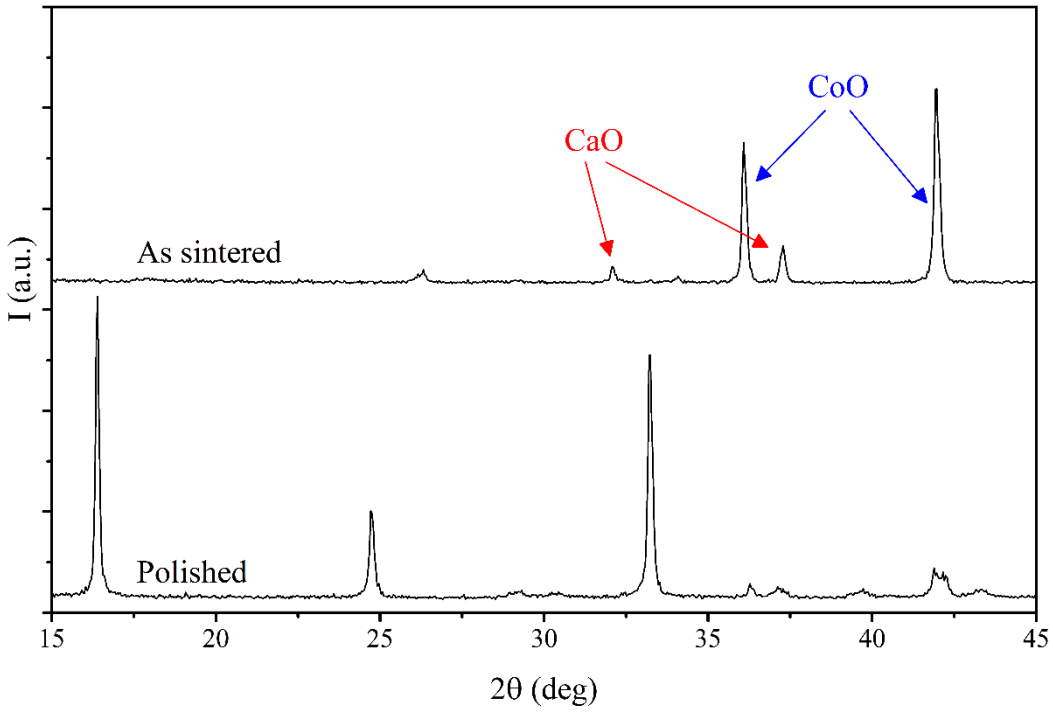

Figure 3-9 XRD patterns of CCO samples before (top) and after (bottom) polishing with grinding paper. The reducing environment of the HP-FAST apparatus causes the surface of the sample to be reduced into CaO and CoO, as it can be seen from the presence of only the respective diffraction peaks in the "as sintered" pattern.

As a result, undoped calcium cobaltite samples were FAST sintered using moderate uniaxial pressure between 70 and 180 MPa and temperatures between 873 K and 1073 K. Fig. 3-10 show the dependence of relative density from sintering temperature and applied uniaxial pressure for undoped CCO samples, measured using the Archimedes' method and calculated considering a theoretical density of 4.677 g/cm^3[96].

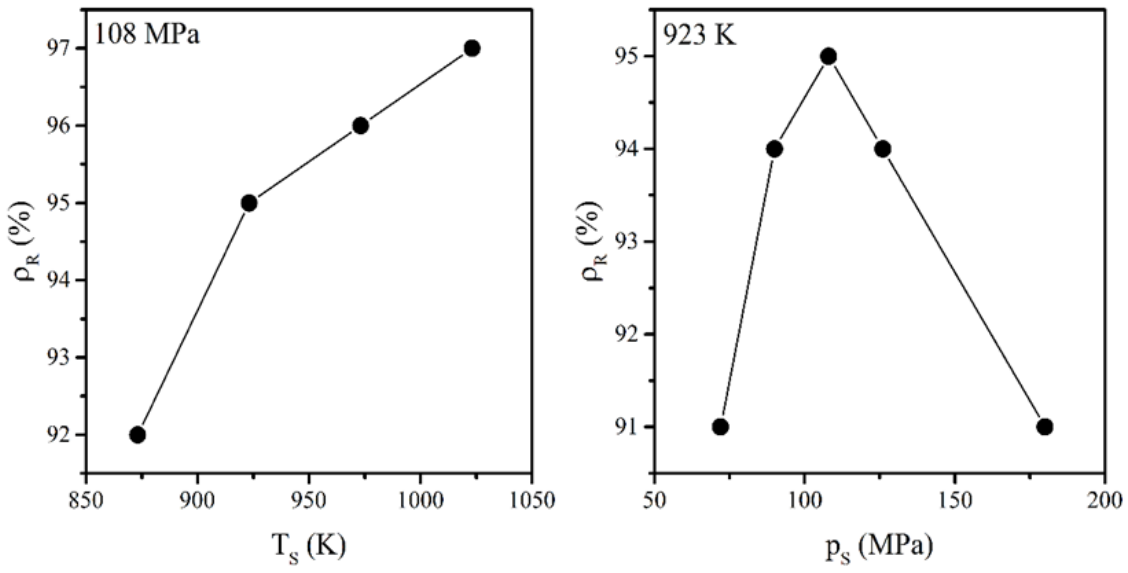

Figure 3-10 Dependency of the relative density from the sintering temperature (left) and the applied uniaxial pressure (right). The densities were calculated using the Archimedes' method.

At a sintering temperature of 923K it was observed as a pressure increase produced at first an increase in relative density, from 91% at 72 MPa to 95% at 108 MPa, followed by a significant decrease. So, 108 MPa was chosen as optimal sintering pressure for the CCO-A powders. Varying the sintering temperature in the interval between 873 and 1023 K it was observed a regular increase in relative density 92% to 98%.

3.2.1.3. Thermoelectric properties of undoped CCO

The thermoelectric properties relative to undoped calcium cobaltite samples sintered according to the procedure described previously (108 MPa, 923 K, d_R=95%) were measured using the 4P1 and S1 apparatuses and are reported in the following. The electrical conductivity as a function of temperature is shown in fig. 3-11.

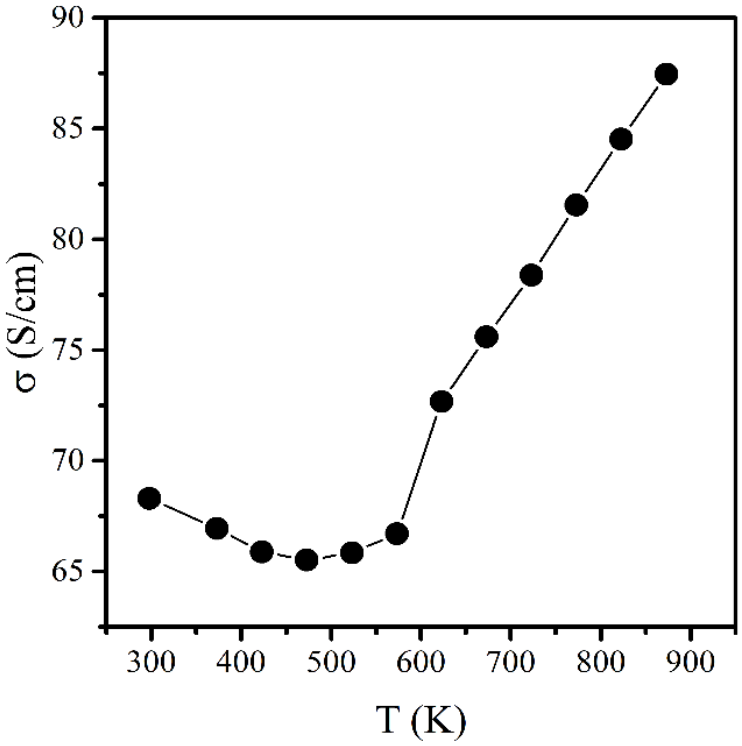

Figure 3-11 Electrical conductivity of undoped CCO sample. At about 500 K it is possible to observe the metal-semiconductor transition temperature typical of CCO.

In the considered interval of temperature, σ first shows a metal behavior, decreasing from 68 S/cm at room temperature to 66 S/cm at about 500 K, and then it starts to behave as a semiconductor with σ increasing with temperature up to 87 S/cm at 873 K. The presence of a metal-to-semiconductor transition temperature, where the sign of the dσ/dT derivative reverses, is typical for the undoped $Ca_3Co_4O_9$ and it was already reported in the literature[97]–[99]. It is associated to a structural change governed mainly by the Ca_2CoO_3 layer and connected to the variation of the lattice parameter *a*, b_1 and b_2 with temperature. Moreover, a small fraction of localized Co atoms change spin in the temperature range between 380 and 410 K, which might provide a less resistive path for the electrical transport[38].

The temperature dependence of the Seebeck coefficient for the same sample is presented in fig. 3-12.

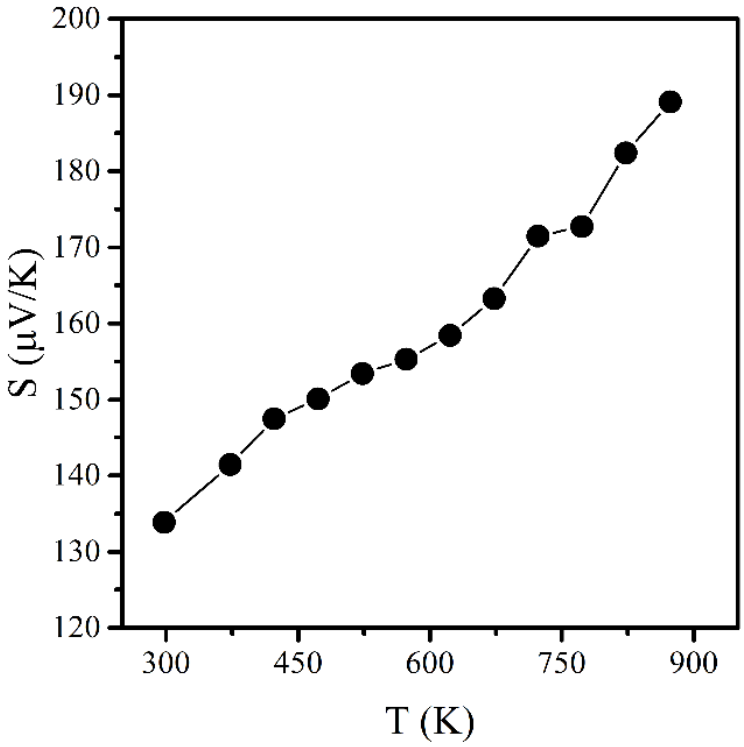

Figure 3-12 Seebeck coefficient of undoped CCO sample. The p-type conduction is confirmed by the positive sign of the Seebeck coefficient.

The positive sign of the Seebeck coefficient confirms a conduction mechanism that is mainly driven by holes. The thermopower increases almost linearly with the temperature from 134 μV/K at room temperature to 189 μV/K at 873 K and the temperature dependence can be associated to the typical behavior of a metallic conductor, modified considering the thermal activated conductivity, that can be described by the general equation:

$$S \approx \frac{\pi^2 {k_B}^2 T}{eE_F}$$

The simultaneous coexistence of a high electrical conductivity and of a large thermopower in calcium cobalt oxides contrasts with what is expected by the theory for conventional semiconductors, where *S* usually decreases with increasing the carrier concentration. However, this behavior is not always strictly followed, in particular by compounds presenting a strongly electron related structure, such in the case of $Ca_3Co_4O_9$, where the energy bands are deeply interconnected each other giving rise to a complex electronic structure.

Here, the large Seebeck coefficient can be accounted for with the Boltzmann-type metallic electrical conduction as described in 2004 by Takeuchi *et al*[100].

The change in sign in the slope of the electrical conductivity produces a change in the slope in the curve of the power factor (fig. 3-13).

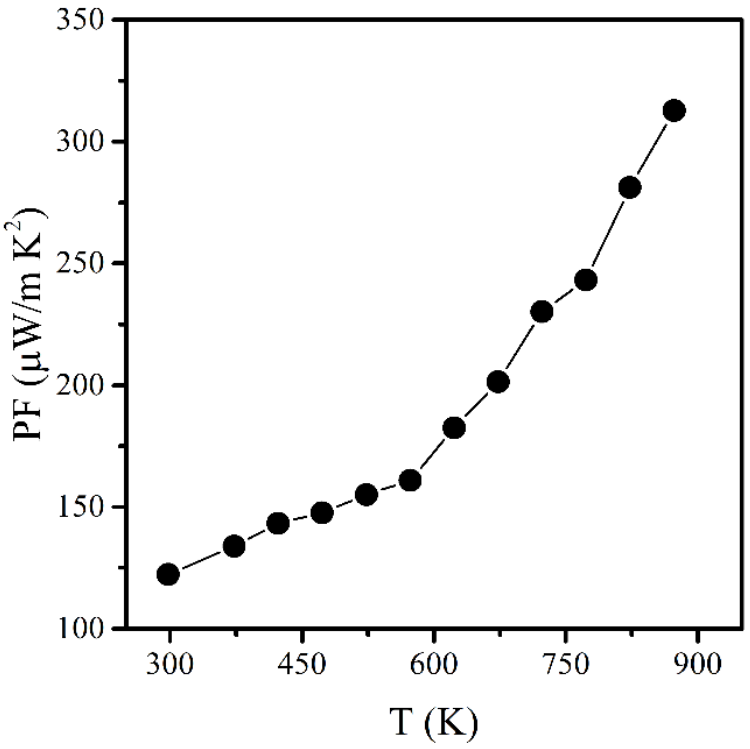

Figure 3-13 Power factor of undoped CCO sample.

The *PF* values ranged from 122 μW/m K^2 at room temperature to 313 μW/m K^2 at 873 K. These values are comparable to the data reported in literature for undoped $Ca_3Co_4O_9$ prepared *via* SPS sintering[101], [102] and confirms the reliability of this technique to obtain highly textured samples.

Fig 3-14 shows the total thermal conductivity of SPS-textured calcium cobaltite from room temperature to 873 K, together with the electronic and the phononic contributions, measured with the LFA apparatus and calculated using the Wiedemann-Franz law and by subtraction from the total κ, respectively.

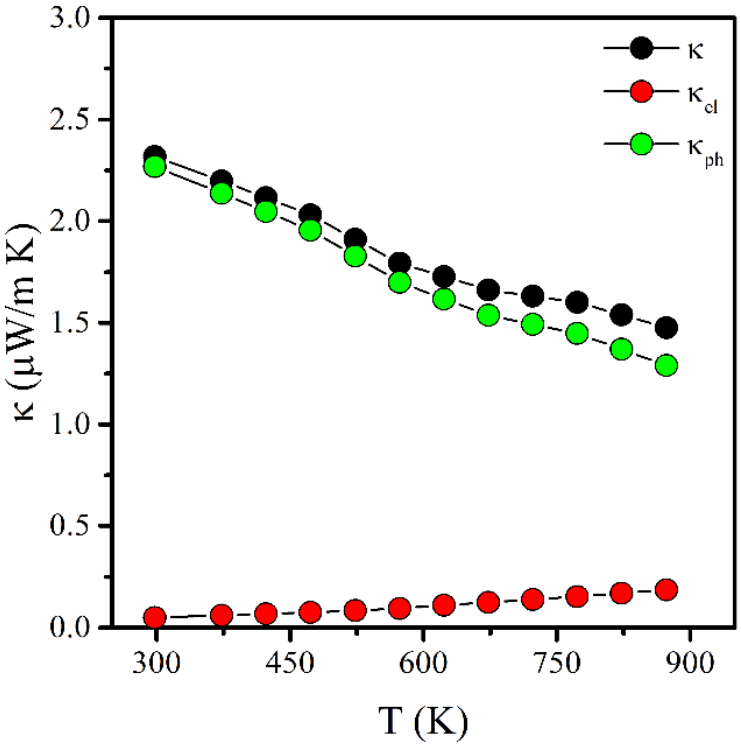

Figure 3-14. Total thermal conductivity (black) of undoped CCO sample. In figure are reported also the electronic (red) and phononic (green) contributions calculated using the Wiedemann-Franz law.

As expected, thermal conductivity of calcium cobaltite resulted driven mainly by the lattice vibrations. The electronic contribution is negligible at low temperatures, but becomes more and more important with increasing *T*.

Fig 3-15 shows the thermoelectric figure of merit calculated using the measured thermal conductivity and considering a κ two times higher.

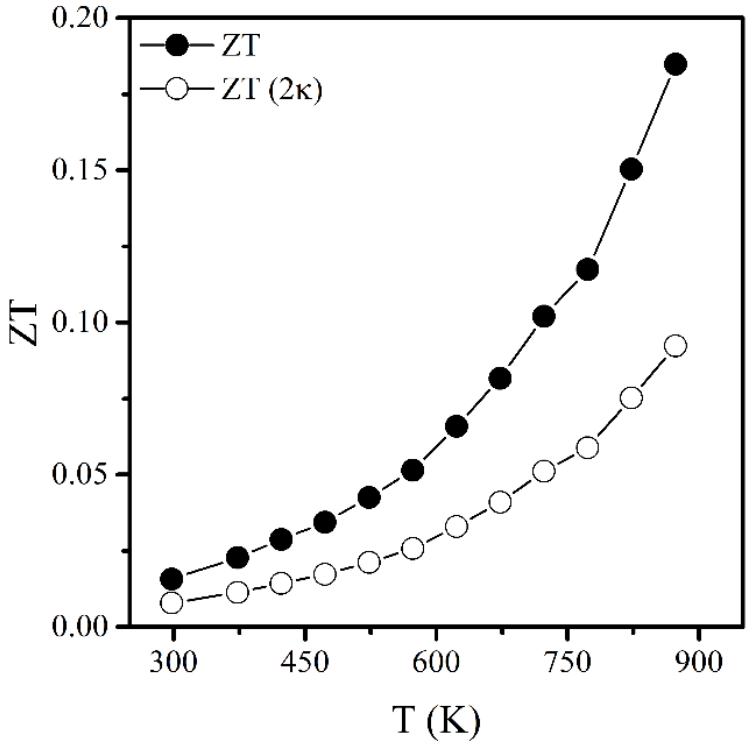

Figure 3-15 Figure of merit of undoped CCO sample (black). In figure is reported also the figure of merit calculated considering a two-fold in-plane thermal conductivity (white) according to ref. [70].

ZT increased with temperature in the whole temperature range, with the highest value of 0.18 measured at 873 K. However, some considerations about the anisotropy of the samples should be given, to avoid the possible overestimation of the figure of merit:

- The thermal conductivity was measured perpendicular to the conduction layer (out-of-plane) because of geometrical requirements of the LFA apparatus, which allows to measure the thermal transport parameters only in the direction perpendicular to the layers. On the other hand, the power factor was calculated considering the in-plane (parallel) electrical conductivity (also in this case due to the geometry of the 4P1 apparatus), while the Seebeck coefficient was not affected by anisotropy;
- We have no exact indications about the degree of anisotropy of CCO, but the out-of-plane thermal conductivity of samples sintered under a uniaxial pressure of 50 MPa is about a half compared to the relative in-plane conduction[70];

- We used a sintering pressure of 108 MPa, more than two times higher compared to ref [70], so it is reasonable to expect a significant degree of anisotropy, thus a larger in-plane thermal conductivity;
- Considering a double in-plane thermal conductivity (2κ), the resultant figure of merit is 0.09, closer to the values also reported in literature for comparable samples[70].

For these reasons, in fig. 3-15 are reported the *ZT* values considering both the measured and the two times higher thermal conductivities.

3.2.2. Reduction of the thermal conductivity

3.2.2.1. Milling of the powders

As introduced in chapter 2.1, one of the strategies pursued in this work in to improve the figure of merit of calcium cobaltite consisted in the reduction of its thermal conductivity by means of nanostructuring. The reduction in the grain size of the starting powder to the nanometric range has been achieved using a ball milling treatment. This technique resulted to be very effective as it allowed to obtain a dramatic change in the microstructure and in the crystallinity of CCO, even using relatively mild conditions. A suitable amount of CCO powder (about 2.5 g) has been weighted and put into a tungsten carbide jar equipped with 5-mm-diameter tungsten carbide balls, with a sphere-to-powder mass ratio of 20:1. The jars were then sealed and inserted into the planetary mill together with a second jar containing silica and spheres in equal mass. Initially it was tested a milling treatment at 400 rpm for 12 h divided in 24 step of 30 minutes each, with pauses of 30 minutes between every step. Fig. 3-16 shows the diffraction pattern of the milled powder after different times of treatment.

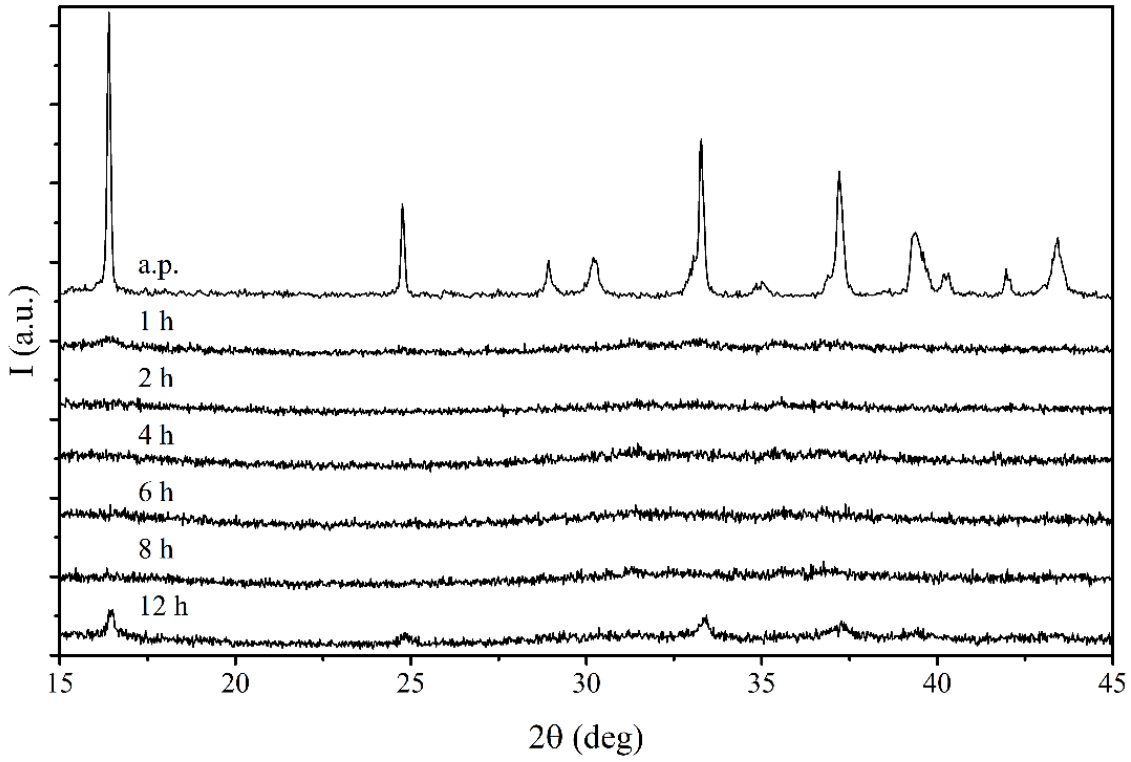

Figure 3-16 XRD patterns of CCO powders continuously ball milled at 400 rpm for 12 h. Within the first hour, the intensity of the peaks resulted dramatically reduced and large broadened bands can be observed. The last portion presents the diffraction peaks because of the non-optimized milling conditions.

It can be observed that just after the first hour of milling all the diffraction peaks resulted dramatically reduced in intensity and broadened into large bands, from which it was possible to calculate a grain size of about 4 nm. An increasing of the milling treatment from 4 to 8 hours produced no further significant change. This aspect can be considered a benefit in terms of purity of the final product, as prolonged the ball milling treatments can produce significant contamination. However, even after 12 hours of treatment some diffraction peaks resulted still unexpectedly present in the pattern. It was noted, however, that most of the powder adhered to the internal walls of the jars, leaving only a small portion in direct contact with the spheres. A scraping of the jar walls and mixing of the powder at the end of every cycle (30 minutes) was performed, while the milling procedure was reduced to 4 hours. XRD pattern were taken after every hour of treatment, the results are reported in fig. 3-17.

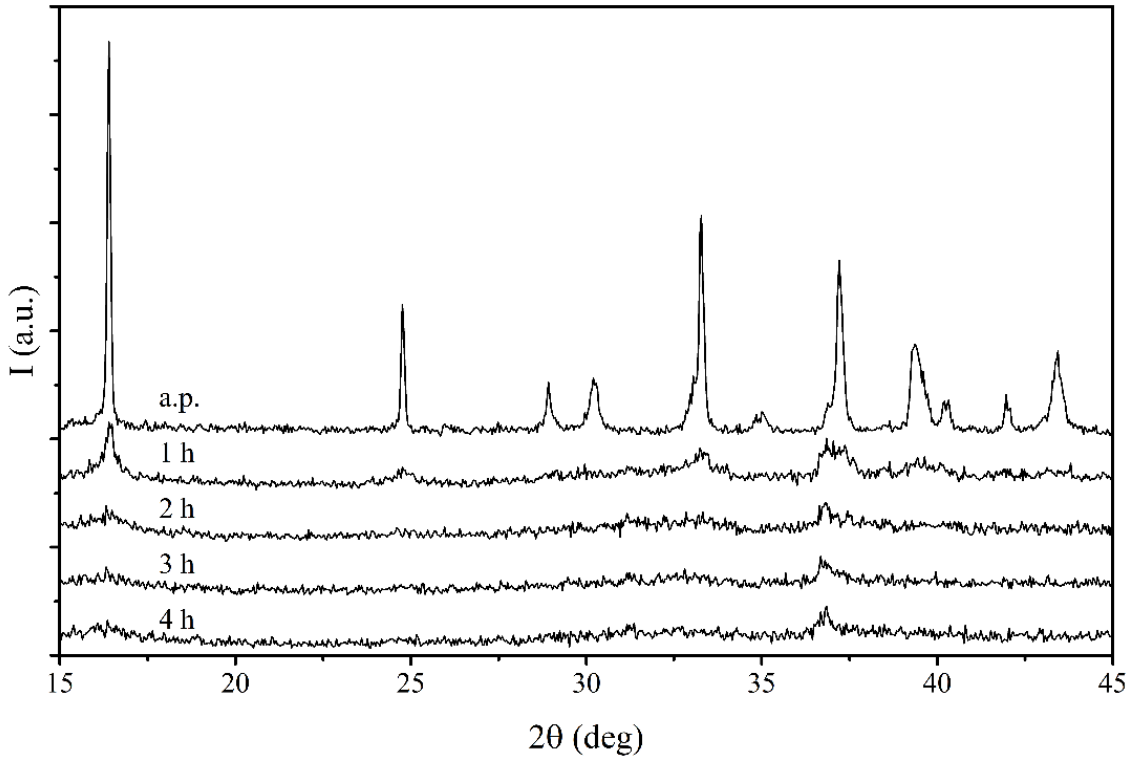

Figure 3-17 XRD patterns of CCO powders ball milled with the optimized procedure at 400 rpm from 1 to 4 hours. The complete broadening of the diffraction peaks can be obtained after the third hour of treatment. Using the Scherrer equation the determination of a grain size of 4 nm was still possible.

After the first hour of treatment the intensity of the diffraction peaks was reduced, and the grain size decreased from the sub-micrometric range to about 34 nm as shown in fig. 3-18 and reported in tab. 3-2, where the trend with milling time of the grain size and the peak intensity of the *0020* reflection were reported.

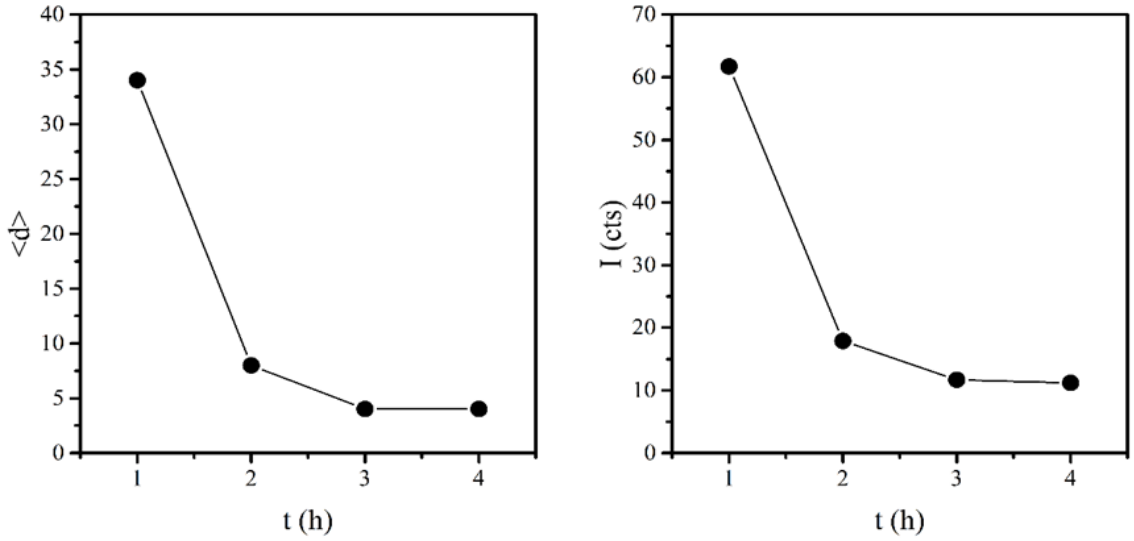

Figure 3-18 trend with milling time of the grain size and the peak intensity of the 0020 *reflection.*

Table 3-2 trend with milling time of the grain size and the peak intensity of the 0020 *reflection.*

t (h)	<d> (nm)	I (cts)
1	34	62
2	8	18
3	4	12
4	4	11

The milling treatment was effective in reducing the lamellar habitus of the powder (fig. 3-19) which became also less voluminous. After the second hour of treatment the grain size was reduced to 8 nm. After the third hour of treatment, only broad bands could be observed, from which it was still possible to calculate a grain size of about 4 nm using the residual *0020* peak. Any further increase in the milling time didn't produce additional reduction in the grain size. At the end of the milling the CCO powder is characterized by the presence of large agglomerates of nanoparticles. Remarkable, as noted before, was the loss of the lamellar *habitus* of the powders, producing a more isotropic shape of the grains.

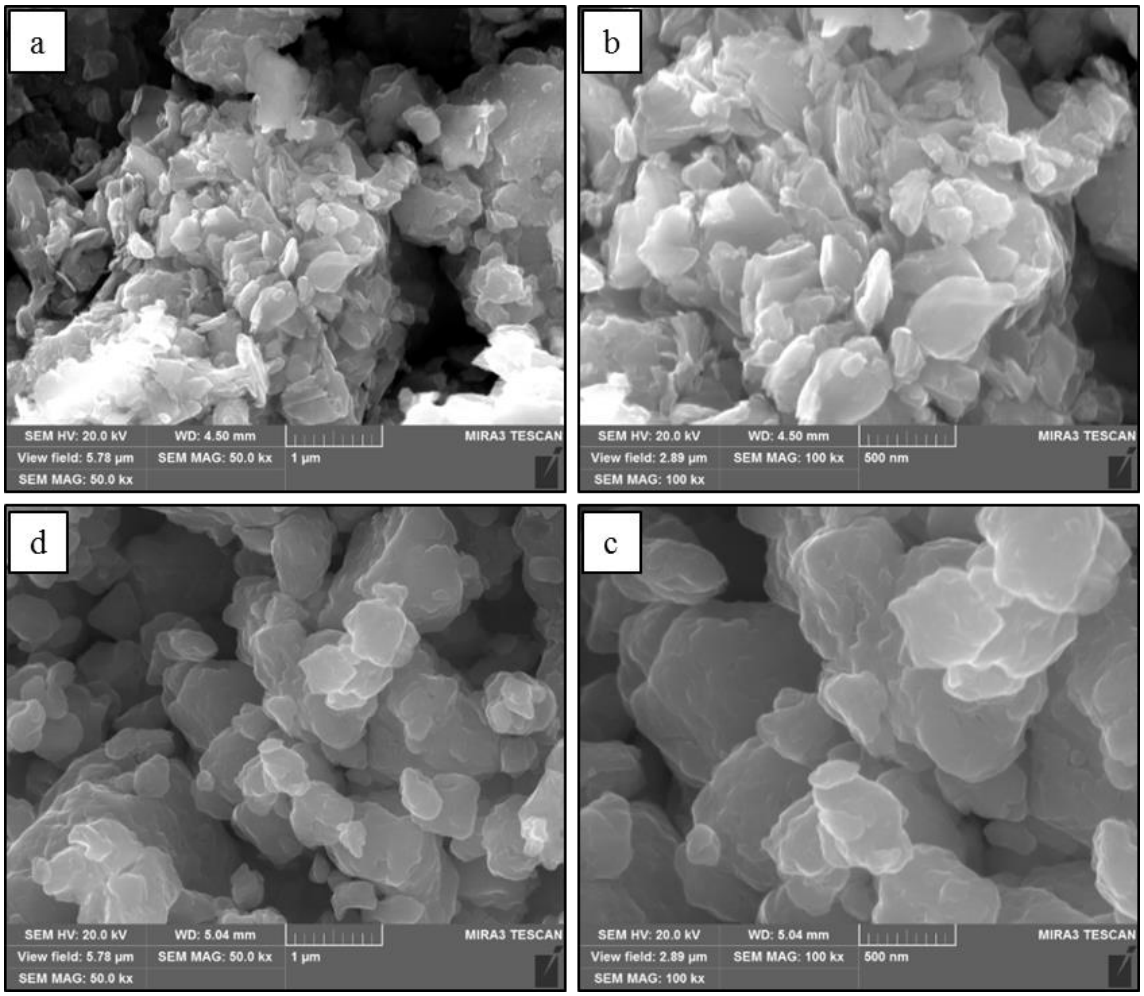

Figure 3-19 SEM micrographs at different magnification of CCO powders milled at 400 rpm for 1(a, b) and 4(c, d) hours. In the latter case, only large agglomerates of isotropic nanoparticles are visible rather than the single particles.

Trying to reduce even further the grain size, the ball milling was performed also at 600 rpm. This increase, however (fig. 3-20), was not enough to produce the full amorphization of the CCO powders since residual diffraction peaks were still present.

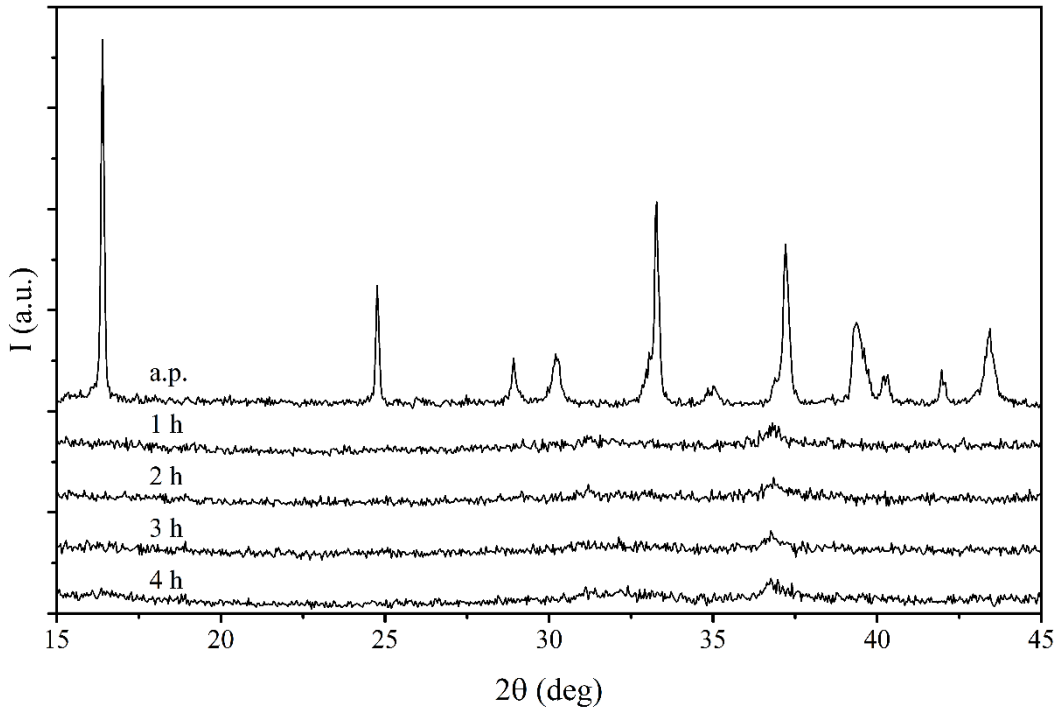

Figure 3-20 XRD patterns of CCO powders ball milled with the optimized procedure at 600 rpm from 1 to 4 hours. The complete broadening of the diffraction peaks can be obtained after the first hour of treatment.

However, the increase of the milling speed to 600 rpm allowed to obtain the almost complete amorphization after just one hour of treatment, a result equivalent to one obtained at 400 rpm for 3 hours. However, considering the increased WC contamination, the 400 rpm / 3 h condition was chosen as the optimal milling procedure. The calcium cobaltite powders prepared using this method will be referred as "milled", or CCO-BM. The milling procedures were performed on powders obtained using the method A (CCO-A), characterized by the largest grain size. The same procedure was performed also on CCO-B powders to observe the influence of a smaller starting grain size. Fig. 3-21 shows the XRD pattern of the B-CCO powder before and after the milling treatment. However, the diffraction pattern relative to the *nanometric* (CCO-B-BM) and *sub-micrometric* (CCO-A-BM) after milling resulted identical.

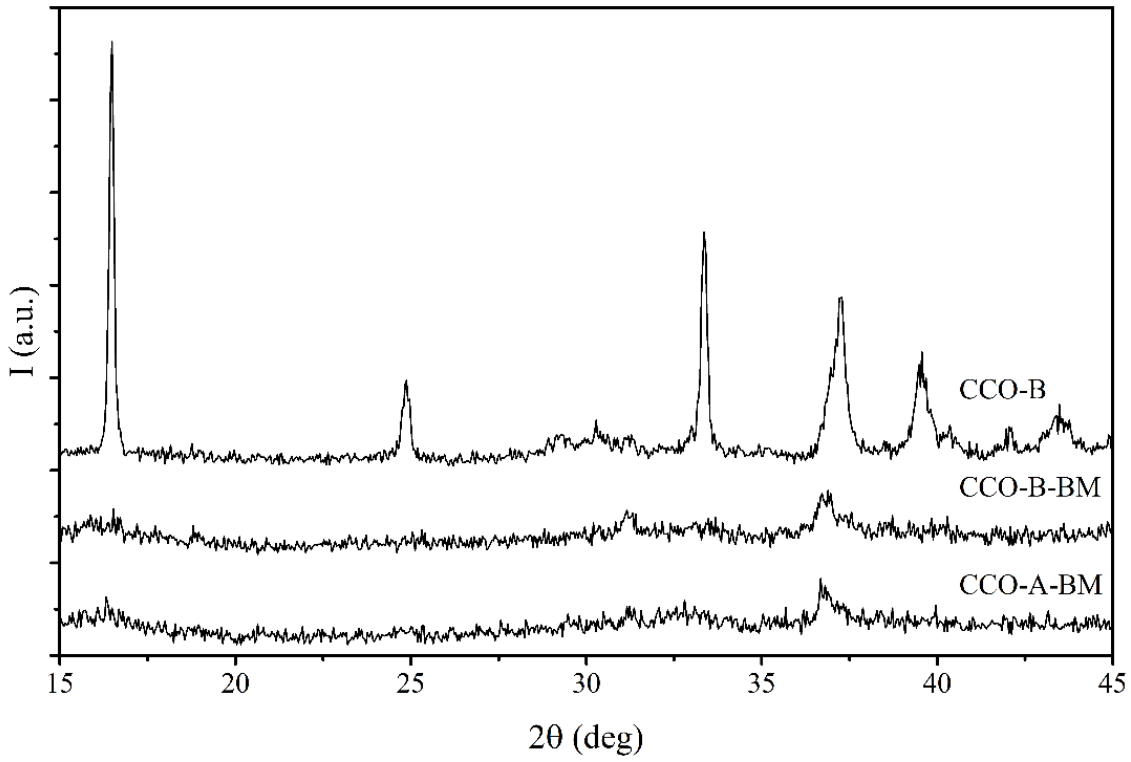

Figure 3-21 XRD patterns of ball milled CCO powders (400 rpm / 3h) annealed with method A and with method B with respect to the diffraction pattern of method "B" CCO. Different starting grain size has no effect on the final dimension of the particles.

3.2.2.2. EXAFS and XANES characterization

The effect of the ball milling was investigated also by means of EXAFS and XANES measurements on powders milled at 400 rpm for 4 h and at 600 rpm for 8 h. Transmission XAS (X-ray Absorption Spectroscopy) data were collected at the LISA beamline (European Synchrotron Radiation Facility, ESRF, Grenoble, experiment HC-1582) at the Co-K edge [1], as a function of *T* at 80, 100, 150, 200 and 300 K. A Si(111) double crystal monochromator was used; the harmonic rejection was realized by Pd mirrors, having a cut-off energy of 20 keV, and a ion chambers as detectors. The energy calibration has been made by measuring the absorption spectrum of metallic Co. For the measurements, a properly selected amount of finely ground CCO-A and CCO-BM powders as to yield an edge jump close to unity, was thoroughly mixed with cellulose and pressed into pellets. CCO-BM powders milled at 400 rpm/ 4h and 600 rpm / 8 h were used for the experiment. It should be noted the experiment was carried out before the optimization of the ball milling procedure. The reproducibility in energy has been assured by measuring simultaneously the XAS spectra of Fe and Au foils, and for every scan found to be better than 0.1 eV. Spectra of CoO and Co_3O_4, used as standards for Co(II) and Co(III), respectively, were also measured in transmission mode.

For the XANES (X-ray Absorption Near Edge Structure) analysis the spectra were processed by subtracting the smooth pre-edge background fitted with a straight line. The EXAFS extraction and data analysis were performed by means of the ATHENA and EXCURVE codes, respectively. For the pre-edge peak analysis, the pre-edge was first isolated by subtracting a smooth background fitted with a polynomial, and then the peak was fitted by the appropriate amount of Gaussian functions.

Fig. 3.22 shows the XANES spectra of CCO-A at 80 K. The spectra of CoO and Co_3O_4 standards are also shown for comparison.

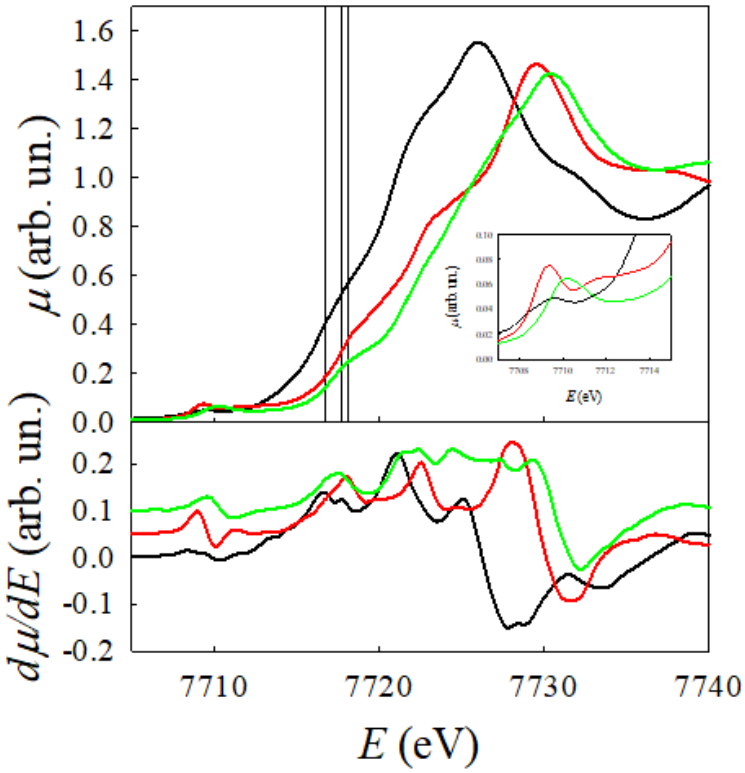

Figure 3-22 XANES spectra of CCO-A (red line) at 80 K The spectra of CoO (black line) and Co_3O_4 (green line) standards are also shown for comparison. The black vertical lines are the absorption edges of the samples: CoO, Co_3O_4 and CCO-A, from left to right.

The edge energy position is determined by the binding energy of the Co 1s electrons, that in turn is controlled by the coulombic potential. This can be screened by the outer (valence) electrons: as a result, the edge shifts at larger energies with increasing oxidation state. The edge energy position of CCO-A is slightly larger than that that of Co_3O_4, which supports the nominal Co(III) oxidation state that can be derived from the $Ca_3Co_4O_9$ composition. This is also supported by the energy position of the absorption maximum. However, there are several features on the absorption edge pointing towards the presence of different Co atom with different local electronic structure. First, the edge has an initial rise at ca. 7718 eV, pointing towards the presence of some Co in a lower oxidation state. Indeed, at this energy, the spectrum of Co_3O_4 shows a first rise as well: multiple scattering calculations[103] show that at this energy the main contribution is from Co(II) in the tetrahedral sites of the spinel structure. The main inflection point of the Co-K edge in CCO is then at ca. 7722 eV, which is coincident with that of Co_3O_4, but the edge has then a further rise at higher energy, which may indicative of some Co in a higher oxidation state. This is better evidenced by the derivative XANES spectra shown in the lower panel. It should be noted that the presence of both Co(II) and Co(IV) has been already suggested[104].

However, the local electronic structure of cobalt in calcium cobaltite possibly show further complexity. Indeed, the pre-edge region, shown in the inset of the upper panel of fig. 3-22, shows a larger intensity for CCO compared both to CoO and Co_3O_4. The pre-edge peak is originated by dipole-forbidden 1s-3d transition, and its intensity is determined by deviations of the local symmetry from having the inversion center and by the number of holes in the 3d states. The larger intensity found for CCO is therefore symptomatic of larger structural disorder and is compatible with the incommensurate structure, in which Co ions lack the inversion symmetry[36]. On the other hand, the pre-edge peak is affected by the same chemical shift affecting the energy position of the main edge. Indeed, the position of the centroid of pre-edge peaks in Fe compounds was used to precisely asses the oxidation state[105]. For applying this method in the present case, the pre-edge was isolated as described in the experimental, fitted by the minimum amount of Gaussian functions, and the centroid was then calculated. The results are shown in fig. 3-23.

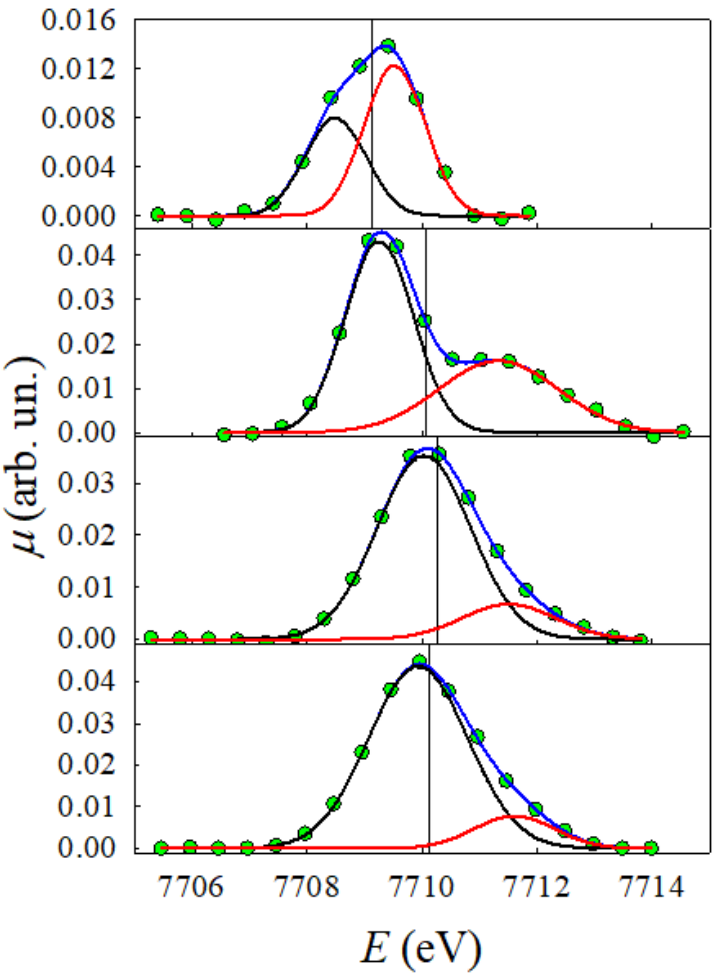

Figure 3-23 From top to bottom, pre-edge peaks of CoO, Co_3O_4, CCO-A-BM (400 rpm/4 h) and CCO-A-BM (600 rpm/8 h).

For CoO, the pre-edge is constituted by two peaks, corresponding to the final states $1s^1\ t_{2g}^6\ e_g^2$ and $1s^1\ t_{2g}^5\ e_g^3$, corresponding to Co(II) in high spin configuration in the octahedral crystal field of the NaCl structure. For Co_3O_4, the pre-edge is constituted by two peaks as well, corresponding to the final states $1s^1\ e^4\ t_2^4$ and $1s^1\ t_{2g}^6\ e_g^1$, corresponding to Co(II) in the tetrahedral crystal field (with no inversion symmetry, and therefore larger intensity) and Co(III) in low spin configuration in the octahedral crystal field of the spinel structure, respectively. For ball milled CCO-A, the centroid position is larger than that of Co_3O_4, thus confirming the mean oxidation state close to Co(III). However, the absence of a clear tail on the low energy side points towards the absence of localized (on the experimental timescale, which is of the order of 10^{-12}-10^{-15} s) Co(II) states. On the contrary, a clear tail is present on the high energy side, which confirms the presence of localized Co(IV). It can be therefore concluded that formally Co(II) rapidly exchange holes with Co(III), thus yielding Co(IV), in agreement with the *p* character of charge carriers in CCO[104].

Fig. 3-24 shows the XANES spectra of CCO-A and of CCO-BM powders milled at 400 rpm/4 h and at 600 rpm/8 hours.

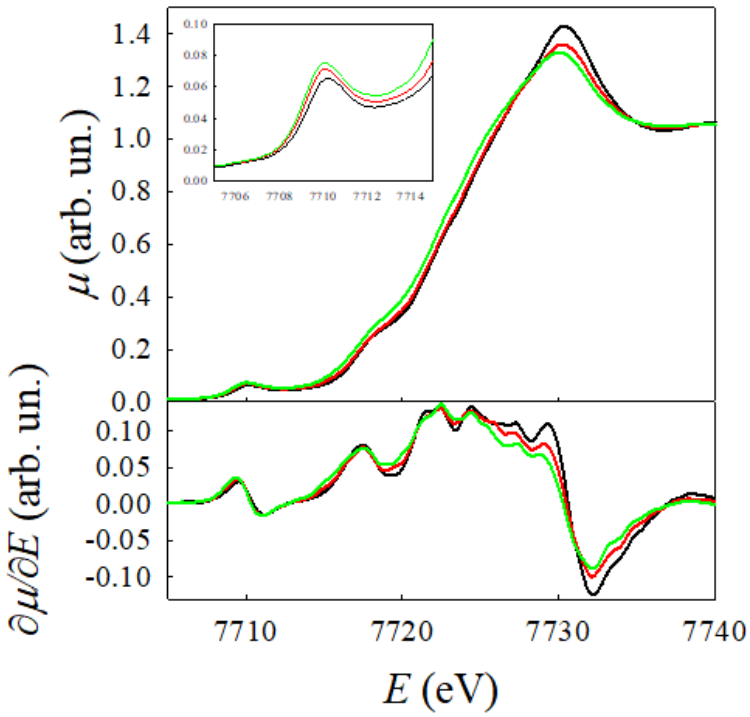

Figure 3-24 XANES spectra of CCO-A (black line) and of CCO-BM powders milled at 400 rpm/4 h (red line) and at 600 rpm/8 hours (green line).

It is readily seen that ball milling induces an important smearing of the spectral features, indicating an increase of structural disorder, and, if boosted to 600 rpm for 8 h, an apparent reduction. This is made more evident in the inset of fig. 3-24, where the pre-edge peaks of the three samples are shown in detail: increasing the work done by ball milling increases the intensity of the pre-edge peak, showing a larger disorder, and a shift towards lower energies, indicative of a decrease in the mean oxidation state of Co. Indeed, if the pre-edge peak of the sample ball milled for 8 h at 600 rpm is analyzed as previously described (see bottom panel in fig. 3-23), an increase of both amplitude and width of the lower energy Gaussian is found, together with a net shift at lower energies of the centroid. On the contrary, the high energy tail remains almost unchanged, which may be indicative that the ball milling induces a larger structural disorder in the Ca_2CoO_3 layers. Structural disorder induced by ball milling is also seen in Fig. 3-25, where EXAFS spectra and the corresponding Fourier Transforms at 80 K of the three CCO samples are compared.

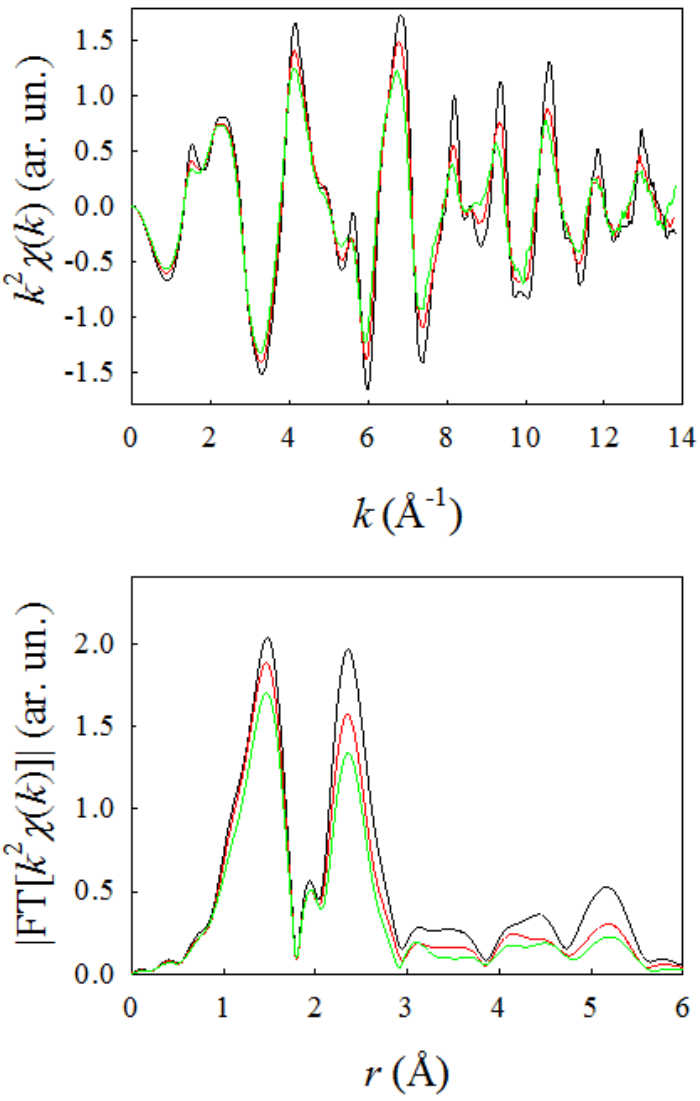

Figure 3-25 EXAFS spectra and the corresponding Fourier Transforms at 80 K of the three CCO samples. CCO-A (black line), and ball milled CCO at 400 rpm/4h (red line) and at 600 rpm/8h (green line).

The marked decrease in the amplitude of the EXAFS oscillations and therefore of the magnitude in the FT peaks indicates an increase in structural disorder. In the EXAFS FT, the peak between ca. 1 and 1.8 Å is representative of the nearest neighbor oxygen shell in both the Ca_2CoO_3 and CoO_2 layers, while the peak in between ca. 1 and 1.8 Å is due only to the Co next nearest neighbors in the CoO_2 layers. Accordingly, the EXAFS spectra of the three samples at all the temperatures investigated in this work could be fitted according to the structural model described in tab. 3-3.

Table 3-3 Structural model used to fit the EXAFS spectra of the three CCO samples.

Shell	***N***	**Atom**	***r* (Å)**	**σ^2 (Å^2)**
Cluster 1 CoO_2 layer, n=0.6				
1	3	O	1.8574	$3(1)x10^{-3}$
2	3	O	1.9651	$3(1)x10^{-3}$
3	6	Co	2.8073	$34(6)x10^{-4}$
Cluster 2 Ca_2CoO_3 layer, n=0.4				
3	O	O	1.855	$3(1)x10^{-3}$
3	O	O	2.350	$14(9)x10^{-3}$

It should be further noted that: 1) the distances reported in tab. 1 are averaged over several coordination shells, due to the intrinsic disorder of the $Ca_3Co_4O_9$ structure, 2) peaks at larger distances appear in the EXAFS FT, but their amplitude is small and therefore their contribution was neglected in the EXAFS fittings, and 3) only the EXAFS Debye-Waller factors were used as fitting parameters: in addition, to avoid unnecessary correlations between the fitting parameters, the Debye-Waller factors of the oxygen shells below 2 Å were constrained to be equal. An example of the fit quality is given by Fig. 3-26 were the spectrum of the as such CCO sample at 80 K is shown.

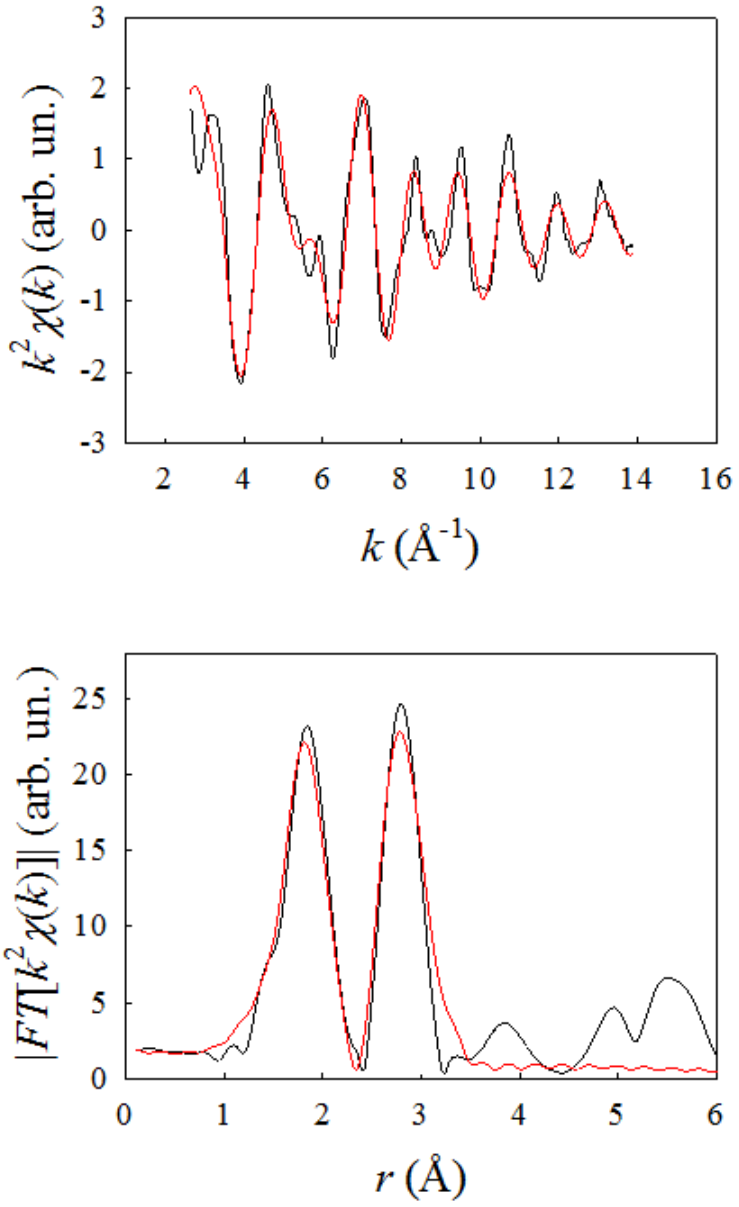

Figure 3-26 EXAFS and relative Fourier Transform of CCO-A sample.

The fitting parameters are also reported in tab. 3-3. When plotted against *T* (fig. 3-27) the EXAFS Debye-Waller factor for the three sample show an impressive flat trend, thus proving the static character of the structural disorder in CCO.

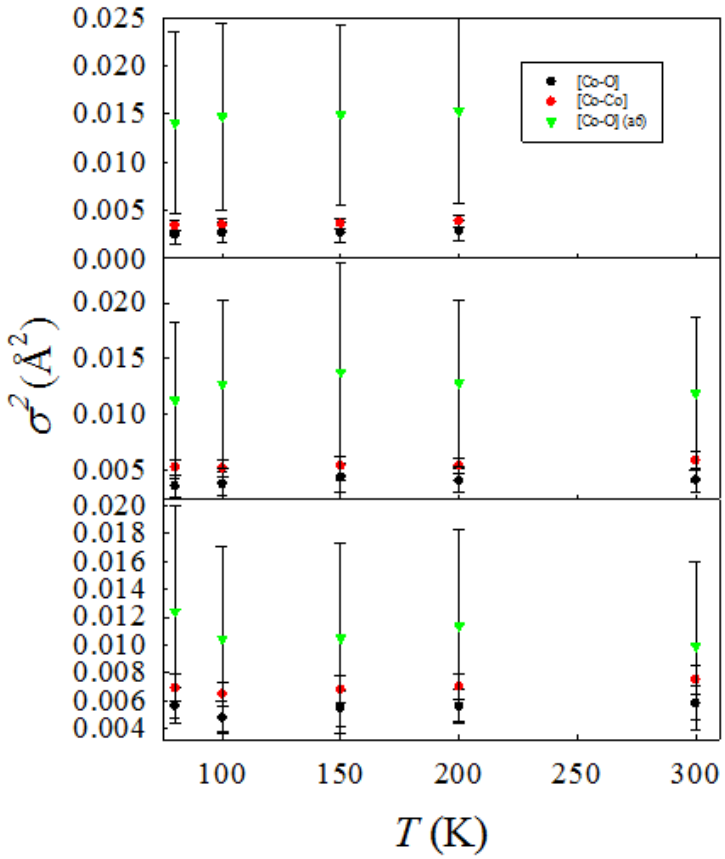

Figure 3-27 Debye-Waller factors of Co-O (black) and Co-Co (red) in the CoO_2 layers, and Co-O in the Ca_2CoO_3 layers (green). Samples under investigation were CCO-A (top), milled CCO at 400 rpm/4 h (middle) and milled CCO at 600 rpm/8 h (bottom).

In addition, a global increase is found with increasing ball milling time and energy; this is particularly evident for the Co-Co distance within the CoO_2 layers, in agreement with the qualitative trend of fig. 3-25.

3.2.2.3. Sintering of the milled powders

One of the most interesting aspects of the ball milling treatment was in the possibility of using higher uniaxial pressures during sintering. This allowed to reduce even further the sintering temperatures. The milled powders, in fact, did not show the anomalously high plastic deformation observed in the starting powders, deriving probably form their lamellar habitus. The possibility to reduce the sintering temperature is crucial for maintaining their nanostructure. During the sintering processes however, the almost amorphous milled powder show evidences of reorganization and recrystallization. In fig. 3-28 are reported the grain size and the XRD of the *0020* reflection of sintered CCO-BM samples as a function of the sintering temperature.

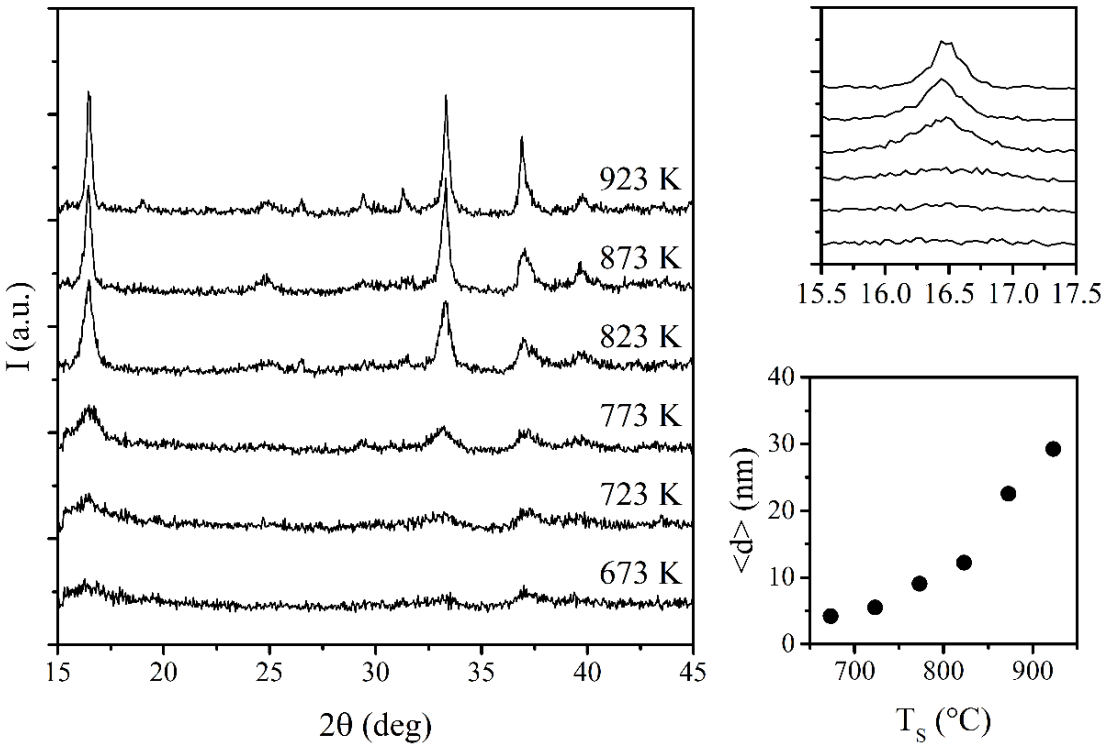

Figure 3-28 XRD patterns of CCO-BM samples sintered at different temperatures (left). In the right panels are reported the focus on the 0020 reflection and the trend of the grain size against the temperature.

The sample remains almost completely amorphous (grain size ~5 nm) up to 723 K, while starting from 773 K a significant increase in the main peak intensity is observed, although the grain size remained considerably small (9 nm). Further increase in the sintering temperature to 823 K caused an increase up to 12 nm, while at 873 K and 723 K, the grain size were 23 nm and 29 nm, respectively.

Considering the formation of the mixture of calcium and cobalt oxides produced by the surface reduction at T_S > 873 K, which resulted hard to remove from these high-density samples, the optimal sintering temperatures for ball milled powder were defined to be between 673 and 823 K. Starting from these temperatures, densification curves for CCO-BM samples starting were build considering different sintering uniaxial pressures (170, 180, 290 and 430 MPa) and the results are reported in fig 3-29.

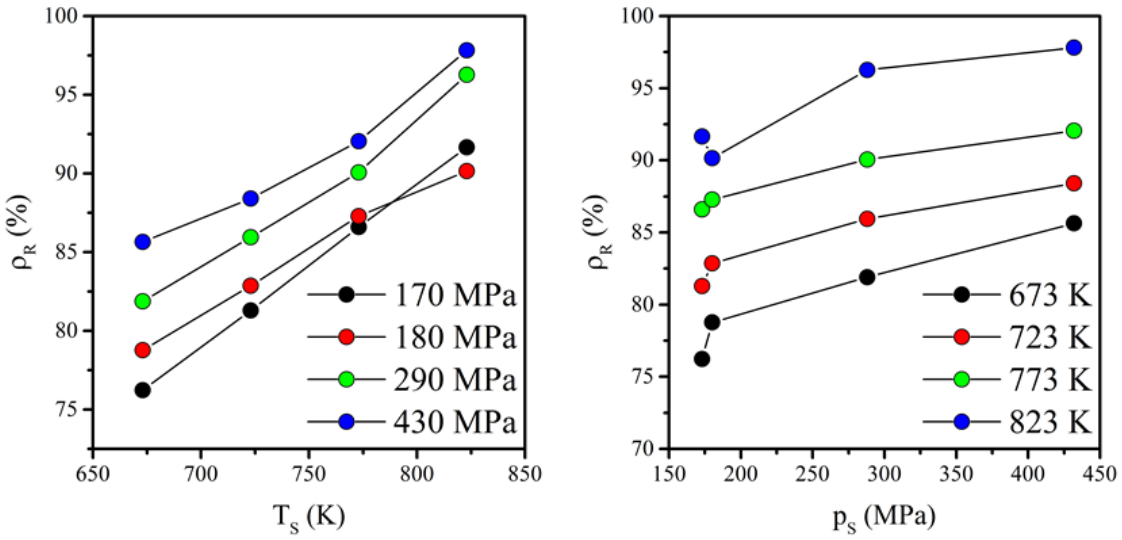

Figure 3-29 Relative densities of the CCO-BM samples as a function of the sintering temperature and the applied uniaxial pressure.

The relative density increased almost linearly with the sintering temperature. ρ_R increased also linearly with increase in the sintering pressure. There was a deviation from the linear trend in the samples sintered at the two lower pressures, which led to a higher density (92%) for the sample sintered at 170 MPa compared to the one sintered at 180 MPa at the same T_S (90%). This samples, however, was the only one obtained using a 10-mm die, which required about four times the quantity of powder necessary to obtain a sample. Fig. 3-30 shows the micrographs of the sample sintered at 673 K/180 MPa.

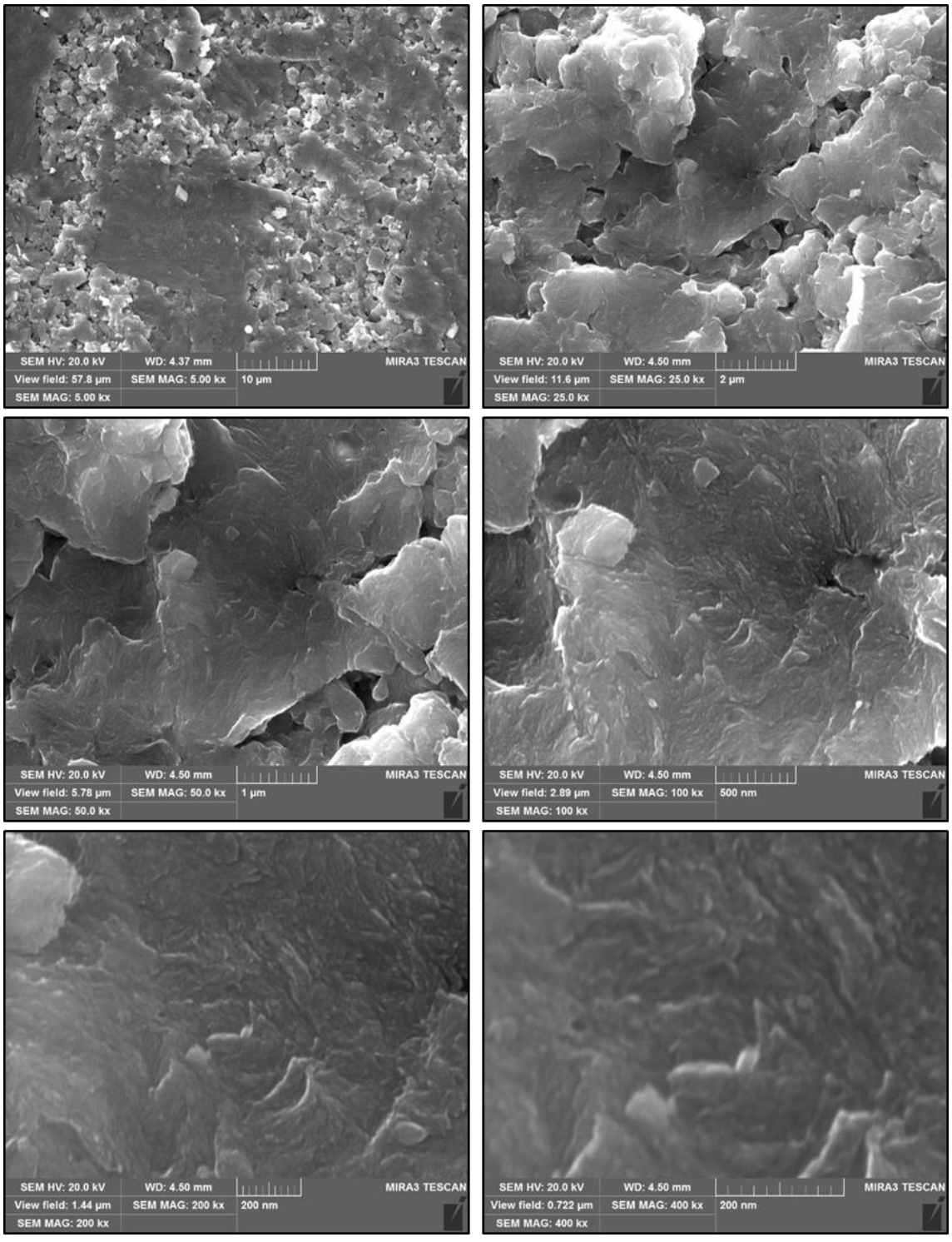

Figure 3-30 SEM micrographs of the CCO-BM sample sintered at 673 K under a uniaxial pressure of 180 MPa.

The sample resulted characterized by large agglomerates of well compacted nanograins with a uniform microstructure alternated by high-porosity regions. However, even at high magnifications (400kx) it wasn't possible to evidence the grain size and no indications of anisotropy could be observed.

3.2.2.4. Thermoelectric properties of CCO samples from ball milled powders

The study of the thermoelectric properties of sintered ball milled calcium cobaltite was performed on different set of samples. The first set (set1) consisted in dense CCO-BM samples sintered at 723, 773 and 823 K under a uniaxial sintering pressure of 430 MPa (tab. 3-4). The samples were characterized using the 4P1 and S1 apparatuses:

Table 3-4 List of the sintering conditions for CCO-BM samples of set1.

Sintering	ρ_R	<d>
430 MPa / 723 K	88%	6 nm
430 MPa / 773 K	92%	9 nm
430 MPa / 823 K	98%	12 nm

Fig. 3-31 shows the thermoelectric properties (σ, S and PF) of these samples compared to a submicrometric CCO sample.

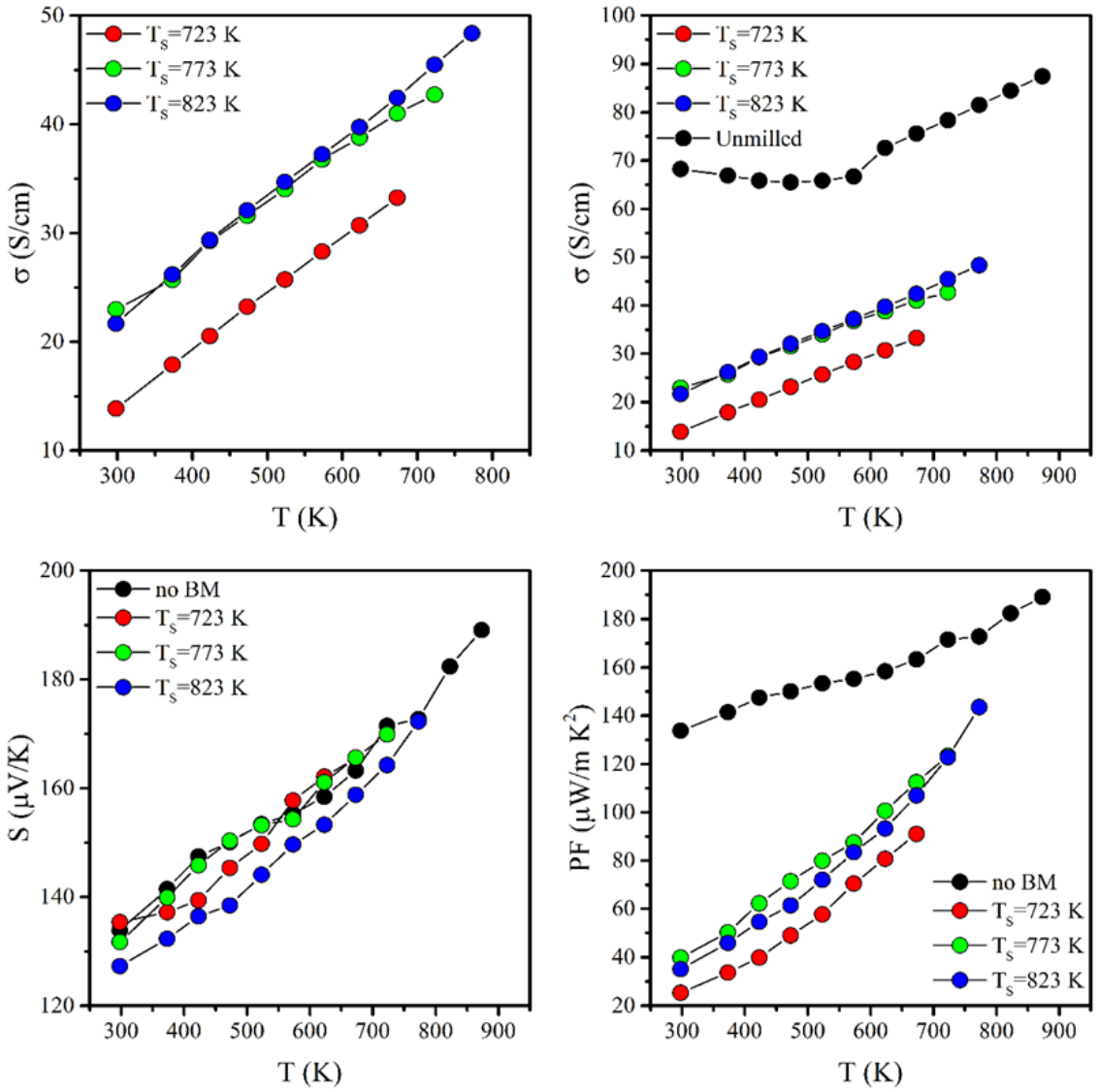

Figure 3-31 Thermoelectric properties of CCO-BM samples (set1) compared to the submicrometric CCO sample.

The samples sintered from milled powders exhibited a semiconductor behavior, with σ increasing almost linearly in all the range of temperature investigated, despite in semiconductors σ generally is proportional to -E/kT. However, also in this case this behavior might be related to the complex electronic structure of calcium cobaltite. The electrical conductivity increased generally both with grain size and relative density. The largest differences could be observed between the samples sintered at 723 and 773 K, while a further increase to 823 K didn't produce any other significant increase. The highest σ-value of 48 S/cm was observed at 773 K that is about a half of the electrical conductivity of the sub-micrometric sample measured at the same temperature (82 S/cm).

These results were not unexpected. It is well known, in fact, that a reduction of the grain size to the nanometric range can produce a reduction in the electrical conductivity[106], although the extent of this effect is generally not quite limited in electronic conductors.

At the same time, the Seebeck coefficients of the ball milled samples increased with temperature in the same way of the submicrometric one, and were nearly identical, with no significant differences, in terms of values, between the amorphized and the sub-micrometric samples, despite the sample sintered at 823 K exhibited the lowest thermopower among all the samples. Because of the lowest electrical conductivity of the ball milled samples, also their calculated power factors resulted generally lower compared to the submicrometric sample. The best *PF* of 144 $\mu W/K^2m$ at 773 K for the sample sintered at 823 K was 40% lower compared to the power factor measured at the same temperature of the sub-micrometric sample (243 $\mu W/K^2m$). At room temperature the difference is larger in magnitude as the *PF* of the submicrometric sample is more than 3 times higher. A second set of samples (set2) was used for the study of the thermal conductivity, together with the other thermoelectric properties, of the ball milled samples. Two groups of similar samples (tab. 3-5) were prepared with a diameter of 12.7 mm (a dimension determined by the laser flash apparatus used for the measurements), while the electrical conductivity and the Seebeck coefficient were measured using the 4P1, S1 and 4PS2 apparatuses:

Table 3-5 List of the sintering conditions for CCO-BM samples of set2.

Sample	Sintering	ρ_R	<d>
CCO-A	100 MPa / 823 K	70 %	> 200 nm
CCO-A-d	100 MPa / 1073 K	94 %	> 200 nm
CCO-B	100 MPa / 823 K	66 %	80 nm
CCO-BM	100 MPa / 723 K	70 %	5 nm

A first sample was sintered at the highest temperature allowing to keep the material in the quasi-amorphous state obtained after the milling process (723 K). On samples of this diameter the highest uniaxial sintering pressure was limited to 100 MPa; a limitation due to the compressive strength of the graphite. Under these conditions the sample relative density was limited to about 70%. To investigate the effect of the grain size on the thermal conductivity a A-CCO and a B-CCO sample were sintered at 823 K obtaining comparable density values (70% and 66%, respectively). The grain size was sub-micrometric (>200 nm) for the CCO-A sample and 80 nm for the CCO-B sample.

The comparison was made also against an CCO-A sample sintered at 1073 K and characterized by a relative density of 94%.

Fig. 3-32 shows the thermal diffusivity and the thermal conductivity of this set of samples measured with the LFA apparatus from RT to 1073 K.

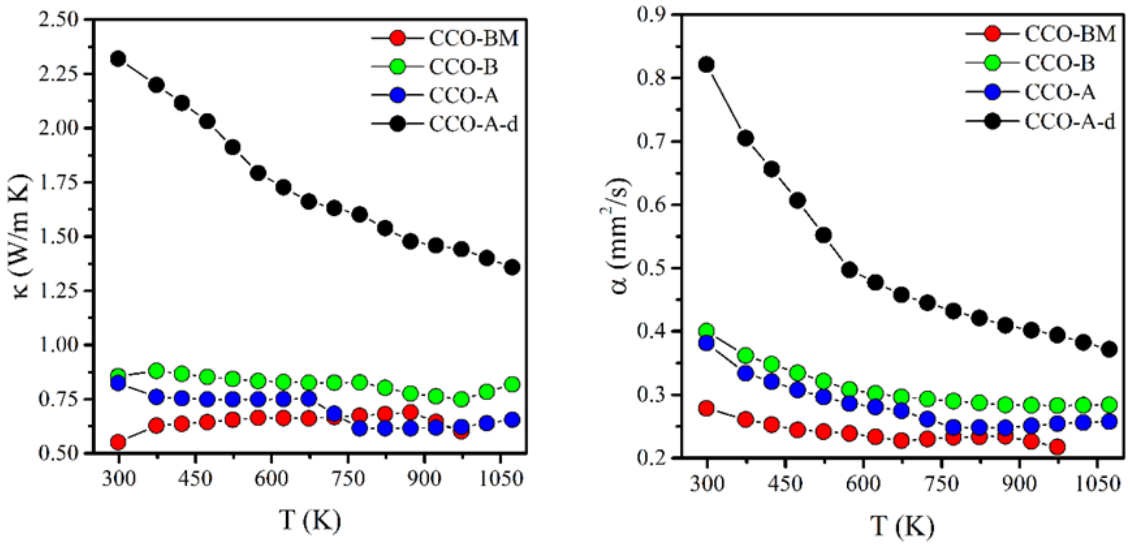

Figure 3-32 Thermal conductivity (left) and thermal diffusivity (right) of the CCO samples (set2).

Both thermal conductivity (κ) and thermal diffusivity (α) were strongly affected by the porosity of samples and by their grain size. In fact, the highest values were obtained for the fully dense CCO-A sample presenting sub-micrometric grain size with κ values decreasing with increasing temperature from 2.3 to 1.4 W/Km. At the same time, for the three samples with the same relative density, the thermal conductivity and diffusivity didn't follow a linear dependence on the grain size. In particular, the largest values of κ and α were observed for the CCO-B sample. The sample that exhibited the lowest thermal conductivity was the one sintered from ball milled powders (CCO-BM), at least up to 650 K, then an inversion in κ can be observed with the lowest values that can be obtained with the CCO-A sample up to 1073 K. This indicates that in presence of a high level of porosity the role of the grain size appears to be minimized and that the pores acted as main phonon-scattering center. Nevertheless, considering the porous samples only, the ball milling treatment induced a clear reduction of the thermal conductivity with respect to samples characterized by larger grain size. In fact, the thermal conductivity of CCO-BM is about 36% lower compared to the CCO-B sample.

Fig. 3-33 shows the electronic and phononic contribution to the thermal conductivity calculated using the Wiedemann-Franz law.

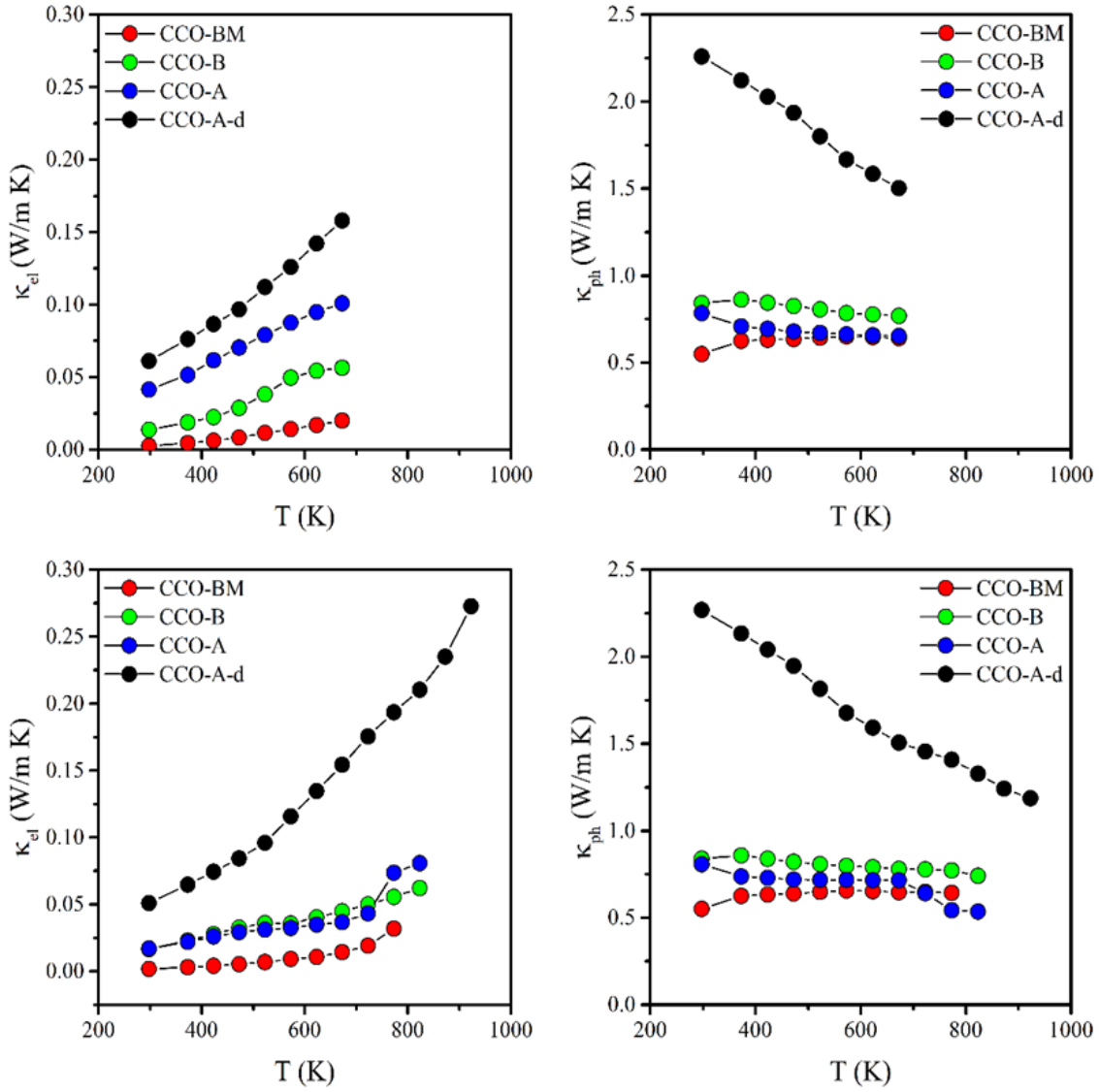

Figure 3-33 Electronic (left) and phononic (right) contribution to thermal conductivity calculated with the Wiedemann-Franz law using the electrical conductivity data measured using the 4P1 (top) and 4PS2 (bottom) apparatuses.

As expected, the electronic contribution is considerably lower compared to the phononic part of the thermal conductivity. From this analysis resulted more evident the strong effect that the porosity, more than the nanometric grain size, played in the scattering process of phonons.

Fig. 3-34 shows the electrical conductivity of the samples determined using the two measurements apparatuses.

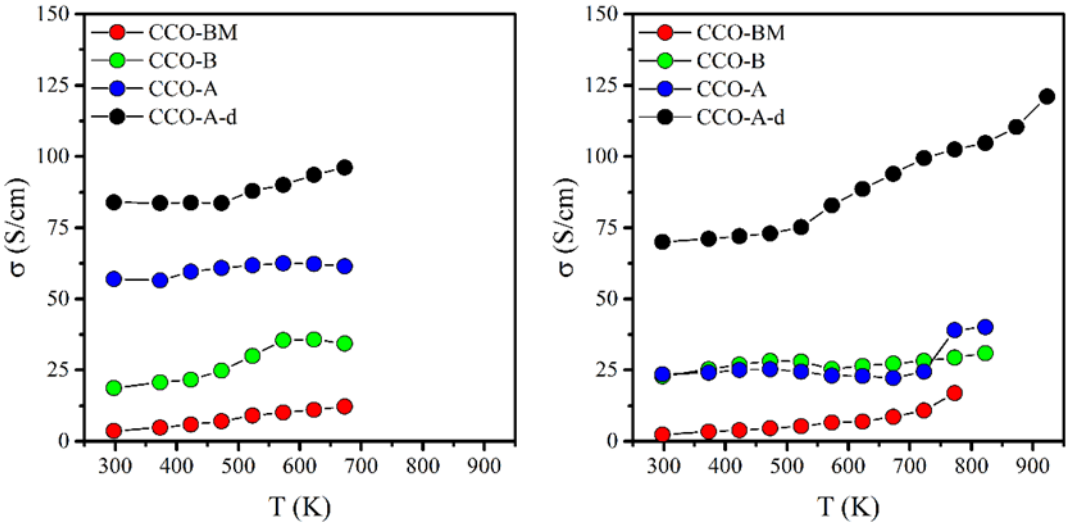

Figure 3-34 Electrical conductivity of CCO samples (set2) measured using the 4P1 (left) and 4PS2 (right) apparatuses.

Both systems allowed to obtain quite similar σ values for almost all the same samples. Only the CCO-A sample exhibited significantly lower σ values using the 4PS2 compared to the 4P1 measurement setup. Here, some considerations should be given:

- Samples measured with both setups were sintered under the same conditions of pressure and temperature;
- Considering only the grain size and the porosity of the samples, one should expect to measure the electrical conductivity measured with the setup 4P1;
- The electrical and thermal conductivities should follow closely the same dependency with respect to the grain size, but σ (4P1) did not reflect the dependency of κ (fig. 3-33). It was followed by the electrical conductivity measured with the setup 4PS2.

These results suggest that there could be some different factors which affected positively the electrical conductivity of the samples, that can be accountable to the different measurement apparatuses. Moreover, the CCO-A and CCO-BM samples showed a sudden increase in σ starting from 750 K that could be attributed to sintering and/or grain size effect. The same was not observed for the CCO-B sample. In any case, all the samples showed a semiconductor behavior with the electrical conductivity that increased with increasing temperatures, in all the. Moreover, the CCO-BM sample didn't show the low-temperature metal behavior typical of calcium cobaltite as evidenced by the disappearing of the metal-to-semiconductor transition temperature (T_S) [97]–[99].

So, T_S could have been shifted to even lower temperatures (lower than RT) or with a grain size as low as 5 nm CCO could act only as semiconductor. On the contrary, the electrical conductivity of CCO-A and CCO-B samples, showed an opposite response at the transition temperature, showing a metal-like conduction behavior starting at 600 K, since from this temperature the electrical conductivity stared to decrease. The comparison between samples measured with the 4P1 apparatus presenting different grain sizes and relative densities allowed to obtain some insights on the relative influence of density and grain size on the electrical conductivity. Considering the samples CCO-A and CCO-A-d, the increase of the porosity produced a moderate reduction of the electrical conductivity from 96 S/cm to 61 S/cm at 673 K, that remained quite constant at all temperatures. The pores can be considered an insulating phase that influences the electrical conductivity according to the effective medium theory (*EMT*)[107]:

$$\sigma = \frac{(3\varphi - 1)\sigma_1}{2}$$

Where σ is the effective electrical conductivity, φ is the volume fraction of the $Ca_3Co_4O_9$ phase and σ_1 is the electrical conductivity of the CCO particles. However, considering a relative density of 70% (φ=0.7), the total electrical conductivity resulted identical to σ of the dense sample, making this approach not appropriate to explain the reduction of the electrical conductivity. The differences in the electrical conductivity of the same samples measured with the 4PS2 apparatus are considerably higher, as the highest values of the electrical conductivity at the same temperature of 723 K (before the sudden increase in σ) are 24 S/cm and 100 S/cm for the porous and the dense CCO samples, respectively. These differences could be related to the different contact resistance of the apparatus and to the different methods used to determine the electrical conductivity. The influence of grain size, on the other hand, can be deduced comparing the electrical conductivities of sample CCO-A, CCO-B and CCO-BM. These samples, although being characterized by lower relative density values, exhibited a strong reduction of the electrical conductivity deriving from the reduction of the grain size. In fact, considering the values measured with 4P1apparatus and a grain size of 500 nm for the CCO-A sample, a decrease in the electrical conductivity from 61 S/cm to 34 S/cm (44% reduction) is produced by a decrease of the grain size from 500 nm to 80 nm, while a decrease from 80 nm to 5 nm induced a reduction of 65% in σ (from 34 S/cm to 12 S/cm). However, it must be considered that the density of the grain boundaries is not a linear function with respect to the grain size, so, the reduction of the electrical conductivity is more and more important, as long as the particle size is reduced. The differences observed with the conductivities measured with the 4PS2 apparatus, instead, are similar in importance considering the CCO-B and CCO-BM samples, while the differences between the CCO-A and the CCO-B samples are minimal.

Fig. 3-35 shows the Seebeck coefficient relative to the same sets of samples described before and measured with both apparatuses.

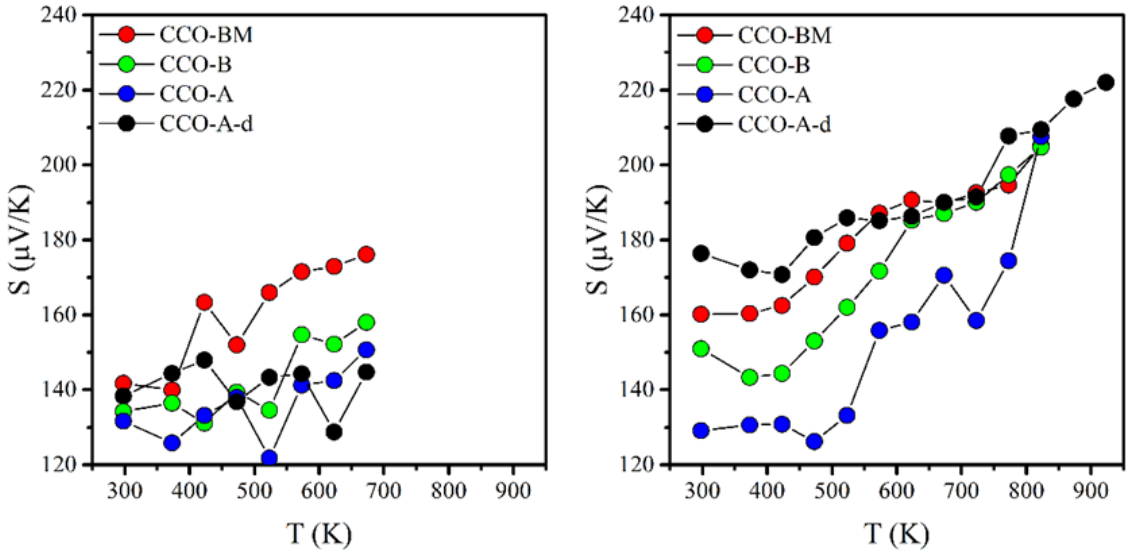

Figure 3-35 Seebeck coefficient of CCO samples (set2) measured using the S1 (left) and 4PS2 (right) apparatuses.

Some differences are observed between the values relative to the samples presenting different density, different grain size, and measured with two different instruments. First of all, the milling treatment didn't affect the nature of the charge carriers, as the samples keep showing a *p*-type behaviour. It can also be observed that the *S* values measured with the S1 cell and the 4PS2 setup are similar for all the samples, in particular at high temperatures, which means that the two setups produce nearly identical results, and that there are no differences in measuring the thermopower in a direction perpendicular or parallel to the conduction planes. The only difference can be observed for the dense CCO-A sample, which in the first case exhibited considerable lower *S* values and even further measurements on different comparable samples led to identical Seebeck coefficients (fig. 3-12). Considering only the samples with the same density, it can be seen that the reduction of the grain size caused an increase in the Seebeck coefficient, although quite limited. In the literature, a small increase in the Seebeck coefficient has been sometimes reported in nanostructured materials[108], although no firm physical basis for this increase could be presented. This effect appeared to be more evident at lower temperatures and from the data collected using the S1 apparatus, with room temperature *S* values for the CCO-A sample of 129 μV/K against the Seebeck coefficient of the CCO-BM sample of 160 μV/K. However, these differences tended to be cancelled by increasing the temperature.

Finally, considering the CCO-A and CCO-A-d samples, some indications of the effect of the density can be deduced, as with the S1 apparatus no differences can be observed, while with the 4PS2 setup the difference is considerable (at RT) with a larger Seebeck coefficients of 176 μV/K for the dense sample.

However, this result contrasted with the EMT theory for the Seebeck coefficient[107]:

$$S = \frac{6\kappa\langle S_i D_i\rangle}{1 - 3\langle \kappa_i D_i\rangle}$$

where $\langle S_i D_i\rangle$ and $\langle \kappa_i D_i\rangle$ indicates the volume average of the Seebeck coefficient and thermal conductivity, respectively, and D_i contains the electrical and thermal conductivity of the *i*-th phase.

$$D_i = \frac{\sigma_i}{(\kappa_i + 2\kappa) + (\sigma_i + 2\sigma)}$$

Since the thermal-electrical properties of the pores are considered as null, the Seebeck coefficient of the sample should be equal regardless the porosity.

Fig. 3-36 shows the power factor calculated for all the samples.

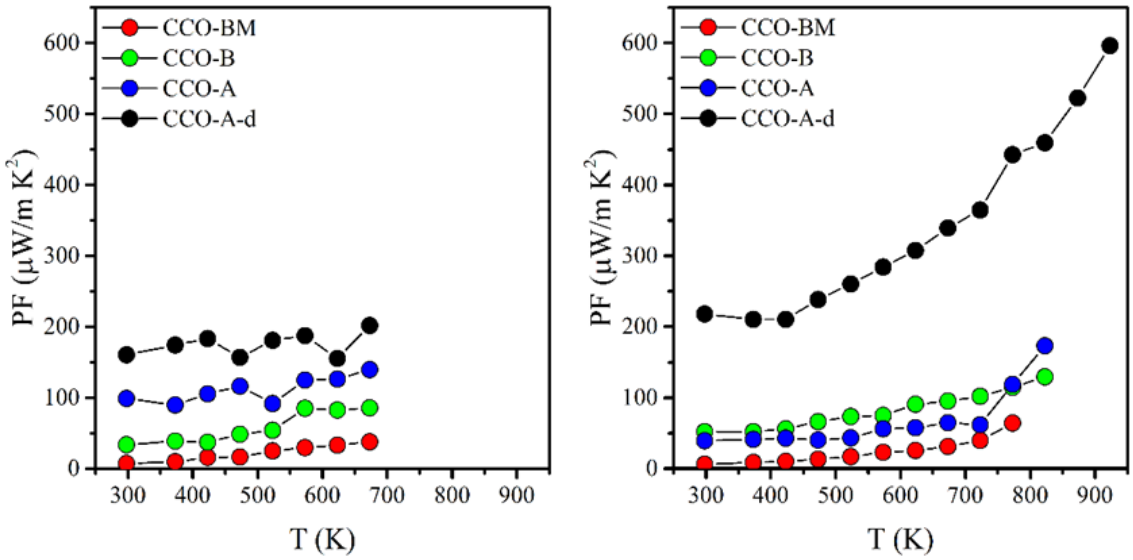

Figure 3-36 Power factor of CCO samples (set2) calculated using the S1 (left) and 4PS2 (right) apparatuses.

By considering the data from the electrical conductivity and the Seebeck coefficient measured with the 4P1 and S1 apparatuses, it can be seen that the dependency of the power factor from the relative density and the grain size followed closely the trend shown by the electrical conductivity, as the difference in this parameter between the various samples resulted much more relevant than the difference in the Seebeck coefficient, despite the quadratic dependency of the power factor from *S*.

As a result, the CCO-BM sample resulted the less performant, with *PF* values ranging between 7 $\mu W/K^2m$ at room temperature to 38 $\mu W/K^2m$ at 673 K.

Considering the reduction of the electrical conductivity induced by the porosity, the best power factor presented by samples obtained using milled powders is, in fact, almost four times lower compared to the best *PF* calculated for the submicrometric analogous (CCO-A, 139 $\mu W/K^2m$), while for the CCO-A-d sample it increased up to 202 $\mu W/K^2m$ at 673 K. In the same way, also the power factors calculated using the data calculated with the 4PS2 setup were affected by the differences in the electrical conductivity of the respective samples. The power factors of CCO-B and CCO-BM samples were similar to that measured using the 4P1 and S1 apparatuses, while for the CCO-A sample the difference between the two measurements could be described using the same explanations given for the electrical conductivity. The dense CCO-A-d sample, instead, showed an interesting power factor of 597 $\mu W/K^2m$ which is among the highest values between pure calcium cobaltite[109], [110] reported in literature.

Finally, in fig. 3-37 are reported the figures of merit of this set of samples, calculated using the data determined from 4P1, S1 and 4PS2 measurements.

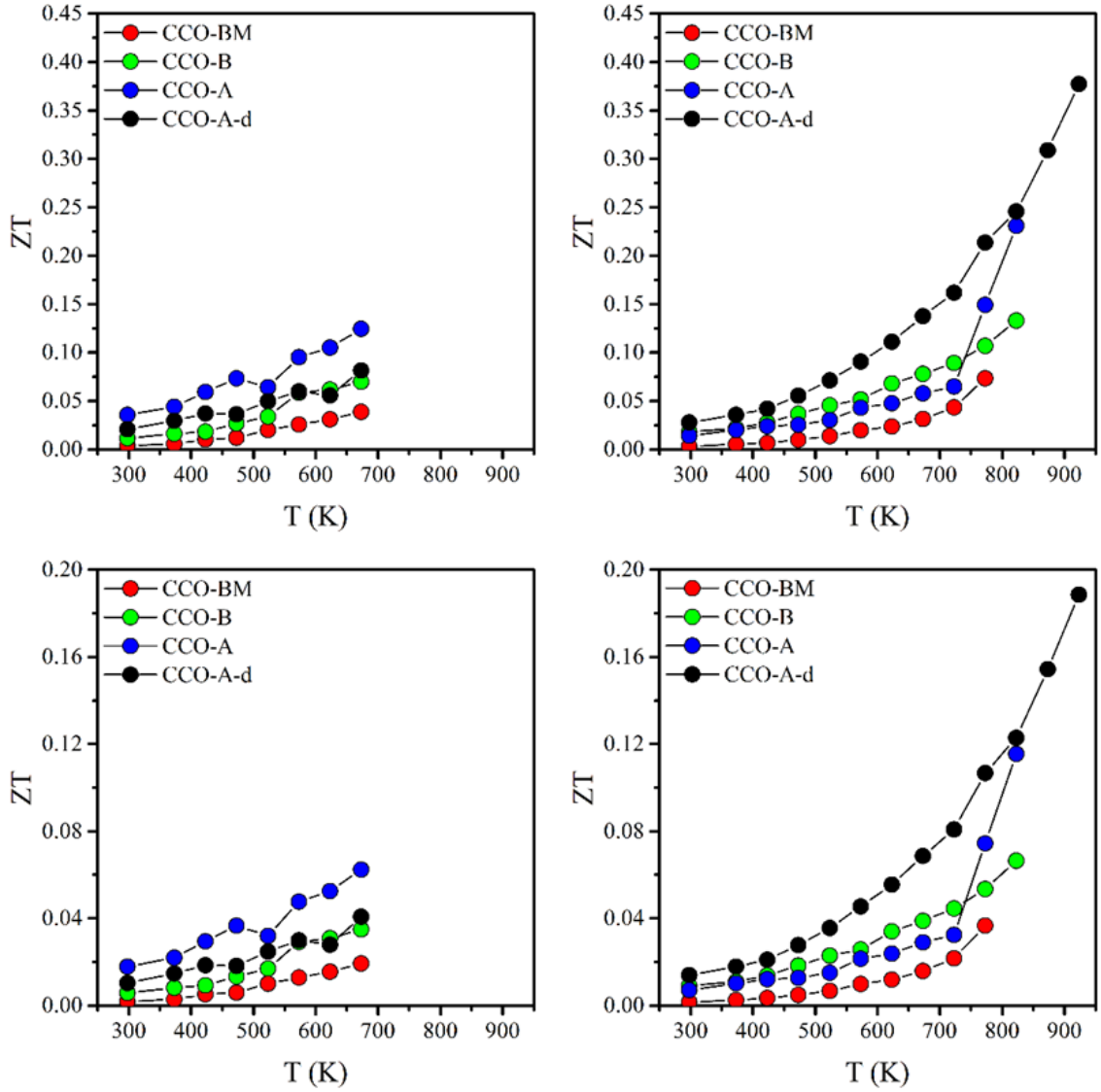

Figure 3-37 Figure of merit of CCO samples (set2) calculated using the data from S1 (left) and 4PS2 (right) apparatuses.

Also in this case, the figure of merit was calculated considering the possible anisotropic effect induced by the in-plane and out-of-plane thermal conductivity, as already made in section 3.2.1.3. Hence, since σ and κ have been measured along two mutually perpendicular directions, these values must be considered as indicative, due also to the presence of a significant porosity in most samples and to the presence of texturing, particularly in samples presenting larger grain sizes. However, since the milling treatment reduced the anisotropy of the nanoparticles, it was reasonable to think that the thermal conductivity of the CCO-BM sample should be not too far to the real values.

At the same time, also the real thermal conductivity of the CCO-A and CCO-B samples could be as closer to the LFA data as the grain size decreased, since the simultaneous effect of porosity and particles dimension should reduce the effect of the anisotropy. Fig. 3-37 shows that the best figure of merit can be achieved, as expected, with samples presenting the larger grain size. However, with 4P1 and S1 measurements, the best *ZT* was calculated for the porous CCO-A (*ZT*=0.12 at 673 K) sample rather than the dense one (*ZT*=0.08 at 673 K). In fact, the differences between the electrical conductivities and the Seebeck coefficients (and so between the power factors) of these two samples were small enough to make the large difference in their thermal conductivities the discriminating factor to achieve the highest figure of merit. On the contrary, using the 4PS2 data, the largest figure of merit of 0.38 at 923 K was calculated for the CCO-A-d sample thanks to its higher power factor. This value is comparable to those achieved with many of the most efficient doping strategies (see Introduction) so, in this case, the use of the measured out-of-plane thermal conductivity could have played a major role in increasing *ZT*. At the same time, using a two-times lower in-plane thermal conductivity, the resulting figure of merit is of 0.19, which still is among the highest figure of merit of undoped calcium cobaltite[110]. The figure of merit of CCO-BM sample is, instead, considerably lower because of the strong reduction of the electrical conductivity caused by the simultaneous effect of porosity and amorphization.

In conclusion, the reduction of the grain size and the sintering of dense bulk samples maintaining the nanometric grain size can be obtained using the HP-FAST sintering approach in mild operating conditions, though the thermoelectric performances of these samples are considerably lower compared to samples characterized by larger grain size and anisotropy. However, it must be noted that the thermal conductivity and the figure of merit of the amorphized calcium cobaltite could be measured only on samples strongly affected by the porosity because of the instrumental limitations of both the HP-FAST and the LFA apparatuses. As expected, the dense amorphized samples exhibited significantly higher power factors compared to their porous analogous (CCO-BM), but their thermal conductivity could be measured. If the thermal conductivity of these samples could be reduced by the nanostructure like the porosity did, the figure of merit of these dense samples could be high enough to make milled CCO even more competitive than it already is between *p*-type thermoelectric oxides.

3.2.3. CCO doping with Ag

In the previous section we have evidenced how the amorphization of calcium cobaltite caused a strong reduction of its electrical conductivity. Trying to reduce this effect, we investigated the possibility to increase the electrical conductivity through doping. In particular, Ag was chosen as suitable dopant in substitution of Ca^{2+}. Its ability to increase both σ and S, by increasing carrier concentrations and mobility, while reducing κ it has been largely reported in the literature[49], [111]. As for undoped calcium cobaltite, the synthesis of Ag-doped CCO is traditionally performed by means of solid state routes while the use of sol-gel routes is still poorly investigated. For these reasons we investigated the possibility of synthesizing this compound using the same wet-chemistry approach used for undoped calcium cobaltite.

3.2.3.1. Synthesis of the doped powders

The synthesis of Ag-doped calcium cobaltite powders corresponding to the general formula $Ca_{3-x}Ag_xCo_4O_9$, were carried out using the same procedure described previously for undoped calcium cobaltite. Stoichiometric quantity of $AgNO_3$ in quantity equal to x=0.1, 0.3 and 0.5, corresponding to 2, 6 and 10 wt%, was added to the solution along with the other metal nitrates, keeping constant the ratio between the citric acid and the metal cations. These powders will be referred as CCO-Ag10, CCO-Ag30 and CCO-Ag50, respectively. The addition of silver nitrate made the swelling of the gel during the drying step more accentuated and the organic precursor easier to decompose. Further annealing treatments have been carried out with the same procedure used for the undoped cobaltite, following the method A: a suitable quantity of the organic precursor was inserted into an alumina crucible and then heated using a muffle furnace at 1073 K for 2 hours. Fig. 3-38 shows the XRD pattern of silver doped calcium cobaltite powders with different Ag content, compared to undoped $Ca_3Co_4O_9$.

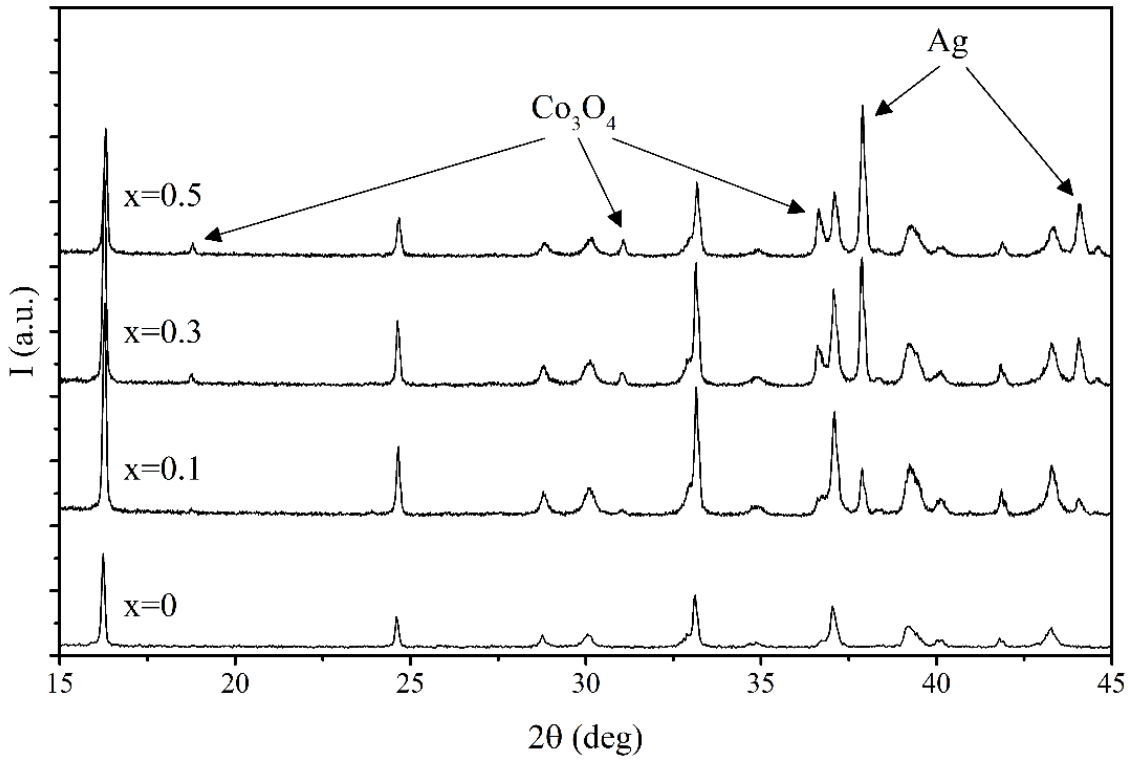

Figure 3-38 XRD patterns of Ag-doped CCO powders samples with different silver amount (x=0, 0.1, 0.3 and 0.5). The formation of metallic silver and of the cobalt dicobalt (Co_3O_4) phase can be observed by the presence of the respective diffraction peaks.

It can be seen that the addition of silver in the sol gel mixture led to the formation of two secondary phases together with the calcium cobaltite phase, which were identified as the metallic silver (Ag) and the cobalt dicobalt (Co_3O_4) phases. The metallic silver is produced when the citric acid is burned out during calcination, in fact, a local reducing atmosphere is induced leading to the reduction of the silver cations. On the other hand, the Co_3O_4 phase is produced because of the change in the Ca/Co ratio in the synthesis environment. In fact, the pure calcium cobaltite phase can be obtained only in a narrow interval of Ca/Co ratio as evidenced by its phase diagram illustrated in fig. 3-39[112].

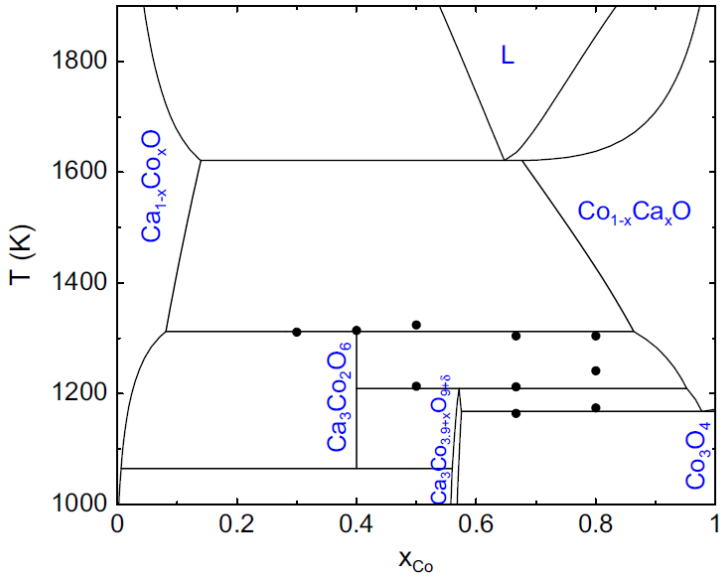

Figure 3-39 Phase diagram of the CoO/CaO system. Taken from ref. [112].

The more calcium is substituted, the more the molar ratio is shifted to the right side of the phase diagram ending in the region where the Co_3O_4 is formed, hence, powders with higher content of silver exhibited greater quantity of impurity. Using the specific function of the HighScore plus software, a quantification of the phases has been estimated. For x=0.1 the amount of the metallic silver and the cobalt dicobalt phase were calculated both equal to 1.7 %. Increasing the doping quantity to x=0.3, the phases were present in a quantity equal to 4.9% and 5.9% respectively. Finally, for x=0.5 the metallic silver phase was present at 7.8% while Co_3O_4 at 10%. Despite the presence of secondary phases, the powders were ball milled and sintered and the thermoelectric properties measured. It must be said that rather than producing a real doping, the addition of silver resulted in the formation of a composite material, although throughout the chapter the term "doping" will be used.

3.2.3.2. Sintering of the doped powders

For the thermoelectric characterization, two different set of samples characterized by a different level of porosity were sintered using the HP-FAST apparatus, in order to investigate the effect of the sample density. The first set (set1) consisted in 3 samples (one for every composition) which were sintered at 723 K under a uniaxial pressure of 100 MPa and that were characterized by an absolute density of about 3.5 g/cm^3. These porous samples will be referred as CCO-Ag10, CCO-Ag30 and CCO-Ag50.

The second set of samples (set2) was obtained by sintering the same powders at 923 K under a uniaxial pressure of 180 MPa to achieve an absolute density of about 4.5 g/cm^3, these samples will be labeled as CCO-Ag10-d, CCO-Ag30-d and CCO-Ag50-d, with the letter "d" used to identify the samples with higher density. Tab. 3-6 summarizes these two set of samples.

Table 3-6 Sintering conditions of the silver doped samples characterized for their thermoelectric properties.

Set1			
Sample	T_S (K)	p_S (MPa)	ρ (g/cm^3)
CCO-Ag10	723 K	100 MPa	3.27
CCO-Ag30			3.13
CCO-Ag50			3.32
Set2			
Sample	T_S (K)	p_S (MPa)	ρ (g/cm^3)
CCO-Ag10-d	923 K	180 MPa	4.42
CCO-Ag30-d			4.49
CCO-Ag50-d			4.53

The density of these samples is reported as the absolute density because of their composite nature, for which it was difficult to calculate a theoretical density. The typical diffraction pattern of sintered samples is reported in fig. 3-40.

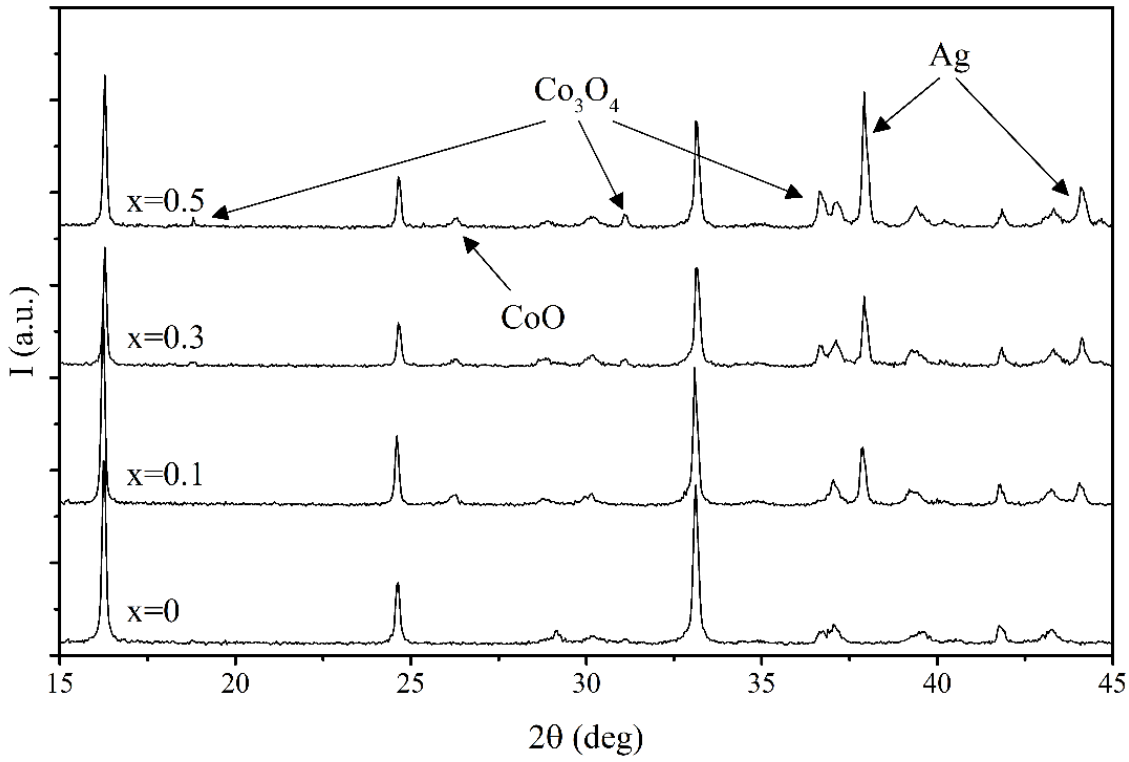

Figure 3-40 XRD patterns of Ag-doped CCO samples with different silver amount (x=0, 0.1, 0.3 and 0.5). The presence of the extraneous peaks relative to the Ag and Co_3O_4 phase evidences how the impurities are maintained even after the sintering procedure.

Also in these samples, due to the anisotropic morphology of the particles, the intensity of all the peaks relative to the *00l0* family of planes resulted intensified compared to the other reflections. Moreover, as already observed in the diffraction pattern of the powders, the amount of the secondary phases increased with increasing the silver content. The extraneous peak around 2θ=26° was identified as CaO but its intensity could not be related to the silver content and it was probably due to the formation of a superficial oxide layer deriving from the reduction of the surface during the sintering process. To avoid this interference before any further thermoelectric measurements, the surface of the samples was polished in order to remove this layer. The phase quantification of the metallic silver was of 6%, 9% and 10%, for x=0.1, 0.3 and 0.5, respectively. These values are all higher compared to the quantification performed on the respective powder, which means that the reducing HP-FAST environment might have converted more Ag^+ into metallic silver. The presence of metallic silver can be easily observed from the SEM micrograph reported in fig. 3-41 taken using the backscattered and relative to the sample sintered form CCO-Ag50 powders, where the presence of brighter areas indicates a phase containing atoms with higher atomic number (Ag, in this case).

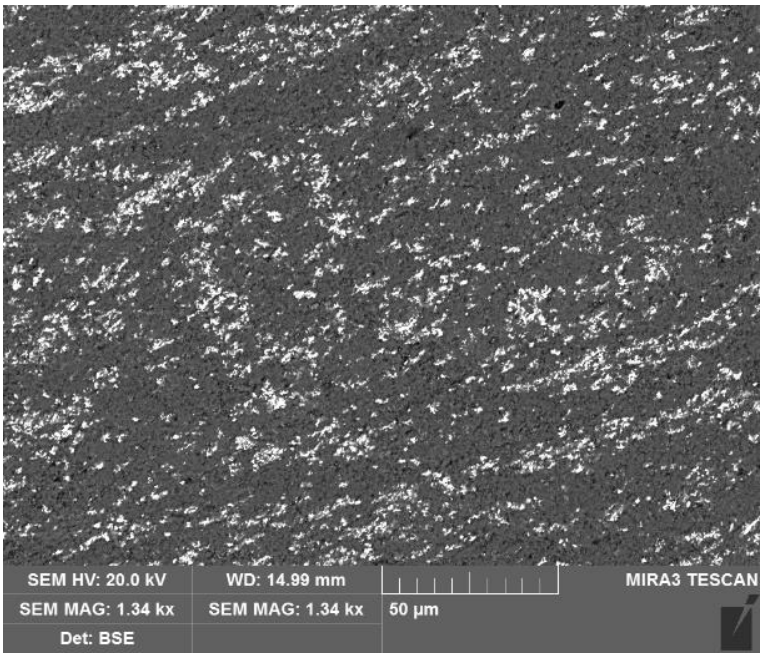

Figure 3-41 SEM micrograph of the CCO-Ag50 sample taken using the detector for backscattered electrons. Brighter areas correspond to Ag-rich particles.

The EDX analysis (fig. 3-42) performed on darker areas of the sample, which should correspond to the calcium cobaltite phase, do not evidence any peak relative to Ag atoms. This suggests that all the silver added to the reaction mixture is eventually reduced during the annealing or the sintering into metallic silver phase and didn't enter the structure of the calcium cobaltite.

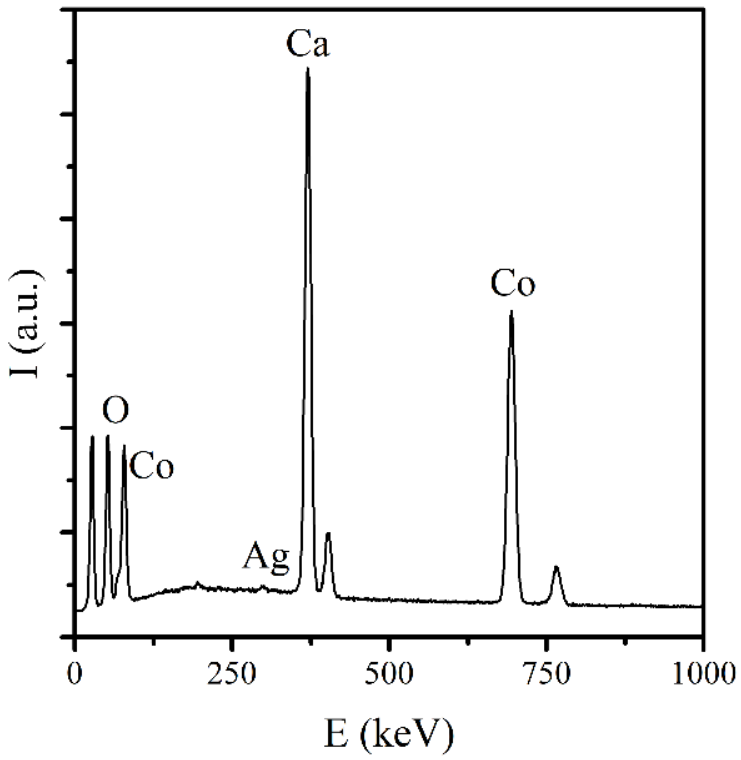

Figure 3-42 EDX spectrum of the darker areas of fig. 3-41. No peaks relative to Ag are present suggesting the absence of effective silver doping.

3.2.3.3. Thermoelectric properties of Ag-doped CCO samples

The thermoelectric properties of Ag-doped submicrometric samples were measured using only the 4P1 and S1 apparatuses for the for electrical conductivity and Seebeck coefficient. Unfortunately, no measurements of the thermal conductivity of these samples were performed, so the comparison with values found in literature will be analyzed up to the power factor. Fig. 3-43 show the electrical conductivity of porous and dense samples compared to porous and dense undoped CCO samples.

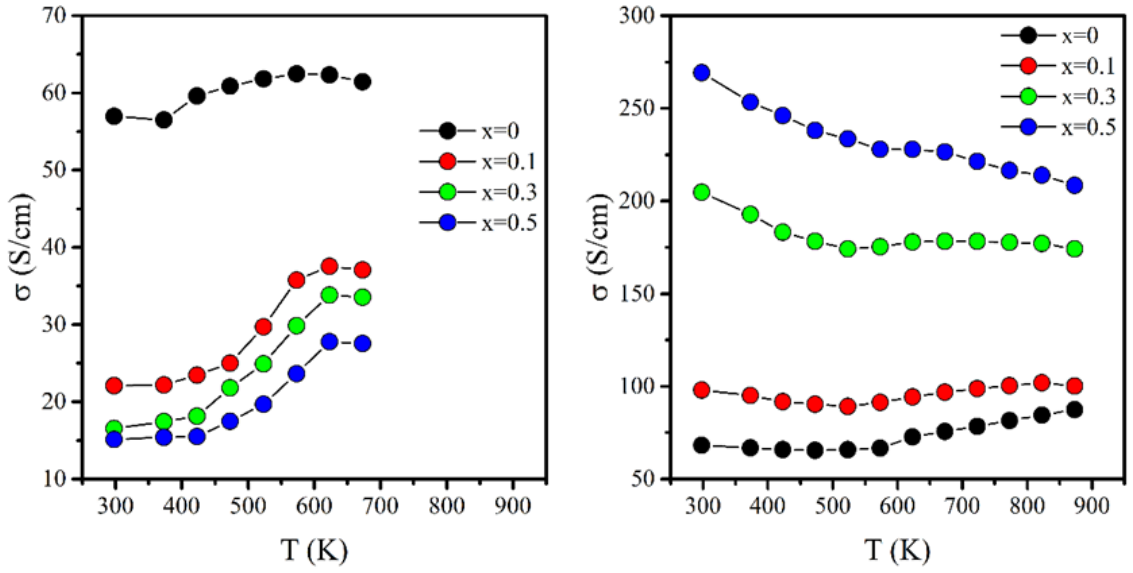

Figure 3-43 Electrical conductivity of set1 (left) and set2 (right) Ag-doped CCO samples.

Contrary to what expected, the electrical conductivity of first set of porous samples (left) was generally two times lower compared to the undoped calcium cobaltite regardless from the silver content and it decreased while increasing *x*. In fact, the highest σ relative to Ag-doped samples was of 38, 34 and 28 S/cm at 623 K for x=0.1, 0.3 and 0.5, respectively, while for undoped CCO it was of 62 S/cm at the same temperature. Moreover, by looking at the trend of the electrical conductivity against the temperature, it was possible to observe three different regions. In the first, from RT to 450 K, σ increased of about 5%, in the second region, up to 650 K, the increase was more evident, with an increase of about 50%. In the last region, instead, the electrical conductivity started to decrease following a typical metallic behavior. However, this sudden decrease was also observed for undoped CCO-A and CCO-B samples, so it could be related somehow to the presence of porosity in anisotropic samples. On the other hand, the electrical conductivity of the dense samples (right) was more than one order of magnitude higher compared to the porous ones and as expected σ increased with increasing the silver content. The highest σ of 269 S/cm was measured at room temperature for the CCO-Ag50-d sample, which is more than four times higher compared to the electrical conductivity of the undoped sample measured at the same temperature (68 S/cm at RT), while for x=0.3 and x=0.1 the increase is more contained, in particular for the sample CCO-Ag10-d (98 S/cm at RT). In fact, the increase of the electrical conductivity with the silver content didn't follow a linear trend (fig. 3-44, left) since an increase in the silver from x=0 to x=0.1 produced a relative small increase in σ, from x=0.1 to x=0.3 the increase in the electrical conductivity was considerably larger, while from x=0.3 to x=0.5 the increase was moderated, a trend that could be explained with the percolative-like behavior described in fig. 3-44 (right)[113].

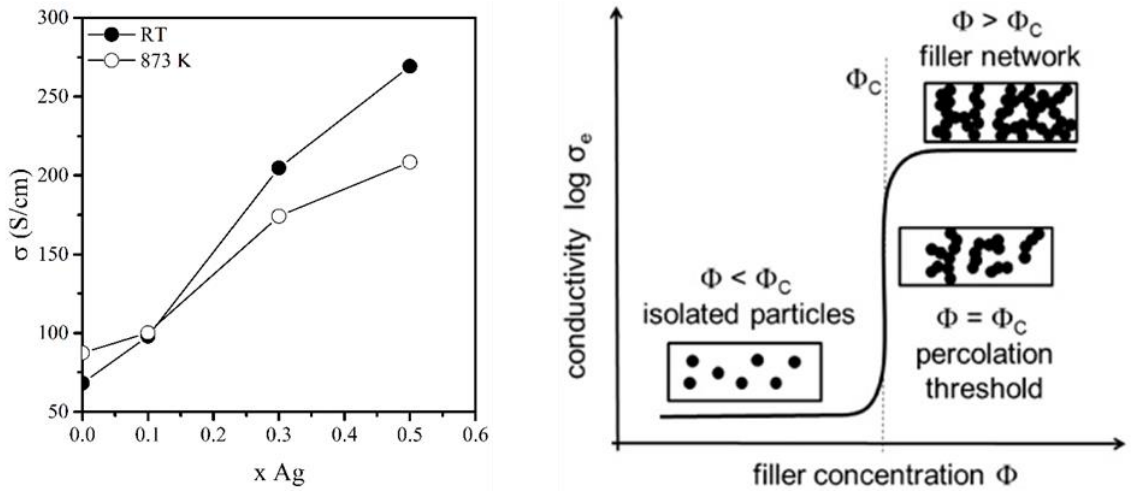

Figure 3-44 Room temperature and 873 K electrical conductivity against the Ag content (left.) The trend resembles the percolative-like behavior reported in the right panel. Taken from ref. [113].

With a small quantity of metallic silver phase, the Ag particles are well dispersed and segregated in the CCO matrix, but still leading to a moderate increase in the overall conductivity. Increasing the silver amount, the dispersed silver starts to get in contact and a sudden strong rise in σ is observed. Further increase in the electrical conductivity is observed with x=0.5, although the increase is less marked. Supposedly, further increase in the silver content would have led to a plateau σ value close to that of metallic Ag. All the silver doped samples exhibited both a semiconductor and a metallic behavior, depending on the amount of metallic silver. With higher silver content the electrical conductivity is governed by the metallic behavior, *vice versa*, with lower silver content the semiconductor behavior is the most significant, in fact:

- CCO-Ag50-d exhibited a metallic behavior in all the investigated range of temperatures, apart from a small attenuation of the negative slope between 550 and 650 K, with σ constantly decreasing from 269 S/cm at RT to 208 S/cm at 873 K;
- CCO-Ag30-d showed an initial decrease of the electrical conductivity from 205 S/cm at RT down to 174 S/cm 523 K, then σ increased slightly up to 178 S/cm at 723 K, then it started to decrease again down to 174 S/cm at 873 K;
- CCO-Ag10-d showed an initial decrease of the electrical conductivity from 98 S/cm at RT to 89 S/cm at 523 K, then σ increased up to 102 S/cm at 823 K. A small reduction to 100 S/cm at 873 K was observed.

The Seebeck coefficient of porous and dense samples is reported in fig. 3-45.

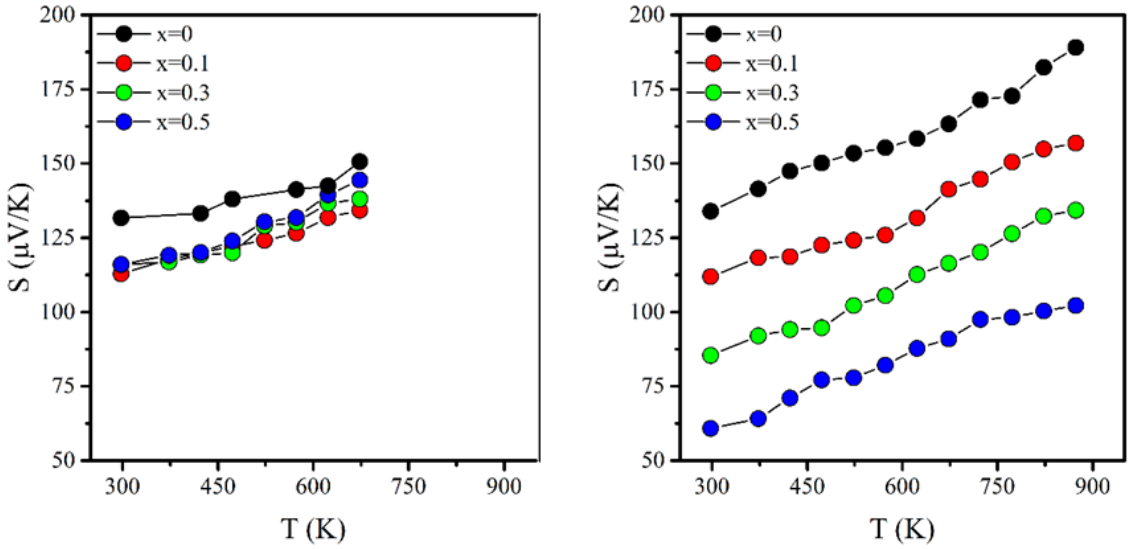

Figure 3-45 Seebeck coefficient of set1 (left) and set2 (right) Ag-doped CCO samples.

The Seebeck coefficients of porous samples (left) were generally lower compared to the undoped analogous because of the presence of the metallic silver phase, but higher compared to the thermopower of the dense ones (right). This could be explained by the presence of pores which kept the metallic silver phase well separated thus limiting its effect on the transport properties. Moreover, the trend of *S* with respect to the silver content in porous samples seemed to be related, inversely, to the dependency of the electrical conductivity against *x* (fig. 3-43, left), despite the differences between the *S* values of the various samples were still quite small. On the contrary, the differences between the thermopower of dense silver doped samples were more relevant. In fact, the Seebeck coefficient at 873 K is 157 μV/K for *x*=0.1 and 102 μV/K for *x*=0.5, which are respectively 17% and 46% lower compared to the undoped dense sample, also in this case inversely following the trend of the electrical conductivity with the silver content. In any case, the strong effect of the metallic silver phase on the electrical conductivity didn't affect the nature of the main charge carriers because for all the samples the sign of the Seebeck coefficient remained unaltered (positive). Thus, the large quantity of electrons provided by the metallic silver acted mainly as strong compensator toward the holes of calcium cobaltite leading to the low observed thermopower values.

The power factor of these set of samples is reported in fig. 3-46.

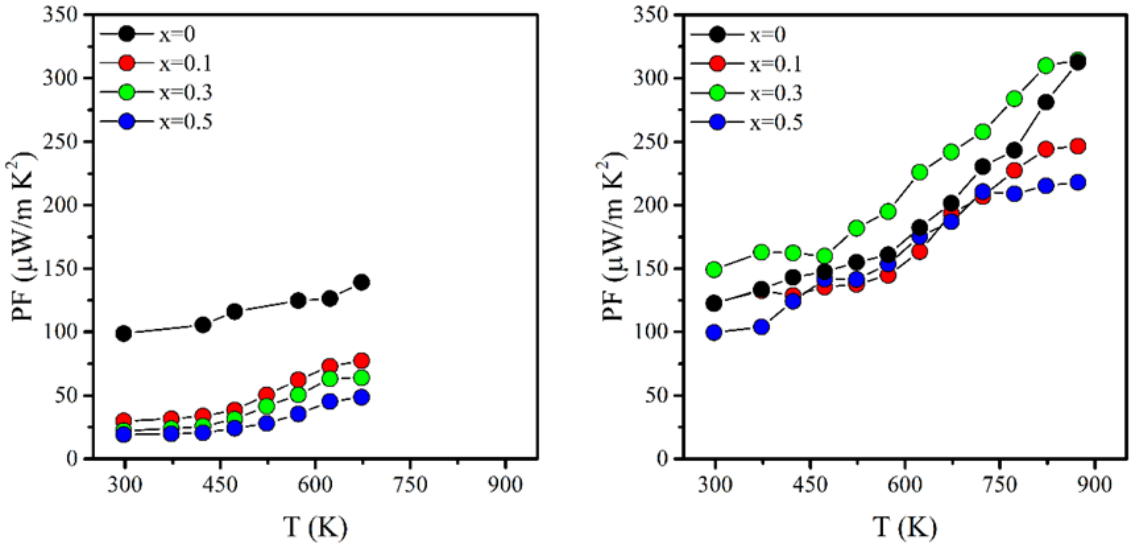

Figure 3-46 Power factor of set1 (left) and set2 (right) Ag-doped CCO samples.

In the case of porous silver doped samples, the power factor resulted considerably lower compared to the undoped calcium cobaltite, due to the simultaneous combination of lower electrical conductivity and thermopower which led to a reduction, at best, of about 55% at 673 K ($PF_{x=0}$=139 μW/K^{2}m, $PF_{x=0.1}$=77 μW/K^{2}m). In the case of the dense samples, the highest power factor was achieved with a silver content equal to 0.3, as its *PF* was generally higher in all the investigated range of temperature compared to the undoped dense CCO sample. The power factors of the other two dense samples (CCO-Ag10-d and CCO-Ag50-d) were similar to the *PF* of undoped sample, and similar each other (between 450 K and 750 K) because of opposite reasons, leading to the same results:

- CCO-Ag10-d has larger S and lower σ compared to CCO-Ag50-d;
- CCO-Ag50-d has larger σ and lower S compared to CCO-Ag10-d.

At higher temperature (T>750 K), the *PF* of the undoped sample is significantly larger, because of larger Seebeck coefficient and semiconductor-like electrical conductivity.

3.2.3.4. Milling of Ag-doped CCO powders and HP-FAST sintering

Since the main drawback of the reduction of the grain size was the reduction of the electrical conductivity and since large electrical conductivities can be achieved with x=0.5, CCO-Ag50 powders were treated using the standard ball milling procedure (400 rpm / 3 h). Fig. 3-47 shows the diffraction pattern of the CCOAg50-BM powder.

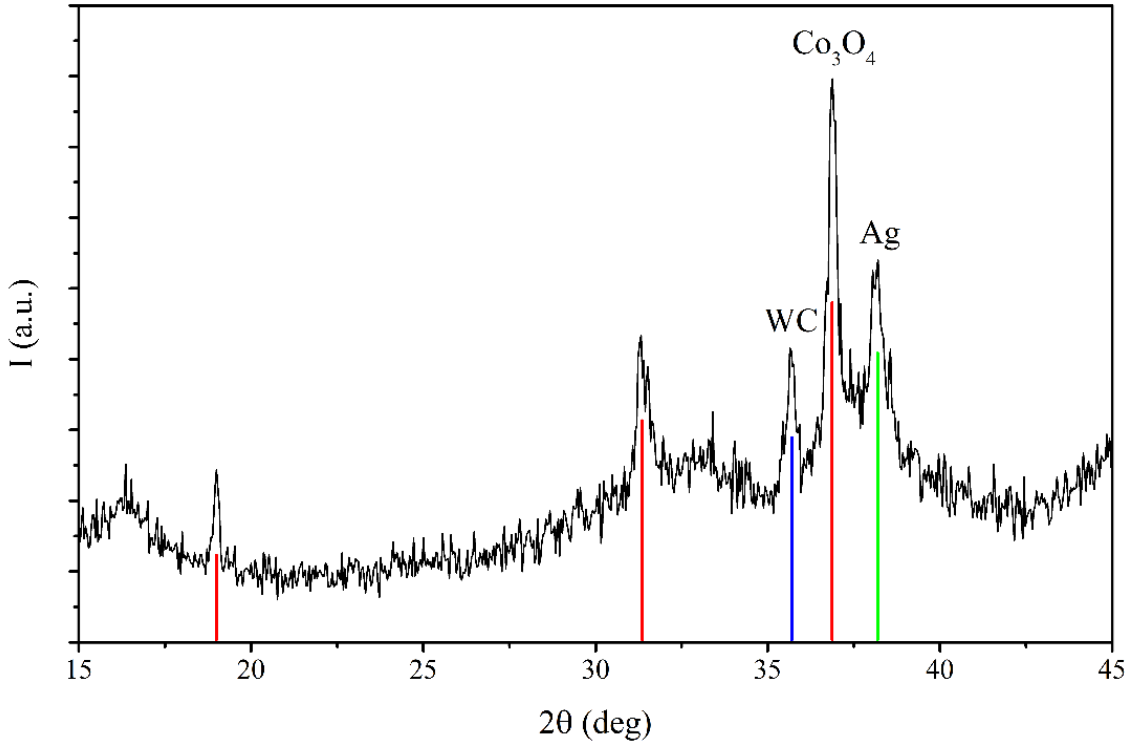

Figure 3-47 XRD pattern of milled CCO-Ag50 powder. Milling conditions are 400 rpm/3 h. The red peaks belong to the Co_3O_4 phase, the blue peak to the WC phase and the green peak to the Ag phase.

After the milling procedure, the CCO-Ag50 powder was characterized by a grain size of ~3 nm, calculated using the Scherrer equation on the *0020* peak of the calcium cobaltite phase (2θ=16.5°), confirming the effectiveness of the ball milling procedure even using doped powders. Also in this case, secondary phases were observed. The extraneous peaks were assigned to the Co_3O_4 phase (red line), deriving from the non-stoichiometry of the compound, and to the metallic silver phase (green line), that is the product of the chemical reduction occurring during the annealing of the powder. In this case, only the *111* reflection of Ag was present, while the *002* peak, which lies at 2θ=44.4°, could not be observed, maybe because of some modifications in the morphology of the silver particles causing an orientation along other crystallographic directions. Finally, some tungsten carbide phase (WC, blue line), a contamination caused by the ball milling treatment, was also observed.

However, the quantification of the phases was not possible because of the presence of only a single peak of the calcium cobaltite phase.

CCO-Ag50-BM samples, were sintered using the HP-FAST apparatus and according to the sintering conditions used for undoped powders (723 K and 823 K and 430 MPa). The XRD pattern of these samples are reported in fig. 3-48.

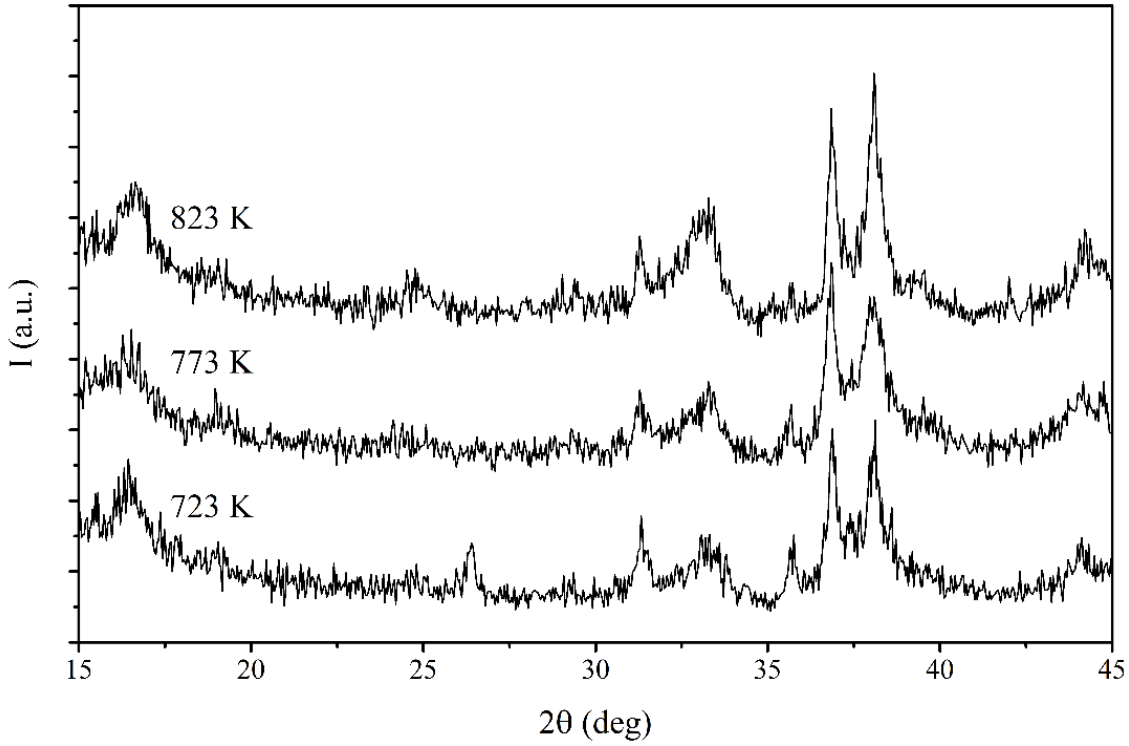

Figure 3-48 XRD patterns of CCO-Ag50-BM samples sintered at different temperatures. Compared to what observed for undoped CCO, a grain size of few nanometers (6 nm) can be maintained even at the highest sintering temperature.

Milled CCO-Ag50 samples (tab. 3-7) showed comparable diffraction patterns in term of peaks intensity.

Table 3-7 List of CCO-Ag50 samples used for the thermoelectric characterization.

Sample	T_S (K)	p_S (MPa)	ρ (g/cm^3)	<d> (nm)
CCO-Ag50-BM	723	430 MPa	4.69	4
	773		4.81	3
	823		4.95	5

Surprisingly, no modification in the FWHM of the *0020* reflection of the calcium cobaltite phase was observed, indicating a limited grain growth. This was in contrast with the behavior observed in the case of the undoped powder, where a sintering temperature of 823 K was enough to induce an evident recrystallization of the milled powders. In fact, the grain size of the silver doped samples, calculated using the Wiedemann-Franz law on the *0020* reflection, was maintained between 3 and 5 nm even at the highest sintering temperature. Supposedly, it can probably be related to the presence of secondary phases that hindered the diffusion of the material limiting the grain growth. These samples were also characterized by a density that increased with the sintering temperature from 4.69 to 4.95 g/cm^3. These values are higher compared to the sub-micrometric Ag-doped samples, a result that can be explained considering the higher sintering pressure and the lower grain size, which helped to increase the degree of sintering. However, also the noteworthy presence of secondary phases with larger density could affect the overall values.

3.2.3.5. Thermoelectric properties of CCO samples sintered from ball milled Ag-doped powders

The electrical conductivity was measured only using the four-probe electrochemical cell used for the other CCO samples and the Seebeck coefficient with the 4P1 and S1 apparatus. Fig. 3-49 shows the electrical conductivity of the milled silver-doped samples compared to the undoped CCO-BM (right) and the submicrometric CCO-Ag50-d samples (left). As undoped CCO-BM samples, only the one sintered at 823 K was chosen as comparison. The choice was made considering its overall thermoelectric properties and the largest temperature interval investigated.

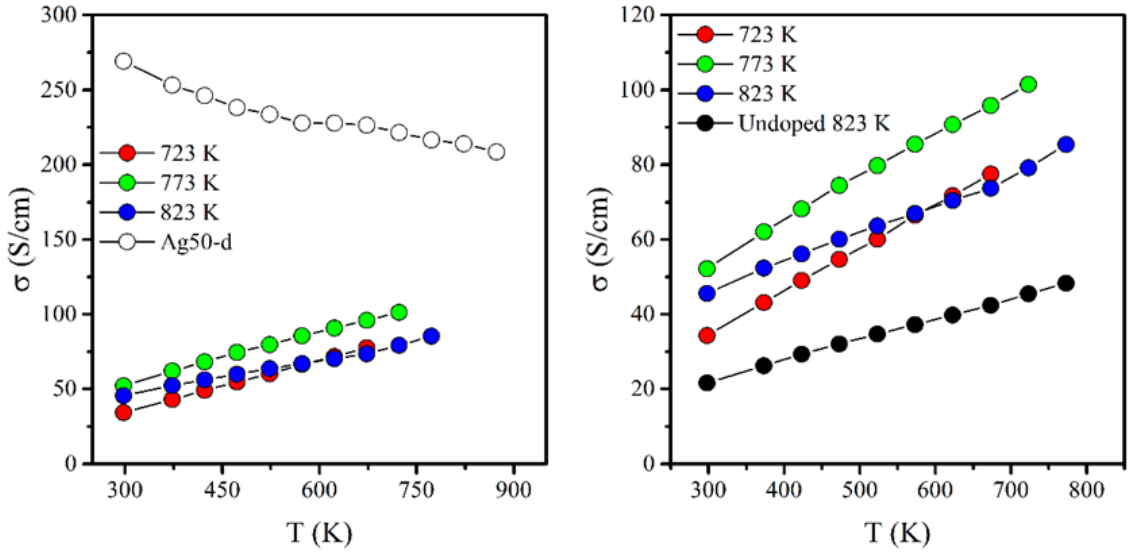

Figure 3-49 Electrical conductivity of CCO-Ag-50 samples (red, green and blue point) with respect to the submicrometric analogous (white, left) and to the undoped CCO-BM sample (black, right).

As expected, the milling of the powder induced a decrease of the electrical conductivity, by about a factor of 6 at room temperature.

A decrease by about a factor of 2 was observed at higher temperatures. The difference between the electrical conductivities of the sub-micrometric and the milled samples, in fact, was resulted reduced mainly because of the general semiconductor behavior of the CCO-Ag50-BM samples compared to the metallic conduction observed for the submicrometric analogous. In particular, the change of the conduction behavior from metallic to semiconducting can be related somehow to the presence of a large quantity of different secondary phases that affected the electrical conductivity. At the same time, the silver doping resulted efficient in increasing the electrical conductivity of the ball milled CCO. The highest electrical conductivity of 100 S/cm was achieved at 723 K for the sample sintered at 773 K, twice the electrical conductivity of the undoped sample (σ_{723K}=45 S/cm). It also showed the largest σ in all the temperature range. However, the sample sintered at the 823 K showed an anomalous trend against the temperature, leading to the lowest observed electrical conductivity starting from 673 K.

The Seebeck coefficients of the milled doped samples are reported in fig. 3-50.

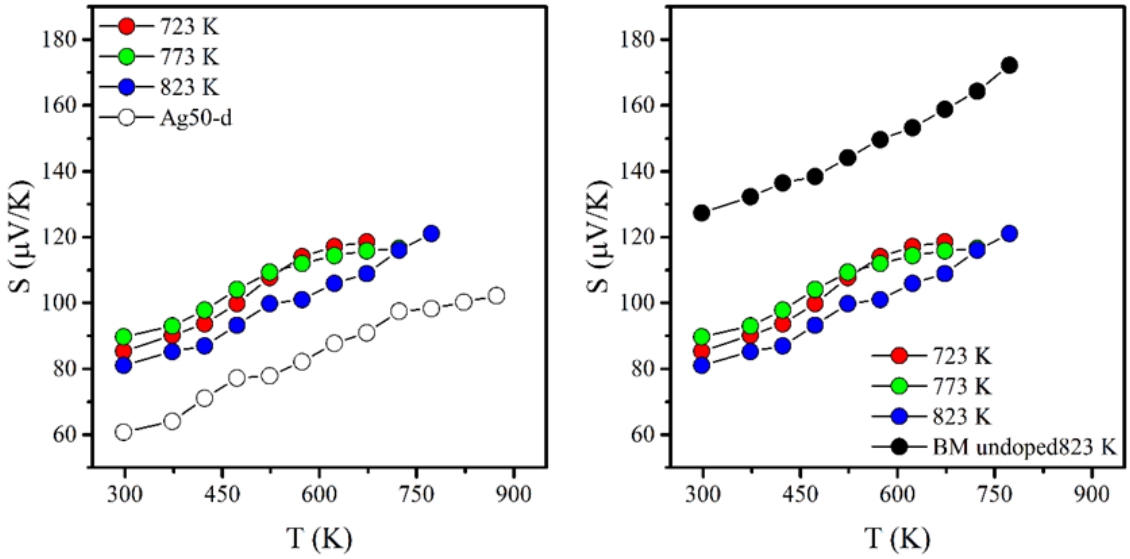

Figure 3-50 Seebeck coefficient of CCO-Ag-50 samples (red, green and blue point) with respect to the submicrometric analogous (white, left) and to the undoped CCO-BM sample (black, right).

All the milled samples exhibited a Seebeck coefficient that is generally higher (30-50% at room temperature) compared to their submicrometric analogous, but these differences diminished while increasing the temperature. In fact, the milled sample sintered at 823 K showed a *S* value of 121 μV/K at 773 K against 98 μV/K of the sub-micrometric one at the same temperature, an increase of about 20%. However, CCO-Ag50-BM and CCO-Ag50-d should exhibit the same, or at least very close, Seebeck coefficients as they were obtained starting from the same powder.

This could lead to two possible conclusions: the reduction of the grain size plays an important role in increasing the Seebeck coefficient or, like the electrical conductivity, the differences are related to the presence of different secondary phases, which concur in increasing the overall Seebeck coefficient. The comparison between the CCO-Ag50-BM samples and the respective undoped CCO-BM sample evidenced a general decrease of the thermopower of the doped samples, as expected from the presence of the *n*-type metallic silver phase compensating the *p*-type behavior of the calcium cobaltite.

The calculated power factors are reported in fig. 3-51.

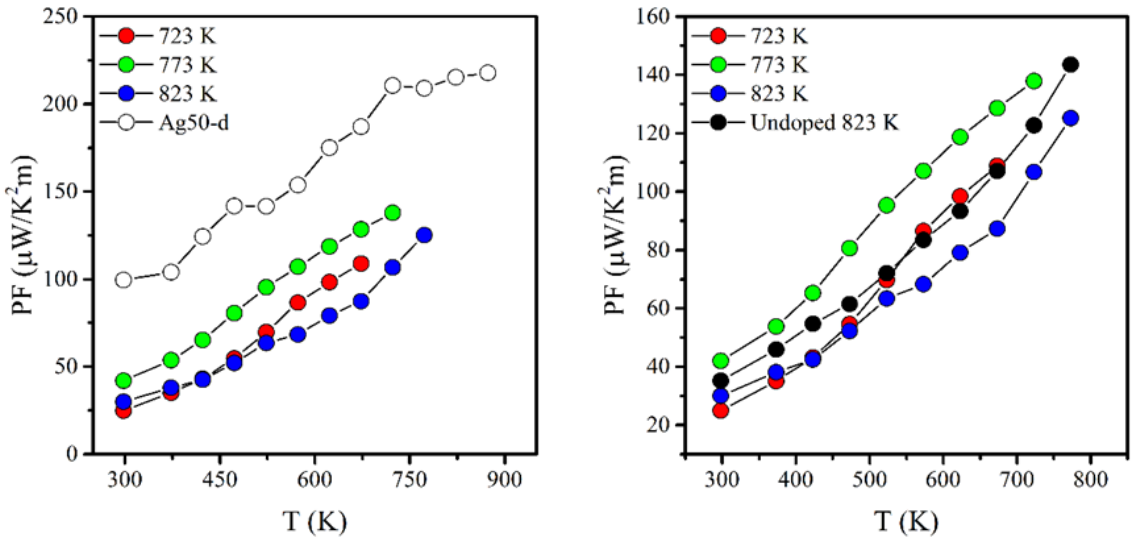

Figure 3-51 Power factor of CCO-Ag-50 samples (red, green and blue point) with respect to the submicrometric analogous (white, left) and to the undoped CCO-BM sample (black, right).

Compared to the unmilled CCO-Ag50-d sample, the power factors of all the CCO-Ag50-BM samples are generally lower. However, the reduction of the *PF* which resulted from the ball milling treatment was slightly lower in magnitude compared to what has been observed between undoped milled and unmilled calcium cobaltite (fig. 3-31). At the highest investigated temperature of 723 K, the best power factor among BM samples was of 138 $\mu W/K^2m$, about 34% lower compared to the *PF* of the equivalent submicrometric sample (211 $\mu W/K^2m$) – for undoped powders the reduction was of about 40%. At room temperature the PF of the submicrometric sample was at best slightly more than two times higher, while for undoped powders the difference was larger (about four times higher). Considering the ball milled cobaltite, the doped samples sintered at 723 and 823 K exhibited a power factor equal or even lower compared to the undoped equivalent. Only the Ag-doped sample sintered at 773 K showed a slight increase of the *PF*. The reason lied mostly in its high electrical conductivity, as the differences in the Seebeck coefficients between the doped

samples were not so significant. On the contrary, the higher *S* of the undoped milled sample was not enough to compensate its lower σ.

In conclusion, the addition of silver has been confirmed to increase the electrical conductivity of calcium cobaltite in both submicrometric and nanometric morphology. However, the annealing procedure of the sol-gel synthesis caused the reduction of all the added silver, which resulted in the formation of a Ag-metallic phase, rather than replacing the calcium atoms, thus explaining both the metallic-like electrical conductivity and the significant reduction of the Seebeck coefficient. This, in turn, affected the power factor making the x=0.3 composition the only one showing interesting values. The same results (increase of σ, decrease of *S*) were observed in milled samples, but they behave as semiconductors, rather than metals, despite the presence of metallic silver. It can be deduced that the thermal conductivities of these silver doped samples, at least for the submicrometric ones, could be higher compared to the undoped calcium cobaltite. At the same time, the theoretical reduction of the thermal conductivity induced by the nanostructure (and maybe thanks to the presence of secondary phases), could make the combination of ball milling and doping a useful tool for improving the thermoelectric properties of calcium cobaltite.

3.2.4. CCO with bimodal microstructure

A last possible strategy to improve the thermoelectric properties of calcium cobaltite could be the combination of micro and nanostructure through the preparation of composite samples sintered from submicrometric and milled powders. The main purpose was to preserve the high conduction properties of calcium cobaltite together with the eventual reduction of the thermal conductivity induced by the presence of dispersed nanoparticles as scattering centers for phonons.

3.2.4.1. Preparation of bimodal powders and HP-FAST sintering

Composite between milled (nanophase) and submicrometric (matrix) powders were prepared according to different composition: 5, 10 a 20 wt% in nanophase. To obtain 1 g of composite powder, the suitable amount (50, 100 or 200 mg) of ball milled cobaltite was dispersed under stirring into 100 ml of acetone and sonicated for 20 minutes to disrupt the agglomerates of nanopowders leading to a uniform dark black dispersion. Then, the remaining quantity (950, 900 and 800 mg) of sub-micrometric powder was added to the dispersion following the same procedure: under stirring followed by a 20 minutes sonication. Finally, the acetone was let evaporating at room temperature overnight and the powder was dried in an oven furnace before being collected. A second stock of powder was prepared with the same procedure, but once collected, it was mixed for 24 hours to homogenize the composite powder. It should be noted that it was impossible to determine the morphology and the microstructure because the presence of the nanophase could not be detected neither with SEM investigation or with XRD techniques, as it can be seen from the diffraction patterns reported in fig. 3-52.

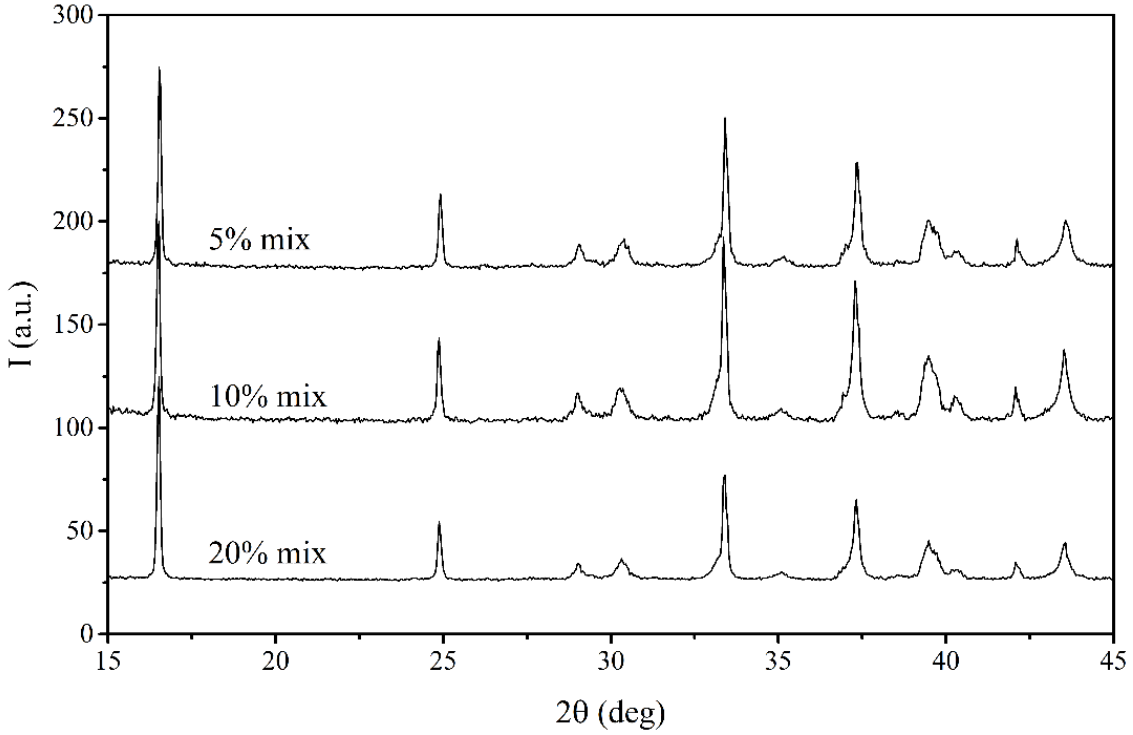

Figure 3-52 XRD patterns of CCO powders with bimodal composition. The presence of the nanometric phase cannot be observed.

Mixed and unmixed powders were sintered using the same sintering temperatures used for the densification of milled powder (723, 773 and 823 K), to investigate the possible effect of the grain size of the nanophase on the thermoelectric properties of these composite samples. The addition of the nanophase, and the stirring procedure reduced the volume of the powders, allowing us to use high uniaxial pressures, reducing the plastic deformation of the material. Sintering pressure of 500 MPa (for BM powder p_S=430 MPa) was used to ensure good level of densification. Fig. 3-53 shows the densification curves of mixed and unmixed composite powders.

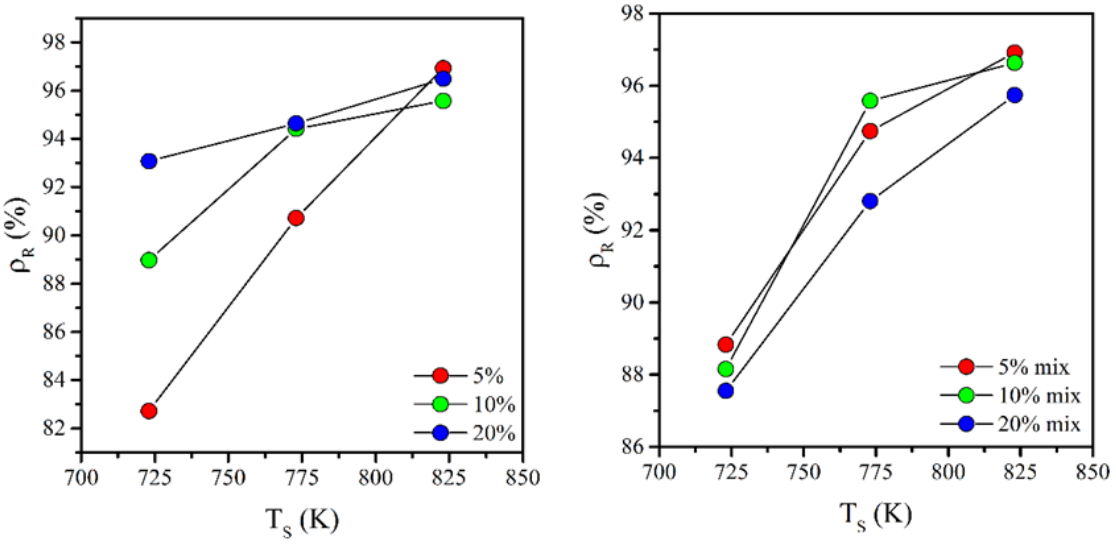

Figure 3-53 Relative density of the samples against the sintering temperature for CCO sample with different bimodal composition. On the left, samples sintered from unmixed bimodal powders. On the right, samples sintered from 24 h-mixed bimodal powder.

The relative densities (ρ_R) of all the samples obtained from mixed powders (right) increased with increasing the sintering temperature (T_S) from about 88% to about 98%. The highest densities were achieved with lower amount of nanophase while with 20% amount of nanophase the relative densities are generally lower. One explanation could be the possible hindering effects caused by the presence of nanoparticles which acted as obstacles for the densification of the larger grains of the matrix. However, this was not observed for unmixed powders (left), since their density resulted proportional to the amount of nanophase, with slightly higher values (from 93 to 95%) for the sample containing 20% wt of nanometric CCO.

3.2.4.2. Thermoelectric properties of bimodal samples

Samples from mixed and unmixed powders (tab. 3-8) were characterized by their thermoelectric properties up to the power factors using the 4P1 and S1 apparatus. No thermal conductivity measurements could be carried out.

Table 3-8 List of bimodal CCO samples for the thermoelectric characterization.

Sample	Sintering	$\rho_{R\ (\%)}$
5%	723 K / 500 MPa	83
	773 K / 500 MPa	91
	823 K / 500 MPa	97
10%	723 K / 500 MPa	89
	773 K / 500 MPa	94
	823 K / 500 MPa	96
20%	723 K / 500 MPa	93
	773 K / 500 MPa	95
	823 K / 500 MPa	96
5% mix	723 K / 500 MPa	89
	773 K / 500 MPa	95
	823 K / 500 MPa	97
10% mix	723 K / 500 MPa	88
	773 K / 500 MPa	96
	823 K / 500 MPa	97
20% mix	723 K / 500 MPa	88
	773 K / 500 MPa	93
	823 K / 500 MPa	96

Fig. 3-54 shows the Seebeck coefficient of samples sintered from mixed and unmixed powders.

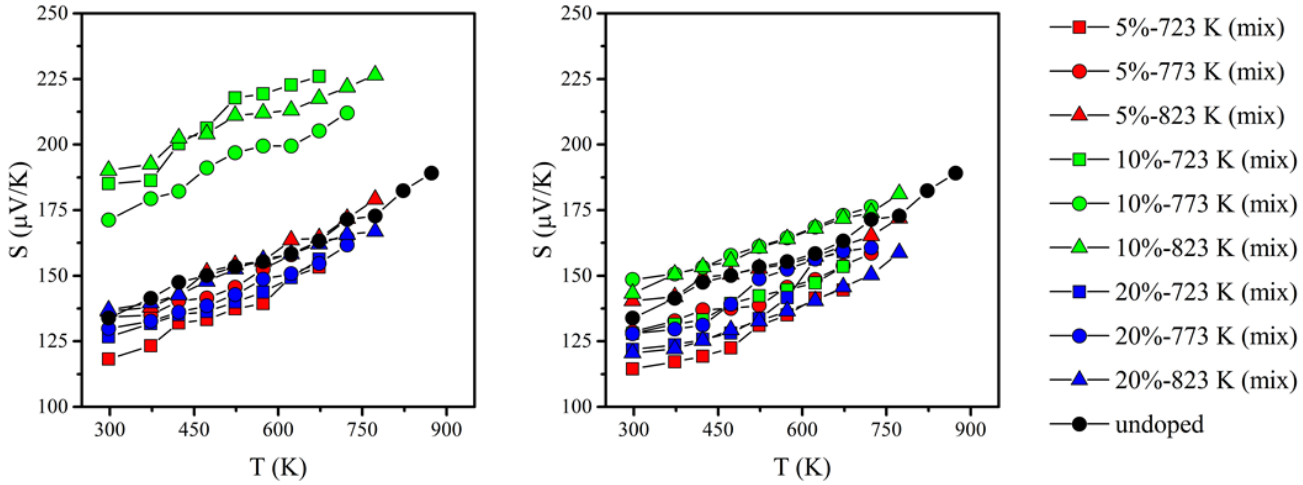

Figure 3-54 Seebeck coefficient of CCO powders with bimodal composition sintered from mixed (right) and unmixed (left) powders.

The formation of composite powders resulted in an evident increase of the Seebeck coefficients of the unmixed 10% samples (left), compared to the non-composite sample. In particular, a *S* values of 226 μV/K could be achieved for samples sintered at 823 K and 723 K, despite for the second one, this large thermopower was obtained at lower temperatures, at 673 K. It was almost 40% higher compared to the Seebeck coefficient of the non-composite sample measured at the same temperature (S=163 μV/K). At the same time, the formation of composite also led to lower Seebeck coefficients, for example in the case of the 5% sample sintered at 723 K. Its thermopower increased from 118 μV/K at RT to 153 μV/K at 673 K, while the Seebeck coefficient of the non-composite sample increased from 134 μV/K to 163 μV/K in the same temperature range. All the 20% samples exhibited mostly lower values. An overall reduction could be observed also for samples sintered from mixed powders (right).

The least efficient sample resulted the 5% mix sample sintered at 723 K, its values increased with temperature from 114 μV/K to 145 μV/K. Only two samples showed an improvement of the Seebeck coefficient, those prepared from 10%-mix powders and sintered at 823 K and 723 K; the same sintering conditions that were used to prepare the most efficient samples from unmixed powders in terms of thermopower.

We can attribute the large increase of the Seebeck coefficient to a possible occurrence of the energy-filtering effect. This effect consists in the presence within a uniform matrix (the bulk) of potential barriers (V_b) which cause the scattering (the “filtering”) of charge carriers with energy lower than V_b.

Reducing the charge carriers' concentration and their energy should lead to a significant increase in the thermopower that compensates, and even surpasses in magnitude, the reduction of the electrical conductivity from less charge carriers. However, some conditions should be theoretically followed to achieve an effective energy-filtering effect[114]:

a) There is an optimal potential barrier height to produce the energy filtering effect. Under this value, the potential barriers have no effect on the scattering of the charge carriers, while above this value, the potential barriers are too high so that the increase of the Seebeck coefficient is overcompensated by the reduction of the electrical conductivity;
b) The spacing between the potential barriers should be lower than the mean free path of the main charge carriers to prevent relaxation effects canceling out the energy filtering enhancement;
c) The nanoprecipitates should be in correspondence of the grain boundaries.

Systematic studies were not performed about this effect, so the attribution of the energy filtering as the reason behind the increase of the Seebeck coefficient should be considered only as one possible explanation.

However, another hint pointing to this effect could be observed by looking at the electrical conductivities of composite samples reported in fig. 3-55.

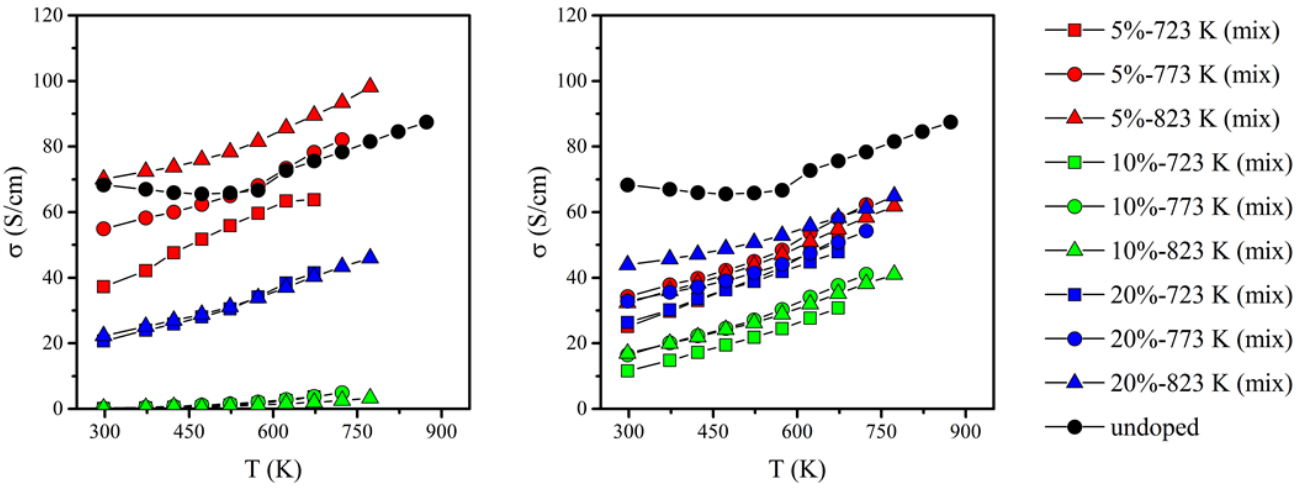

Figure 3-55 Electrical conductivity of CCO powders with bimodal composition sintered from mixed (right) and unmixed (left) powders.

By considering the samples obtained from unmixed powders (left), it can be seen that the electrical conductivities of all the 10% samples were nearly identical each other in the whole range of temperature and considerably lower compared to the non-composite one and the other composite 5% and 20% samples.

he highest σ was of 4 S/cm, more than one order of magnitude lower compared to the non-composite sample. This seemed to agree with the highest Seebeck coefficients observed in these samples (fig. 3-54, left) and it could be the result of strong scattering effect that filtered most of the charge carriers, even the more energetic, leading back to the point "a" described in the previous page. Moreover, also the electrical conductivity of all the 20%-composite samples, resulted lower compared to the non-composite sample, with no differences between each other. The electrical conductivity of the sample sintered at 773 K could not be measured. On the contrary, a high electrical conductivity was observed for the 5%-composite samples sintered at 773 K and 823 K. In fact, the largest σ of 98 S/cm was achieved at 773 K for the sample sintered at 823 K, which is about 20% larger compared to the electrical conductivity of non-composite sample at the same temperature. Considering all the samples prepared from mixed powders (right), and regardless from the sintering temperature, all the electrical conductivities resulted significantly lower compared to that of the non-composite sample. However, while the 5% and 20% samples exhibited close values of σ, the electrical conductivities of all the 10% samples were even lower, although considerably larger compared to their unmixed equivalents.

The calculated power factors are reported in fig. 3-56.

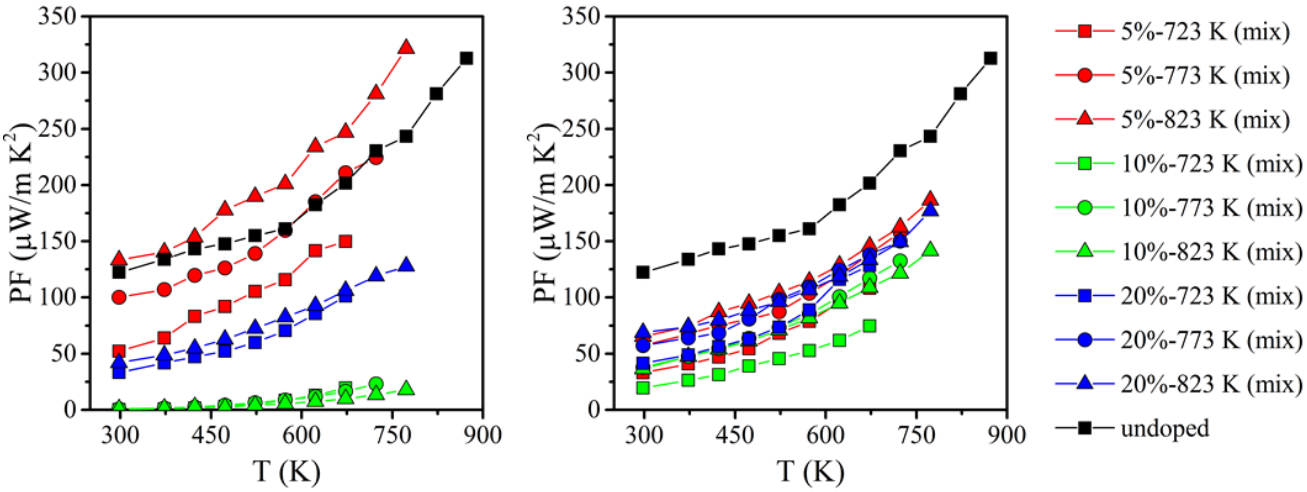

Figure 3-56 Power factor of CCO powders with bimodal composition sintered from mixed (right) and unmixed (left) powders.

Regarding the samples from unmixed powders (left), the dramatic reduction of the electrical conductivities of all the 10% samples resulted in the lowest power factors between all the samples, despite the significant increase of the Seebeck coefficient. A low *PF* of 23 $\mu W/K^2m$ was calculated at 723 K for the sample sintered at 773 K. On the contrary, a larger power factor of 321 $\mu W/K^2m$ at 773 K was achieved for the 5%-composite sample sintered at 823 K, an increase of about 30% compared to the *PF* of the non-composite sample at the same temperature (243 $\mu W/K^2m$). Instead, for composite samples prepared from mixed powders (right), all the power factors resulted lower compared to the non-composite sample as a result from the general reduction of both electrical conductivity and Seebeck coefficient.

It is evident that there are hints about the occurrence of the energy filtering effect, at least for the unmixed 10% samples, as its Seebeck coefficient resulted increase. The bimodal approach, however, resulted efficient with only one composition: the unmixed 5% composite powder. The sample sintered at 823 K, in fact, showed a large power factor mainly because of the increase of the electrical conductivity. This improvement could be related to the presence of nanograins in a suitable amount to improve the electrical contacts between the CCO particles. With other compositions, no significant improvement could be obtained. It must be said that in unmixed powders there could be inhomogeneity issues that could affect strongly the thermoelectric properties of samples sintered from the same batch of powders, but this could not be investigated since it was impossible to exactly determine the actual concentration of the nanophase.

3.3. Conclusions

Pure calcium cobaltite can be easily obtained by a modified Pechini synthesis, where only stoichiometric metal nitrates, citric acid and water are used, followed by an annealing step which leads to different grain size based on the specific method used (method A or method B in the text). Different strategies have been used to improve the thermoelectric properties of calcium cobaltite. First, the reduction of the grain size to reduce the thermal conductivity seems to be a promising strategy to achieve this goal. Particle size lower than 5 nm can be easily obtained by a mild ball milling treatment (400 rpm / 3 h) and, regardless from the formation of impurity which is mostly related to the usury of the specific jar and spheres, it leads to a reduction of the electrical conductivity of dense samples (ρ>90%) by a factor of 2 which could be largely compensated by the reduction of the thermal conductivity. The Seebeck coefficient resulted unaffected. However, the thermal conductivity of these dense samples could not be measured because of both geometrical restrictions of the Laser Flash Apparatus and the sintering temperature that is limited to 823 K to avoid unwanted grain growth, but it is expected to be low, having a large impact on the figure of merit.

The ball milling approach has been applied on silver doped powders. The addition of silver nitrates induced the formation of metallic silver together with the calcium cobaltite phase that affected strongly both positively and negatively the thermoelectric properties of CCO, improving σ and reducing S compared to the undoped oxide. However, in samples sintered from milled doped powders the Seebeck coefficient and the electrical conductivity have been increased and reduced, respectively, compared to the micrometric counterpart. Also in this case, the thermal conductivity could not be measured, but with the presence of metallic silver it is expected to be particularly high.

In any case, the ball milling treatment can be considered one useful strategy to study the thermoelectric properties of nanometric calcium cobaltite and it can be applied to both the doped and the undoped material. Surely, this approach goes to the opposite direction with respect to the common texturing strategies which aims to highlight the anisotropy of CCO, and the results shown in this thesis are not encouraging in this sense, but with further optimizations (milling speed and time, choice of dopant, sintering conditions) the ball milling treatment could lead to a strong reduction of κ without negatively affecting σ, giving a real improvement in terms of figure of merit.

Finally, an approach based on the formation of bimodal composites between milled and micrometric CCO have been investigated. The largest improvement of more than 40% of the Seebeck coefficient has been observe in unmixed 10% wt composite material together with a dramatic reduction of the electrical conductivity of about one order of magnitude, which resulted in a strong reduction of the power factor.

The only improvement of the *PF* compared to the non-composite material was observed in unmixed 5% wt samples thanks to an improvement of σ. However, these results have been achieved with unmixed powders, and so susceptible to composition inhomogeneity, considering also the difference in the thermoelectric properties observed in comparison to the mixed material, which resulted all lower with respect to the non-composite cobaltite. For these reasons, more investigations are necessary to understand the large improvement observed in *S*, since it could be an important tool to achieve an improvement of the figure of merit.

4. Zinc oxide

4.2. Introduction

Zinc oxide (ZnO) is a II-VI oxide semiconductor with a direct band gap of 3.37 eV. It is transparent to visible light and it has a high exciton binding energy of ~60 meV. Wurtzitic ZnO, the most stable and common polymorph at ambient conditions, has a non-centrosymmetric hexagonal crystal structure with lattice parameter a=3.30 Å and c=5.21 Å consisting in alternating layers of tetrahedrally coordinated O^{2-} and Zn^{2+} ions stacked along the c direction (fig. 4-1).

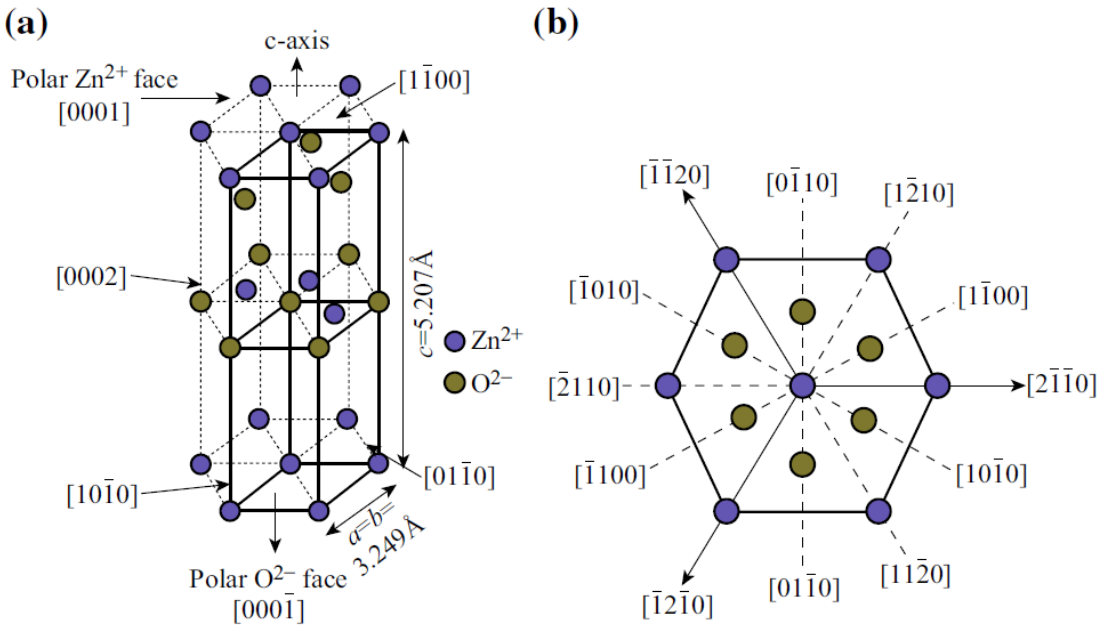

Figure 4-1 Crystal Structure of zinc oxide (a) and crystal planes of the wurtzite structure (b). Taken from ref.[115]

Because of these atomic terminations, ZnO crystals present nonpolar lateral surfaces and a polar basal plane (*0001*) which give rise to a spontaneous electric dipole, producing significant pyroelectric and piezoelectric properties. Pure ZnO is an *n*-type semiconductor because of the native presence of oxygen vacancies and zinc interstitials, even in absence of intentional doping. However, the origin of the *n*-type behavior is still debated, since oxygen vacancies have been found to be deep donors which cannot contribute to the *n*-type conduction while still compensating an eventual *p*-type doping[116]. At the same time, zinc interstitials and antisites are shallow donors but have high formation energies under *n*-type conditions, thus being unstable as isolated point defects[117]. It has been suggested that the actual reason behind the *n*-type conductivity if ZnO could imply the unintentional incorporation of some impurities during the synthesis processes[118].

Owing to the combinations of its optical and electrical properties, ZnO finds application in several technological fields such as gas sensing[119], [120], photovoltaics[121], [122] or piezoelectrics[123], [124] and it has attracted particular attention also in the field of the thermoelectricity, thanks to its high thermal stability in air (T_M =2248 K), its low cost and no toxicity. Undoped ZnO is by itself a high-resistive material, but theoretical calculations have demonstrated that a figure of merit close to the unit can be obtained if the carrier concentrations is properly optimized[125]. For twenty years now, the most employed dopant for ZnO in thermoelectrics was aluminium[126], [127], which produces an *n*-type doping and dramatically increases the electrical conductivity[128]. The solubility limit of Al^{3+} has been reported to be lower than 0.5 mol% [129], but it can be increase by co-doping with gallium[130].

ZnO presents a high thermal conductivity, a characteristic that strongly limits its practical application as a thermoelectric material. Most of the available studies in this area aim to improve its figure of merit by reducing κ_{ph}. Following this strategy, ZT of 0.65/0.60 at 1273 K was achieved using a dual doping strategy with Al and Ga[131], [132]. Jood and co-workers achieved a ZT~0.44 at 1000 K thanks to a 20-fold reduction of the thermal conductivity using a composite of Al-doped ZnO and $ZnAl_2O_4$ nanoprecipitates[133]. More recently, Wu achieved a figure of merit of ~0.54 at 1173 K using $Zn_{1-x}Ni_xO$/polyparaphenylene ($Zn_{1-x}Ni_xO$/PPP) organic-inorganic hybrid materials[134]. The *p*-type doping of ZnO received much less attention; questions have also been risen concerning the reproducibility of the results and the stability of the *p*-type conductivity. None of the few studies reported in literature involves thermoelectric applications. It has been demonstrated that shallow acceptor levels are of fundamental importance for obtaining an efficient, highly conductive *p*-type doping, but most of available acceptors resulted inappropriate. Among them, native zinc oxide defects such as zinc vacancies (V_{Zn}) have the lowest formation energy in *n*-type or oxygen rich ZnO, but they act mainly as compensation centers for the electrons rather than contribute to conductivity and tend to form clusters that may not be useful for the *p*-type doping in ZnO[135], [136]. All the potential extrinsic dopants such as group-1 elements (Li, Na and K)[137] or group 11 elements (Cu, Ag, Au) in substitution of Zn and group 15 elements (P, As, Sb) in substitution of O are all deep acceptors not producing an effective increase in the electrical conductivity. Recently, Isherwood reported that alloying with CuO could produce ZnO-based material with a low resistive *p*-type conduction mechanism[138], that is associated to the transition from the wurtzitic structure of zinc oxide to the tenorite structure of CuO, while *p*-type conduction can be observed from field effect curve in electrospun La-doped ZnO[139]. The only possible candidate is substitutional nitrogen on oxygen site (N_O).

Since nitrogen is the closest element to oxygen in terms of electronegativity and energy of the valence *2p* states, and since it's the closest to oxygen even in terms of atomic radius, it is expected it might produce a minimum strain in ZnO.

Films of ZnO nanorods (NRs) can be considered in principle as ideal planar unileg thermoelectric generators. Their geometry, in fact, strongly suggest the possibility to use them in thermoelectric devices. The extended nanostructure of NRs should in principle reduce considerably the thermal conductivity of ZnO, allowing to take advantage of its relevant Seebeck coefficient. Very few examples of ZnO nanorod-based devices can be found in the literature. Norouzi[140] reported a prototype unileg device based on vertically aligned Al-doped nanorods, where the thermoelectric effect is generated along the length of the nanorods (fig. 4-2).

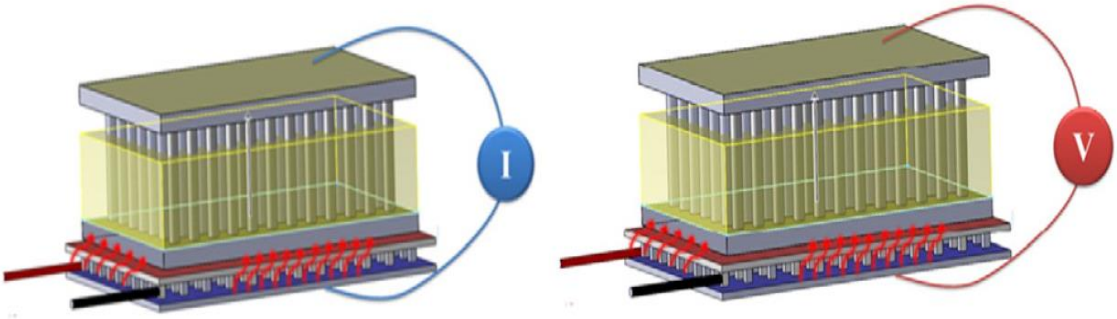

Figure 4-2 Unileg ZnO-based thermoelectric device as proposed by Norouzi[140]. The thermoelectric potential and current are measured along the length of the nanorods.

The preparation of the device, however, is quite complex. In fact, it requires the subsequent deposition of sputtered metal layers and the presence of a polymeric material to prevent possible short-circuiting between the elements of the device. Furthermore, due to the limit in the NR length, the distance between the hot and cold part of the device is limited to few microns, so only very ΔT of few K can be exploited. Finally, the highest temperature achievable on the hot side is limited by the thermal stability of the polymeric material. Another example of device that makes use of NRs films has been proposed by Dalola *et al*[141]. In this case the thermoelectric effect is produced in a direction parallel to the substrate (fig. 4-3).

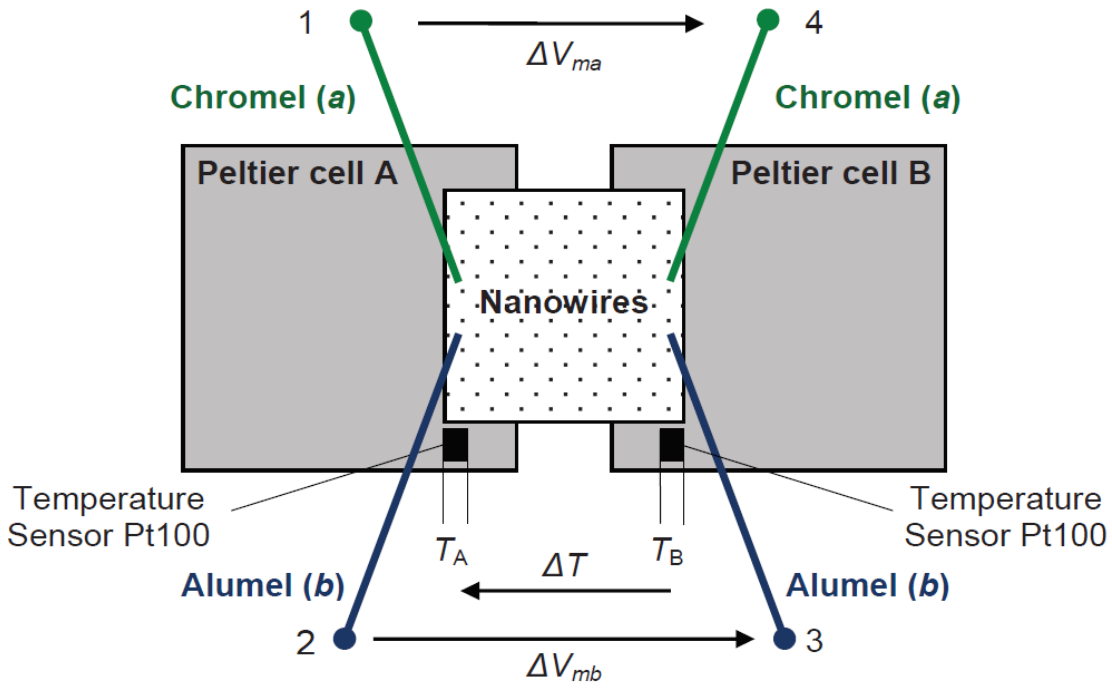

Figure 4-3 Unileg ZnO based thermoelectric device as proposed by Dalola[141]. The thermoelectric effect is produced in a direction parallel to the substrate. Large temperature gradients over wide surfaces can be exploited.

In principle, this geometry allows to take advantage of large temperature gradients over wide surfaces, as the two electrodes are place at the extremities of the substrate. However, the surface density and the overall quality of the film of nanorods used by Dalola *et al.* was quite poor and it was not optimized for the application.

Zinc oxide is also a good piezoelectric material and the possibility to exploit the thermo- and the piezoelectric properties simultaneously could represent an alternative strategy for improving the overall efficiency of a TEG device based on ZnO nanorods. Piezoelectricity is the natural ability of certain compounds to convert mechanical stress into a potential difference and *vice versa* and it is measured by the piezoelectric coefficient:

$$D = P/\sigma$$

where P is the polarization and σ is the stress applied. Piezoelectricity occurs in those materials characterized by a non-centrosymmetric crystal structures (*e.g.* wurtzite or zincblende) because in these structures a mechanical deformation induces the asymmetric displacement of the positive and negative ions with respect to each other, thus generating a potential difference in the whole crystal. Among tetrahedral oxides, zinc oxide exhibits the highest piezoelectric effect, but the harvestable piezoelectric energy can be even higher for its nanostructures because the Young's modulus of ZnO decreases with size, thus allowing to convert more mechanical energy into electric energy[142].

Moreover, zinc oxide can generate a potential within a wide range of frequency vibrations, from a few Hz to thousands of kHz, but the piezoelectric coefficient of ZnO nanostructures decreases while increasing the frequency of the vibration, while for the bulk counterpart it remains constant[143].

The improvement of the thermoelectric properties of ZnO followed a strategy that was based on four main points:

1. The increase of the NRs electrical conductivity by means of an effective *p*-type doping using nitrogen as the dopant;
2. The reduction of the thermal conductivity using NR characterized by a high aspect ratio;
3. The coupling of the thermoelectric and piezoelectricity through the develop of a unique architecture that allows to maximize both effects.

4.3. Results and discussion

Films of ZnO nanorods were prepared using both uniform and patterned geometries following a two-step procedure that has been optimized by our research group in a previous work[144]. This strategy allows to obtain a thin film of fully *c*-oriented high aspect ratio nanorods. The films are obtained deposition at first a thin layer of ZnO nanoparticles. This film acts as a seed layer for the subsequent hydrothermal growth of the ZnO NRs. The seed layer can eventually be patterned through soft lithography, allowing obtaining patterned layers of NR with excellent accuracy.

4.3.1. Synthesis of the seed layer

The first step of the synthesis consisted is the deposition onto an adequate substrate of a seed layer of zinc oxide nanoparticles which acts as a nucleation centre for the growth of the nanorods. The homogeneous nucleation of ZnO from the solution is unfavourable as it requires a considerable activation energy because the crystal-solution interfacial energy is high, while the heteronucleation (e.g., from a seed layer) is energetically more favourable, with smaller crystal-substrate interfacial energy[145]. The deposition of the seed layer is based on a synthetic approach briefly illustrated in (fig. 4-4).

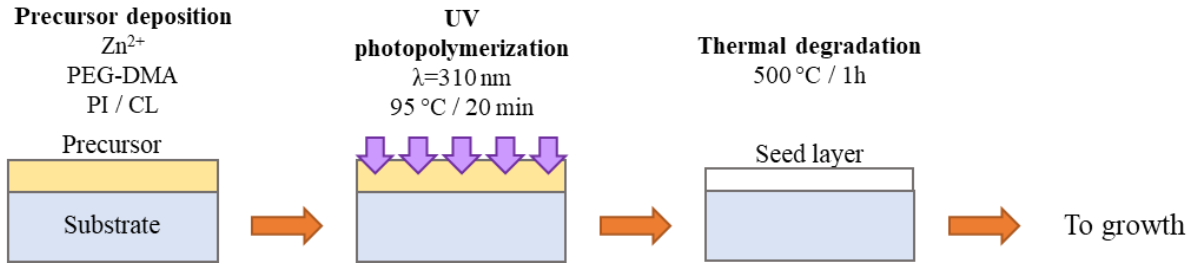

Figure 4-4 Schematic illustration of the synthesis of the seed layer. Deposition of the organic precursor, UV photopolymerization and thermal degradation of the metal loaded hydrogel.

This method is based on the use of a metal loaded hydrogel, a polymeric network that incorporates large quantities of metallic cations. The hydrogels, which can be easily deposited by spin-coating or related techniques, represent, in fact, an ideal tool for the synthesis of thin films of metal oxides. The procedure to obtain the metal loaded hydrogel is based on the photopolymerization of an organic precursor in methanol containing an oligomer (38% w/w), a photoinitiator (PI, 9% w/w), a crosslinker (CL, 7% w/w) and a metal cation source (10% w/w), according to the following procedure:

Two solutions were prepared, one named solution A containing 1 g of poly(ethylene glycol)dimethacrylate (PEG-DMA, M_n 550), 0.25 g of 2,2-Dimethoxy-2-phenylacetophenone (PI) and 0.5 g of methanol, and one named solution B containing 0.86 g of zinc nitrate hexahydrate ($Zn(NO_3)_2 \cdot 6H_2O$) and 1.5 g of methanol. Then, 1 g of solution A is mixed with 0.325 ml of solution B and 0.1 g of trimethylolpropane benzoate diacrylate (CL). One droplet (~25 μl) of the resulting solution was spin-coated onto the substrate, typically represented by glass or silicon, using a three-step speed sequence at 500 rpm-15 s / 1500 rpm-50 s / 1850-5s. Prior to use, 13x19 mm glass substrates were cut from Menzel Gläser microscope slides, washed carefully with acetone 99.9%, sonicated for 30 minutes and then heated at 573 K for at least 5 minutes in order to improve their wettability, otherwise an inhomogeneous deposition of the solution is observed. The spin-coated solution was exposed to UV radiation (λ_{max}= 310 nm) for at least 20 minutes and heated at 368 K to induce the photopolymerization of PEG-DMA and to obtain a film of metal loaded hydrogel. This film was then annealed at 723 K for 1 hour with a heating rate of 5 K/min to remove the organic matrix and form the seed layer of ZnO nanoparticles. This technique presents a low toxicity of the reagents and allows an easy fine tune of the thickness of the film and of the dimension of the metal oxide nanoparticles by changing the viscosity of the organic solution (PEG-DMA/solvent mass ratio) and of the annealing conditions. The typical morphology of the seed layer obtained from thermal decomposition of the metal loaded hydrogel at 723 K in shown in fig. 4-5[146].

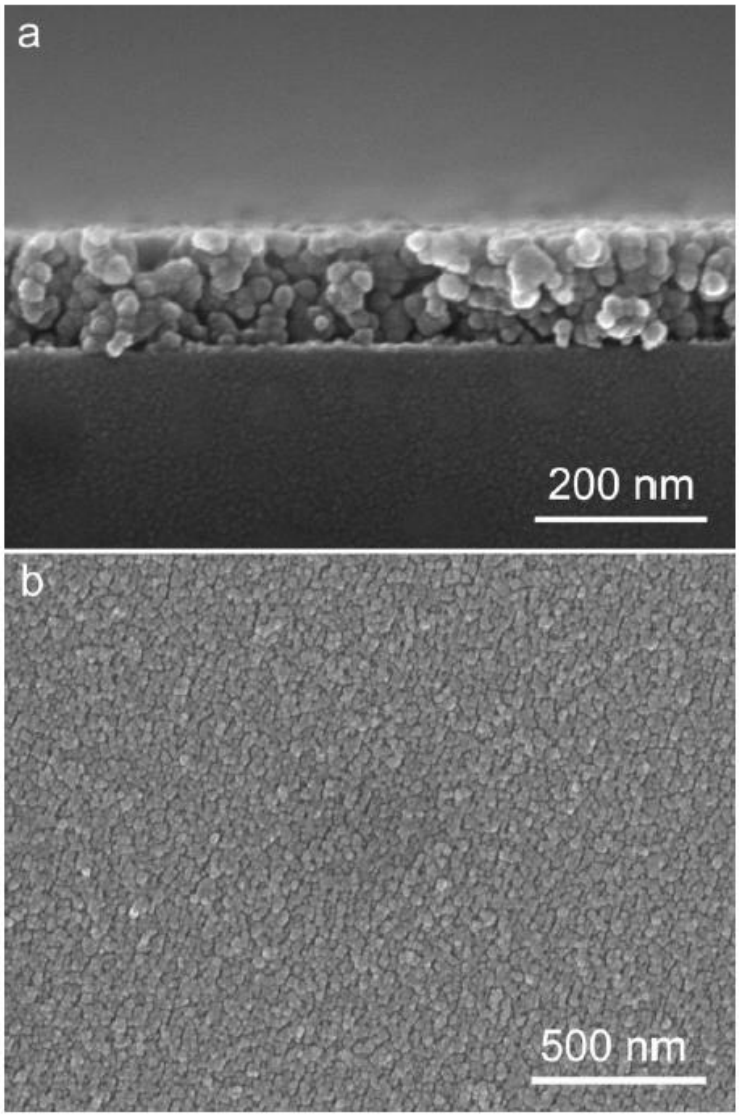

Figure 4-5 SEM micrographs of the seed layer.

The film was characterized by a thickness of about150 nm and was composed of uniform nanoparticles presenting a diameter of about 20 nm and a good level of sintering and adhesion to the substrate.

4.3.2. Patterning of the seed layer

The patterning of the seed layer was obtained by means of a soft-lithography technique. This approach makes use of elastomeric mould acting on liquid precursors uniformly deposited on the substrate. The techniques allows to print complex patterns (rows, dots, circuits)[147] and can be used according to different strategies (fig. 4-6), such as replica moulding, microcontact printing, micromoulding or transfer printing[148].

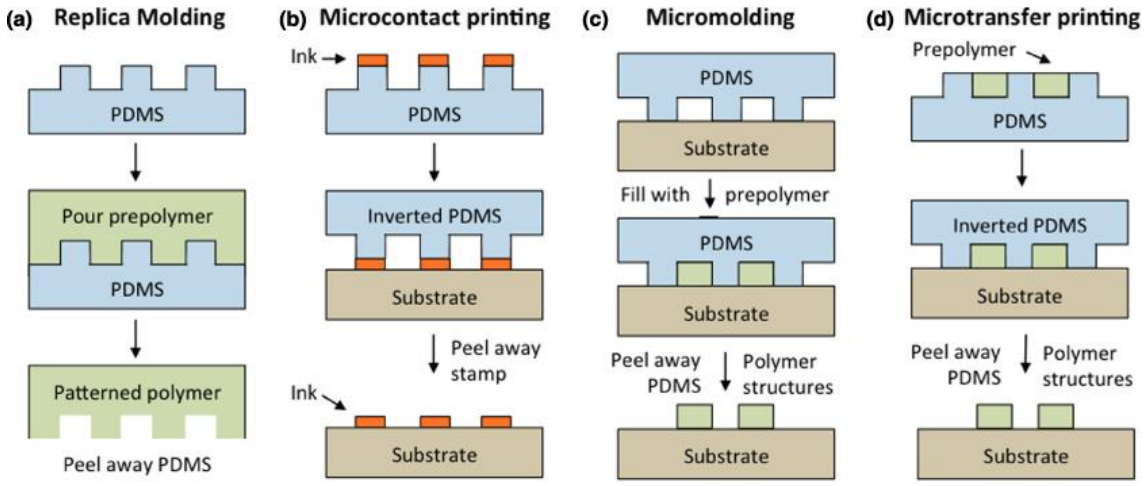

Figure 4-6 Different soft-lithography approaches. Replica molding, microcontact printing, micromolding and microtransfer printing. Taken from ref. [148].

The elastomeric mould is usually made of polydimethylsiloxane (PDMS), a flexible, transparent and highly hydrophobic polymer which is realized casting the PDMS onto a silicon master that presents the negative replica of the desired pattern. In our case the pattern was represented by parallel rows characterized by width and spacing between 1 and 80 µm wide. The siliconic precursor was obtained by mixing a base and a curing agent (SYLGARD 184 Silicone Elastomer Kit) in a 10:1 ratio by weight. The mixture was then manually stirred and the incorporate air was removed by means of a vacuum pump. Once casted onto the master, the mixture was cured at 333 K for 24 hours. In our specific case, the design of the seed layer has been obtained using a micromolding strategy briefly illustrated in fig. 4-7.

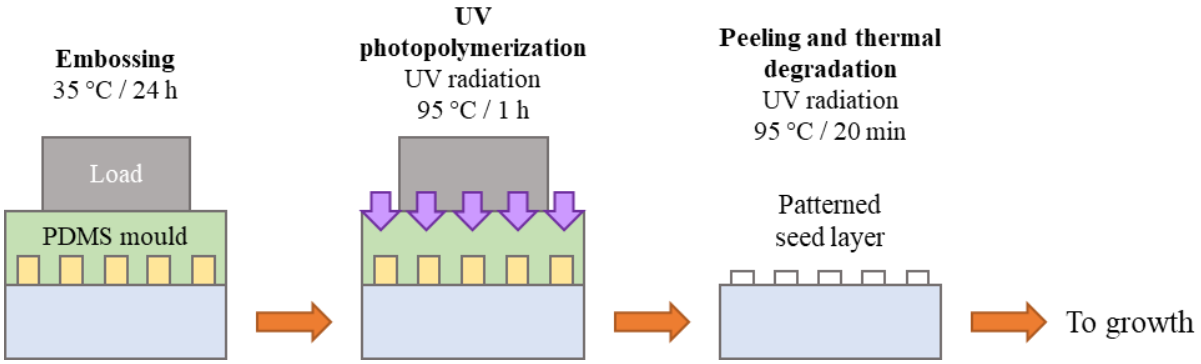

Figure 4-7 Schematic illustration of the synthesis of the patterned seed layer. Deposition and embossing of the precursor using a PDMS mold, UV photopolymerization, peeling of the mold and thermal degradation of the metal loaded hydrogel.

The PDMS mould (the negative of the pattern) was placed onto the film of the polymeric precursor, which was spin-coated onto a 26x26 mm glass substrate previously cleaned with piranha solution (3:1 mixture of sulphuric acid (H_2SO_4) and H_2O_2 30% w/w), to guarantee an optimal cleaning of the substrates. Then, a pressure of ~100 kPa was applied to ensure a good adhesion between the mould and the substrate and finally the setup was heated at 308 K overnight. The UV-photopolymerization took one hour rather than few minutes, as it was carried out in presence of the mould. In this case, in fact, the UV-irradiation should be performed by the lateral sides of the film, thus attenuating the radiation reaching the precursor. Finally, the mould was peeled off and the patterned metal loaded hydrogel was heated treated using the same conditions described in the previous section.

4.3.3. Hydrothermal growth of nanorods

The growth of high aspect ratio nanorods (sometimes referred as nanowires) has been obtained through a hydrothermal approach using the following procedure: two water solutions were prepared, the first, named solution C, containing 50 mM of zinc nitrate hexahydrate which acts as metal cation source and the second, named solution D, containing 50 mM of hexamethylenetetramine (HMT), 4.5 mM polyethylenimine (PEI) and ammonium hydroxide (NH_4OH) in nominal concentration between ~540 and ~580 mM. 40 ml of solution C was added dropwise under stirring to solution D which is placed inside a 100-ml capacity Duran® Laboratory. The substrates were immersed in this solution with the seed layer facing the wall of the bottle and treated at 363 K for 5 hours. At the end the samples were removed from the growth solution, rinsed several times with distilled water and dried in air at room temperature. In this process the ammonium hydroxide (other amino-compounds can be employed) is used to keep the pH solution at about 10.5, as the alkaline environment is a necessary condition for the growth of the nanorods[149]. The pH is controlled also by the tertiary cyclic amine hexamethylenetetramine, a weak base which gradually hydrolyses forming formaldehyde (HCHO) and ammonia (NH_3)[150]. HMT is also supposed to act as bivalent ligand towards the zinc ions[151] and to attach the nonpolar faces of the ZnO crystals, enhancing the growth along the *c* direction[152]. Ammonia keeps also the concentration of the Zn^{2+} ions at a suitable level of supersaturation, allowing the heteronucleation to take place. If the concentration of ammonia is too high, the supersaturation is reduced, hindering the heteronucleation and producing even the dissolving the seed layer. On the other hand, when the ammonia concentration is too low the concentration of Zn^{2+} ions is too high to produce the homogeneous nucleation of ZnO. The reactions that take place during the hydrothermal growth in presence of HMT are listed below:

$$HMT + 6H_2O \leftrightarrow 4NH_3 + 6HCHO$$

$$NH_3 + H_2O \leftrightarrow {NH_4}^+ + OH^-$$

$$Zn^{2+} + NH_3 \leftrightarrow [Zn(NH_3)_4]^{2+}$$

$$Zn^{2+} + 2OH^- \leftrightarrow Zn(OH)_2$$

$$Zn(OH)_2 \leftrightarrow ZnO + H_2O$$

The role of the polyethyleneimine is mainly to passivate the nonpolar lateral surfaces of ZnO crystals (fig. 4-8) reducing the growth of the nanorod along these directions thus increasing the aspect ratio.

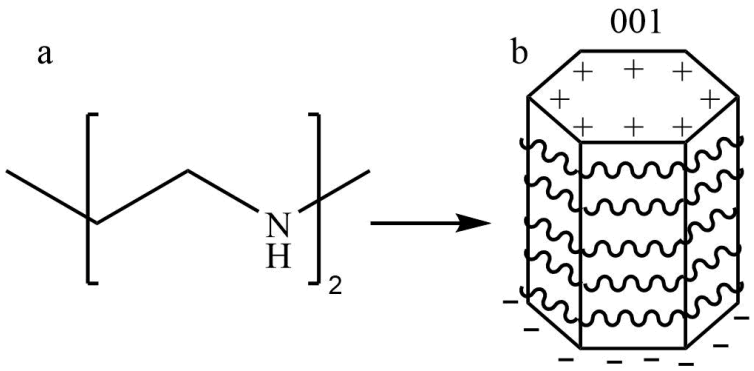

Figure 4-8 Chemical structure (a) and work principle (b) of PEI. The polyethyleneimine passivates the nonpolar lateral surfaces of ZnO crystals promoting the growth of the nanorods along the c-direction.

Moreover, in case of homogeneous nucleation PEI passivates the nuclei of ZnO once they reach a critical dimension, blocking them from further growth. However, if the concentration of polyethyleneimine is too high it attaches indiscriminately on both polar and nonpolar faces of the ZnO crystals, blocking the transfer of Zn^{2+} ions from the solution to the crystal. The morphology of the seed layer and the positioning of the substrates within the reactor affect the final appearance of the film as well. In general, the density of the NR decreases and their diameter increases as the seed layer thickness increases [153], [154]. However, if the seed layer is too thin the NR growth is not obtained, as part of the seed layer is dissolved in the early stage of the process in order to reach the correct level of supersaturation in proximity of the interface. Regarding the positioning of the substrate in the reactor, it was found that the growth of the NR is obtained only if the seed layer is placed leaning against the wall of the reactor. This can probably be explained considering that small difference of concentrations can produce convective flows that might eventually destroy the region of supersaturation at the interface between the growth solution and the surface of the ZnO seeds. Placing the substrate in proximity of the reactor wall inhibits probably this phenomenon.

The high level of alignment of the nanorods produced through this method can be deduced from the XRD diffraction pattern reported in fig. 4-9.

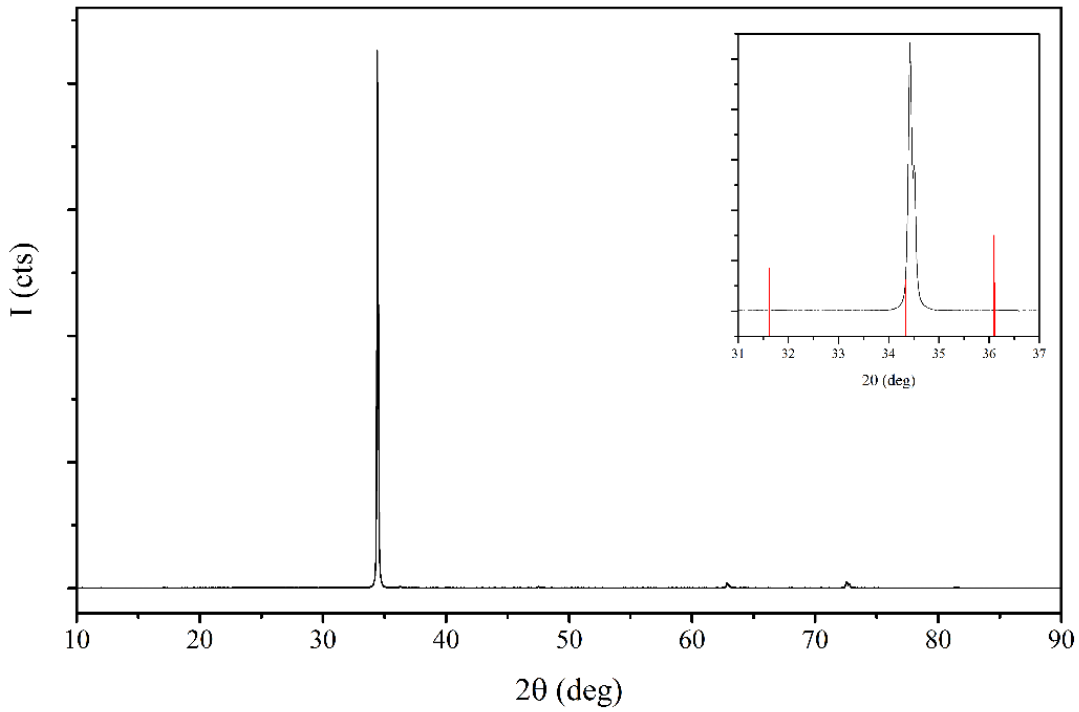

Figure 4-9 XRD pattern of the ZnO nanorods. The presence of only the 002 reflection confirms the complete alignment of the nanorods. In the inset, the 2θ interval of the most intense peaks of ZnO (In red, from left to right: 100, 002 and 101 reflections).

The pattern has been recorded using a Bruker D8 Advance diffractometer using the CuKα radiation (λ=1.54 Å) in a suitable range of 2θ (from 10° to 90°) to include all the main peaks of wurtzitic ZnO. In this interval, however, only the peak relative to the *002* reflection is observed, while the other peaks are not visible. This indicates that the NR are completely oriented along the *c*-axis. Fig. 4-10 shows two low magnification SEM micrograph of a homogeneous film from which it is possibile to observe the uniform distribution of the nanorods.

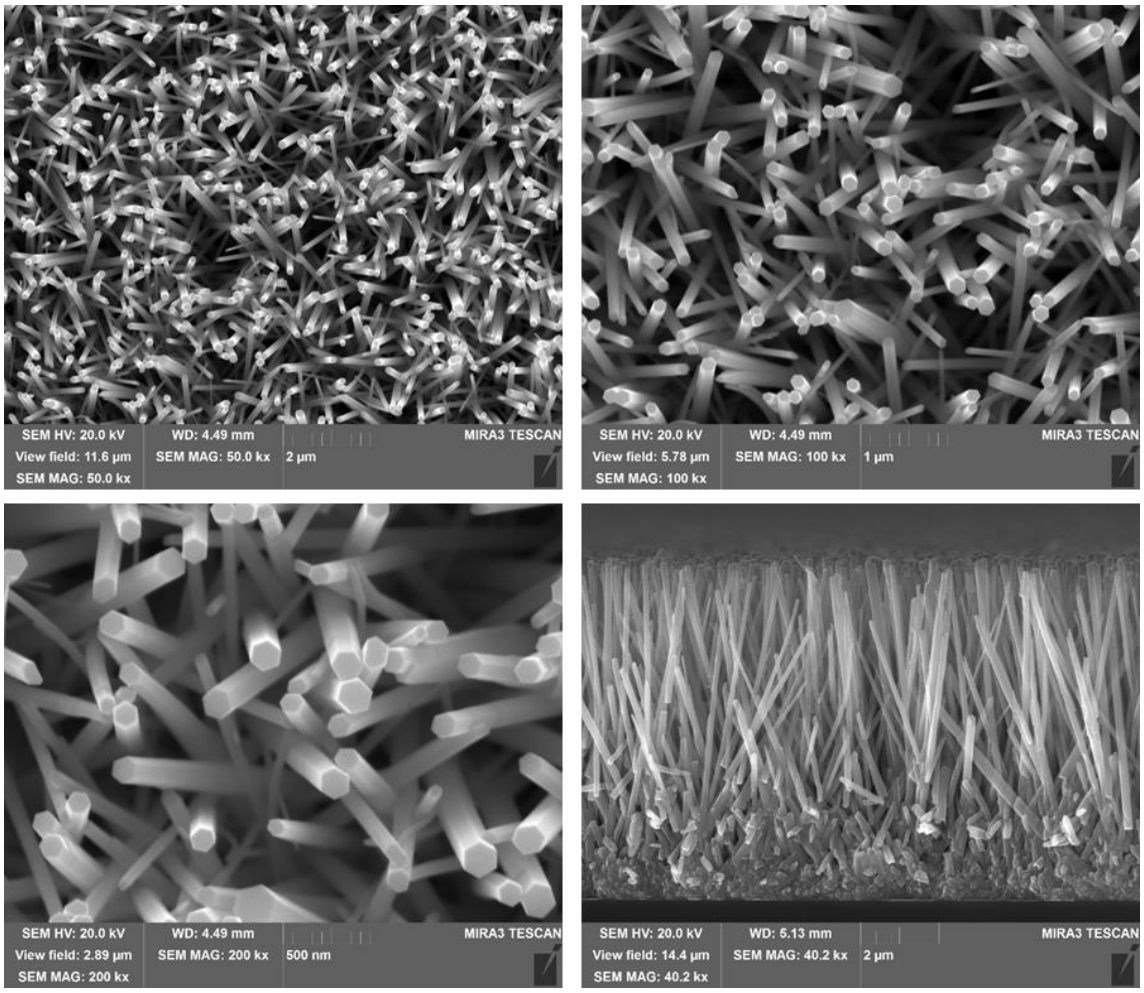

Figure 4-10 SEM micrographs of the uniform film of ZnO nanorods. A diameter of about 100 nm and a mean length beween 7 and 8 µm can be measured.

Images at higher magnifications allow to observe the hexagonal habitus of the ZnO NRs, reflecting their wurtzitic structure. Interconnections are formed between the nanorods, which are important in defining the lateral electrical conductivity of the film. The bottom right panel of fig. 4-10 shows the cross-section of a typical films of nanorods obtained using the procedure described previously. Here it is possible to appreciate the density of the nanorods and the large number of interconnections between them. The nanorods are between 7 and 8 µm long with a diameter of 106 (± 38) nm. The aspect ratio is between 66 and 75.

The nanorods grown on a patterned seed layer are shown in (fig. 4-11).

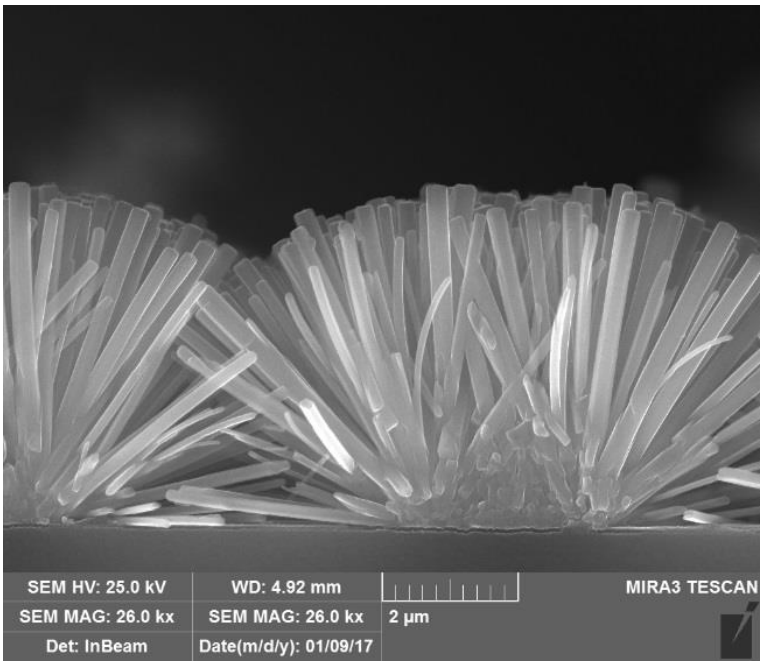

Figure 4-11 SEM micrograph representing the general aspect of a patterned film of nanorods.

It has been found that the quality of the soft-lithographic procedure depended strongly from the width of the rows in the pattern. In fact, using 20 µm-wide rows the mold cannot completely remove the precursor solution from the spaces between the rows, leaving a thin residual film onto which the nanorods can still grow, producing an imperfect pattern, as shown in fig. 4-12.

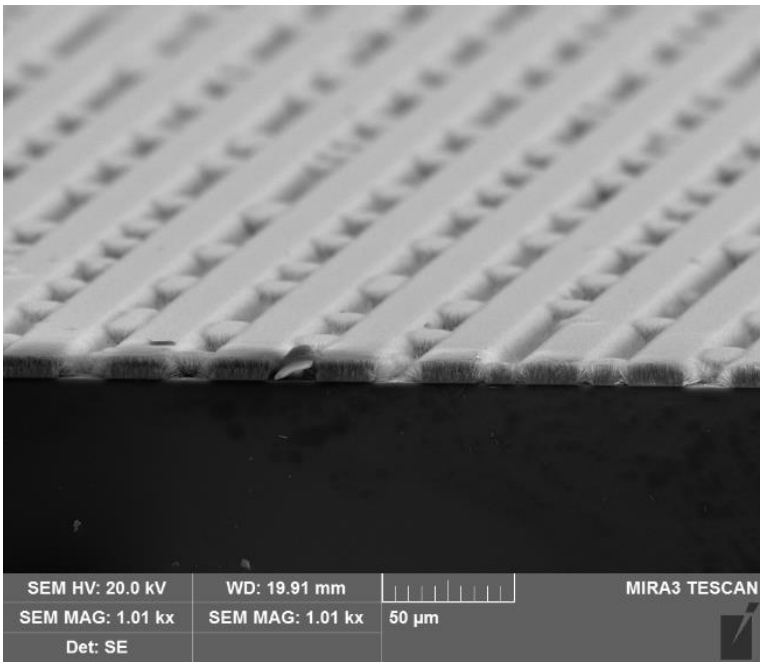

Figure 4-12. SEM micrograph of a patterned film with 20 µm-wide rows. The precursor cannot be removed completely, leaving a residual film between the rows and producing an imperfect pattern.

However, considering the length of the nanorods (6-8 μm) narrower spaces between the lines are required in order to obtain connections between the NRs grown on adjacent lines. Fig. 4-13 (a, b, c, d) shows the top and the side view at different magnifications of a typical patterned film of NRs grown using 5 μm-wide lines 5 μm apart.

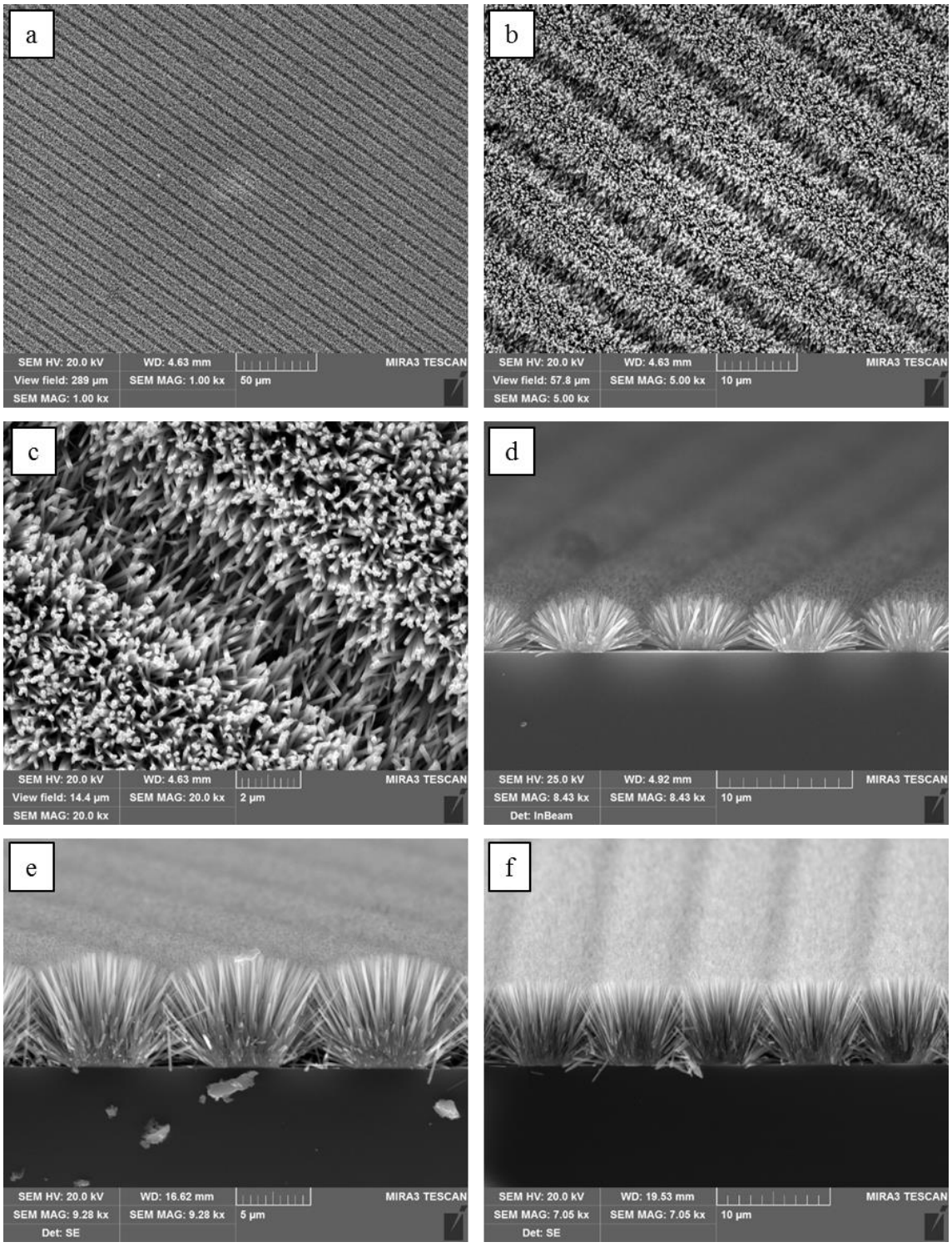

Figure 4-13 SEM micrographs of patterned seed layer with different width of the rows. In a, b, c and d, the top and the lateral view of the sample with 5 µm wide lines. In e and f, the lateral view of the sample with 4 and 3 µm wide lines, respectively.

From this image it is possible to appreciate the interconnections formed between nanorods belonging to different lines and the absence of residual film between them.

Even with 3 and 4 µm-wide lines (spaced respectively 3 and 4 µm) it is possible to obtain a well-defined pattern (fig. 4-13, e and f). However, further decrease to 2 µm results in a less precise patterning with nanorods so close to each other leading to a situation that doesn't differ too much from the uniform films (fig. 4-14).

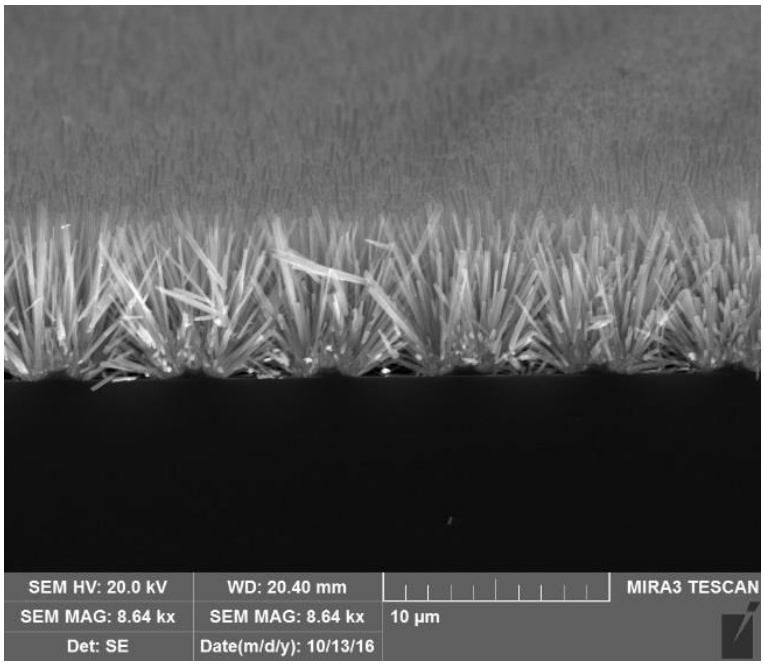

Figure 4-14 Lateral view of the sample with 2-µm wide lines. The aspect doesn't differ too much from the uniform film.

4.3.4. Nitrogen doping of ZnO nanorods

Two different approaches have been investigated in order to obtain the ZnO *p*-type doping with nitrogen. One approach was based on a hydrothermal procedure the other on a gas-solid reaction. In both cases the doping produced a change in the color of the ZnO NRs that turned from white to orange, as the doping produce a modification in the ZnO the band gap.

4.3.4.1. Hydrothermal doping

4.3.4.1.1. Doping procedure

The first method was based on approach originally proposed by Ding and co-workers[155]. It consisted in a hydrothermal treatment of ZnO NRs with hexamethylenetetramine (HMT) as doping agent. The doping procedure consisted in placing the NRs layers on the bottom of a Duran® glass bottle containing a 10 mM solution of HMT and to treat them thermally at 363 K for 24, 48 or 72 hours. Then, the samples were rinsed with distilled water and dried in oven at 333 K for 24 hours before a rapid annealing at 723 K for 5 minutes. It is supposed that the HMT could hydrolyze in solution according to the following reactions:

$$(CH_2)_6N_4 + 10H_2O \leftrightarrow 6HCHO + 4NH_3 \cdot H_2O$$

$$NH_3 + H_2O \leftrightarrow NH_4^+ + OH^-$$

$$NH_3 \rightarrow NH_2^- + H^+$$

The nitrogen doping is promoted by the high pressure generated during the hydrothermal process and by formation of ammonium compounds which act as source of N atoms, coordinating to the zinc atoms. Fig. 4-15 shows the SEM micrographs of the nanorods doped using this solution strategy. The samples treated for 24 and 48 hours (a, b, c, d) present a morphology identical to that of the undoped NRs. On the contrary, after a 72-hours (figure e,f) treatment the nanorods resulted homogeneously covered by a thin layer of a material which presumably consisted in some zinc hydroxides precipitated during the process and that reduce the electrical properties of the film.

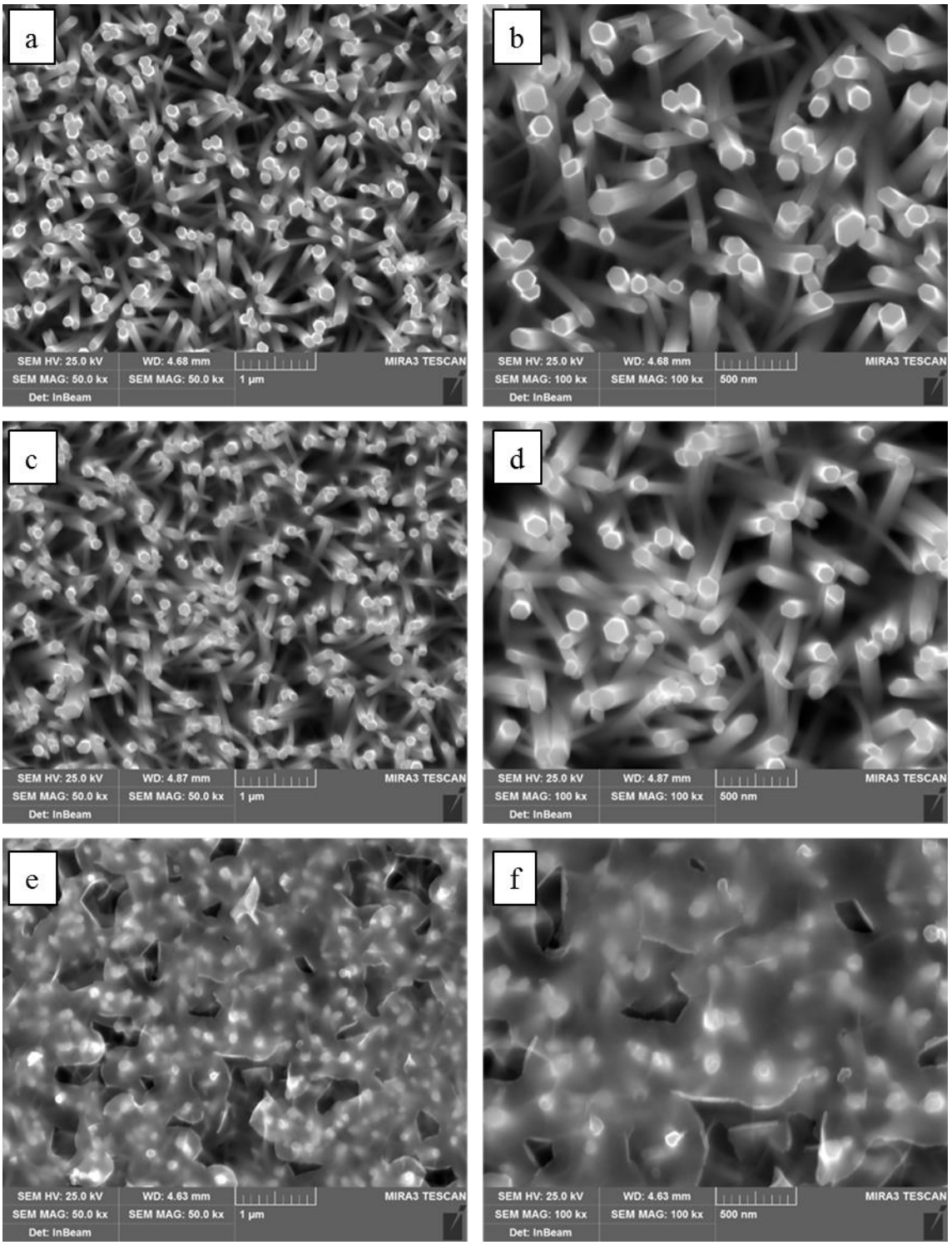

Figure 4-15 SEM micrographs of uniform film of ZnO nanorods doped according to the hydrothermal approach. After 24 and 48 hour (a, b and c, d, respectively) the morphology is identical to the undoped film. After 72 hours of treatment (e, f) the nanorods results homogeneously covered by a thin layer of some zinc hydroxides precipitated during the process.

4.3.4.1.2. Sample characterization

Fig. 4-16 shows the electrical conductivity and the thermoelectric voltage of the samples doped according to the hydrothermal strategy for different the treatment duration.

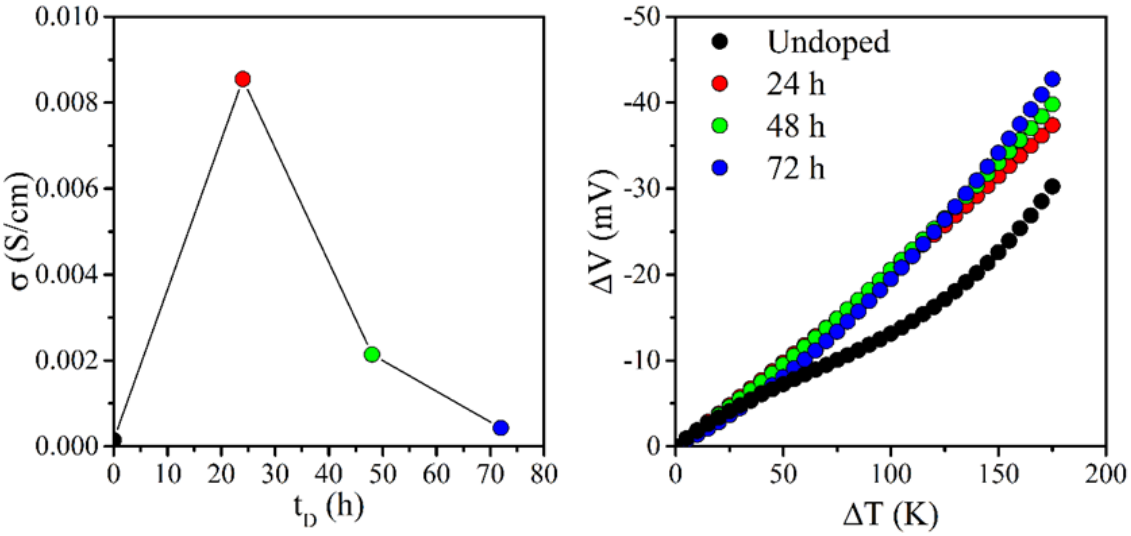

Figure 4-16 Room temperature electrical conductivity (left) and thermoelectric potential (right) of uniform films of nanorods doped according to the hydrothermal method and compared to the undoped film.

The best result (σ=9x10^{-3} S/cm) was obtained with a 24 hours treatment, which resulted in an electrical conductivity that was about two orders of magnitude higher compared to the undoped sample (σ = 1.5x10^{-4} S/cm). Increasing the duration to 48 and 72 hours the electrical conductivity was 2x10^{-3} S/cm and 4x10^{-4} S/cm, respectively. At the same time, a slight increase of the thermoelectric voltage was observed, with the highest values measured for the sample treated for 72 hours ($\Delta V_{\Delta T=175K}$=43 mV), about 50% higher compared to the undoped sample ($\Delta V_{\Delta T=175K}$=30 mV). Despite these results, the hydrothermal doping strategy has been considered unsatisfactory. Although significant, the increase in electrical conductivity was not enough to allow using the material as a thermoelectric generator. Trying to increase further the electrical conductivity, we investigated different concentration of HMT (5 and 20 mM), but that led to even lower electrical conductivities. The output voltage of this set of samples is reported in the right panel of fig 4-16. Regardless the duration of the treatment, all the samples showed a similar output voltage in the considered range of temperature, with values that slightly increased as the duration of the treatment increased. The potential difference for ΔT = 175 K was 37 mV, 40 mV and 43 mV for the samples treated for 24, 48 and 72 hours respectively, which was significantly higher compared to that of the of undoped sample.

4.3.4.2. Gas-phase doping

4.3.4.2.1. Doping procedure

The second doping strategy consisted in a high temperature treatment of ZnO NR in a flux of ammonia gas, which acts directly as a source of N atoms. This procedure was based on the work of Huang *et al* [156] which reported a synthetic method for obtaining N-doped *p*-type ZnO thin films prepared by sputtering and doped directly into the sputtering chamber by introducing high purity NH_3, Ar and O_2 gases. It is proposed that the method involves the following reactions:

$$NH_3 \rightarrow NH_2^- + H^+$$

$$Zn + NH_3 + O_2 \rightarrow Zn[O(or)NH(s)] + H_2O(v)$$

The doping is due to the formation of strongly bonded N-H groups which are incorporated into the structure of ZnO and that have the same valence of the oxygen ions. The hydrogen atom, which lies in an interstitial site because of its small size, neutralizes the free hole created by the nitrogen acceptor and lowers the N-atom energy, which in turn results in the possibility of incorporating larger concentrations of dopant. Ammonia can also substitute zinc atoms forming $(NH_3)_{Zn}$, thanks to its 7 eV lower formation energy in oxygen-rich environment compared to other acceptors[136], [157]. Moreover, the $(NH_3)_{Zn}$ interstitial could capture an hydrogen atom to form $(NH_4)_{Zn}$ which acts as a source of holes in ammonia-doped zinc oxide.

The doping procedure was performed using the apparatus described in fig. 4-17 similar to that reported by Vuong *et al* [158].

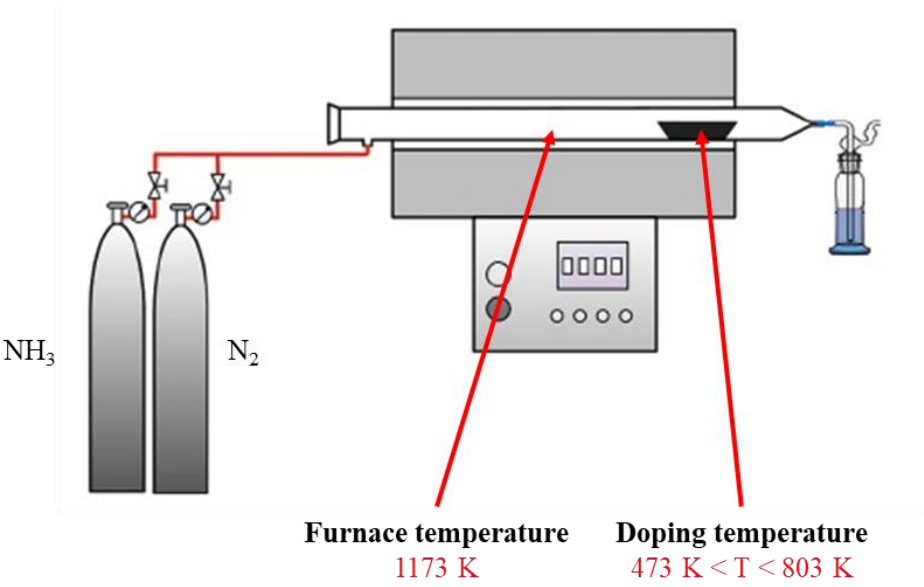

Figure 4-17 Schematic illustration of the apparatus used for the gas-phase doping of the uniform film of ZnO nanorods.

NH_3 gas was fluxed into a quartz tube inserted into a tube furnace set at 1173 K to promote the thermal decomposition of the ammonia, while the samples are positioned vertically in a colder zone between 473 and 803 K. The highest doping temperature was chosen according to the thermal stability of the substrates and to the stability of NRs in an ammonia-rich environment. Preliminary tests, in fact, evidenced as at high temperatures the glass substrates undergo some deformation, which resulted detrimental for the seed layer, while the NH_3 has shown some corrosive effect on the nanorods. The doping procedure was performed using a specifically made alumina support and lasted for 2 hours. The heating from RT to 1173 K was performed with a heating ramp of 15 K/min in flux of N_2, the gas flow was switched to the NH_3 gas once the setpoint was reached. At the end of the procedure the furnace was let to cool naturally.

4.3.4.2.2. Sample characterization

Fig. 4-18 shows the electrical conductivity at room temperature and at 473 K of uniform NRs films doped at different temperatures (the σ value at x=0 is indicates the electrical conductivity of the undoped sample).

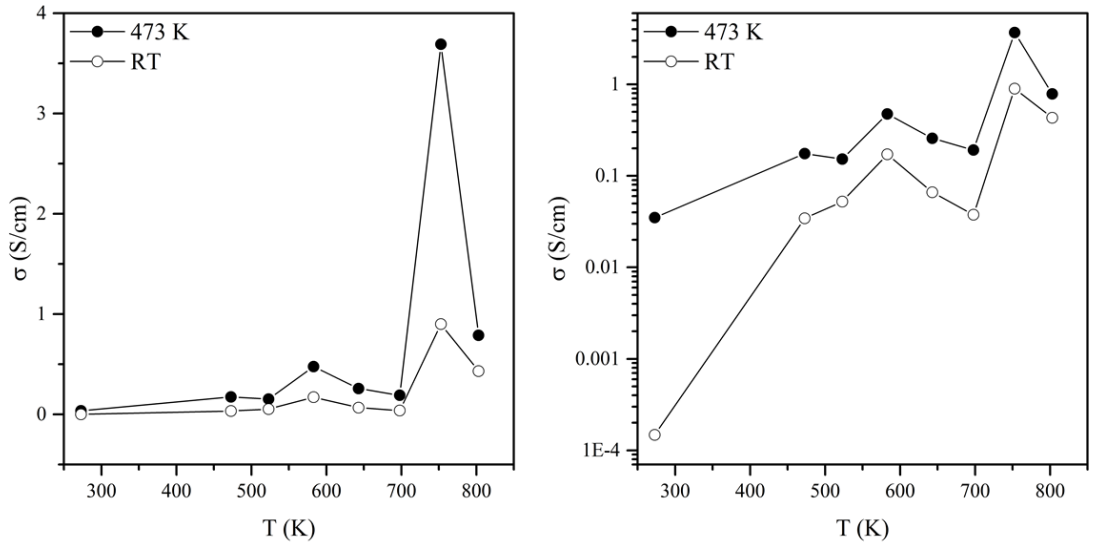

Figure 4-18 Room temperature and 473 K electrical conductivity of uniform film of nanorods doped at different temperature and compared to the undoped sample (reported as doped at 273 K).

From 473 to 698 K an increase of more than three orders of magnitude could be achieved, but the most interesting result was obtained increasing the doping temperature at 753 K. In fact, an electrical conductivity of 3.69 S/cm at 473 K was obtained. At higher doping temperatures (T_D=803 K), σ started to decrease, presumably because of a corrosive effect of ammonia, that caused a sort of chemical etching compromising the electrical contact between the nanorods.

This is confirmed by the SEM micrographs in fig. 4-19, showing as the ends of the nanorods began to lose their hexagonal *habitus* while the lateral surface resulted eroded.

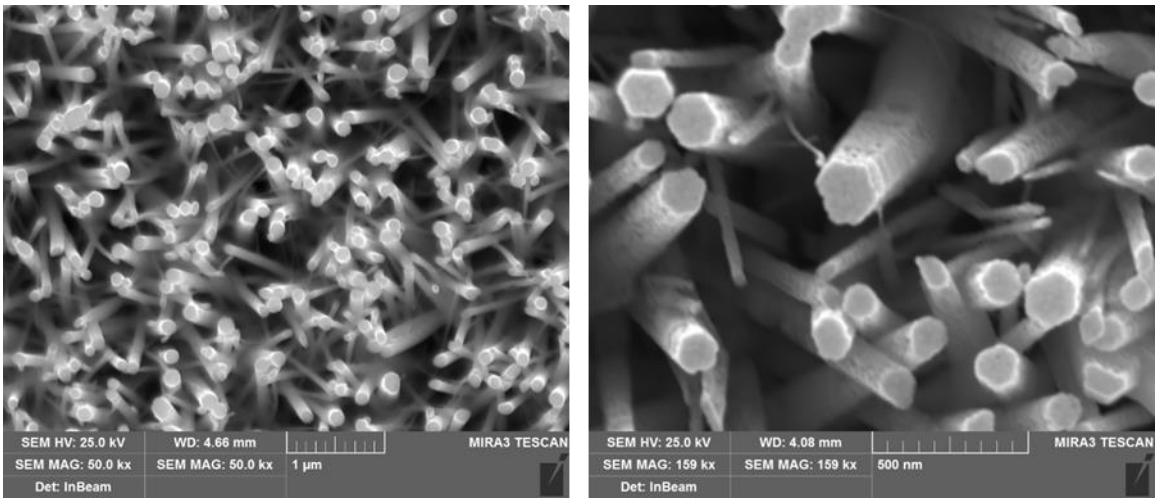

Figure 4-19 SEM micrographs of ZnO nanorods gas-doped at 803 K. The corrosive effect of ammonia is clearly visible from the eroded lateral surfaces of the nanorods.

On the opposite, all the samples doped at lower temperatures appeared completely identical to the undoped sample. The patterned samples, characterized by 3, 4 or 5 μm-wide lines, were all treated in NH_3 at the 753 K. The results are reported in tab. 4-1.

Table 4-1 Room temperature and 473 K electrical conductivity of patterned films of nanorods doped using ammonia at 753 K against the width of the rows. An overall improvement is observed for all the patterned samples with respect to the uniform sample doped at the same temperature.

Width (μm)	σ_{RT} (S/cm)	σ_{473K} (S/cm)
Homogeneous	0.90	3.69
3	5.48	8.50
4	12.29	17.41
5	5.06	7.82

In all cases, the electrical conductivities of the patterned samples along a direction perpendicular to the lines resulted higher compared to the homogeneous counterpart, with σ-values almost increased by a factor of 6 in the case of the 4 μm-wide sample at 473 K. T

his result is particularly interesting and apparently counterintuitive, since the conductivity is measured along a direction where the seed layer is not continuous. It must be attributed to the presence of more extensive interconnections between the NRs growing on the edges of the lines, despite a significant reduction in the overall amount of ZnO NRs present in these samples. The differences in conductivity observed between samples characterized by lines of different width can probably be interpreted also on the basis of geometrical interaction between the NRs growing on the edge of neighbor lines. More details regarding the thermoelectric characterization of homogeneous and patterned samples are reported in the following. The thermal stability of the ZnO NRs has been investigated for temperatures up to 1273 K. For this characterization the glass substrate could not be used and uniform film of nanorods were grown onto silicon substrates with dimension of ~25x25 mm using the same procedure described in the previous sections. Once obtained, the NRs were heated in a tube furnace at 973, 1123 and 1273 K for two hours. The SEM micrographs reported in fig. 4-20 shows the morphology of the samples after the heating treatment.

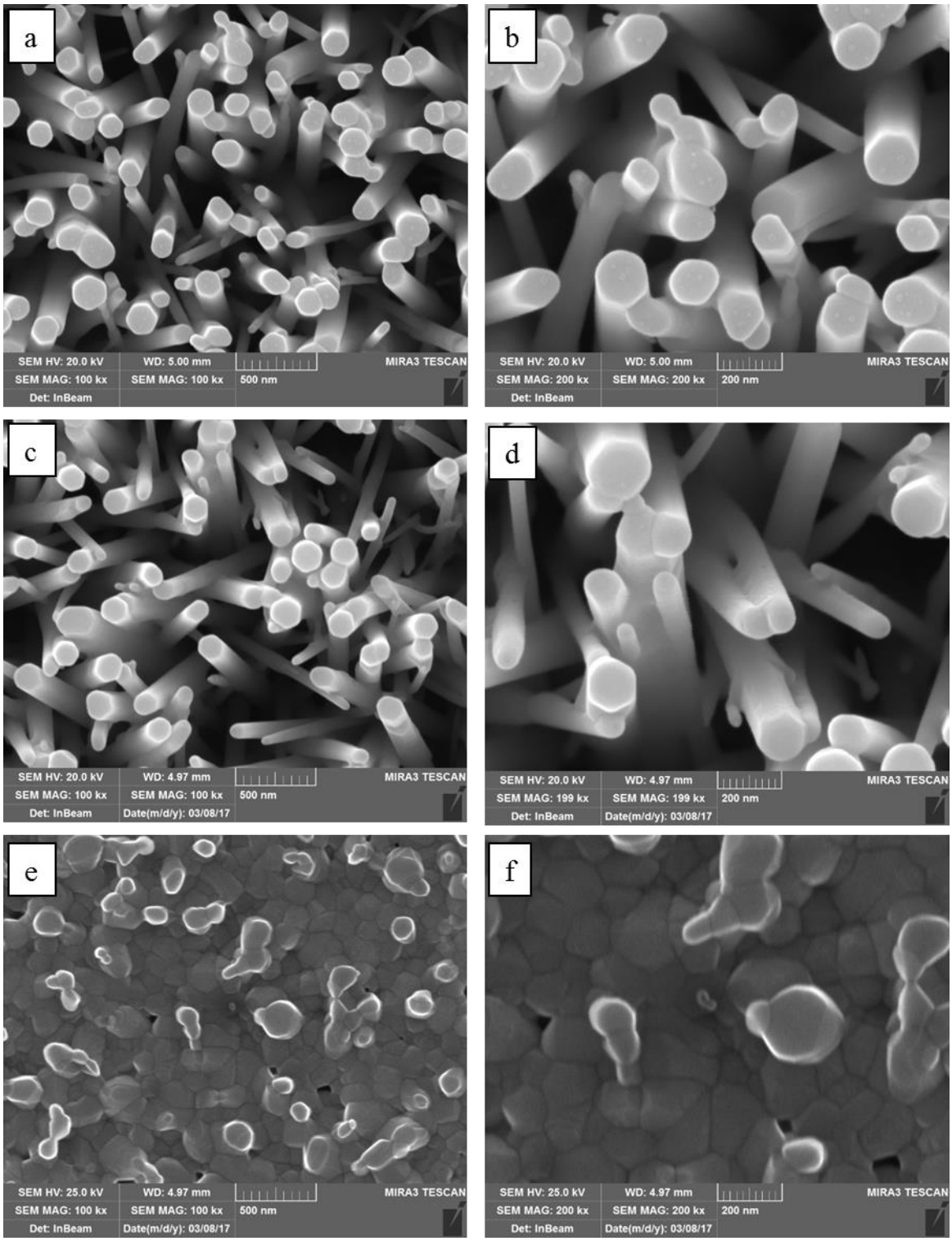

Figure 4-20 SEM micrographs of uniform film of ZnO nanorods grown on silicon substrate and treated at 973 (a, b), 1123 (c, d) and 1273 K (e, f) for two hours. Evidences of sintering effect can be observed starting from 1123 K while the at 1273 K the nanostructure is completely lost.

At 973 K, the morphology of the film is maintained quite intact though there are evidences of initial sintering effects between the single nanorods which also start losing their hexagonal structure.

Increasing the temperature to 1123 K led to a significant level of sintering, which is clearly evidenced in high magnification images that show the formation of the typical “neck” between the NRs. At 1273 K, the nanostructure is completely lost and the morphology is similar to that of a uniform porous film of nanoparticles. For these reasons, it is suggested that 973 K can be considered a limit operating temperature for the film of ZnO nanorods, though further investigation on longer annealings are necessary to better understand the long-term stability of thermoelectric devices based on ZnO nanostructures.

Substrates can strongly influence the thermoelectric properties of a thin film [159]. So, in order to take full advantage of the nanostructure of the ZnO NRs the removal of the substrates has been investigated. Several approaches have been attempted, but with limited success. NRs have been grown onto polyethylene substrates with a thickness of 250 μm. The removal of the substrate has been performed by a simple thermal process. Since the polymeric substrate cannot sustain the annealing to 773 K required for the realization of the seed layer using the metal loaded hydrogel approach, the seed layer was deposited using the RF sputtering technique. The polyethylene was cut into 10x10 mm squares, a dimension that was determined by the size of the mask used to lock the substrates in the apparatus. To test the quality of the sputtering process, the seed layer was first deposited onto a 10x10 mm quartz substrate, and the nanorods were grown using the same procedure described in the previous paragraphs. Zinc oxide powder (Sigma-Aldrich) was used as the target material and it was sputtered for 30 minutes with a power input of 140 W and under a flux of Argon of 20 sccm, while the pressure of the chamber was kept at 0.018 mbar. From the XRD diffraction pattern (fig. 4-21) of the seed layer it is possible to observe the presence of only the *002* reflection which indicates that the resulting film is almost fully oriented along the *c* direction and from the FWHM of the peak a grain size of 70 nm was calculated using the Scherrer equation.

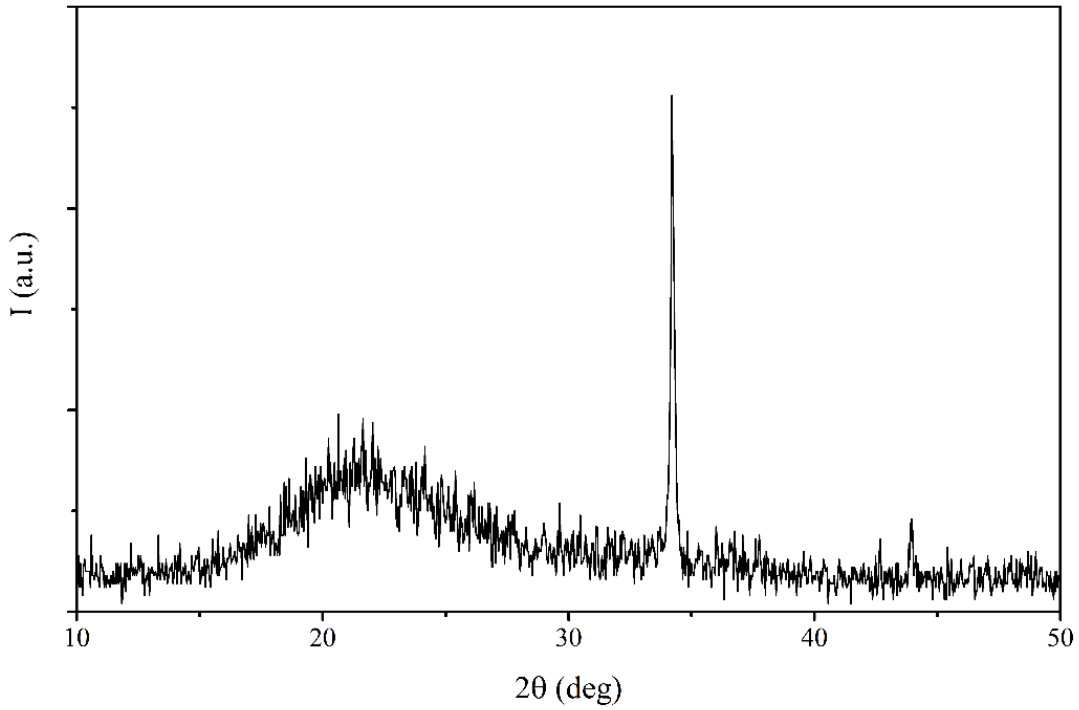

Figure 4-21 XRD pattern of the sputtered seed layer. The film is completely oriented along the c-direction as it can be observed from the presence of only the 002 diffraction peak.

The thickness of the seed layer was measured using the KLA-Tencor P-6 Surface Profiler. This apparatus consists in a stylus probe which applies a specific force on the surface of a sample and that is physically moved along a portion of the sample area. As it scans the surface, the probe monitors the feedback force applied by the sample pushing up against the stylus allowing for the surface height to be measured and reconstructed. Fig. 4-22 shows the profilometry scan of the seed layer of ZnO which resulted thick ~270 nm.

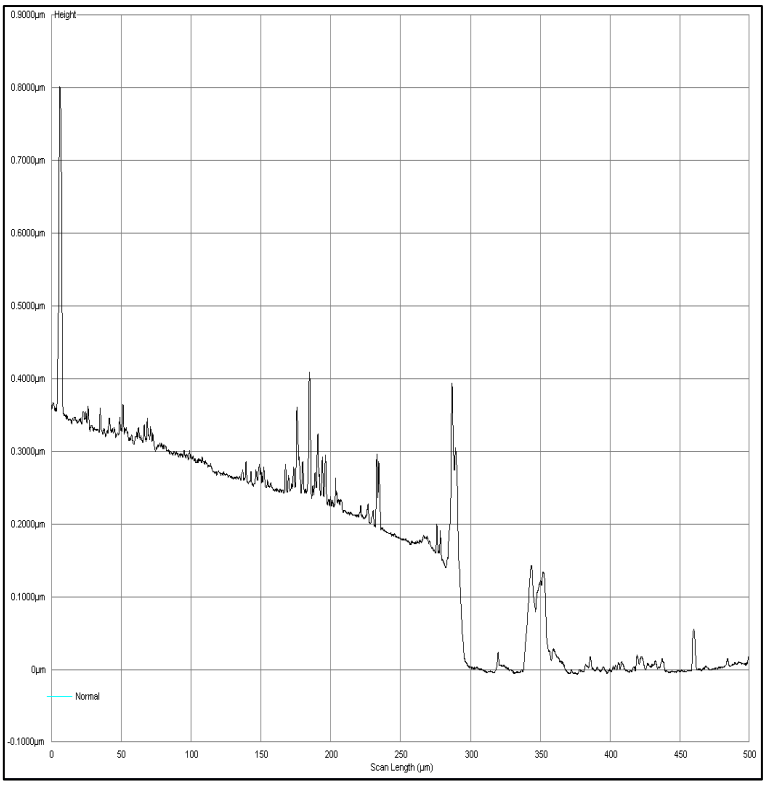

Figure 4-22. Profilometry scan of the sputtered seed layer.

The measure was performed in a range of 500 µm, with the abscissa indicating the width of the interval, using a force applied by the stylus probe of 2 mg. The region between 300 and 500 µm is relative to the quartz substrate and it was the reference point of the substrate as the thickness of the seed layer is calculated by difference between the substrate and the film. The quartz in that portion was kept safe from the sputtering deposition by covering one edge with an adhesive tape. The average of the signals around 450 µm was used as the "zero" while the two peaks around 350 µm are presumably extraneous residual left by the handling of the substrate. The rest of the signal is relative to the seed layer, the peak near 300 µm is the film which was lifted by the tape using for covering the quartz, the series of peaks from 150 to 250 µm can be ascribed to the intrinsic roughness of the sputtering technique and the peak near 0 µm is relative to other residuals. It must be said that the signal of the sample has an increasing trend which goes from the end of the quartz region down to the origin of the *x* axis, this trend can be explained by the fact that the mask attenuates the sputtering on the edges of the substrate. This is visually evidenced also by the iridescent colour of the borders of the quartz indicating a thinner film.

The SEM micrographs of the nanorods grown onto a sputtered quartz seed layer show that the morphology of the crystals is quite inhomogeneous in terms of width, length and orientation (fig. 4-23).

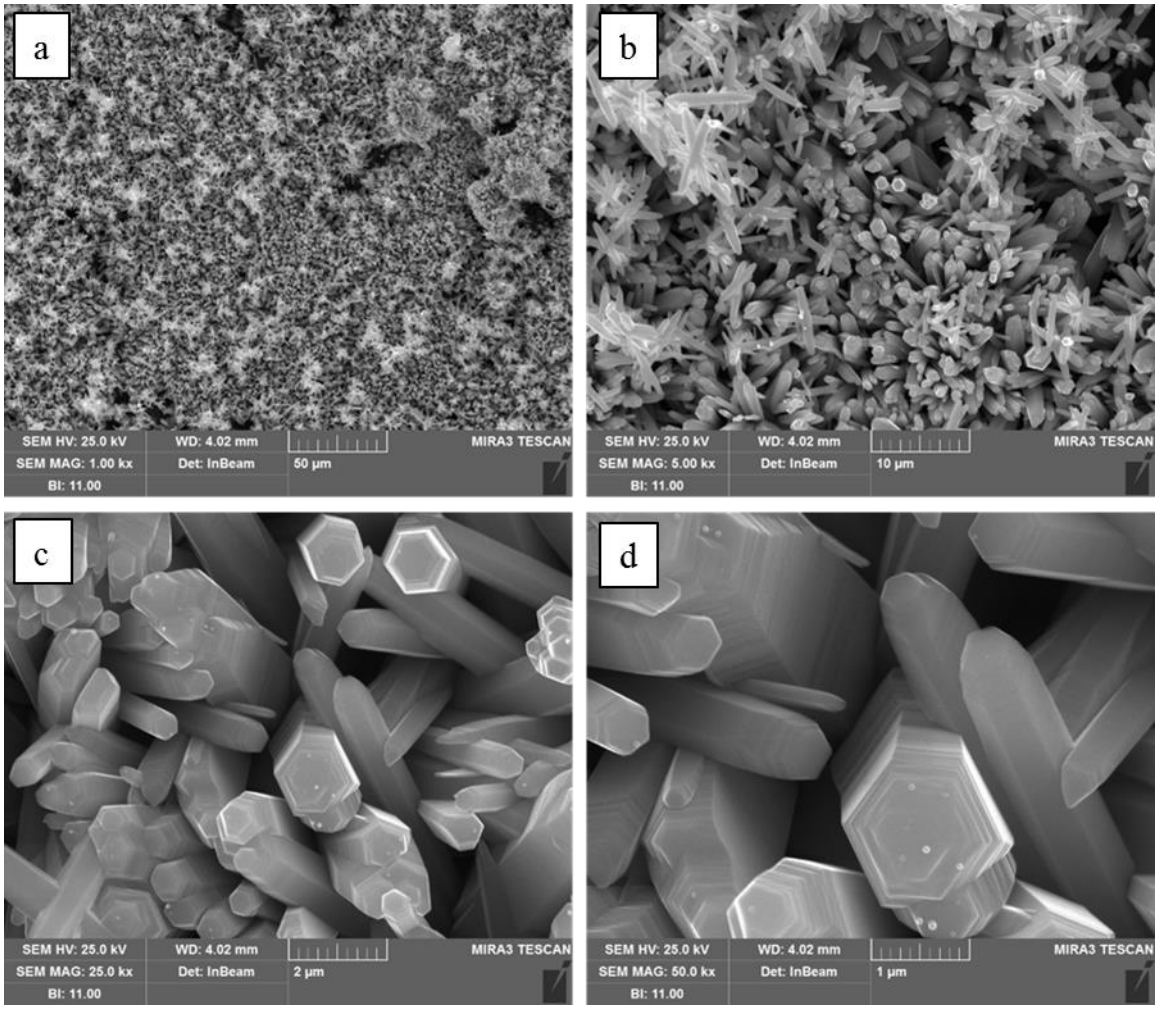

Figure 4-23 SEM micrographs of ZnO nanorods grown onto a sputtered seed-layer on a quartz substrate. Nanorods are not aligned and can be larger than 1 µm leading to a low aspect ratio.

In fact, diameters of hundreds of nm can be observed as well as nanorods larger than 1 µm. Moreover, nanorods resulted not perfectly aligned and characterized by a smaller aspect ratio. This unwanted morphology could be directly related to the morphology of the sputtered seed layer, which is characterized by larger ZnO particles.

Despite the undesired morphology of the nanorods, an attempt to remove the polyethylene substrate was made. The samples were inserted into a tube furnace and then heated at 773 K for 1 hour with a heating ramp of 1 K/min but at the end of the treatment the film resulted completely disaggregated. One possible explanation of this result could be that the organic substrate was too thick and underwent strong mechanical deformation during the thermal decomposition

Another strategy that was investigated to remove the substrate consisted in its selective dissolution by chemical etching. Silicon was used as substrate and a 20%wt solution of KOH in distilled water was used as the etching media [160]. Fig. 4-24 schematically shows the system used to perform the removal of the substrate.

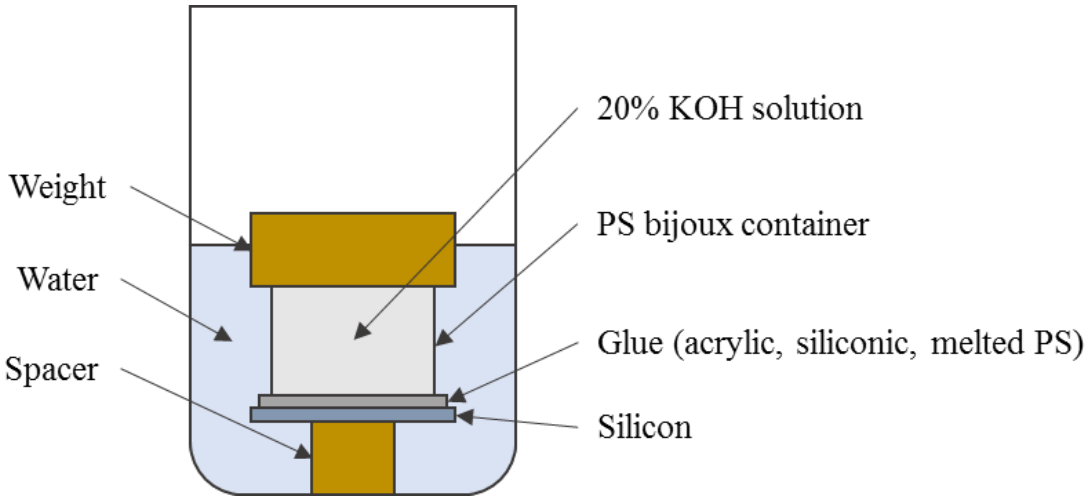

Figure 4-24 Schematic illustration of the setup used for the selective dissolution of the silicon substrate. A KOH solution is poured into container of polystyrene sealed by means of a glue and kept in contact with the substrate, and a weight is used to avoid the leakage of the solution. The setup is then heated at 353 K through different approaches.

The unpolished side of a piece of silicon wafer was scratched with an abrasive paper to remove the eventual silicon oxide layer and to create a rough surface to facilitate the etching. To create the container for the KOH solution, the top of a polystyrene container was cut and then fixed on the rough surface of the silicon using three different strategies: an acrylic glue, a silicon rubber compound and the same polystyrene melted. The setup was inserted into a beaker and kept lifted from the bottom to avoid the direct contact of the silicon with the glass and KOH solution was poured into the space defined by the container. Finally, the container was capped under a minimum load to avoid leakage, and two heating procedure were used:

I. The setup was surrounded by distilled water and then heated at 353 K overnight
II. The setup was heated at 353 K overnight using an oven furnace

Unfortunately, in the first case we observed the degradation of both the acrylic glue and the silicon rubber and the leakage of the KOH solution which resulted ineffective and induced the partial corrosion of all the silicon substrate, even of the polished face which would result in the impossibility to obtain the deposition of the seed layer. On the other hand, the top of the container came unglued from the silicon surface as soon as it was cooled to room temperature before being used. In the second case, the sealant used to isolate the container was only the silicon rubber.

Here, the KOH solution evaporated before dissolving the silicon. For these reasons, the removal of the substrate by corrosive attack was considered an inefficient way to obtain a bare film of nanorods.

Since zinc oxide was characterized also for its piezoelectric properties, the nanorods must be grown onto thinner substrates allowing a good mechanical deformation. For this purpose, the synthesis of the NRs was performed also onto 24x24 mm cover glass slides. As these substrates are fragile and subjected to thermal stress, it is necessary to pay particular attention during the annealing step as it can induce the cracking of the glasses, hence the substrates must be arranged onto a flat surface which act as mechanical support. This is also the reason because the piezoelectric properties were measured only for the undoped ZnO nanorods. In fact, during the doping procedure with ammonia gas the substrates must be maintained in a vertical position which doesn’t ensure enough mechanical support.

4.3.5. Thermoelectric and piezoelectric properties

4.3.5.1. Uniform films of N-doped ZnO nanorods

Since the samples are not composed by a compact material, but by an aggregate of NRs, the electrical conductivity is always underestimated, as the actual cell constant (l/A_S) is always lower compared to a dense homogeneous film. However, as this error is similar for all the samples, it is still possible to compare different samples.

The temperature dependence of the electrical conductivity (σ) for samples composed by uniform films of NRs doped at different temperatures (T_D, doping temperature) is reported in fig 4-25.

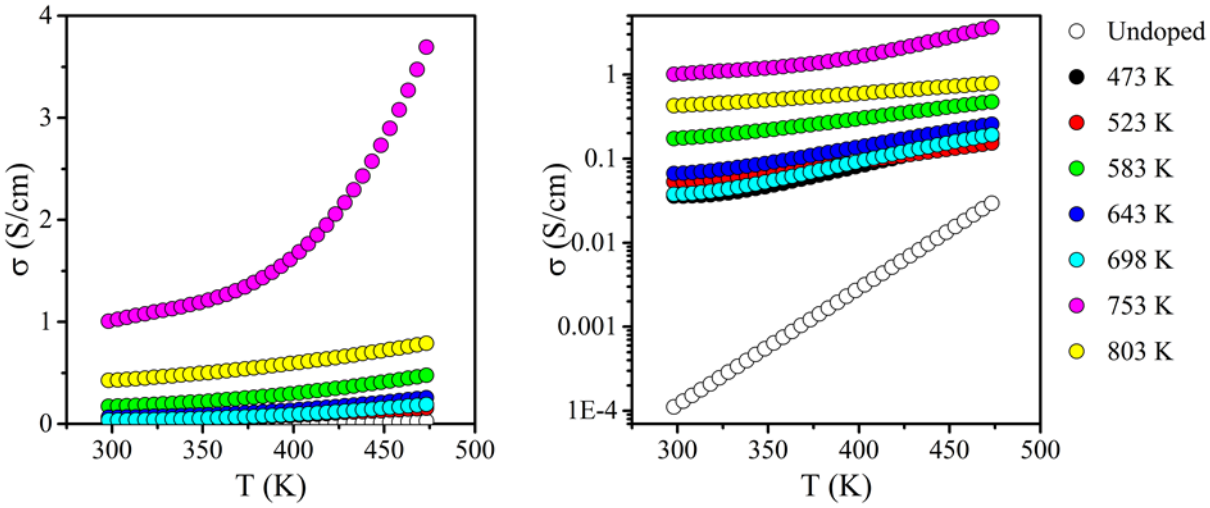

Figure 4-25 Electrical conductivity against the temperature of uniform films of ZnO nanorods doped through the gas-phase approach.

All the samples exhibited a semiconductor behavior. As already mentioned in section previous sections, the highest electrical conductivity (3.69 S/cm at 473 K) was obtained with the sample doped at 753 K. The electrical conductivities of the samples doped between 469 K and 698 K resulted generally similar to each other, with higher values obtained with the sample doped at 583 K. Despite the corrosive effect of ammonia, the electrical conductivity of sample doped at 803 K ranged from 0.43 S/cm at RT to 0.75 S/cm at 473 K, almost one order of magnitude lower. Reference values for the electrical resistivity of *p*-type ZnO can be found in the work by Kim on thin films of phosphorus-doped ZnO which reported electrical condictivity values ranging between 1.7 S/cm and 0.2 S/cm [161]. Regarding the nitrogen doping, Huang[156] reported an increase of the electrical conductivity of ZnO films of four orders of magnitude (up to ~1 S/cm), while Reynolds reported a RT conductivity of 0.2 S/cm for films of ZnO annealed in a nitrogen-rich environment[162].

Bian reported values relative to *p*-type N-doped ZnO films prepared by spray pyrolysis. A resistivity of $1.7x10^{-2}$ and $3.02x10^{-2}$ S/cm were reported, corresponding to an electrical conductivity of 58.8 and 33.1 S/cm in presence and in absence of In as co-dopant, respectively. However, it must be reminded that all these reported conductivities were relative to compact films, which theoretically present better connections between grains and almost full density. In our case the conductivity was calculated considering the nanorods as a compact film, although their density is actually quite low. Literature evidences of *p*-type doping of homogeneous films of ZnO nanorods prepared *via* a hydrothermal method can be found in the work by Thangavel[163] reporting electrical resistivity values at room temperature of 4.48 S/cm and 3.92 S/cm for 3% K and 3% Ag doped samples, respectively, corresponding to an electrical conductivity of 0.22 S/cm and 0.25 S/cm and comparable to the sample doped at 583 K.

To evaluate the stability of the doping, samples doped at 753 K were heat treated at 573, 673 and 773 K for 1, 2, 5 and 10 hours. Fig. 4-26 shows the ratio R/R_0 between the resistance before (R_0) and after (R) the thermal treatment against the duration of the treatment.

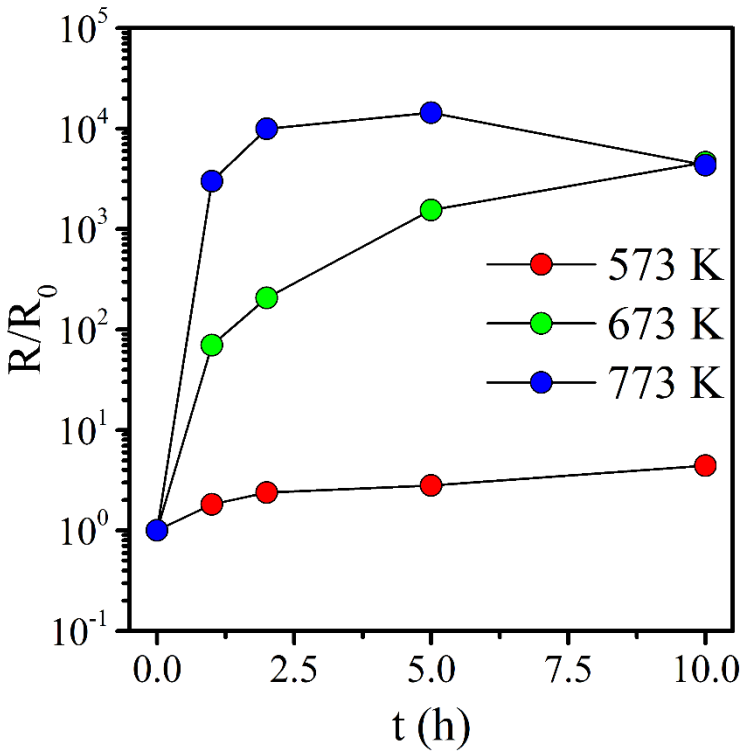

Figure 4-26 Stability of the nitrogen doping in uniform ZnO nanorod samples against the duration of the treatment for different temperature of the treatment. The stability is reported as the ratio between the resistance after(R) and before (R_0) the thermal treatment.

At 773 K, the doping effect disappeared within the first hour of treatment since the measured resistance was about four orders of magnitude higher.

Increasing the treatment led to further increase of the resistance until five hours, when *R* started to slightly decrease again suggesting eventual sintering phenomena improving the overall conductivity.

Decreasing the temperature of the treatment to 673 K, the increase of the resistance was constant for all the duration of the treatment and changed from about two orders of magnitude after the first hour to about four orders of magnitude after ten hours, with a trend also indicating further possible increase of *R*. Even at 573 K an increase of the resistance was observed, despite it was less and restricted to a factor of 4 after the end of the treatment. These results indicate that the nitrogen doping with ammonia is strongly susceptible to moderate temperature and that eventual large-scale applications could be restricted to low-temperature conversion processes.

Fig. 4-27 shows the thermoelectric voltage generated by our samples for values ranging from 0 to 175 K.

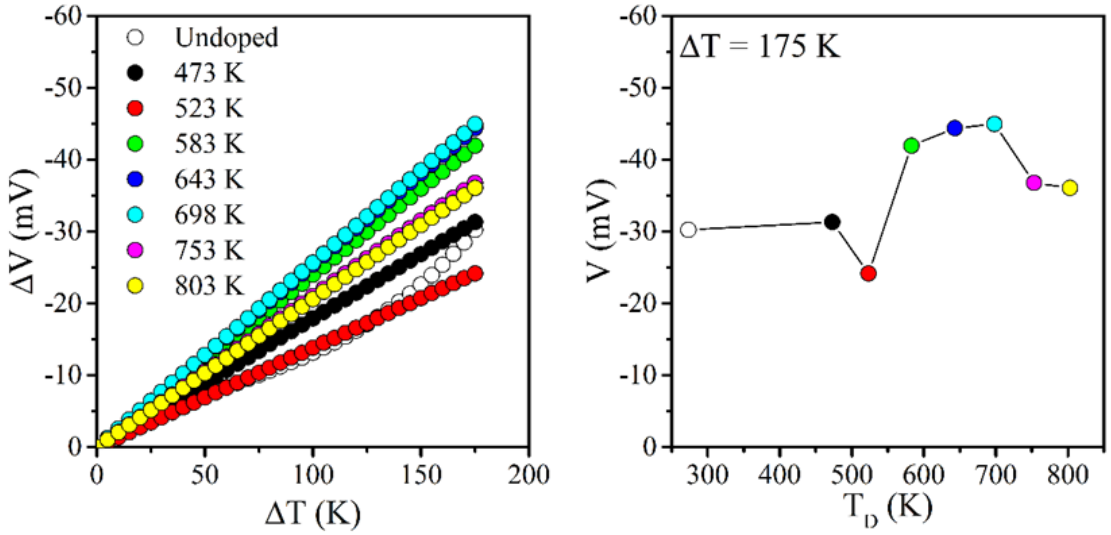

Figure 4-27 Thermoelectric potential against the temperature difference (left) of uniform films of ZnO nanorods doped through the gas-phase approach. The dependency on the doping temperature under a temperature difference of 175 K is reported in the right panel.

All the samples show a potential difference increasingly negative as the temperature difference increases, confirming the *p*-type conduction mechanism of the nitrogen doped samples. The negative potential values are expected since the measurement apparatus measures the potential as:

$$\Delta V = V_H - V_C$$

where V_H is the potential at the hot side and V_C the potential at the cold side. When the primary charge carriers are holes, such in the case of N-doped ZnO, a partially positive charge is generated on the cold side and a partially negative charge on the hot side, thus leading to an overall negative potential difference.

For all the doped samples, the thermoelectric potential increases almost linearly in the considered interval of ΔT, with the highest ΔV values measured for the samples doped at 643 and 698 K, corresponding to 44 and 45 mV respectively at ΔT = 175 K. Considering the same ΔT, all the samples produced a thermoelectric potential 24 and 42 mV without showing any specific trend with the doping temperature as illustrated in the right panel of fig. 4-27. Compared to other unileg ZnO-based TEG's prototypes found in literature, the nanorods resulted generally less efficient in terms of output voltage. For example, a potential difference of 10 mV at ΔT = 30 K has been reported by Yang *et al* for a single Sb-doped ZnO nanobelt[164], while Norouzi *et al* reported an output voltage of 0.1 mV at 337 K for an array of vertically aligned Al-doped nanorods under a temperature gradient of 1 K[140]. However, in the first case the values corresponded to the response of a single NR, while in the second case the thermoelectric properties were limited to low temperatures and have been measured along the thickness of the film rather than its width and the comparison can be difficult. Similar values have been reported by Fan regarding a dual-leg generator consisting in Zn-based *p*- and *n*-type materials, where a single p-n junction generated an output voltage of 47 mV under a temperature difference of 203 K[165]. Moreover, in all the cited examples, the ZnO part of the TEG is *n*-doped, since in literature there are no studies on *p*-type ZnO used as thermoelectric material.

It must be noted that also undoped ZnO behaved as a *p*-type material, though it should be *n*-type, leading to a thermoelectric potential with positive sign. It is supposed that this behavior could be directly related to the synthesis procedure. In fact, nanorods were grown using a concentration of hexamethylenetetramine equal to 25 mM, close to the concentration used in the hydrothermal doping (10 mM). It is possible, hence, that HMT could have sourced nitrogen species to zinc oxide leading to the unexpected *p*-type conductivity.

Fig. 4-28 shows the thermoelectric current generated by the samples as a function of the temperature difference.

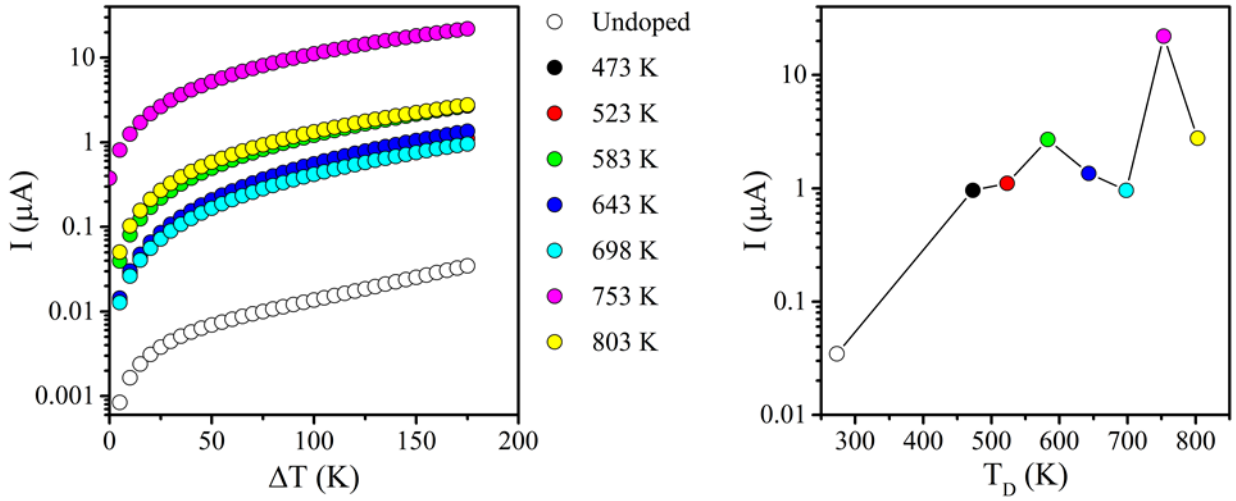

Figure 4-28 Thermoelectric current against the temperature difference (left) of uniform films of ZnO nanorods doped through the gas-phase approach. The dependency on the doping temperature under a temperature difference of 175 K is reported in the right panel.

For all doped samples, I was calculated using an external reference resistance (R_L) of 100 Ω while for the undoped sample R_L was 10 k Ω. Also in this case the output currents are reported in the graph as negative values, as the typical negative potential of the p-type have been divided by a positive R_L value, however they will be considered as positive in the following discussion. The highest output current of 22 μA was measured for the sample doped at 753 K under a temperature difference of 175 K, which resulted three orders of magnitude higher compared to the electric current generated by the undoped sample (I=0.03 μA). The currents measured for the other nitrogen doped samples as a function of the doping temperature strictly followed the trend of σ against T_D (right panel of fig. 4-28). Considering ΔT = 175 K, all the samples doped in the range of temperatures between 473 and 698 K show similar low currents between 0.96 and 1.35 μA, but the one doped at 583 K shows a higher output current of 2.69 μA close to the sample doped at 803 K (2.77 μA). Evidences of output current from *p*-type ZnO can be found in the study regarding the single Sb-doped nanobelt[164] which generates 194 nA with a temperature difference of 10 K, which normalized is comparable or even higher compared to the p-type nanorods, but also in this case the comparison is made considering two very different conditions.

Fig. 4-29 shows the output power of the N-doped ZnO NRs films calculated by multiplying the voltage and the current in the whole range of temperature.

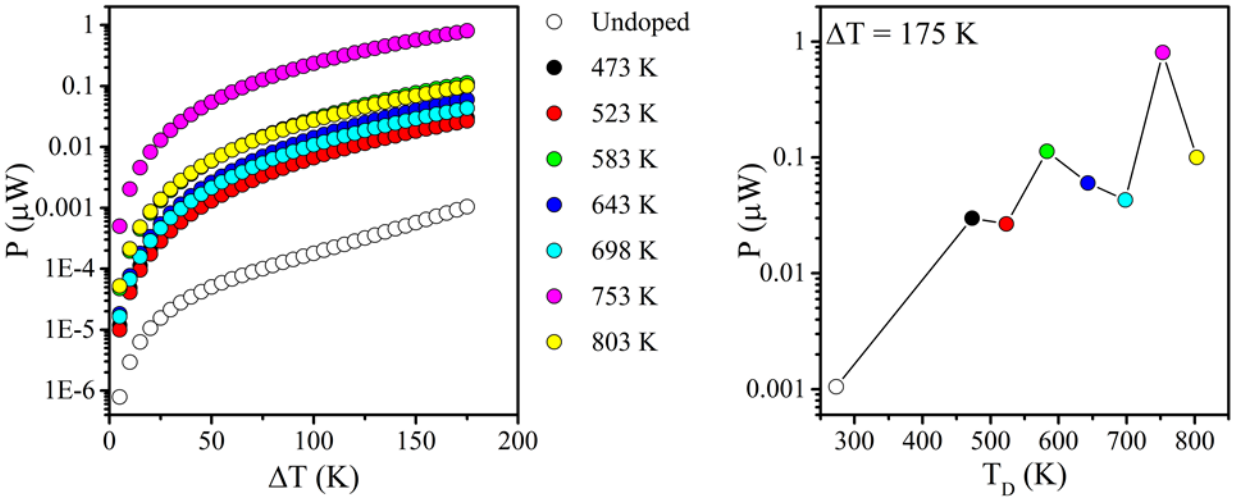

Figure 4-29 Calculated output power against the temperature difference (left) of uniform films of ZnO nanorods doped through the gas-phase approach. The dependency on the doping temperature under a temperature difference of 175 K is reported in the right panel.

The power values follow the same trend against the doping temperature as in the case of the generated current (right panel of fig 4-29).

The highest power of 0.8 μW was calculated for the sample doped at 753 K and was almost three orders of magnitude higher compared to the power generated by the undoped sample (1.05×10^{-3} μW), while the samples doped in the interval between 473 and 698 K showed values ranging from 0.027 μW and 0.113 μW. The output power of the sample doped at 803 K was 0.1 μW. The maximum output power found in literature for Zn-based thermoelectric generator is the value of 246.3 μW reported by Fan[165] which is more than two orders of magnitude higher compared to our best nitrogen doped sample, but the same consideration made before regarding the comparison with devices characterized by very different materials and geometries must be reminded. Moreover, the unileg geometry of the film of nanorods leads necessarily to lower efficiencies compared to the most efficient dual-leg devices.

As described previously, the Seebeck coefficient of nitrogen doped ZnO was measured using the integral method from the slope of the ΔV *vs.* T_{hot} curve. For every samples, the best fit was obtained using the linear function, so the thermopower resulted to be constant in all the investigated range of temperature (tab. 4-2).

Table 4-2 Seebeck coefficient determined by the integral method of uniform films of ZnO nanorods doped through the gas-phase approach. The Seebeck coefficients are considered constant in the investigated range of temperatures (from 298 K to 473 K) because the curves of the thermoelectric potential are fitted with a linear function.

T_D (K)	S (μV/K)
Undoped	137
473	146
523	112
583	194
643	209
698	212
753	171
803	168

The trend of *S* with the doping temperature followed the same irregular dependency of the output voltage with T_D (Fig. 4-30). The highest Seebeck coefficient of 212 μV/K was obtained with the sample doped at 698 K, the lowest *S* of 112 μV/K with the sample doped at 523 K.

All these coefficients are lower compared to the 408 μV/K value reported by Bian for both continuous film of N-doped ZnO[166] and, especially, compared to the extremely large 1477.1 μV/K of N-In-codoped ZnO films[167]. In this case, however, the stability of the p-type doping is limited to 517 K, a temperature at which a *p*-type to *n*-type conversion was observed.

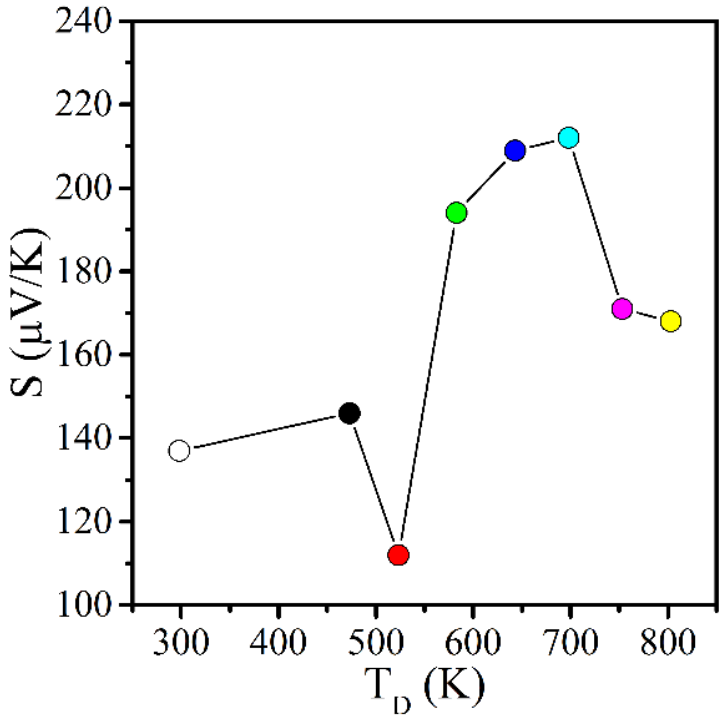

Figure 4-30 Seebeck coefficient of uniform films of ZnO nanorods doped through the gas-phase against the doping temperature.

Finally, the power factor for our *p*-type samples is reported in fig. 4-31.

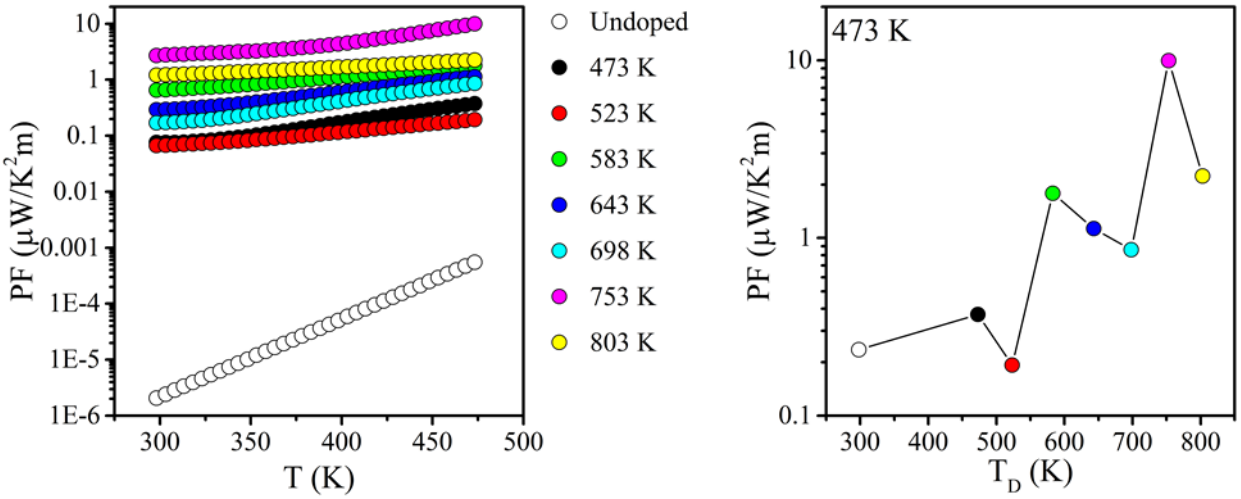

Figure 4-31 Calculated power factor against the temperature (left) of uniform films of ZnO nanorods doped through the gas-phase approach. The dependency on the doping temperature at 473 K is reported in the right panel.

In general differences of about one order of magnitude can be observed in the range of doping temperature between 473 K and 698 K. The lowest *PF* of 0.19 μW/K^{2}m was calculated at 523 K and the highest (1.78 μW/K^{2}m) 583 K.

At the same time, the thermal treatment performed at 753 K resulted quite effective in increasing the power factor of about another order of magnitude, leading to a *PF*-value of 9.94 $\mu W/K^2m$, while doping at 803 K reduced the performance of down to 2.23 $\mu W/K^2m$. The power factor of the undoped sample was of 0.24 $\mu W/K^2m$, hence, 583 K could be considered as the minimal doping temperature to observe a significant increase of the thermoelectric properties of doped sample, but to achieve the best results in term of doping effectiveness a doping temperature of 753 K must be used.

4.3.5.2. Patterned films of N-doped ZnO nanorods

As it was anticipated previously, the use of patterned NRs films induced a further overall increase of the electrical conductivity, due to the more efficient geometry of the electrical contacts between the nanorods. Fig. 4-31 shows the electrical conductivity of the patterned samples against the temperature, also compared to the analogous uniform sample.

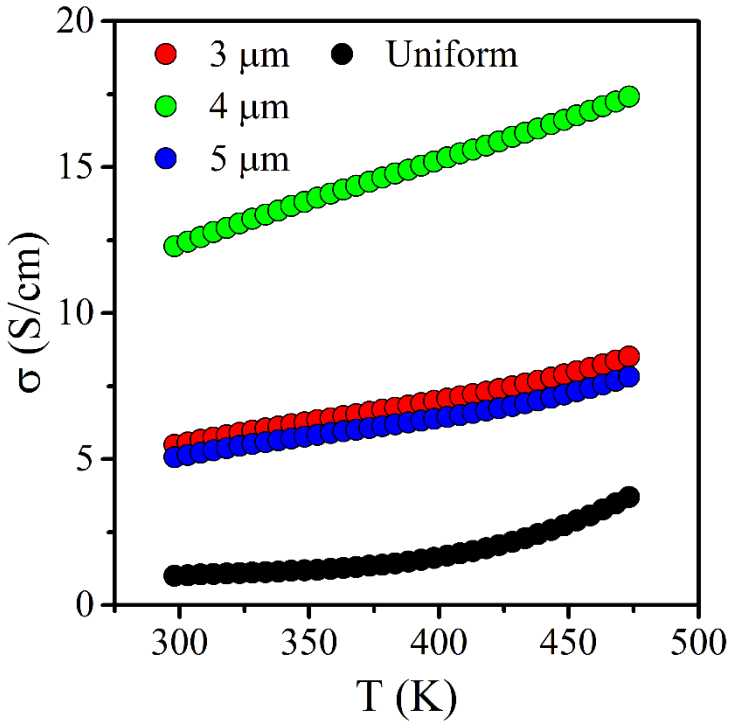

Figure 4-32 Electrical conductivity against the temperature of patterned film of ZnO nanorods characterized by 3, 4 and 5-μm wide rows (red, green and blue points, respectively) doped at 753 K with the gas-phase approach. For comparison, also the electrical conductivity of the uniform sample doped at the same temperature is reported.

While the samples characterized by lines 3 and 5 μm wide exhibited similar σ values, increasing with T from 5.48 and 5.06 S/cm to 8.50 and 7.82 S/cm, respectively, the electrical conductivity of the 4 μm sample varied between 12.29 to 17.41 S/cm.

The thermoelectric potential of these samples is shown in fig. 4-32. The calculated Seebeck coefficient (table) followed almost inversely the differences observed in the electrical conductivities.

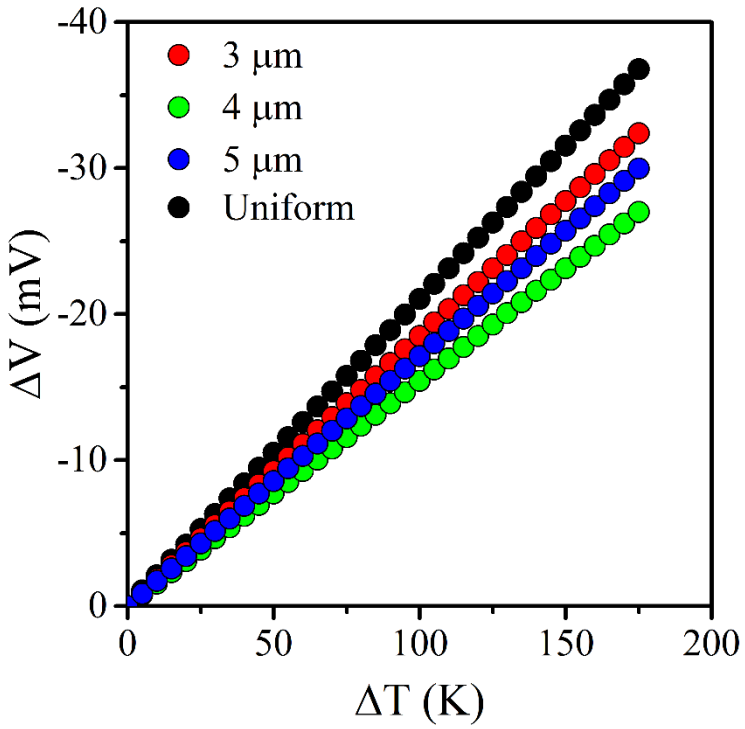

Figure 4-33 Thermoelectric potential against the temperature difference of patterned film of ZnO nanorods characterized by 3, 4 and 5-μm wide rows (red, green and blue points, respectively) doped at 753 K with the gas-phase approach. For comparison, also the thermoelectric potential of the uniform sample doped at the same temperature is reported.

Table 4-3 Seebeck coefficient determined by the integral method of patterned film of ZnO nanorods characterized by 3, 4 and 5-μm wide rows doped through the gas-phase approach. The Seebeck coefficients are considered constant in the investigated range of temperatures (from 298 K to 473 K) because the curves of the thermoelectric potential are fitted with a linear function.

Sample	S (μV/K)
Homogeneous	171
3 μm	153
4 μm	129
5 μm	141

In fact, the highest thermoelectric potential of 37 mV (ΔT=175 K) was measured for the sample presenting a uniform film of NRs, while the patterned films ones exhibited quite similar values: 30 and 32 mV for the 5 μm and the 3 μm and 27 mV, the lowest value being for the most conductive sample (4 μm rows). This reduction corresponded to a decrease of the Seebeck coefficient of about 25%, from 171 μV/K for the uniform sample to 129 μV/K of the 4 μm patterned sample.
Fig. 4-33 shows the thermoelectric current generated by this set of samples.

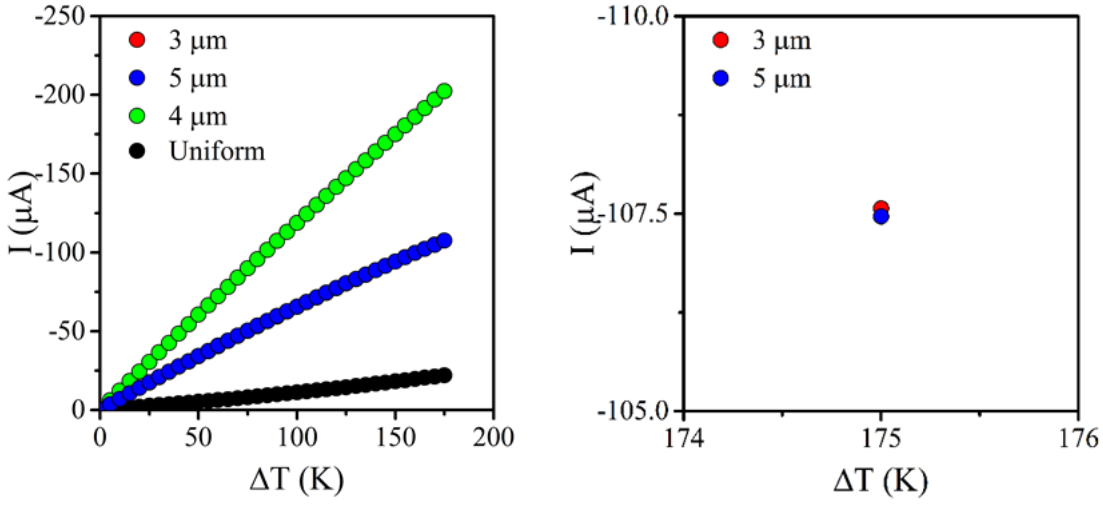

Figure 4-34 Thermoelectric current against the temperature difference of patterned film of ZnO nanorods characterized by 3, 4 and 5-μm wide rows (red, green and blue points, respectively) doped at 753 K with the gas-phase approach. For comparison, also the current of the uniform sample doped at the same temperature is reported. In the right panel, a detail of the small differences observed between the currents of the 3 and 5-μm samples.

As for the electrical conductivity, the patterning led to an evident increase of the current generated. The increase of *I* from the uniform to the 4 μm-patterned sample was about one order of magnitude for a ΔT=175 K, from 22 to 202 μA, respectively, while the increase induced by the 3 and 5 μm was of about a factor of 5. These samples showed also nearly identical currents (*I*=107/108 μA at ΔT=175 K) as it could be seen in the right panel of fig. 4-33.

The same trend could be observed in the electric power generated by the samples (fig. 4-34).

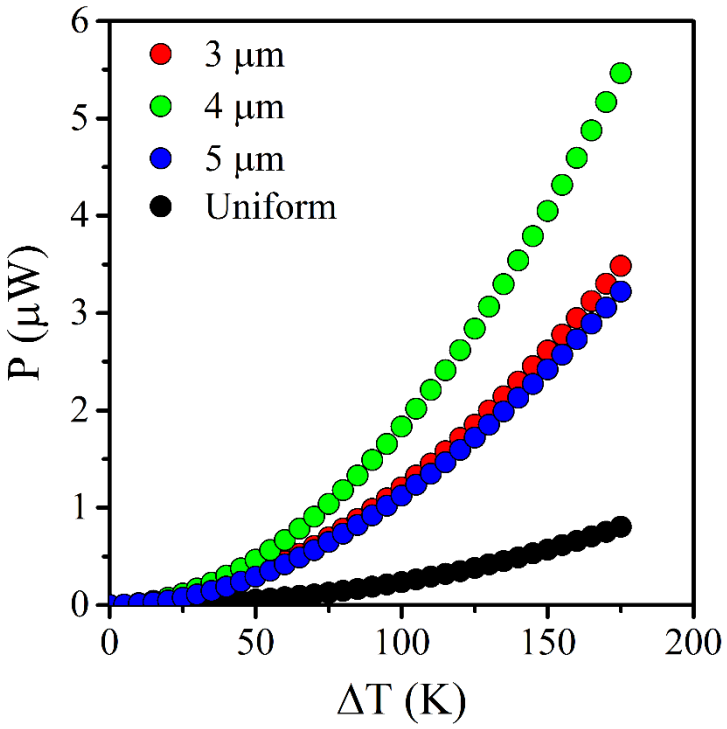

Figure 4-35 Calculated output current against the temperature difference of patterned film of ZnO nanorods characterized by 3, 4 and 5-μm wide rows (red, green and blue points, respectively) doped at 753 K with the gas-phase approach. For comparison, also the power of the uniform sample doped at the same temperature is reported.

The magnitude of the increase of *P* was of about a factor of 7 with the most efficient sample (4 μm), which reached a maximum power of 5.46 μW at ΔT=175 K compare to 0.80 μW of the uniform analogous.

Finally, the power factor of the uniform and patterned samples is reported in fig. 4-35.

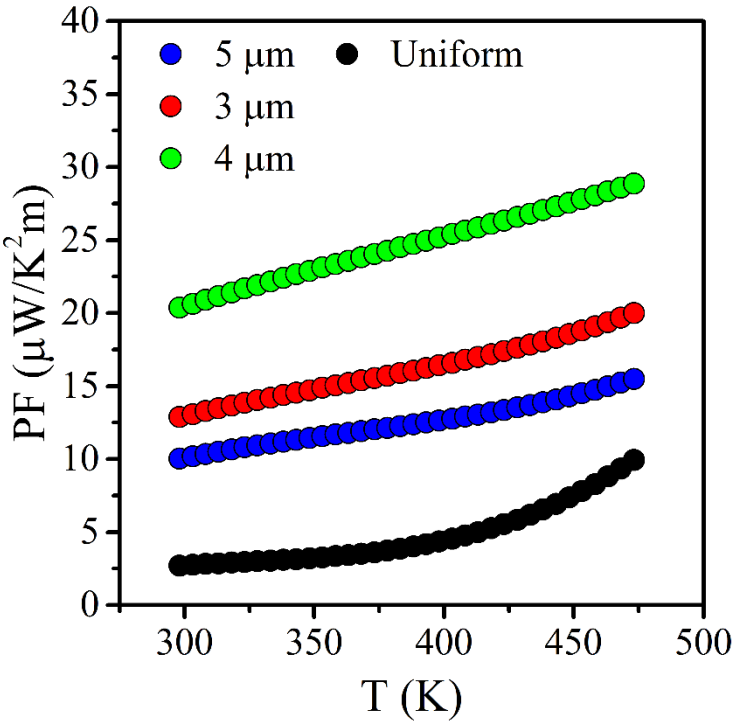

Figure 4-36 Figure 4-37 Calculated power factor against the temperature of patterned film of ZnO nanorods characterized by 3, 4 and 5-μm wide rows (red, green and blue points, respectively) doped at 753 K with the gas-phase approach. For comparison, also the power factor of the uniform sample doped at the same temperature is reported.

Also in this case, the dependency of *PF* from the film architecture is observed. The 4 μm-patterned sample resulted the most efficient in terms of the power factor indicating as the increase of the electrical conductivity was enough to compensate the reduction of the Seebeck coefficient. At the same time, the highest *S* of the uniform sample was enough to reduce the differences with all the patterned samples so that the best increase of the performances achieved with the patterning was reduced to a factor of 3 (from 10 $\mu W/K^2m$ to 29 $\mu W/K^2m$).

A preliminary characterization of the properties of ZnO nanorods were measured using the simple experimental apparatus schematically described in fig. 4-36 on a uniform film of undoped NRs.

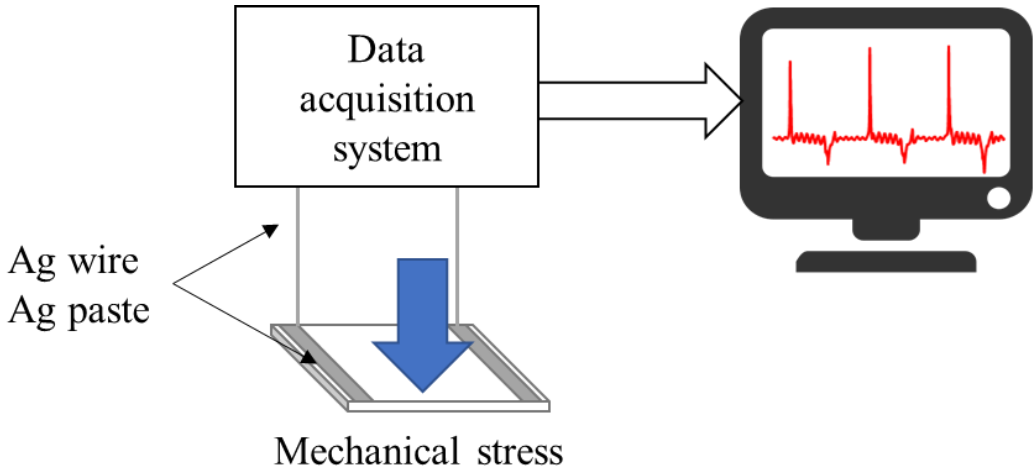

Figure 4-38 Schematic illustration of the setup for the measurement of the piezoelectric potential. The sample produces a piezoelectric voltage after the application of a mechanical stress. The signal is recorded by a data acquisition system connected through a couple of silver wires.

The electric contacts were made using a conductive silver paint, two Ag wires were connected to the sample in correspondence of the paint using a silicone sealant paste (RS components) and then connected to a data acquisition device (Measurement Computing USB-1608) controlled by the software Tracer DAQ. The piezoelectric voltage generated after a rapid manual mechanical deformation is reported in fig. 4-37.

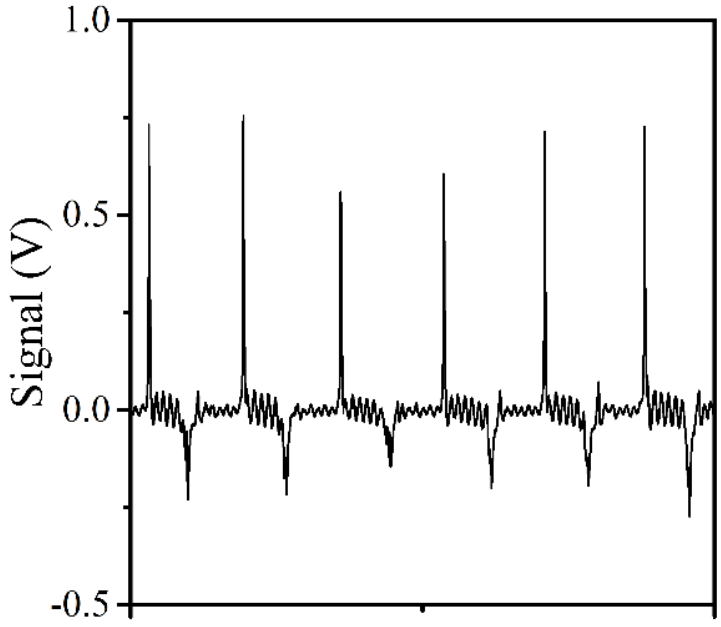

Figure 4-39 Piezoelectric voltage generated by a uniform film of undoped ZnO nanorods. Potential differences close to 1V can be obtained.

The signal shows asymmetric peaks which assume both positive and negative values with the highest positive value deriving directly from the mechanical input, while the less intense negative potential caused by the dumped oscillation induced in the glass substrates. The maximum voltage generated by the uniform NR film of was calculated to be about 1 V.

4.4. Conclusions

The hydrothermal approach has been confirmed to be an effective strategy to obtain well-defined uniform and patterned thin films of high aspect ratio zinc oxide nanorods. At the same time, hydrothermal doping using HMT as the dopant source was not efficient in realizing a high conductive *p*-type material. Slightly harsher conditions using high temperature treatment in flux of ammonia gas were instead required to achieve an improvement of the RT electrical conductivity of about four orders of magnitude in uniform samples (doping temperature, T_D=803 K) which, in turns, resulted in in an improvement of the room temperature power factor of about six orders of magnitude, while the Seebeck coefficient followed an irregular trend against the doping temperature. From the point of view of thermoelectric generators, the improvement of the output power was driven mainly by the improvement of the output current which followed the same trend of the electrical conductivity with T_D, as they are strictly related. Most important, the better geometry of the electrical connections between different lines of nanorods in patterned samples had a positive effect on the conductive properties of *p*-type ZnO. This approach led to a further improvement of the electrical conductivity and, generally, of all the thermoelectric properties (the Seebeck coefficient was slightly reduced) of about a factor of 3-5 at 473 K for the sample characterized by lines of 4 μm. These results, together with the strong theoretical reduction of the thermal conductivity induced by the large number of interfaces and/or alternate absence of the film, should lead to a large improvement in terms of *ZT*. However, the stability of the doping has been observed to be strongly related to the external temperature.

Piezoelectric characterization showed that high potential differences close to 1 V could be obtained after a moderate mechanical stress of the substrate, suggesting the possibility to engineer an efficient piezoelectric generator.

5. Strontium barium niobate

5.1. Introduction

Strontium barium niobate ($Sr_xBa_{1-x}Nb_2O_6$, SBN) is a *n*-type oxide with a band gap of about 3 eV that finds application in several functional and technological applications as in photocatalysis[168], relaxor ferroelectricity[169] optoelectronics[170] and piezoelectricity[171]. SBN has also been studied for its thermoelectric properties resulting in a promising figure of merit of ≈1 [172]. These features are related to the crystal structure. SBN-based materials are solid solutions with a wide Ba/Sr composition range that belongs to the tetragonal tungsten bronze type (TTBs). TTBs are composed of corner-sharing oxygen octahedra inducing the formation of different sites that can be filled by different cations. These channels can be classified as A1, A2, B and C and the general formula of the tungsten bronze structures can be written as $(A1)_2(A2)_4C_4(B1)_2(B2)_8O_{30}$. The 12-fold coordinated tetragonal A1 sites and the 15-fold coordinated pentagonal A2 sites are often occupied by alkali and alkali-earths, B sites are generally transition metals and C accommodates only small atoms[173]. Based on the level of occupancies the TTBs structures can be denoted as “unfilled bronze” if the A sites are partially vacant, “filled bronze” if the A sites are all occupied and “stuffed bronze” if both the A and the C sites are filled[174]. So, the chemical flexibility of TTBs allows the introduction of several different atoms, offering the opportunity of fine tuning the properties of the structures. Strontium barium niobate crystallizes in the *P4bm* space group of the tetragonal system[175] with lattice parameters *a, b* = 12.4504(3) Å and *c* = 3.9325(1) Å[176] at room temperature. A1 sites are occupied only by Sr atoms while larger A2 sites can be filled by both strontium and barium cations, C sites are empty and niobium fills the B sites forming in the unit cell a single layer of five NbO_6 octahedra sharing their vertices[174], [177] that are placed in parallel to the *ab* plane, as represented in fig. 5-1[177].

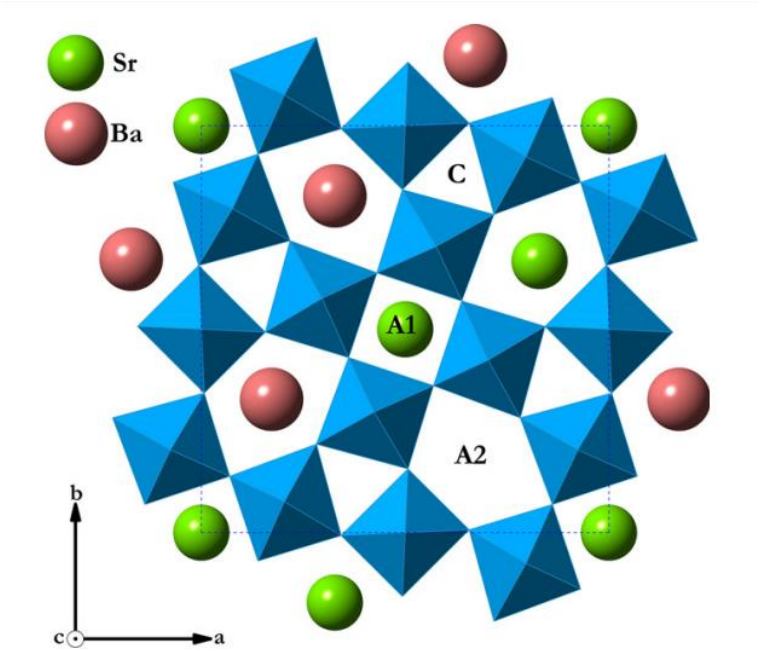

Figure 5-1 Crystal structure of strontium barium niobite. In blue, the oxygen octahedra. Taken from ref. [177].

The phase stability of the basic tetragonal phase depends on the synthesis temperature and on the relative quantities of the cations. The maximum Ba content in the SBN structure is 80% and is almost independently from the temperature, on the contrary the maximum Sr content depends on the temperature and increase from 62% at 1473 K up to 84% at 1723 K (fig. 5-2)[178].

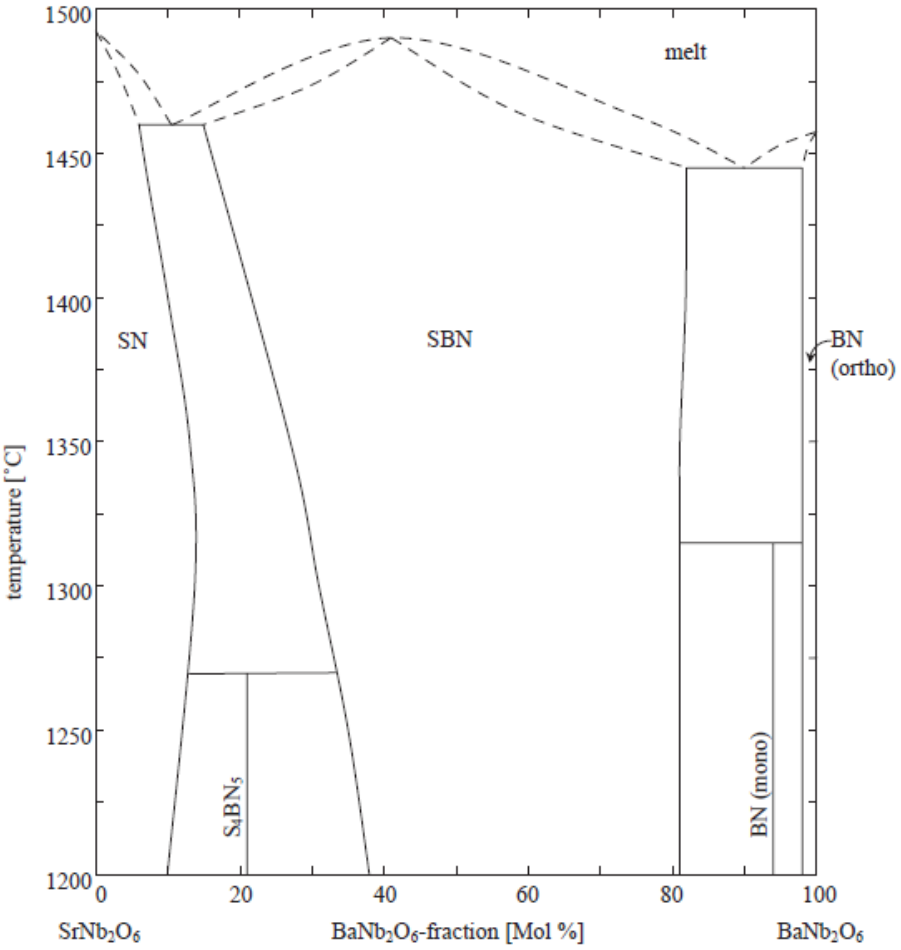

Figure 5-2 Phase diagram of the SrO-BaO-Nb2O5 system.

The interest in the thermoelectric properties of SBN relies in the combination of an intrinsically low thermal conductivity of its complex tungsten bronze structure (down to 0.8 W/Km for a single crystal[179]), high electrical conductivity and moderate Seebeck coefficient, that in single crystals result in a power factor of 41 $\mu W/K^2cm$, as reported by Lee *et al*[180]. Strong crystal anisotropies have also been reported, as the thermoelectric power factor is higher along the *c* direction[181]. In addition, some anomalies in the thermopower of SBN could be observed parallel to the c-axis around the ferroelectric–paraelectric phase transition temperature (T_C), as in the case of another ferroelectric material, $BaTiO_3$[182], suggesting the occurrence of possible coupling between the thermoelectric–ferroelectric properties. Transition temperature of $Sr_xBa_{1-x}Nb_2O_6$ depends on strontium and barium content and may vary between 325 K and 470 K for *x* varying between 0.25 and 0.75 [183].

Thermoelectric properties of SBN are strongly related to its level of oxygen substoichiometry, as the formation of oxygen vacancies is compensated by the generation of free electrons:

$$O_O{}^x \rightarrow V_O{}^{\cdot\cdot} + 2e' + \frac{1}{2}O_2(g)$$

However, reoxidation has been reported to occur from 573 K in air[179], decreasing the performances of strontium barium niobate and forcing the high temperature thermoelectric properties to be measured in inert atmosphere. Doping of SBN ceramics at low levels (few %) has already been investigated [184]–[189], although none of these investigations reported informations on the thermoelectric properties.

The aim of this research was to study the effect of high levels of doping with aliovalent cations and of the oxygen reduction on the structure and the thermoelectric properties of SBN-based materials with nominal 0.5/0.5 Sr/Ba compositions (SBN50, SBN100*x*) synthesized from solution chemistry. Attention was placed on the effectiveness of the dopants to add mobile carriers and modify the band structure, providing an effective way of tuning the electrical conductivity and the Seebeck coefficient. The dopants we investigated were zirconium and molybdenum, that probably substitute Nb in quantity between 10 and 12.5%, while potassium and yttrium were used in substitution of Sr at doping levels near 40%. K has been used instead of rubidium to ensure that the dopant replaces Sr instead of Ba.

5.2. Results and discussion

5.2.1. Synthesis of the SBN powders and HP-FAST sintering

Strontium barium niobate materials could be prepared following different approaches: for polycrystalline material solid state routes[190], sol-gel synthesis[191], [192] or solution combustion synthesis[179] have been employed, while the preparation of SBN thin film was achieved by pulsed laser deposition techniques, RF sputtering of polymeric routes[193]. In this work, doped and undoped SBN powders were prepared by base-catalyzed co-precipitation. Aqueous solutions of strontium nitrate ($Sr(NO_3)_2$), barium nitrate ($Ba(NO_3)_2$) and niobium ammonium oxalate ($C_4H_4NNbO_9 \cdot xH_2O$) were mixed under stirring in the amounts required by the stoichiometry. For the doped samples potassium nitrate, (KNO_3), ammonium molybdate tetrahydrate ($(NH_4)_6Mo_7O_{24} \cdot 4H_2O$), zirconium oxynitrate hydrate ($ZrO(NO_3)_2 \cdot 6H_2O$) and yttrium nitrate ($Y(NO_3) \cdot 6H_2O$) were used and the water content of the hydrated salts were previously measured or checked by thermogravimetric analysis. The starting solutions were mixed in order to obtain the following compositions: $K_{0.2}Sr_{0.3}Ba_{0.5}Nb_2O_6$, $Y_{0.25}Sr_{0.25}Ba_{0.5}Nb_2O_6$, $Sr_{0.5}Ba_{0.5}Zr_{0.2}Nb_{1.8}O_6$, $Sr_{0.5}Ba_{0.5}Mo_{0.2}Nb_{1.8}O_6$. Then, diluted ammonia was added drop-wise until a white precipitate was obtained. This was filtered, washed with distilled water, dried to 453 K and isostatically pressed into a pellet. The compacted power was then fired for 24 hours at 1423 K, allowed to cool down to room temperature, and grinded in an agate mortar. The Y-doped material underwent further thermal treatment. After synthesis, each product was divided into two batches. One was used as prepared and will be denoted throughout the chapter as “oxidized sample”, while a “reduced” powder batch was obtained by treating the powders in a homemade high-pressure field assisted sintering (HP-FAST) apparatus that was used as a tool for realizing the chemical reduction, without applying any pressure. The powders were placed in a 10-mm diameter graphite crucible positioned between two graphite plungers inside an SPS die. An electric current was flown through the system to achieve a heating rate of 200 K /min up to a final temperature of 1273 K. At the end of the treatment, SBN powders turned from white to distinctively gray/blue in color. Y-doped powders were treated also at 1423 and 1523 K, the details will be explained further on. The samples obtained using this procedure were distinctively gray in color, while all starting samples were white. FigXRDredox shows the X-ray diffraction patterns of oxidized and reduced undoped SBN powders (Cu-Kα radiation, wavelength = 1.54 Å).

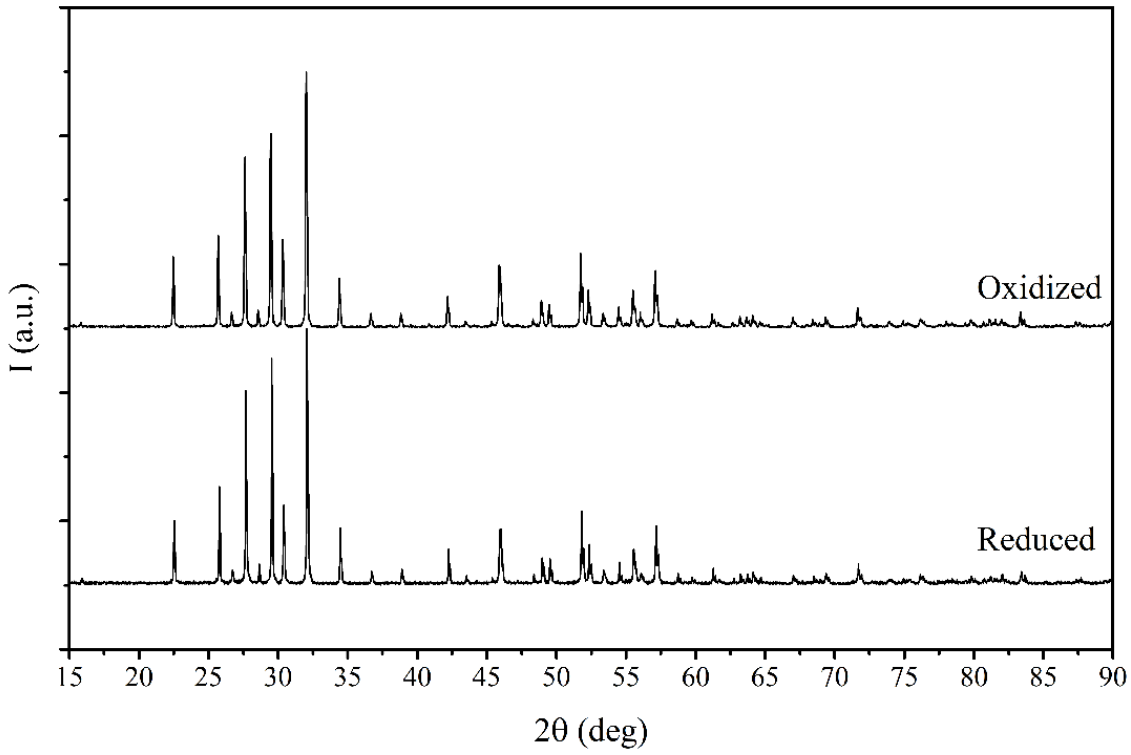

Figure 5-3 XRD patterns of the oxidized and reduced SBN powders.

Both samples appear to be single-phase, as confirmed by Rietveld refinement according to an established crystallographic model [194]. For either oxidized or reduced molybdenum- and zirconium-doped powders (x=0.2), full occupancies of both niobium sites have been observed and the diffraction patterns didn't show any presence of secondary phases, proving the possibility to introduce large quantity of dopant without phase separation. In the case of potassium and yttrium doping (x=0.2 for K and x=0.25 for Y), the structural analysis confirmed the substitution on the Sr/Ba site could be driven at percentage as high as 40% still resulting in a single-phase material. Moreover, considering that the ion radii of the IX and XII coordination shell (1.55 and 1.64 Å, respectively) of K+ are larger than those of both Sr^{2+} and Ba^{2+} cations (1.31/1.44 Å and 1.47/ 1.61 Å, respectively[195]), it was assumed that potassium would replace strontium in the larger A2 site (normally occupied by both Sr^{2+} and Ba^{2+}) while the Sr^{2+} in the A1 site was not substituted. In the case of yttrium, it was observed the presence of extraneous peaks in the diffraction pattern of both oxidized and reduced powders at 2θ = 28.6°, 30.2°, 32.7°, and 47.9°, as can be observed from the inset in fig. 5-4, that did not disappear even after prolonged thermal treatments.

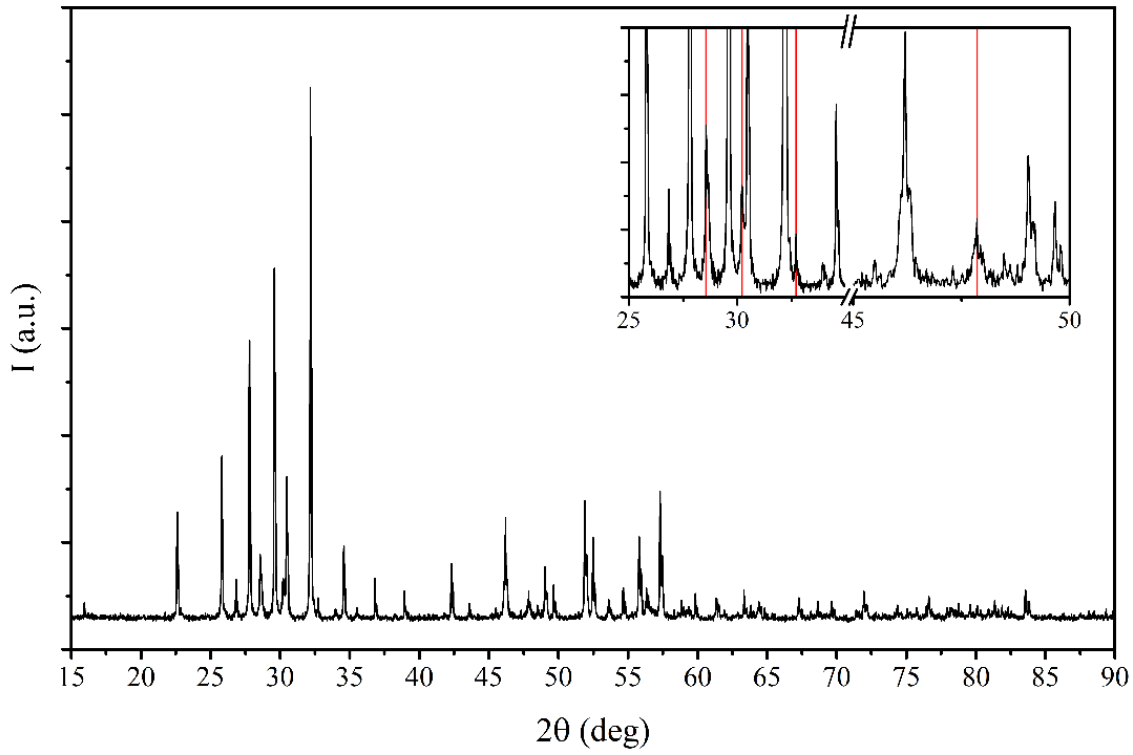

Figure 5-4 XRD pattern of the SBN Y-25powder. Single-phase material could not be obtained because of the presence of the $YNbO_4$ phase, as observed by its diffraction peaks evidenced in the upper-right inset.

These peaks belong to the monoclinic yttrium niobate phase ($YNbO_4$) [196]. The yttrium niobate content was calculated to be 3.0% and 7.6% for the oxidized and the reduced powders, respectively, leading to a cationic composition of the SBN phase close to $Sr_{0.26}Ba_{0.53}Y_{0.18}Nb_2O_6$, which corresponds to a doping level of 36%, slightly below the starting stoichiometry of 50%. The important aspect of the doping on the A sites was that strontium could be easily replaced in large amount without affecting the phase stability. This can be related to the characteristics of the tungsten bronze structure, which is capable to accommodate larger or smaller (>12%) cations inside oxygen cages that are much bigger that the ions. Doping produced strong modification in the lattice parameter of strontium barium niobate. The evidences of this effect are made clear by resorting to a typical analysis which relates the structural parameter with a discrepancy factor that was given by the ratio:

$$\frac{r_0 - r'}{r_0}$$

$$r' = x \cdot r + (1 - x) \cdot r_0$$

where x is the mole fraction of the dopant, r_0 is the size of the replaced ion (Sr or Nb, in this case), and r is the size of the replacing ion (Mo, Zr, K or Y).

Fig. 5-5 shows the correlation between the *a* and *c* lattice constant and the discrepancy parameter of doped powders.

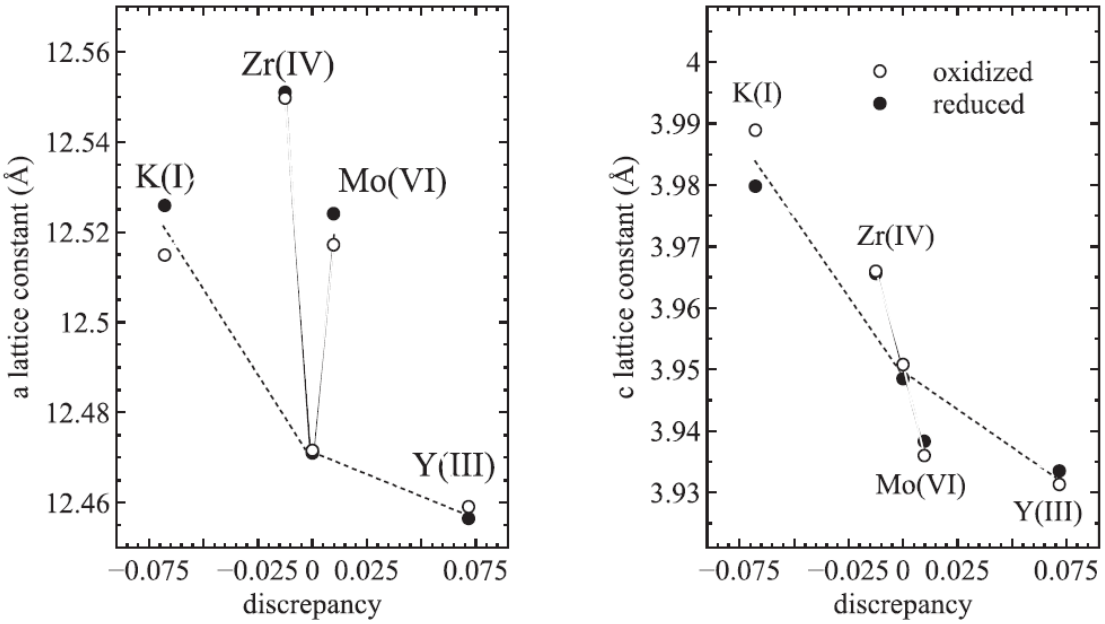

Figure 5-5 Discrepancy factors for "a" and "c" lattice constants.

Regardless from the reduction level, the substitution of strontium with smaller or larger cations affected the width of the *ab* plane since it is essentially related to the spacing between the rows of NbO_6 octahedra. It was found that the for the *a* lattice parameter, the variations deriving from the doping on the A (Sr substitution) site was mainly driven by size effects and it was quite contained, as the increase of the side of the tetragonal cell was only about 0.6% moving from yttrium to potassium. On the contrary, substitution of niobium on the B site, the centre of the oxygen octahedra, was independent from the dimension of the substituent atom and produced an increase with both molybdenum and zirconium, that are cations having a higher and lower oxidation state, respectively. This effect is expected for covalently bonded atoms, where both the addition or the removal of electrons in antibonding or bonding states concur in weakening the covalent character of the bond, thus increasing the bond distance. In the case of the *c* parameter, instead, the variation of the height of the unit cell appeared to be controlled by ion size effects only, as a regular trend with the discrepancy factor could be observed for both substitution on the A and on the B sites, which also corresponded to different slopes. The *a* parameter was affected by an amount of about 1.5% passing from Y to K. Finally, the effect of the chemical reduction on the lattice constant seemed to be negligible in almost all cases, and only in the case of K-doped powders a larger effect was observed.

Information about the electronic status (oxidation state and injection of charge carriers) of doped and undoped SBN in both reduced and oxidized state were obtained by X-ray spectroscopy techniques.

XAS spectra were recorded in transmission mode at the LISA-BM08 beamline71 (European Synchrotron Radiation Facility, ESRF, Grenoble, Fr) at the Nb–K edge. A Si(*311*) double crystal were employed as monochromator and the harmonic rejection was obtained by Pd mirrors, having a cut off energy of 20 keV. For the measurements, an amount of sample appropriate to give a unit jump in the absorption coefficient at the edge was weighted, thoroughly mixed with cellulose and pressed into pellet. For the XANES data analysis, the spectra were first pre-edge subtracted by fitting with a straight line, and then normalized to unit absorption 600 eV above the absorption edge, where the EXAFS oscillations are no more visible. Nb_2O_5 and Nb 2-ethylhexanoate were used as standards for Nb(V) and Nb(IV), respectively. Fig. 5-6 show the XAS spectra and the derivative of the XANES at the Nb-K edge of the oxidized SBN samples and of the niobium standards.

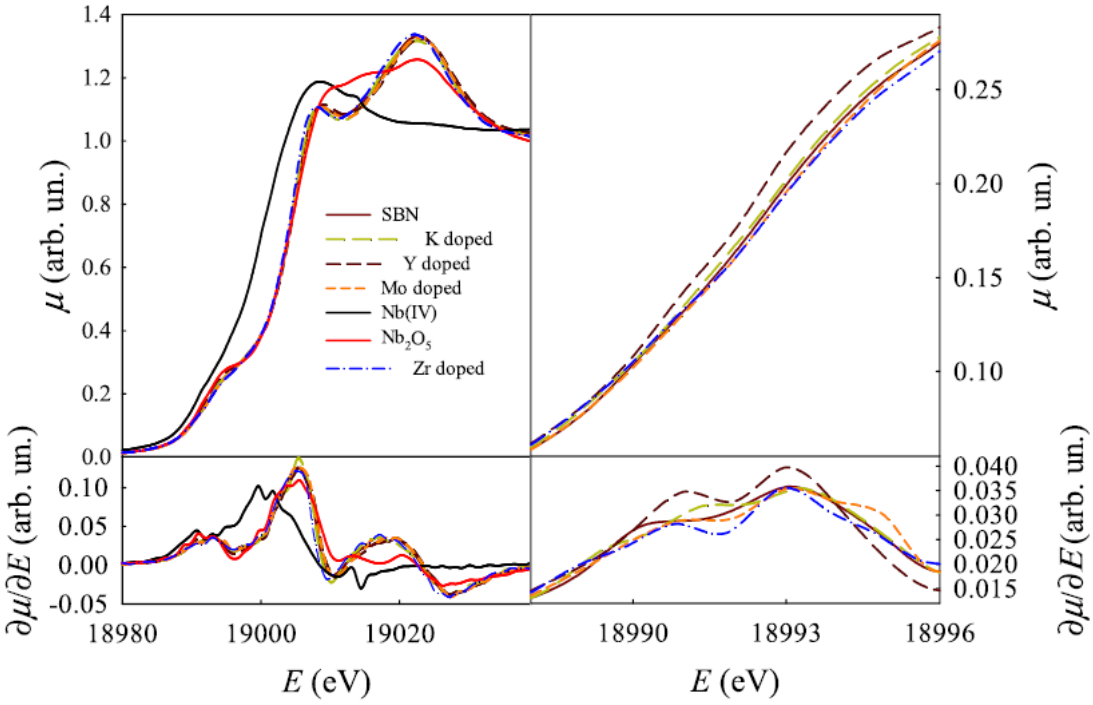

Figure 5-6 XAS spectra (upper panels) and the derivative (lower panels) of the XANES at the Nb-K edge of the oxidized SBN samples and of the niobium standards.

The absorption edges of the SBN samples agreed with the position of the Nb(V) standard while the absorption of the Nb(IV) standard occurred at lower energy, thus confirming the Nb(V) oxidation state of all the samples. At the same time, the shape of the XANES of the SBN was considerably different compared to the Nb_2O_5 standard as expected for their different crystal structures, but both showed a broad pre-edge feature at about 18993 eV due to the 1s→4d transition.

By considering the differences between the various doped and the undoped powders, as shown in the right site of the picture, the largest intensity of the pre-edge peak was achieved with the Y-doped sample, the lowest one with the Zr-doped SBN while the K-, Mo- and the undoped samples, exhibited intermediate values. These experimental results were contrary to what expected by a simple two-band the model of a pre-transition oxide where higher- or lower-valence dopant cations give rise to localized states that inject electrons or holes into the nearby conduction or valence band, respectively, decreasing the spectral weight. In fact, substitution with higher-valence (compared to Sr) Y-doping induced an increase in the absorption coefficient, while lower-valence (compared to Nb) Zr-doping led to a reduction of μ. So, it was assumed that the model could not be used and that the influence on the spectral weight was the result of several concurrent effects concerning the size of the dopant cation, the site filled and the effect on the covalent degree of the bond with oxygen. The reduction didn't modify the pre-edge peaks as it can be observed in fig. 5-7. In fact, while the XAS analysis probes the cation substitution, which affects the spectroscopic features of empty Nb states, the marked increase of the electrical conductivity is related to an increase of the density of mobile charge carriers and arises from a modification of the oxygen states directly controlled by the chemical reduction.

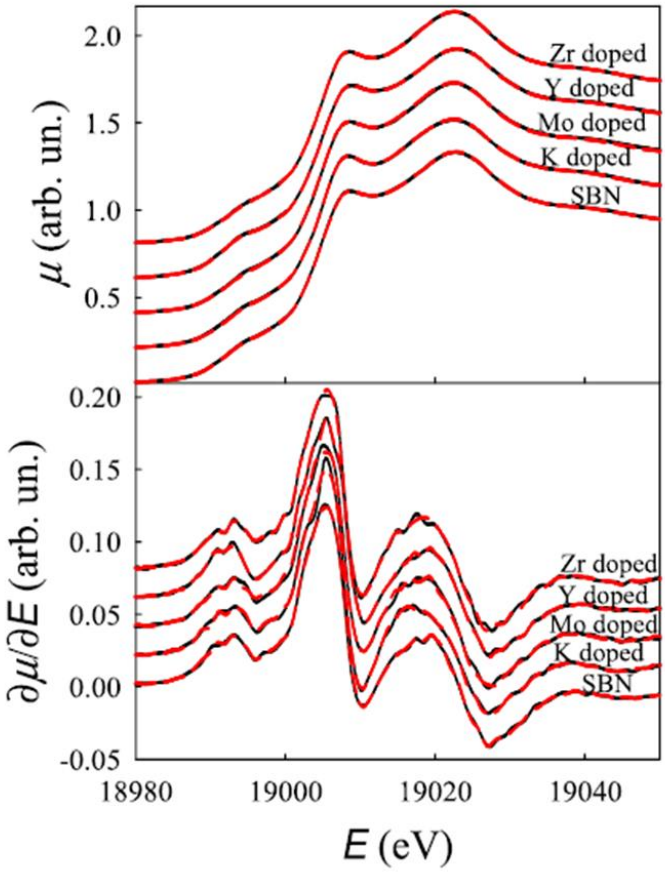

Figure 5-7 XANES spectra (upper panel) and their derivatives (lower panel) of the doped SBN powders.

The electrical conductivity and the Seebeck coefficient of SBN materials were measured on cylindrical samples, 5 mm in diameter, sintered using the HP-FAST apparatus and described in chapter 2. About 100 mg of reduced SBN powder was placed in suitable graphite dies and heated up to 1273 K under a uniaxial pressure of 500 MPa and finally cooled down at room temperature. In these conditions densities higher than 90% were achieved. The set of samples used for the thermoelectric characterization is reported in tab- 5-1. The labels were given according to the composition of the starting powders.

Table 5-1 List of SBN samples used for the thermoelectric characterization.

Sample	Composition	T_S (K)	p_S(MPa)
SBN	$Sr_{0.5}Ba_{0.5}Nb_2O_6$	1273	500
SBN K20	$K_{0.2}Sr_{0.3}Ba_{0.5}Nb_2O_6$		
SBN Y25	$Y_{0.25}Sr_{0.25}Ba_{0.5}Nb_2O_6$		
SBN Zr20	$Sr_{0.5}Ba_{0.5}Zr_{0.2}Nb_{1.8}O_6$		
SBN Mo20	$Sr_{0.5}Ba_{0.5}Mo_{0.25}Nb_{1.75}O_6$		

5.2.2. Thermoelectric properties of SBN samples

Thermoelectric properties were measured using the 2P1 apparatus for the electrical conductivity, the S1 apparatus for the Seebeck coefficient and by means of the PPMS apparatus for the determination of the thermal conductivity.

Fig. 5-8 shows the electrical conductivity of SBN samples against the temperature and as a function of the discrepancy factor.

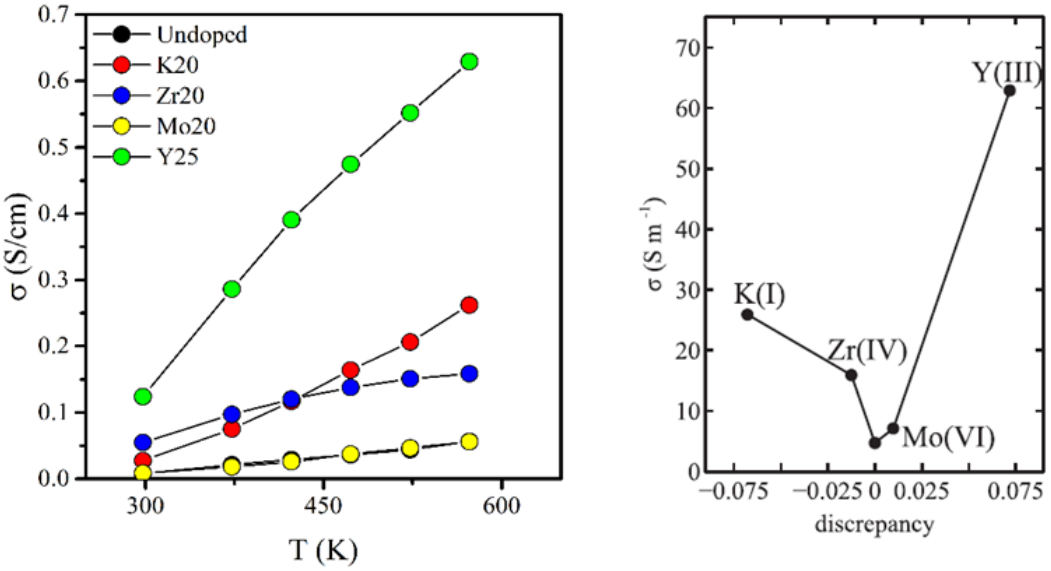

Figure 5-8 Electrical conductivity of doped and undoped SBN samples against the temperature (left) and against the discrepancy factor (right) at 573 K.

All the samples showed a semiconducting behaviour (σ increasing with T). The largest impact on the electrical conductivity was observed in samples doped with yttrium, with an increase of more than one order of magnitude compared to the undoped SBN sample. At 573 K its electrical conductivity reached values of 0.63 S/cm, while in absence of doping the electrical conductivity at the same temperature was of 0.06 S/cm. K- and Zr-doped samples exhibited intermediate behaviour, while the substitution of niobium with molybdenum did not produce any change in the conductivity. The effect of the chemical reduction on the electrical conductivity was measured to be of about eight orders of magnitude as it can be observed from fig. 5-9 where the trend relative to reduced and oxidized SBN-Y25 sample are reported.

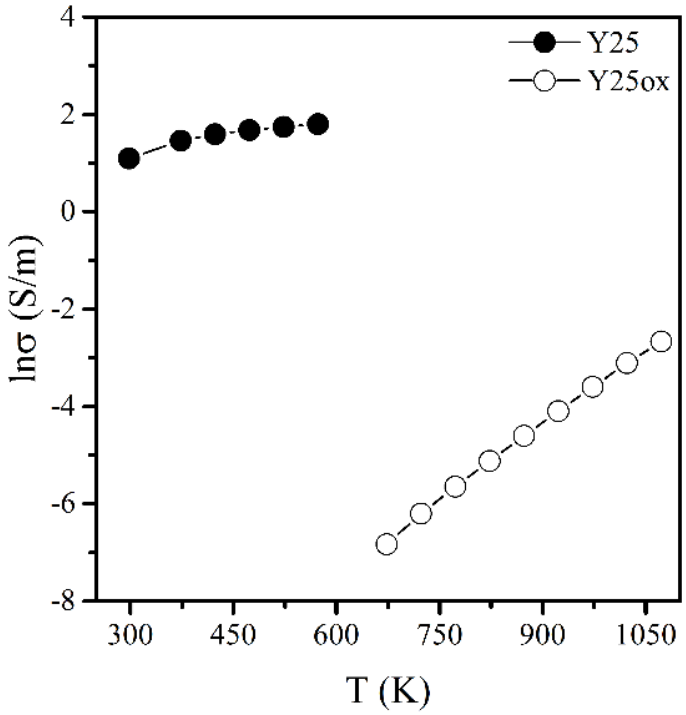

Figure 5-9 Electrical conductivity of the reduced (black) and oxidized (white) SBN Y25 samples. The oxidation causes a reduction of the electrical conductivity of more than eight orders of magnitude.

From the electrical conductivities of the SBN samples it was possible to estimate the activation energy of the conduction mechanism (fig. 5-10).

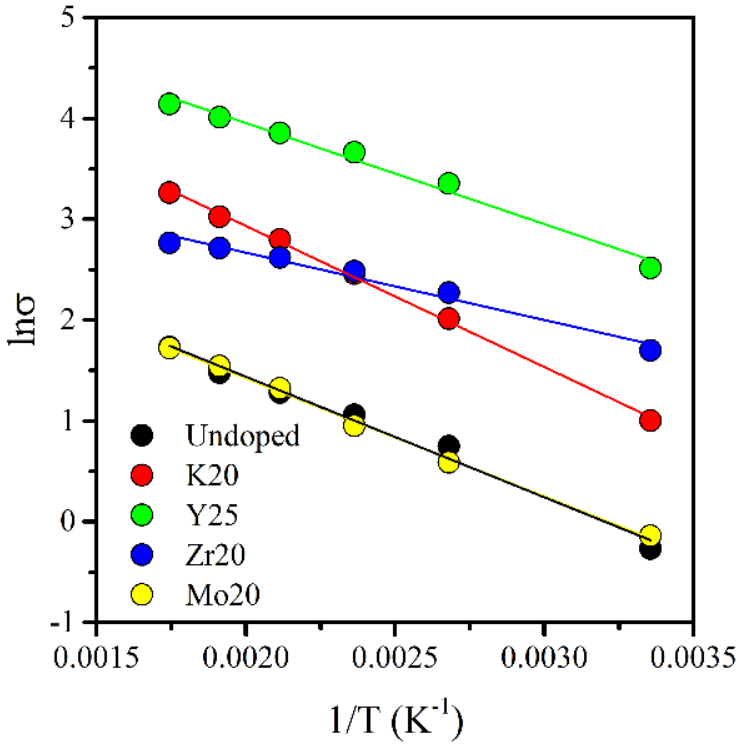

Figure 5-10 Arrhenius plot of the doped and undoped SBN samples.

The activation energies are reported in tab. 5-2.

Table 5-2 Activation energies of the doped and undoped SBN samples determined from the Arrhenius.

Sample	E_A (eV)	R^2
SBN	0.10	0.988
SBN K20	0.12	0.998
SBN Y25	0.09	0.986
SBN Zr20	0.06	0.977
SBN Mo20	0.10	0.998

The conduction didn't follow a linear trend in the Arrhenius coordinates, at least for some samples. A satisfactory degree of linearity was achieved only in the case of the SBN-K20 and the SBN-Mo20 samples. This behaviour could be associated to a change of the conduction mechanism with the temperature, from semiconducting to polaron hopping behaviour [181].

However, the observed electrical conductivity is almost three orders of magnitude lower in respect to values reported in the literature [179]. The highest σ-value for the undoped sample reduced at 1273 K was around 55 S/cm at 573 K, while the SBN sample reduced at the same temperature with HP-FAST exhibited an electrical conductivity of 0.06 S/cm. This can derive from a low level of reduction of the materials and/or from the random orientation of the grains, producing a microstructure very different from the textured microstructure reported in the literature [181]. To force the reduction, the SBN-Y25 powder, that produced samples characterized by the highest electrical conductivity, was further annealed in the FAST apparatus according to the procedure previously described. The annealing temperature was increased to 1423 K and 1523 K and then the powder was sintered at the same higher temperatures. Fig. 5-11 shows the electrical conductivities of these samples.

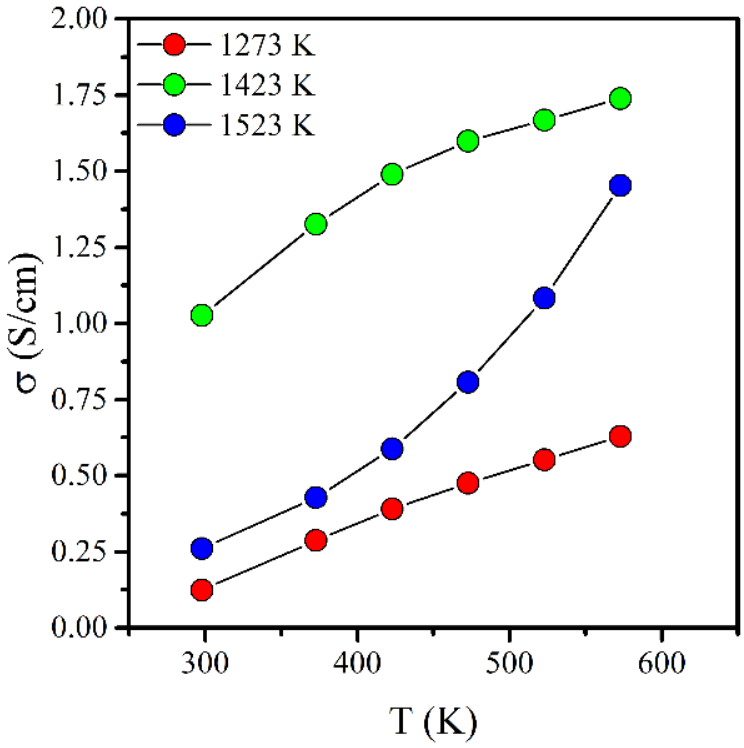

Figure 5-11 Electrical conductivity of SBN-Y25 samples sintered from powders annealed using the HP-FAST apparatus at different temperatures.

It can be seen that an increase of the annealing/sintering temperature didn't correspond to a regular increase in σ. The highest electrical conductivity of 1.74 S/cm at 573 K was achieved with the sample reduced and sintered at 1423 K. It presents a conductivity that was more than three times higher compared to the electrical conductivity of the sample treated at 1273 K (σ_{573K} = 0.63 S/cm). The increase was evident, but still much lower than the values reported in the literature.

The Seebeck coefficient of the reduced doped samples is shown in fig. 5-12 together with the trend with the discrepancy factor.

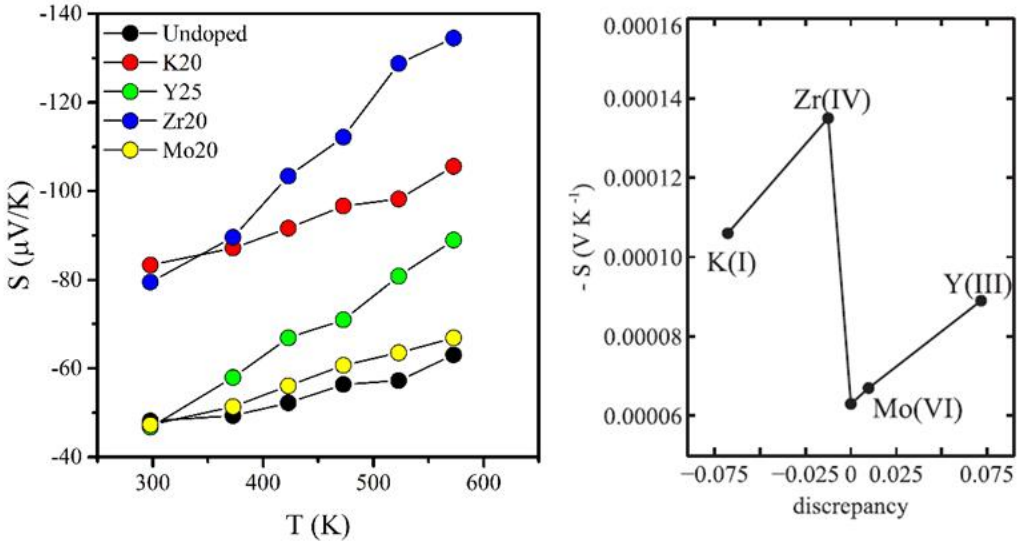

Figure 5-12 Seebeck coefficient of doped and undoped SBN samples against the temperature (left) and against the discrepancy factor (right) at 573 K.

The sign of the Seebeck coefficient is negative for all the samples, confirming that electrons are the primary charge carriers in these samples. The trend as a function of the dopant atom, instead, was not regular and doping induced an increase in the Seebeck coefficient of all the samples. The highest increase in the Seebeck coefficient was observed for the SBN-Zr20 sample, with S=-135 μV/K at 573 K, almost two times the Seebeck coefficient of the undoped sample (S=-63 μV/K at 573 K). The other samples presented intermediate values, with the molybdenum doping resulting the less effective.

The Seebeck coefficients of the reduced SBN samples are similar to those found in literature. In particular, the thermopowers are comparable to what reported by Dandeneau et al[179] for polycrystalline samples. However, these values are lower if compared with fully *c*-oriented samples, as according to this microstructure capable to achieve a Seebeck coefficient larger than 200 μV/K[181]. The Seebeck coefficients of oxidized samples could not be measured because of the high electrical resistivity of the samples.

The calculated power factor of the reduced samples is reported in fig. 5-13.

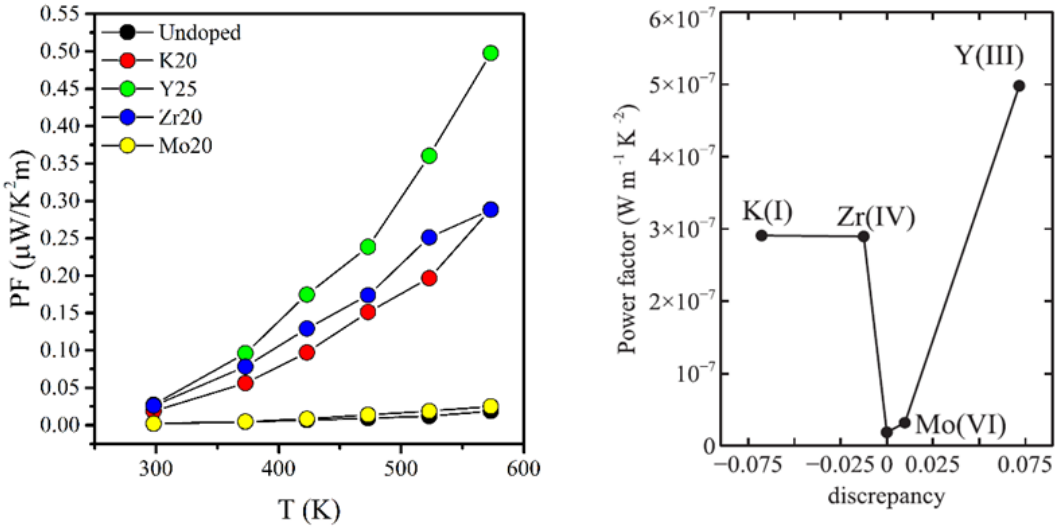

Figure 5-13 Power factor of doped and undoped SBN samples against the temperature (left) and against the discrepancy factor (right) at 573 K.

Because of the largest increase in the electrical conductivity, the SBN-Y25 sample resulted the most efficient in terms of power factor, with a calculated *PF*-value of 0.49 μW/K^{2}m, an overall increase by a factor of 30 compared to the undoped sample. Molybdenum doping resulted the least efficient, showing a Seebeck coefficient and an electrical conductivity comparable to those of the undoped sample. SBN-K20 and SBN-Zr20 presented intermediate values, closer to the SBN-Y25 rather than the SBN-Mo20/SBN couple of samples. Also in this case, the general values of the power factor were remarkably lower, as considering the literature equivalent sample, its PF at 573 K was of ~100 μW/K^{2}m, more than two orders of magnitude higher.

Fig. 5-14 shows the thermal conductivity of reduced SNB materials and its changes with doping.

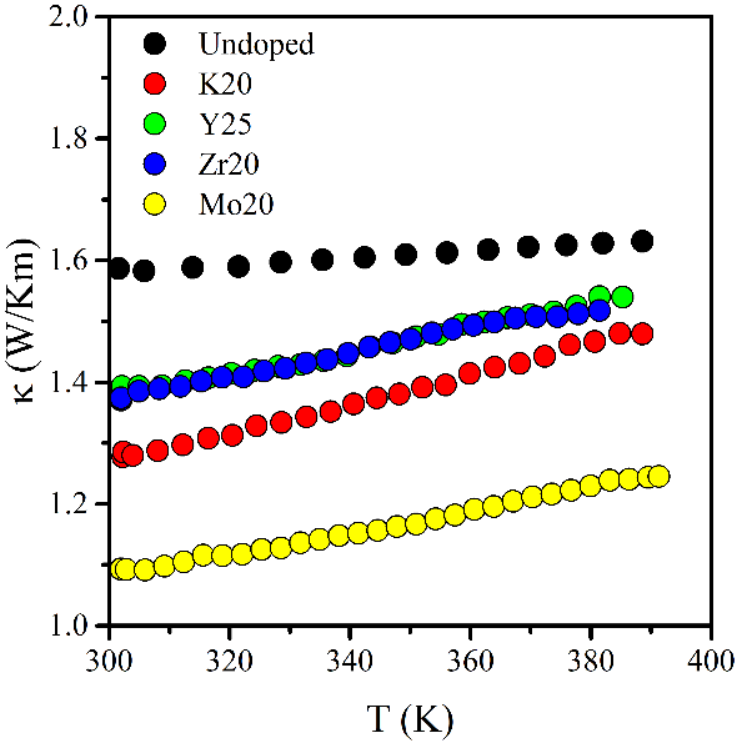

Figure 5-14 Thermal conductivity of doped and undoped SBN samples.

All the samples showed thermal conductivities that increased with temperature. In general, the κ of the doped samples were lower than in undoped samples, confirming the efficiency of the cation substitution in increasing the phonon scattering. The Mo-doped sample showed the lowest thermal conductivity (about 30% lower than the undoped sample).

The figure of merit (fig. 5-15) of the reduced SBN samples was calculated from room temperature to 573 K, extrapolating the thermal conductivity up to this temperature.

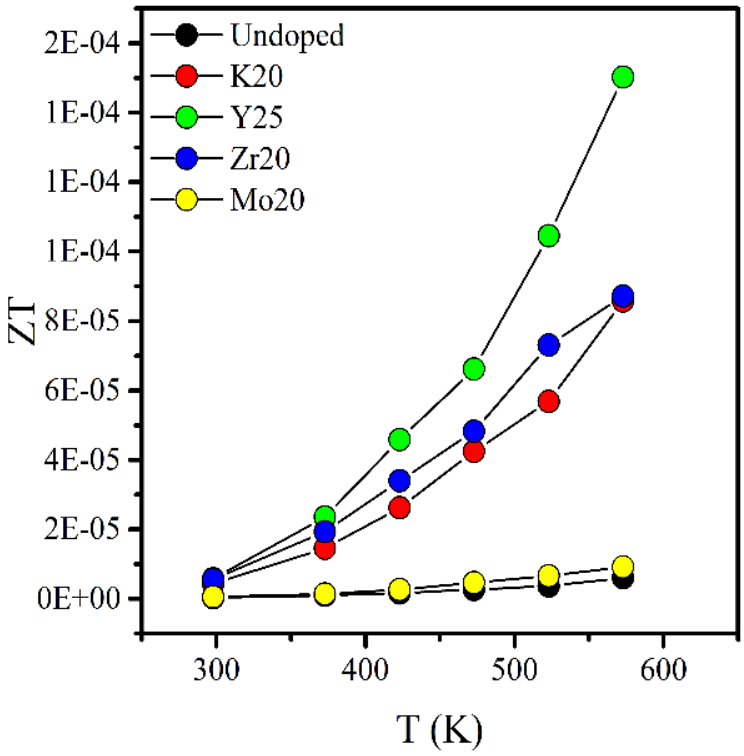

Figure 5-15 Figure of merit of doped and undoped SBN samples.

In the end, potassium and yttrium doping resulted the most performant material among the doped SBN sample, thus indicating that the substitution of strontium atoms was the best choice for increasing the thermoelectric properties of the strontium barium niobate. Substitution of niobium is only effective while using tetravalent zirconium, while the effect of the doping with molybdenum is quite negligible. In any case, as already said for the power factor and because of the limited increase of the electrical conductivity produced by both doping and reduction with HP-FAST, the highest calculated *ZT*'s achieved was around 10^{-4}, a non-competitive values if compared with other n-type oxides and with the other figures of merit of the SBN materials found in literature (around 0.025 at 573 K[179]).

5.3. Conclusions

Strontium barium niobate (SBN) have been synthesized with a solution/precipitation method in the Sr50/Ba50 composition. High levels of doping were investigated for the A sites, replacing Sr with K or Y (up to 40-50%), and for the B site, replacing Nb with 10% of Zr and Mo. The actual substitutions have been verified by XRD analysis and Rietveld refinements. Single phase products have been obtained for all the dopants, with the only exception of yttrium. In this case for x=0.25 peaks belonging to the $YNbO_4$ phase were observed and were quantified to be less than 10%. The chemical reduction of the powders was performed at 1273 K for 5 minutes by using the FAST apparatus as a mean to produce oxygen-poor environment. This strategy did not affect the phase purity of the powders with the only exception of the $YNbO_4$ phase in the Y-doped SBN, that was increased to 7.6% in the reduced powder. Substitution affected the lattice parameter in different ways. The width of the *ab* planes was controlled by the ion size for the substitution on the A sites, while it is almost independent from the nature of the dopant in the case of the substitution of niobium atoms. The *c* lattice parameter was affected only by grain size effect.XAS analysis showed that in all the samples the niobium remained as Nb(V) and that the intensity of the pre-edge peak was affected only by Y- and Zr-doping in a way that was largely unexpected. The thermoelectric properties of strontium barium niobate were confirmed to be strongly affected by the chemical reduction. The electrical conductivity increased by about eight orders of magnitude. The large doping didnot produce any further significant modification. The Seebeck coefficients were higher for the doped samples, thus leading to larger power factors, which were controlled mainly by the differences in σ rather than in S. The thermal conductivities were considerably decreased in the doped samples, due to the phonon-scattering effect of the substituent atoms. Finally, the figure of merit resulted generally improved in all the doped samples, with higher efficiencies achieved with K, Y and Zr, while substitution with molybdenum induced a limited increase in ZT. However, the doping strategy had no effect in increasing the stability of the reduction, since all the samples underwent a re-oxidation starting from 573 K in air, thus limiting the possible high temperature applications of the material.

6. Bibliography

[1] «Statistics». [In linea]. Available at: http://www.iea.org/statistics/.

[2] «Thermoelectric Seebeck | Thermocouple | Electrical Resistivity And Conductivity», *Scribd*. [In linea]. Available at: https://ar.scribd.com/document/249462234/Thermoelectric-Seebeck. [Consultato: 12-lug-2017].

[3] A. F. Ioffe, L. S. Stil'bans, E. K. Iordanishvili, T. S. Stavitskaya, A. Gelbtuch, e G. Vineyard, «Semiconductor Thermoelements and Thermoelectric Cooling», *Phys. Today*, gen. 2009.

[4] C. Dreßler, A. Bochmann, T. Schulz, T. Reimann, J. Töpfer, e S. Teichert, «Transversal Oxide-Metal Thermoelectric Device for Low-Power Energy Harvesting», *Energy Harvest. Syst.*, vol. 2, pag. 25, mar. 2015.

[5] G. J. Snyder e E. S. Toberer, «Complex thermoelectric materials», *Nat. Mater.*, vol. 7, n. 2, pagg. 105–114, feb. 2008.

[6] R. W. Keyes, «High-Temperature Thermal Conductivity of Insulating Crystals: Relationship to the Melting Point», *Phys. Rev.*, vol. 115, n. 3, pagg. 564–567, ago. 1959.

[7] P. Pichanusakorn e P. Bandaru, «Nanostructured thermoelectrics», *Mater. Sci. Eng. R Rep.*, vol. 67, n. 2, pagg. 19–63, gen. 2010.

[8] G. J. Snyder e E. S. Toberer, «Complex thermoelectric materials», *Nat. Mater.*, vol. 7, n. 2, pagg. 105–114, feb. 2008.

[9] D. M. Rowe, *CRC Handbook of Thermoelectrics*. CRC Press, 1995.

[10] D. G. Cahill, S. K. Watson, e R. O. Pohl, «Lower limit to the thermal conductivity of disordered crystals», *Phys. Rev. B*, vol. 46, n. 10, pagg. 6131–6140, set. 1992.

[11] Y. Li *et al.*, «Enhanced thermoelectric performance in rare-earth filled-skutterudites», *J. Mater. Chem. C*, vol. 4, n. 20, pagg. 4374–4379, 2016.

[12] S. Ballikaya e C. Uher, «Enhanced thermoelectric performance of optimized Ba, Yb filled and Fe substituted skutterudite compounds», *J. Alloys Compd.*, vol. 585, pagg. 168–172, feb. 2014.

[13] Y. Tang *et al.*, «Phase diagram of In–Co–Sb system and thermoelectric properties of In-containing skutterudites», *Energy Environ. Sci.*, vol. 7, n. 2, pagg. 812–819, 2014.

[14] B. Sun *et al.*, «Effect of High-Temperature and High-Pressure Processing on the Structure and Thermoelectric Properties of Clathrate Ba8Ga16Ge30», *J. Phys. Chem. C*, vol. 120, n. 18, pagg. 10104–10110, mag. 2016.

[15] B. Du, Y. Saiga, K. Kajisa, e T. Takabatake, «Thermoelectric Properties of p-Type Clathrate Ba8.0Ga15.9ZnySn30.1 Single Crystals with Various Carrier Concentrations», *Chem. Mater.*, vol. 27, n. 5, pagg. 1830–1836, mar. 2015.

[16] S. Chen, N. Logothetis, L. Ye, e J. Liu, «A High Performance Ag Alloyed Nano-scale n-type Bi2Te3 Based Thermoelectric Material», *Mater. Today Proc.*, vol. 2, n. 2, pagg. 610–619, gen. 2015.

[17] C. Zhang *et al.*, «Enhanced thermoelectric performance of solution-derived bismuth telluride based nanocomposites via liquid-phase Sintering», *Nano Energy*, vol. 30, pagg. 630–638, dic. 2016.

[18] Y. Zheng *et al.*, «Mechanically Robust BiSbTe Alloys with Superior Thermoelectric Performance: A Case Study of Stable Hierarchical Nanostructured Thermoelectric Materials», *Adv. Energy Mater.*, vol. 5, n. 5, pag. n/a-n/a, mar. 2015.

[19] L.-D. Zhao *et al.*, «Ultralow thermal conductivity and high thermoelectric figure of merit in SnSe crystals», *Nature*, vol. 508, n. 7496, pagg. 373–377, apr. 2014.

[20] H. Yakabe, K. Kikuchi, I. Terasaki, Y. Sasago, e K. Uchinokura, «Thermoelectric properties of transition-metal oxide NaCo2O4 system», in *XVI International Conference on Thermoelectrics, 1997. Proceedings ICT '97*, 1997, pagg. 523–527.

[21] International Conference on Thermoelectrics e D. M. Rowe, A c. di, *Proceedings of 19th international conference on thermoelectrics, (ICT 2000), Cardiff, UK 20-24th August 2000*. Wales: BABROW Press, 2000.

[22] L. Viciu *et al.*, «Crystal Structure and Elementary Properties of NaxCoO2 (x = 0.32, 0.5, 0.6, 0.75, and 0.92) in the Three-Layer NaCoO2 Family», *Phys. Rev. B*, vol. 73, n. 17, mag. 2006.

[23] M. Backhaus-Ricoult, J. Rustad, L. Moore, C. Smith, e J. Brown, «Semiconducting large bandgap oxides as potential thermoelectric materials for high-temperature power generation?», *Appl. Phys. A*, vol. 116, n. 2, pagg. 433–470, ago. 2014.

[24] J. Sun e D. J. Singh, «Thermoelectric properties of n-type SrTiO3», *APL Mater.*, vol. 4, n. 10, pag. 104803, mag. 2016.

[25] F. P. Zhang, Q. M. Lu, X. Zhang, e J. X. Zhang, «Electrical transport properties of CaMnO3 thermoelectric compound: a theoretical study», *J. Phys. Chem. Solids*, vol. 74, n. 12, pagg. 1859–1864, dic. 2013.

[26] F. Maglia, I. G. Tredici, e U. Anselmi-Tamburini, «Densification and properties of bulk nanocrystalline functional ceramics with grain size below 50nm», *J. Eur. Ceram. Soc.*, vol. 33, n. 6, pagg. 1045–1066, giu. 2013.

[27] J. Martin, T. Tritt, e C. Uher, «High temperature Seebeck coefficient metrology», *J. Appl. Phys.*, vol. 108, n. 12, pag. 121101, dic. 2010.

[28] S. Boldrini *et al.*, «Test Rig for High-Temperature Thermopower and Electrical Conductivity Measurements», *J. Electron. Mater.*, vol. 42, n. 7, pagg. 1319–1323, lug. 2013.

[29] E. Mun, S. L. Bud'ko, M. S. Torikachvili, e P. C. Canfield, «Experimental Setup for the Measurement of the Thermoelectric Power in Zero and Applied Magnetic Field», *Meas. Sci. Technol.*, vol. 21, n. 5, pag. 055104, mag. 2010.

[30] J. Martin, T. Tritt, e C. Uher, «High temperature Seebeck coefficient metrology», *J. Appl. Phys.*, vol. 108, n. 12, pag. 121101, dic. 2010.

[31] M. Shikano e R. Funahashi, «Electrical and thermal properties of single-crystalline (Ca2CoO3)0.7CoO2 with a Ca3Co4O9 structure», *Appl. Phys. Lett.*, vol. 82, n. 12, pagg. 1851–1853, mar. 2003.

[32] Q. M. Lu, J. X. Zhang, Q. Y. Zhang, Y. Q. Liu, e D. M. Liu, «Improved thermoelectric properties of Ca3-xBaxCo4O9 (x= 0∼ 0.4) bulks by sol-gel and SPS method», in *Thermoelectrics, 2006. ICT'06. 25th International Conference on*, 2006, pagg. 66–69.

[33] N. V. Nong, C.-J. Liu, e M. Ohtaki, «Improvement on the high temperature thermoelectric performance of Ga-doped misfit-layered Ca3Co4−xGaxO9+δ (x = 0, 0.05, 0.1, and 0.2)», *J. Alloys Compd.*, vol. 491, n. 1–2, pagg. 53–56, feb. 2010.

[34] N. V. Nong, S. Yanagiya, S. Monica, N. Pryds, e M. Ohtaki, «High-Temperature Thermoelectric and Microstructural Characteristics of Cobalt-Based Oxides with Ga Substituted on the Co-Site», *J. Electron. Mater.*, vol. 40, n. 5, pagg. 716–722, mag. 2011.

[35] J. Pei, G. Chen, N. Zhou, D. Q. Lu, e F. Xiao, «High temperature transport and thermoelectric properties of Ca3−xErxCo4O9+δ», *Phys. B Condens. Matter*, vol. 406, n. 3, pagg. 571–574, feb. 2011.

[36] Y. Miyazaki *et al.*, «Modulated Structure of the Thermoelectric Compound [Ca2CoO3]0.62CoO2», *J. Phys. Soc. Jpn.*, vol. 71, n. 2, pagg. 491–497, 2002.

[37] S. Lambert, H. Leligny, e D. Grebille, «Three Forms of the Misfit Layered Cobaltite [Ca2CoO3] [CoO2]1.62·A 4D Structural Investigation», *J. Solid State Chem.*, vol. 160, n. 2, pagg. 322–331, set. 2001.

[38] T. Wu, T. A. Tyson, H. Chen, J. Bai, H. Wang, e C. Jaye, «A structural change in Ca 3 Co 4 O 9 associated with enhanced thermoelectric properties», *J. Phys. Condens. Matter*, vol. 24, n. 45, pag. 455602, 2012.

[39] Y. Huang *et al.*, «Enhanced Electron Correlation in the In-doped Misfit-Layered Cobaltite Ca3Co4O9 Ceramics», *J. Am. Ceram. Soc.*, vol. 96, n. 3, pagg. 791–797, mar. 2013.

[40] R. F. Klie *et al.*, «Observations of Co4þ in a Higher Spin State and the Increase in the Seebeck Coefficient of Thermoelectric Ca3Co4O9», *Phys. Rev. Lett.*, vol. 108, n. 19, pag. 196601, mag. 2012.

[41] D. Kenfaui *et al.*, «Volume Texture and Anisotropic Thermoelectric Properties in Ca3Co4O9 Bulk Materials», *Mater. Today Proc.*, vol. 2, n. 2, pagg. 637–646, gen. 2015.

[42] D. Kenfaui, D. Chateigner, M. Gomina, e J. G. Noudem, «Anisotropy of the Mechanical and Thermoelectric Properties of Hot-Pressed Single-Layer and Multilayer Thick Ca3Co4O9 Ceramics», *Int. J. Appl. Ceram. Technol.*, vol. 8, n. 1, pagg. 214–226, gen. 2011.

[43] A. Sakai, T. Kanno, S. Yotsuhashi, A. Odagawa, e H. Adachi, «Control of epitaxial growth orientation and anisotropic thermoelectric properties of misfit-type Ca3Co4O9 thin films», *Jpn. J. Appl. Phys.*, vol. 44, n. 7L, pag. L966, 2005.

[44] W. Koshibae, K. Tsutsui, e S. Maekawa, «Thermopower in cobalt oxides», *Phys. Rev. B*, vol. 62, n. 11, pagg. 6869–6872, set. 2000.

[45] S. Saini, H. S. Yaddanapudi, K. Tian, Y. Yin, D. Magginetti, e A. Tiwari, «Terbium Ion Doping in Ca3Co4O9: A Step towards High-Performance Thermoelectric Materials», *Sci. Rep.*, vol. 7, mar. 2017.

[46] G. KIirat, M. A. Aksan, S. Rasekh, M. A. Madre, J. C. Diez, e A. Sotelo, «Decrease of Ca3Co4O9+δ thermal conductivity by Yb-doping», *Ceram. Int.*, vol. 41, n. 10, pagg. 12529–12534, dic. 2015.

[47] T. Zhu e J. M. Zhou, «Effect of Ho Doping on the High-Temperature Thermoelectric Properties of Ca3Co4O9-Based Oxides», *Adv. Mater. Res.*, vol. 228–229, pagg. 947–950, 2011.

[48] G. D. Tang, Z. H. Wang, X. N. Xu, L. Qiu, L. Xing, e Y. W. Du, «Thermoelectric properties of Ca3Co4O9+δ with Lu substitution», *J. Mater. Sci.*, vol. 45, n. 15, pagg. 3969–3973, ago. 2010.

[49] Y. Wang, Y. Sui, J. Cheng, X. Wang, e W. Su, «Comparison of the high temperature thermoelectric properties for Ag-doped and Ag-added Ca3Co4O9», *J. Alloys Compd.*, vol. 477, n. 1, pagg. 817–821, mag. 2009.

[50] Y. Huang, B. Zhao, S. Lin, R. Ang, W. Song, e Y. Sun, «Strengthening of Thermoelectric Performance via Ir Doping in Layered Ca3Co4O9 System», *J. Am. Ceram. Soc.*, vol. 97, n. 3, pagg. 798–804, mar. 2014.

[51] M. Presečnik e S. Bernik, «Microstructural and thermoelectric properties of WO3-doped Ca3Co4O9 ceramics», *Ceram. Int.*, vol. 42, n. 14, pagg. 16103–16108, nov. 2016.

[52] M. A. Torres *et al.*, «Decrease of electrical resistivity in Ca3Co4O9 thermoelectric ceramics by Ti doping», *J. Mater. Sci. Mater. Electron.*, vol. 26, n. 2, pagg. 815–820, feb. 2015.

[53] Y. Fu, S. Lin, Y. Huang, R. Shi, e B. Zhao, «Cr6+ ion doping effects in layered Ca3Co4O9 system», *J. Alloys Compd.*, vol. 613, pagg. 87–92, nov. 2014.

[54] Y. Huang, B. Zhao, S. Lin, R. Ang, e Y. Sun, «Enhanced Thermoelectric Performance Induced by Cr Doping at Ca-Sites in Ca3Co4O9 System», *J. Am. Ceram. Soc.*, vol. 97, n. 11, pagg. 3589–3596, nov. 2014.

[55] D. Zhang, X. Mi, Z. Wang, G. Tang, e Q. Wu, «Suppression of the spin entropy in layered cobalt oxide Ca3Co4O9+δ by Cu doping», *Ceram. Int.*, vol. 40, n. 8, pagg. 12313–12318, set. 2014.

[56] S. Butt *et al.*, «Enhancement of thermoelectric performance in Cd-doped Ca 3 Co 4 O 9 via spin entropy, defect chemistry and phonon scattering», *J. Mater. Chem. A*, vol. 2, n. 45, pagg. 19479–19487, 2014.

[57] G. Constantinescu *et al.*, «Effect of Na doping on the Ca3Co4O9 thermoelectric performance», *Ceram. Int.*, vol. 41, n. 9, pagg. 10897–10903, nov. 2015.

[58] G. Constantinescu, S. Rasekh, M. A. Torres, M. A. Madre, A. Sotelo, e J. C. Diez, «Improvement of thermoelectric properties in Ca3Co4O9 ceramics by Ba doping», *J. Mater. Sci. Mater. Electron.*, vol. 26, n. 6, pagg. 3466–3473, giu. 2015.

[59] G. Constantinescu, S. Rasekh, M. A. Torres, J. C. Diez, M. A. Madre, e A. Sotelo, «Effect of Sr substitution for Ca on the Ca3Co4O9 thermoelectric properties», *J. Alloys Compd.*, vol. 577, pagg. 511–515, nov. 2013.

[60] G. Constantinescu *et al.*, «Influence of Ca substitution by Mg on the Ca3Co4O9 performances», 2014.

[61] S. Porokhin, L. Shvanskaya, V. Khovaylo, e A. Vasiliev, «Effect of NaF doping on the thermoelectric properties of Ca3Co4O9», *J. Alloys Compd.*, vol. 695, pagg. 2844–2849, feb. 2017.

[62] W. Yang, H. Qian, J. Gan, W. Wei, Z. Wang, e G. Tang, «Effects of Lu and Ni Substitution on Thermoelectric Properties of Ca3Co4O9+δ», *J. Electron. Mater.*, vol. 45, n. 8, pagg. 4171–4176, ago. 2016.

[63] D. W. Zhang, X. N. Mi, Y. H. Zhang, Q. S. Wu, e Y. C. Bao, «Effects of Eu and Fe co-doping on thermoelectric properties of misfit-layered Ca3Co4O9+δ», *J. Mater. Sci. Mater. Electron.*, vol. 26, n. 10, pagg. 7490–7495, ott. 2015.

[64] N. Wu, N. Van Nong, N. Pryds, e S. Linderoth, «Effects of Yttrium and Iron co-doping on the high temperature thermoelectric properties of Ca3Co4O9+δ», *J. Alloys Compd.*, vol. 638, pagg. 127–132, lug. 2015.

[65] R. Tian, T. Zhang, D. Chu, R. Donelson, L. Tao, e S. Li, «Enhancement of high temperature thermoelectric performance in Bi, Fe co-doped layered oxide-based material Ca3Co4O9+δ», *J. Alloys Compd.*, vol. 615, pagg. 311–315, dic. 2014.

[66] C. S. Huang, F. P. Zhang, X. Zhang, Q. M. Lu, J. X. Zhang, e Z. Y. Liu, «Enhanced thermoelectric figure of merit through electrical and thermal transport modulation by dual-doping and texture modulating for Ca3Co4O9+δ oxide materials», *J. Alloys Compd.*, vol. 687, pagg. 87–94, dic. 2016.

[67] Y. Zhang, J. Zhang, e Q. Lu, «Synthesis of highly textured Ca3Co4O9 ceramics by spark plasma sintering», *Ceram. Int.*, vol. 33, n. 7, pagg. 1305–1308, set. 2007.

[68] J. G. Noudem, «A new process for lamellar texturing of thermoelectric Ca3Co4O9 oxides by spark plasma sintering», *J. Eur. Ceram. Soc.*, vol. 29, n. 12, pagg. 2659–2663, set. 2009.

[69] M. Prevel *et al.*, «Textured Ca3Co4O9 thermoelectric oxides by thermoforging process», *J. Appl. Phys.*, vol. 98, n. 9, pag. 093706, nov. 2005.

[70] C.-H. Lim *et al.*, «Anisotropy of the thermoelectric figure of merit (ZT) in textured Ca3Co4O9 ceramics prepared by using a spark plasma sintering process», *J. Korean Phys. Soc.*, vol. 66, n. 5, pagg. 794–799, mar. 2015.

[71] T. Yin *et al.*, «Nanocrystalline Thermoelectric Ca3Co4O9 Ceramics by Sol−Gel Based Electrospinning and Spark Plasma Sintering», *J. Phys. Chem. C*, vol. 114, n. 21, pagg. 10061–10065, giu. 2010.

[72] S. Butt *et al.*, «Enhancement of Thermoelectric Performance in Hierarchical Mesoscopic Oxide Composites of Ca3Co4O9 and La0.8Sr0.2CoO3», *J. Am. Ceram. Soc.*, vol. 98, n. 4, pagg. 1230–1235, apr. 2015.

[73] W. W. Sun, W. H. Fan, S. P. Chen, Y. Y. Li, e Q. S. Meng, «The Effect of Nano-SiO2 Addition on Electrical Properties of the Thermoelectric Compound Ca3Co4O9», *Adv. Mater. Res.*, vol. 465, pagg. 292–295, 2012.

[74] C. Chen *et al.*, «Thermopower and chemical stability of Na0.77CoO2/Ca3Co4O9 composites», *Acta Mater.*, vol. 63, pagg. 99–106, gen. 2014.

[75] F. Delorme, P. Diaz-Chao, E. Guilmeau, e F. Giovannelli, «Thermoelectric properties of Ca3Co4O9–Co3O4 composites», *Ceram. Int.*, vol. 41, n. 8, pagg. 10038–10043, set. 2015.

[76] G. Tang, W. Yang, J. Wen, Z. Wu, C. Fan, e Z. Wang, «Ultralow thermal conductivity and thermoelectric properties of carbon nanotubes doped Ca3Co4O9+δ», *Ceram. Int.*, vol. 41, n. 1, pagg. 961–965, gen. 2015.

[77] C. Liu, F. Jiang, M. Huang, B. Lu, R. Yue, e J. Xu, «Free-Standing PEDOT-PSS/Ca3Co4O9 Composite Films as Novel Thermoelectric Materials», *J. Electron. Mater.*, vol. 40, n. 5, pagg. 948–952, mag. 2011.

[78] B. Zheng, Y. Lin, J. Lan, e X. Yang, «Thermoelectric Properties of Ca3Co4O9/Polyaniline Composites», *J. Mater. Sci. Technol.*, vol. 30, n. 4, pagg. 423–426, apr. 2014.

[79] C. D. Ling, K. Aivazian, S. Schmid, e P. Jensen, «Structural investigation of oxygen non-stoichiometry and cation doping in misfit-layered thermoelectric (Ca2CoO3−x)(CoO2)δ, δ≈1.61», *J. Solid State Chem.*, vol. 180, n. 4, pagg. 1446–1455, apr. 2007.

[80] «Oxygen Nonstoichiometry in Layered Cobaltite Ca3Co4Oy», *Jpn. J. Appl. Phys.*, vol. 42, n. 2B, pag. L194, feb. 2003.

[81] M. Karppinen, H. Fjellvåg, T. Konno, Y. Morita, T. Motohashi, e H. Yamauchi, «Evidence for Oxygen Vacancies in Misfit-Layered Calcium Cobalt Oxide, [CoCa2O3]qCoO2», *Chem. Mater.*, vol. 16, n. 14, pagg. 2790–2793, lug. 2004.

[82] D. Moser, L. Karvonen, S. Populoh, M. Trottmann, e A. Weidenkaff, «Influence of the oxygen content on thermoelectric properties of Ca3−xBixCo4O9+δ system», *Solid State Sci.*, vol. 13, n. 12, pagg. 2160–2164, dic. 2011.

[83] M. Schrade, H. Fjeld, T. G. Finstad, e T. Norby, «Electronic Transport Properties of [Ca2CoO3−δ]q[CoO2]», *J. Phys. Chem. C*, vol. 118, n. 6, pagg. 2908–2918, feb. 2014.

[84] S. Urata, R. Funahashi, T. Mihara, A. Kosuga, S. Sodeoka, e T. Tanaka, «Power Generation of a p-Type Ca3Co4O9/n-Type CaMnO3 Module», *Int. J. Appl. Ceram. Technol.*, vol. 4, n. 6, pagg. 535–540, dic. 2007.

[85] I. Matsubara, R. Funahashi, T. Takeuchi, S. Sodeoka, T. Shimizu, e K. Ueno, «Fabrication of an all-oxide thermoelectric power generator», *Appl. Phys. Lett.*, vol. 78, n. 23, pagg. 3627–3629, mag. 2001.

[86] K. Park e G. W. Lee, «Fabrication and thermoelectric power of π-shaped Ca3Co4O9/CaMnO3 modules for renewable energy conversion», *Energy*, vol. 60, pagg. 87–93, ott. 2013.

[87] J. G. Noudem, S. Lemonnier, M. Prevel, E. S. Reddy, E. Guilmeau, e C. Goupil, «Thermoelectric ceramics for generators», *J. Eur. Ceram. Soc.*, vol. 28, n. 1, pagg. 41–48, gen. 2008.

[88] C.-H. Lim, S.-M. Choi, W.-S. Seo, e H.-H. Park, «A Power-Generation Test for Oxide-Based Thermoelectric Modules Using p-Type Ca3Co4O9 and n-Type Ca0.9Nd0.1MnO3 Legs», *J. Electron. Mater.*, vol. 41, n. 6, pagg. 1247–1255, giu. 2012.

[89] M. Bittner, B. Geppert, N. Kanas, S. P. Singh, K. Wiik, e A. Feldhoff, «Oxide-Based Thermoelectric Generator for High-Temperature Application Using p-Type Ca3Co4O9 and n-Type In1.95Sn0.05O3 Legs», *Energy Harvest. Syst.*, vol. 3, n. 3, pagg. 213–222, 2016.

[90] S.-M. Choi, K.-H. Lee, C.-H. Lim, e W.-S. Seo, «Oxide-based thermoelectric power generation module using p-type Ca3Co4O9 and n-type (ZnO)7In2O3 legs», *Energy Convers. Manag.*, vol. 52, n. 1, pagg. 335–339, gen. 2011.

[91] L. R. Pederson, G. D. Maupin, W. J. Weber, D. J. McReady, e R. W. Stephens, «Combustion synthesis of YBa2Cu3O7−x: glycine/metal nitrate method», *Mater. Lett.*, vol. 10, n. 9, pagg. 437–443, feb. 1991.

[92] N. Wu, T. C. Holgate, N. Van Nong, N. Pryds, e S. Linderoth, «High temperature thermoelectric properties of Ca3Co4O9+δ by auto-combustion synthesis and spark plasma sintering», *J. Eur. Ceram. Soc.*, vol. 34, n. 4, pagg. 925–931, apr. 2014.

[93] D.-W. Kim, Y.-D. Ko, J.-G. Park, e B.-K. Kim, «Formation of lithium-driven active/inactive nanocomposite electrodes based on Ca3Co4O9 nanoplates», *Angew. Chem. Int. Ed Engl.*, vol. 46, n. 35, pagg. 6654–6657, 2007.

[94] Y. F. Zhang, J. X. Zhang, Q. M. Lu, e Q. Y. Zhang, «Synthesis and characterization of Ca3Co4O9 nanoparticles by citrate sol-gel method», *Mater. Lett.*, vol. 60, n. 20, pagg. 2443–2446, set. 2006.

[95] M. Gunes e M. Ozenbas, «Effect of grain size and porosity on phonon scattering enhancement of Ca3Co4O9», *J. Alloys Compd.*, vol. 626, pagg. 360–367, mar. 2015.

[96] A. Sotelo *et al.*, «Tailoring Ca3Co4O9 microstructure and performances using a transient liquid phase sintering additive», *J. Eur. Ceram. Soc.*, vol. 36, n. 4, pagg. 1025–1032, mar. 2016.

[97] G. Xu, R. Funahashi, M. Shikano, I. Matsubara, e Y. Zhou, «Thermoelectric properties of the Bi- and Na-substituted Ca3Co4O9 system», *Appl. Phys. Lett.*, vol. 80, n. 20, pagg. 3760–3762, mag. 2002.

[98] Y. Zhou *et al.*, «Thermoelectric properties of highly grain-aligned and densified Co-based oxide ceramics», *J. Appl. Phys.*, vol. 93, n. 5, pagg. 2653–2658, mar. 2003.

[99] Y.-H. Lin, C.-W. Nan, Y. Liu, J. Li, T. Mizokawa, e Z. Shen, «High-Temperature Electrical Transport and Thermoelectric Power of Partially Substituted Ca3Co4O9-Based Ceramics», *J. Am. Ceram. Soc.*, vol. 90, n. 1, pagg. 132–136, gen. 2007.

[100] T. Takeuchi *et al.*, «Contribution of electronic structure to the large thermoelectric power in layered cobalt oxides», *Phys. Rev. B*, vol. 69, n. 12, pag. 125410, mar. 2004.

[101] Y. Liu, Y. Lin, Z. Shi, C.-W. Nan, e Z. Shen, «Preparation of Ca3Co4O9 and Improvement of its Thermoelectric Properties by Spark Plasma Sintering», *J. Am. Ceram. Soc.*, vol. 88, n. 5, pagg. 1337–1340, mag. 2005.

[102] Y. Song e C.-W. Nan, «Preparation of Ca3Co4O9 by polyacrylamide gel processing and its thermoelectric properties», *J. Sol-Gel Sci. Technol.*, vol. 44, n. 2, pagg. 139–144, nov. 2007.

[103] T. Jiang e D. E. Ellis, «X-ray absorption near edge structures in cobalt oxides», *J. Mater. Res.*, vol. 11, n. 9, pagg. 2242–2256, set. 1996.

[104] A. C. Masset *et al.*, «Misfit-layered cobaltite with an anisotropic giant magnetoresistance: Ca3Co4O9», *Phys. Rev. B*, vol. 62, n. 1, pagg. 166–175, lug. 2000.

[105] «Oxidation state and coordination of Fe in minerals: An Fe K-XANES spectroscopic study : American Mineralogist», 01-mag-2001. [In linea]. Available at: https://www.degruyter.com/view/j/ammin.2001.86.issue-5-6/am-2001-5-612/am-2001-5-612.xml.

[106] X. Guo, «Can we achieve significantly higher ionic conductivity in nanostructured zirconia?», *Scr. Mater.*, vol. 65, n. 2, pagg. 96–101, lug. 2011.

[107] H. Wang *et al.*, «Fabrication and thermoelectric properties of highly textured Ca9Co12O28 ceramic», *J. Alloys Compd.*, vol. 582, n. Supplement C, pagg. 294–298, gen. 2014.

[108] H. Ohta *et al.*, «Giant thermoelectric Seebeck coefficient of a two-dimensional electron gas in SrTiO3», *Nat. Mater. Lond.*, vol. 6, n. 2, pagg. 129–34, feb. 2007.

[109] O.-J. Kwon *et al.*, «Thermoelectric properties and texture evaluation of Ca3Co4O9 prepared by a cost-effective multisheet cofiring technique», *J. Mater. Sci.*, vol. 46, n. 9, pagg. 2887–2894, mag. 2011.

[110] J. W. Fergus, «Oxide materials for high temperature thermoelectric energy conversion», *J. Eur. Ceram. Soc.*, vol. 32, n. 3, pagg. 525–540, mar. 2012.

[111] Y. Wang *et al.*, «High temperature transport and thermoelectric properties of Ag-substituted Ca3Co4O9+δ system», *J. Alloys Compd.*, vol. 448, n. 1, pagg. 1–5, gen. 2008.

[112] D. Sedmidubský, V. Jakeš, O. Jankovský, J. Leitner, Z. Sofer, e J. Hejtmánek, «Phase equilibria in Ca–Co–O system», *J. Solid State Chem.*, vol. 194, pagg. 199–205, ott. 2012.

[113] H. Münstedt e Z. Starý, «Is electrical percolation in carbon-filled polymers reflected by rheological properties?», *Polymer*, vol. 98, pagg. 51–60, ago. 2016.

[114] D. Narducci, S. Frabboni, e X. Zianni, «Silicon de novo: energy filtering and enhanced thermoelectric performances of nanocrystalline silicon and silicon alloys», *J. Mater. Chem. C*, vol. 3, n. 47, pagg. 12176–12185, nov. 2015.

[115] R. Kumar, O. Al-Dossary, G. Kumar, e A. Umar, «Zinc Oxide Nanostructures for NO2 Gas–Sensor Applications: A Review», *Nano-Micro Lett.*, vol. 7, n. 2, pagg. 97–120, apr. 2015.

[116] A. Janotti e C. G. Van de Walle, «Oxygen vacancies in ZnO», *Appl. Phys. Lett.*, vol. 87, n. 12, pag. 122102, set. 2005.

[117] A. Janotti e C. G. Van de Walle, «Native point defects in ZnO», *Phys. Rev. B*, vol. 76, n. 16, pag. 165202, ott. 2007.

[118] A. Janotti e C. G. Van de Walle, «Hydrogen multicentre bonds», *Nat. Mater.*, vol. 6, n. 1, pagg. 44–47, gen. 2007.

[119] O. Lupan *et al.*, «Hybridization of Zinc Oxide Tetrapods for Selective Gas Sensing Applications», *ACS Appl. Mater. Interfaces*, vol. 9, n. 4, pagg. 4084–4099, feb. 2017.

[120] M. S. Wagh, G. H. Jain, D. R. Patil, S. A. Patil, e L. A. Patil, «Modified zinc oxide thick film resistors as NH3 gas sensor», *Sens. Actuators B Chem.*, vol. 115, n. 1, pagg. 128–133, mag. 2006.

[121] S. Ben Dkhil *et al.*, «P-type semiconductor surfactant modified zinc oxide nanorods for hybrid bulk heterojunction solar cells», *Sol. Energy Mater. Sol. Cells*, vol. 159, pagg. 608–616, gen. 2017.

[122] W. J. E. Beek, M. M. Wienk, e R. a. J. Janssen, «Efficient Hybrid Solar Cells from Zinc Oxide Nanoparticles and a Conjugated Polymer», *Adv. Mater.*, vol. 16, n. 12, pagg. 1009–1013, giu. 2004.

[123] Z. L. Wang e J. Song, «Piezoelectric Nanogenerators Based on Zinc Oxide Nanowire Arrays», *Science*, vol. 312, n. 5771, pagg. 242–246, apr. 2006.

[124] A. A. M. Ralib, O. Mortada, J. C. Orlianges, A. Crunteanu, M. Chatras, e A. N. Nordin, «Enhanced piezoelectric properties of aluminium doped zinc oxide thin film for surface acoustic wave resonators on a CMOS platform», *J. Mater. Sci. Mater. Electron.*, vol. 28, n. 12, pagg. 9132–9138, giu. 2017.

[125] K. P. Ong, D. J. Singh, e P. Wu, «Analysis of the thermoelectric properties of n-type ZnO», *Phys. Rev. B*, vol. 83, n. 11, pag. 115110, mar. 2011.

[126] M. Ohtaki, T. Tsubota, K. Eguchi, e H. Arai, «High-temperature thermoelectric properties of (Zn1−xAlx)O», *J. Appl. Phys.*, vol. 79, n. 3, pagg. 1816–1818, feb. 1996.

[127] T. Tsubota, M. Ohtaki, K. Eguchi, e H. Arai, «Thermoelectric properties of Al-doped ZnO as a promising oxide material for high-temperature thermoelectric conversion», *J. Mater. Chem.*, vol. 7, n. 1, pagg. 85–90, 1997.

[128] H. Cheng, X. J. Xu, H. H. Hng, e J. Ma, «Characterization of Al-doped ZnO thermoelectric materials prepared by RF plasma powder processing and hot press sintering», *Ceram. Int.*, vol. 35, n. 8, pagg. 3067–3072, dic. 2009.

[129] H. Serier, M. Gaudon, e M. Ménétrier, «Al-doped ZnO powdered materials: Al solubility limit and IR absorption properties», *Solid State Sci.*, vol. 11, n. 7, pagg. 1192–1197, lug. 2009.

[130] «ALUMINUM-CONTAINING ZINC OXIDE-BASED n-TYPE THERMOELECTRIC CONVERSION MATERIAL».

[131] M. Ohtaki, K. Araki, e K. Yamamoto, «High Thermoelectric Performance of Dually Doped ZnO Ceramics», *J. Electron. Mater.*, vol. 38, n. 7, pagg. 1234–1238, lug. 2009.

[132] L. Brockway, V. Vasiraju, M. K. Sunkara, e S. Vaddiraju, «Engineering Efficient Thermoelectrics from Large-Scale Assemblies of Doped ZnO Nanowires: Nanoscale Effects and Resonant-Level Scattering», *ACS Appl. Mater. Interfaces*, vol. 6, n. 17, pagg. 14923–14930, set. 2014.

[133] P. Jood *et al.*, «Al-Doped Zinc Oxide Nanocomposites with Enhanced Thermoelectric Properties», *Nano Lett.*, vol. 11, n. 10, pagg. 4337–4342, ott. 2011.

[134] D. Chen *et al.*, «One-Step Chemical Synthesis of ZnO/Graphene Oxide Molecular Hybrids for High-Temperature Thermoelectric Applications», *ACS Appl. Mater. Interfaces*, vol. 7, n. 5, pagg. 3224–3230, feb. 2015.

[135] J. Bang, Y.-S. Kim, C. H. Park, F. Gao, e S. B. Zhang, «Understanding the presence of vacancy clusters in ZnO from a kinetic perspective», *Appl. Phys. Lett.*, vol. 104, n. 25, pag. 252101, giu. 2014.

[136] K. Tang, S.-L. Gu, J.-D. Ye, S.-M. Zhu, R. Zhang, e Y.-D. Zheng, «Recent progress of the native defects and p-type doping of zinc oxide», *Chin. Phys. B*, vol. 26, n. 4, pag. 047702, 2017.

[137] C. H. Park, S. B. Zhang, e S.-H. Wei, «Origin of p-type doping difficulty in ZnO: The impurity perspective», *Phys. Rev. B*, vol. 66, n. 7, pag. 073202, ago. 2002.

[138] P. J. M. Isherwood, «Copper zinc oxide: Investigation into a p-type mixed metal oxide system», *Vacuum*, vol. 139, pagg. 173–177, mag. 2017.

[139] H. D. Zhang *et al.*, «Fabrication and photoelectric properties of La-doped p-type ZnO nanofibers and crossed p–n homojunctions by electrospinning», *Nanoscale*, vol. 7, n. 23, pagg. 10513–10518, 2015.

[140] M. Norouzi *et al.*, «Thermoelectric energy harvesting using array of vertically aligned Al-doped ZnO nanorods», *Thin Solid Films*, vol. 619, pagg. 41–47, nov. 2016.

[141] S. Dalola *et al.*, «Seebeck effect in ZnO nanowires for micropower generation», *Procedia Eng.*, vol. 25, pagg. 1481–1484, gen. 2011.

[142] S. Dai, M. L. Dunn, e H. S. Park, «Piezoelectric constants for ZnO calculated using classical polarizable core–shell potentials», *Nanotechnology*, vol. 21, n. 44, pag. 445707, 2010.

[143] Z. L. Wang *et al.*, «Semiconducting and Piezoelectric Oxide Nanostructures Induced by Polar Surfaces», *Adv. Funct. Mater.*, vol. 14, n. 10, pagg. 943–956, ott. 2004.

[144] I. G. Tredici, A. Resmini, F. Yaghmaie, M. Irving, F. Maglia, e U. Anselmi-Tamburini, «A simple two-step solution chemistry method for synthesis of micropatterned ZnO nanorods based on metal-loaded hydrogels», *Thin Solid Films*, vol. 526, pagg. 22–27, dic. 2012.

[145] L. Vayssieres, K. Keis, S.-E. Lindquist, e A. Hagfeldt, «Purpose-Built Anisotropic Metal Oxide Material: 3D Highly Oriented Microrod Array of ZnO», *J. Phys. Chem. B*, vol. 105, n. 17, pagg. 3350–3352, mag. 2001.

[146] I. G. Tredici *et al.*, «Mechanisms of Zinc Oxide Nanocrystalline Thin Film Formation by Thermal Degradation of Metal-Loaded Hydrogels», *J. Phys. Chem. C*, vol. 117, n. 47, pagg. 25108–25117, nov. 2013.

[147] A. Resmini *et al.*, «A simple all-solution approach to the synthesis of large ZnO nanorod networks», *J. Mater. Chem. A*, vol. 3, n. 8, pagg. 4568–4577, 2015.

[148] N. C. Lindquist, P. Nagpal, K. M. McPeak, D. J. Norris, e S.-H. Oh, «Engineering metallic nanostructures for plasmonics and nanophotonics», *Rep. Prog. Phys.*, vol. 75, n. 3, pag. 036501, 2012.

[149] H. L. Cao, X. F. Qian, Q. Gong, W. M. Du, X. D. Ma, e Z. K. Zhu, «Shape- and size-controlled synthesis of nanometre ZnO from a simple solution route at room temperature», *Nanotechnology*, vol. 17, n. 15, pag. 3632, 2006.

[150] K. Govender, D. S. Boyle, P. B. Kenway, e P. O'Brien, «Understanding the factors that govern the deposition and morphology of thin films of ZnO from aqueous solution», *J. Mater. Chem.*, vol. 14, n. 16, pagg. 2575–2591, 2004.

[151] I. S. Ahuja, C. L. Yadava, e R. Singh, «STructural information on manganese(II), cobalt(II), nickeL(II), zinC(II) and cadmium(II) sulphate complexes with hexamethylenetetramine (a potentially tetradentate ligand) from their magnetic moments, electronic and infrared spectra», *J. Mol. Struct.*, vol. 81, n. 3, pagg. 229–234, mag. 1982.

[152] S. Baruah e J. Dutta, «Hydrothermal growth of ZnO nanostructures», *Sci. Technol. Adv. Mater.*, vol. 10, n. 1, pag. 013001, 2009.

[153] J. Song e S. Lim, «Effect of Seed Layer on the Growth of ZnO Nanorods», *J. Phys. Chem. C*, vol. 111, n. 2, pagg. 596–600, gen. 2007.

[154] T. A. N. Peiris, H. Alessa, J. S. Sagu, I. A. Bhatti, P. Isherwood, e K. G. U. Wijayantha, «Effect of ZnO seed layer thickness on hierarchical ZnO nanorod growth on flexible substrates for application in dye-sensitised solar cells», *J. Nanoparticle Res.*, vol. 15, n. 12, pag. 2115, dic. 2013.

[155] M. Ding, D. Zhao, B. Yao, B. Li, Z. Zhang, e D. Shen, «The p-type ZnO film realized by a hydrothermal treatment method», *Appl. Phys. Lett.*, vol. 98, n. 6, pag. 062102, feb. 2011.

[156] J. Huang, Z. Ye, H. Chen, B. Zhao, e L. Wang, «Growth of N-doped p-type ZnO films using ammonia as dopant source gas», *J. Mater. Sci. Lett.*, vol. 22, n. 4, pagg. 249–251, feb. 2003.

[157] J. Bang, Y.-Y. Sun, D. West, B. K. Meyer, e S. Zhang, «Molecular doping of ZnO by ammonia: a possible shallow acceptor», *J. Mater. Chem. C*, vol. 3, n. 2, pagg. 339–344, dic. 2014.

[158] N. M. Vuong *et al.*, «H2- and NH3-treated ZnO nanorods sensitized with CdS for photoanode enhanced in photoelectrochemical performance», *J. Power Sources*, vol. 317, pagg. 169–176, giu. 2016.

[159] P. Mele *et al.*, «Effect of substrate on thermoelectric properties of Al-doped ZnO thin films», *Appl. Phys. Lett.*, vol. 102, n. 25, pag. 253903, giu. 2013.

[160] «KOH Etching of Silicon wafers, Silicon Dioxide (SiO2) and Silicon Nitride (SiN)». [In linea]. Available at: http://www.cleanroom.byu.edu/KOH.phtml. [Consultato: 27-giu-2017].

[161] K.-K. Kim, H.-S. Kim, D.-K. Hwang, J.-H. Lim, e S.-J. Park, «Realization of p-type ZnO thin films via phosphorus doping and thermal activation of the dopant», *Appl. Phys. Lett.*, vol. 83, n. 1, pagg. 63–65, giu. 2003.

[162] J. G. Reynolds *et al.*, «Shallow acceptor complexes in p-type ZnO», *Appl. Phys. Lett.*, vol. 102, n. 15, pag. 152114, apr. 2013.

[163] R. Thangavel e Y.-C. Chang, «Investigations on structural, optical and electrical properties of p-type ZnO nanorods using hydrothermal method», *Thin Solid Films*, vol. 520, n. 7, pagg. 2589–2593, gen. 2012.

[164] Y. Yang *et al.*, «Thermoelectric Nanogenerators Based on Single Sb-Doped ZnO Micro/Nanobelts», *ACS Nano*, vol. 6, n. 8, pagg. 6984–6989, ago. 2012.

[165] P. Fan *et al.*, «Low-cost flexible thin film thermoelectric generator on zinc based thermoelectric materials», *Appl. Phys. Lett.*, vol. 106, n. 7, pag. 073901, 2015.

[166] J. M. Bian, X. M. Li, C. Y. Zhang, W. D. Yu, e X. D. Gao, «p-type ZnO films by monodoping of nitrogen and ZnO-based p–n homojunctions», *Appl. Phys. Lett.*, vol. 85, n. 18, pagg. 4070–4072, nov. 2004.

[167] J. M. Bian, X. M. Li, X. D. Gao, W. D. Yu, e L. D. Chen, «Deposition and electrical properties of N–In codoped p-type ZnO films by ultrasonic spray pyrolysis», *Appl. Phys. Lett.*, vol. 84, n. 4, pagg. 541–543, gen. 2004.

[168] D. Fan *et al.*, «Dual Extraction of Photogenerated Electrons and Holes from a Ferroelectric Sr0.5Ba0.5Nb2O6 Semiconductor», *ACS Appl. Mater. Interfaces*, vol. 8, n. 22, pagg. 13857–13864, giu. 2016.

[169] C. M. Dudhe, S. B. Nagdeote, e C. P. Chaudhari, «Ferroelectric Domains in Sr0.5Ba0.5Nb2O6 (SBN50) at Nanolevel», *Ferroelectrics*, vol. 482, n. 1, pagg. 104–112, giu. 2015.

[170] S. Gupta, A. Paliwal, V. Gupta, e M. Tomar, «Study of ferroelectric SBN thin films for electro-optic applications», in *2016 Joint IEEE International Symposium on the Applications of Ferroelectrics, European Conference on Application of Polar Dielectrics, and Piezoelectric Force Microscopy Workshop (ISAF/ECAPD/PFM)*, 2016, pagg. 1–3.

[171] T.-T. Fang, E. Chen, e W.-J. Lee, «On the discontinuous grain growth of SrxBa1-xNb2O6 ceramics», *J. Eur. Ceram. Soc.*, vol. 20, n. 4, pagg. 527–530, apr. 2000.

[172] G. D. Mahan e J. O. Sofo, «The Electrical Conductivity of Strontium-Barium Niobate», *J. Electron. Mater.*, vol. 42, n. 7, pagg. 1375–1376, lug. 2013.

[173] J. H. Chan, J. A. Bock, H. Guo, S. Trolier-McKinstry, e C. A. Randall, «Filled oxygen-deficient strontium barium niobates», *J. Am. Ceram. Soc.*, vol. 100, n. 2, pagg. 774–782, feb. 2017.

[174] X. Zhu *et al.*, «A Crystal-Chemical Framework for Relaxor versus Normal Ferroelectric Behavior in Tetragonal Tungsten Bronzes», *Chem. Mater.*, vol. 27, n. 9, pagg. 3250–3261, mag. 2015.

[175] P. B. Jamieson, S. C. Abrahams, e J. L. Bernstein, «Ferroelectric Tungsten Bronze-Type Crystal Structures. I. Barium Strontium Niobate $Ba_{0.27}Sr_{0.75}Nb_2O_{5.78}$», *J. Chem. Phys.*, vol. 48, n. 11, pagg. 5048–5057, giu. 1968.

[176] J. G. Carrio, Y. P. Mascarenhas, W. Yelon, I. A. Santos, D. Garcia, e J. A. Eiras, «Structure Refinement of (Sr,Ba)Nb2O6 Ceramic Powder from Neutron and X-Rays Diffraction Data», *Mater. Res.*, vol. 5, n. 1, pagg. 57–62, mar. 2002.

[177] J. A. Bock, J. H. Chan, Y. Tsur, S. Trolier-McKinstry, e C. A. Randall, «The Effects of Low Oxygen Activity Conditions on the Phase Equilibria and Cation Occupancy of Strontium Barium Niobate: Changes to SBN Under Low $P\,O_2$», *J. Am. Ceram. Soc.*, vol. 99, n. 10, pagg. 3435–3442, ott. 2016.

[178] C. Nikasch e M. Göbbels, «Phase relations and lattice parameters in the system SrO–BaO–Nb2O5 focusing on SBN (SrxBa1−xNb2O6)», *J. Cryst. Growth*, vol. 269, n. 2, pagg. 324–332, set. 2004.

[179] C. S. Dandeneau, T. W. Bodick, R. K. Bordia, e F. S. Ohuchi, «Thermoelectric Properties of Reduced Polycrystalline Sr0.5Ba0.5Nb2O6 Fabricated Via Solution Combustion Synthesis», *J. Am. Ceram. Soc.*, vol. 96, n. 7, pagg. 2230–2237, lug. 2013.

[180] S. Lee, J. A. Bock, S. Trolier-McKinstry, e C. A. Randall, «Ferroelectric-thermoelectricity and Mott transition of ferroelectric oxides with high electronic conductivity», *J. Eur. Ceram. Soc.*, vol. 32, n. 16, pagg. 3971–3988, dic. 2012.

[181] S. Lee, S. Dursun, C. Duran, e C. A. Randall, «Thermoelectric power factor enhancement of textured ferroelectric SrxBa1–x Nb2O6–δ ceramics», *J. Mater. Res.*, vol. 26, n. 1, pagg. 26–30, gen. 2011.

[182] S. Lee, G. Yang, R. H. T. Wilke, S. Trolier-McKinstry, e C. A. Randall, «Thermopower in highly reduced n-type ferroelectric and related perovskite oxides and the role of heterogeneous nonstoichiometry», *Phys. Rev. B*, vol. 79, n. 13, pag. 134110, apr. 2009.

[183] A. Speghini *et al.*, «Phase transition in $Sr_xBa_{1-x}Nb_2O_6$ ferroelectric crystals probed by Raman spectroscopy», *J. Phys. Appl. Phys.*, vol. 39, n. 23, pagg. 4930–4934, dic. 2006.

[184] I. Bhaumik *et al.*, «Influence of cerium doping on the dielectric relaxation of Sr0.75Ba0.25Nb2O6 single crystal grown by the double crucible Stepanov technique», *J. Alloys Compd.*, vol. 621, pagg. 26–29, feb. 2015.

[185] G. M. Kuz'micheva, L. I. Ivleva, I. A. Kaurova, e V. B. Rybakov, «Structural peculiarities and point defects of undoped and Cr- and Ni-doped Sr0.61Ba0.39Nb2O6 crystals», *Acta Mater.*, vol. 70, pagg. 208–217, mag. 2014.

[186] T. S. Chernaya *et al.*, «X-ray diffraction study of cerium-and thulium-doped (Sr, Ba) Nb2 O6 single crystals», *Crystallogr. Rep.*, vol. 48, n. 6, pagg. 933–938, 2003.

[187] K. P. Guzhakovskaya, A. I. Burkhanov, L. I. Ivleva, e I. E. Tumanov, «The Behavior of Current and Dielectric Response in SBN-75:Cr Single Crystal under Illumination Effect», *Ferroelectrics*, vol. 469, n. 1, pagg. 92–96, set. 2014.

[188] S. M. Kaczmarek *et al.*, «Temperature dependence of PL and EPR spectra of Sr0.33Ba0.67Nb2O6:Cr (0.02mol%) single crystals», *J. Cryst. Growth*, vol. 401, pagg. 798–801, set. 2014.

[189] S. H. Kshirsagar, A. N. Tarale, S. R. Jigajeni, D. J. Salunkhe, S. B. Kulkarni, e P. B. Joshi, «Ferroelectric and Magnetodielectric Properties of Cobalt-Doped SrxBa1−xNb2O6 Ceramics», *J. Electron. Mater.*, vol. 44, n. 7, pagg. 2321–2330, lug. 2015.

[190] P. K. Patro, A. R. Kulkarni, e C. S. Harendranath, «Dielectric and ferroelectric behavior of SBN50 synthesized by solid-state route using different precursors», *Ceram. Int.*, vol. 30, n. 7, pagg. 1405–1409, gen. 2004.

[191] S.-G. Lu, C.-L. Mak, e K.-H. Wong, «Low-Temperature Preparation and Size Effect of Strontium Barium Niobate Ultrafine Powder», *J. Am. Ceram. Soc.*, vol. 84, n. 1, pagg. 79–84, 2001.

[192] S. Wanmei, L. Shijun, S. Ranran, e W. Chunlong, «Investigation of the origin of abnormal grain growth in the sintering process of Sr0. 5Ba0. 5Nb2O6 ceramics without eutectic liquid-phase», *J. Ceram. Process. Res.*, vol. 12, n. 6, pag. 716, 2011.

[193] R. Ottini *et al.*, «Feasibility of electron and hole injection in heavily doped strontium barium niobate (SBN50) Sr0.5Ba0.5Nb2O6 for thermoelectric applications», *J. Appl. Phys.*, vol. 121, n. 8, pag. 085104, feb. 2017.

[194] M. P. Trubelja, E. Ryba, e D. K. Smith, «A study of positional disorder in strontium barium niobate», *J. Mater. Sci.*, vol. 31, n. 6, pagg. 1435–1443, gen. 1996.

[195] «Shannon Radii». [In linea]. Available at: http://abulafia.mt.ic.ac.uk/shannon/ptable.php. [Consultato: 04-set-2017].

[196] S. Ding *et al.*, «Growth, structure, spectral properties and crystal-field analysis of monoclinic Nd:YNbO4 single crystal», *Phys. B Condens. Matter*, vol. 503, pagg. 106–110, dic. 2016.